Optical Properties of Quasiperiodically Arranged Semiconductor Nanostructures

DISSERTATION

zur
Erlangung des Doktorgrades
der Naturwissenschaften
(Dr. rer. nat.)

dem Fachbereich Physik
der Philipps-Universität Marburg
vorgelegt von

Marco Werchner

aus Frankenberg (Eder)

Marburg (Lahn), 2009

Vom Fachbereich Physik der Philipps-Universität Marburg
als Dissertation angenommen am 09. Dezember 2009

Erstgutachter: Prof. Dr. Mackillo Kira
Zweitgutachter: Prof. Dr. Wolfgang Stolz

Tag der mündlichen Prüfung: 18. Dezember 2009

Meiner Familie gewidmet

Alle **Wünſche** werden klein
gegen den, **geſund zu ſein.**
Volksweisheit

Contents

Preface

The here presented PhD work consists of two parts. The first one is entitled *One-Dimensional Resonant Fibonacci Quasicrystals* and deals with the optical properties of an array of aperiodically spaced quantum wells (QWs). It covers the chapters 1 to 7. The second part is about *Resonant Tunneling of Light in Silicon Nanostructures*. The propagation of light through alternating silicon barriers and air gaps as well as corresponding effects of sample design are examined. These investigations and the respective results are presented in the chapters 8 to 12. Each part has its own introduction that guides to the details of the specific investigated system and yields additional information related to that subject. It is the aim of this preface to give an overview of the field of semiconductor physics and applications in order to show how the two investigated topics fit into the whole issue of semiconductor science and technology.

Today, everyday life is strongly dependent on semiconductor technology as a result of the so-called electronic revolution. The beginning of this revolution is marked by the fabrication of the first operable transistor made of germanium in 1947 [1–3]. With the help of the transistor, several constraints of the previously used vacuum tubes could have been overcome. In contrast to these tubes, the transistor needs smaller wattage, produces less heat, needs no pre-glow, is more durable, and allows for smaller devices. A disadvantage of the initially used germanium is its sensitivity to damage already due to temperatures slightly above normal room temperature. The transition from germanium to silicon has provided better stability on cost of lower carrier mobility. At the same time, silicon is less expensive than germanium since it can be gained from sand and is deposited in the earth crust with a much higher concentration than germanium. In consequence, these improvements have resulted in the mass production of a rich spectrum

of applications of the silicon technology. One famous outcome of that development is the portable "transistor radio". The significance of the invention of the transistor is expressed in that the radio even carries the transistor in its name. The general impact of the invention of the transistor was honored by the Nobel Prize already shortly after that invention, even several years before the most important application has seen the light of day. While the transistor has been used as an amplifier in the radios, its real power is in the application as a switch, which allows for transistor logical gates. With the invention and manufacturing of integrated circuits (ICs) [4–6], further miniaturization has become possible, which has paved the way for the personal computers and commonly used electronics as we know them today.

The working speed of the semiconductor devices could have been improved with smaller device sizes since big strides have been made in the fabrication techniques. In addition, more effective mass-production has become available. As a result, semiconductor industry, which is based on silicon technology, has developed quickly. A synonym of that development is the "silicon valley", a hot spot of the semiconductor and in particular of the computer industry which has been booming ever. Nevertheless, a kind of measure for the astonishing pace of the development of that industry is Moore's law [7]. Moore's law predicts from experience a doubling of the number of transistors, that can be fabricated cost-effectively on a computer chip, every two years. That law which was established in 1965 is in good agreement with the progress in chip production up to now.

Apart from personal computers, there is a large variety of semiconductor devices in general. Semiconductor devices have captured virtually every field of science and industry due to their efficiency, versatility, and compactness. These devices are actually all around us and available applications are so wide-spread that it is impossible to give a comprehensive list. However, some examples shall be given though. In form of personal computers, semiconductor chips facilitate word and data processing, programming – and thus further numerical research – as well as internet access and e-mail communication. Besides that, ICs control nearly all further electronic applications as well. ICs are utilized in applications such as cell phones and dishwashers, satellites and cars, TV sets and pocket calculators, industrial assembly lines, handhelds, vacuum cleaners, digital cameras (CCD chips [8]), and many more. Moreover, in medical applications, they are being used as well. Additionally, semiconductor diodes are applied in current flow control; the corresponding diode types include among others the normal p-n junction [9], Zener diodes [10], avalanche diodes [11], and tunneling diodes [12–15].

In contrast to the pure electrical properties, the optical features are put to usage in light emitting diodes (LEDs) [16–18]. When the LED is forward biased, the electrons and holes may recombine under emission of light. Due to the small momentum of a photon, direct semiconductors such as e.g. GaAs are used for optical applications while the indirect semiconductors silicon and germanium are mostly utilized for electronic applications. The wavelength of the emitted light corresponds to the band-gap energy of the respective semiconductor material. LEDs emitting in the visible as well as in the infrared spectral range are known. Due to their high-efficiency, they have a high potential as commercial light sources. Based on the inverse process of light-absorption, photo diodes are used e.g. in solar cells [19–21] for carrier generation or as detectors

[22–24].

If in turn a LED is put in an appropriate cavity, lasing [25, 26] can be achieved and one speaks of laser diodes [27–30]. Improved laser performance is obtained if the active region of the laser is realized in form of double heterostructures of small size [31–33], i.e. if quantum-size effects come to play [34, 35] so that the carriers are confined within the so-called quantum wells (QWs). A QW is a quasi-two-dimensional structure in which carriers are free to move within the QW plane. In contrast, the double-heterostructure setup prevents from free carrier motion perpendicular to the QW plane. Hence, translational invariance is broken [36] and the carriers are confined to the QW layer.

In particular, the lasing works even better if multiple QW (MQW) structures with appropriately chosen QW-QW spacings are used. Semiconductor lasers can be found in CD and DVD players and recorders [37–39], laser pointers [40], bar-code readers [41], and laser printers. Even projectors based on semiconductor lasers have been realized [42, 43]. Further fields of usage cover for instance holography [44] and the pump of other lasers [45, 46].

The above sketched wide field of applications of semiconductor devices is in strong contrast to the formerly quite common attitude towards semiconductors from the 1920s and 1930s. The then point of view is reflected by a judgment of Wolfgang Pauli who doubted semiconductors to be worth much study because *one shouldn't wallow in dirt*[1] [47]. That is, because semiconductors stand in between insulators and conductors so that the semiconductors' properties are easily affected and varied by any impurities. However, the putative bad in fact has turned to good account and proved essentially useful! Indeed, the possibility to manipulate the semiconductor material in a desired controllable way is the central key to manufacture appropriate semiconductor devices.

Today, high-quality fabrication techniques provide nearly perfect samples of – with certain restrictions – almost any desired setup. First, there is molecular beam epitaxy (MBE) [48–50] in which molecular beams are directed to a substrate that is placed in ultrahigh vacuum. The beam molecules then form a new epitaxial layer on top of the substrate. That way, single crystals can be grown layer by layer. Moreover, well-defined high precision interfaces of different materials can be created – as long as these materials can be grown on top of each other. At the same time, dopants can easily and well-controlled be introduced to the material layers. Furthermore, superlattices [51] can be achieved, which leads to new effects like for instance due to QW-QW coupling in MQW systems.

Like in MBE, but slightly different though, layer-wise growth is possible in metal organic vapor phase epitaxy (MOVPE) [52, 53] as well. In contrast to MBE, the substrate is now placed in a gas atmosphere which contains a flow of precursors that lead to the growth of the desired alloy layer after a chemical reaction of these precursors. Depending on the type of deposited material, MBE or MOVPE has to be preferred. The removing of material is possible via etching [54, 55] which needs a preceding preparation step that guarantees the etch selectivity. That first step may be lithography [56, 57] or alterna-

[1] a free translation of the German original, see page 7

tively ion implantation [58–60]. The amount of removed material can be controlled by the etch time. Moreover, focused ion beams (FIB) [61, 62] allow to deposit or directly mill away material with high spacial resolution.

These different manners of manufacture and combinations thereof enable sample design according to the needs of applications. In particular, a prerequisite to enter the mass production stage of applicable devices is a standardized and hence well-controlled and well-understood fabrication process. All the progress made in semiconductor physics and technology wouldn't have been possible without ongoing fundamental research, which has been performed on solid-state physics in general [63–67] and in particular on semiconductors [35, 68–77]. Decades of systematic investigations have lead to a well-founded understanding of the linear properties of semiconductor samples. Similarly, nonlinear properties have already been intensively studied, but they are nonetheless subject of further intense research still today [71, 78–82]. That is because nonlinear effects are intimately related to the internal many-body interactions of a sample and thus allow insight to fundamental microscopic processes, which improves the understanding of the intricate semiconductor many-body system.

Additionally, the possible targeted implementation of quantum-size effects [35, 83] has initiated intense studies of systems with reduced dimensionality like the two-dimensional QWs [34, 84–103], the one-dimensional quantum wires [104–107], and the point-like quantum dots [108–114]. The reduction of the system dimensionality may come along with new, enhanced, weakened, or even suppressed material properties. In particular, the detailed sample structure influences the electronic properties so that the design of the electronic bands becomes possible [115]. Band design in turn directly affects the optical properties since the light field couples to the electronic system.

Similarly, the optical properties can be varied by an appropriate design of the dielectric environment as well [116–120]. Therefore, the profound production abilities make the semiconductors ideal laboratories for quantitative research of fundamental interaction processes [121]. The good understanding of the material properties in turn is the basis of bringing these properties to application. Consequently, semiconductors are directly at the intersection of basic research and applications [35, 122–124]. In particular, applications, sample preparation, and basic understanding assist each other and go hand in hand.

An example for that interplay is the use of laser diodes in communication technology. Higher numbers of simple telephone connections as well as digital services like TV and computer data links have demanded large data rates in telecommunication, which relates to the so-called information revolution. The growing need for more bandwidth has pushed the change from the copper cable to optical fibers [125]. In addition, signal loss could have been significantly lowered using fibers. The typical windows of operation of optical fibers are located around wavelengths of 1.3μm and 1.5μm. Consequently, the intended use of optical-fiber waveguides has called for an appropriate electro-optical coupling of electronic signals to the fiber matching the above wavelengths.

It has been laser diodes that have been capable to provide that link between optics

and electronics. Specifically, the laser emission could have been tuned to match the fiber characteristics. Since optical devices are mainly based on the III-V compounds such as GaAs or InP, the devices developed on purpose of that coupling are built on the knowledge about these III-V compound structures at hand. Thus, lasing at the desired wavelengths has been achieved in e.g. InGaAsP/InP [126], AlGaInAs/InP [127], and GaInNAs/GaAs [128].

In contrast to such III-V devices for optical application, electronics bases on silicon. The performance of both, optical and electronic devices has been optimized strongly throughout the years. However, these developments have taken place independently from each other. Nevertheless, it would be desirable to join these two kinds of semiconductor devices, optical and electronic ones, in a single sample. In particular, merging a lasing device and standard electronics on a single chip would result in smaller sizes, more robustness, and cheaper fabrication. Moreover, a large field of new applications would open as well.

But, lasing is difficult to achieve in silicon structures because of the indirect band gap of silicon. Nevertheless, first promising results on lasing in silicon, obtained via different approaches, have been reported in recent years. External optical pump and the Raman effect [129–131] are used as well as doped silicon [132] and strained germanium films grown on silicon [133, 134]. Another approach directly tries to marry III-V compounds and silicon. This try has lead to silicon evanescent lasers [135–137] and to growing III-V lasers on top of a silicon substrate. The big drawback in the latter is the strong lattice mismatch of the common laser materials and silicon. Contrariwise, the indirect material GaP can be grown dislocation-free on silicon [138, 139]. Only recently, lasing has been achieved in a Ga(NAsP)/GaP material system [140–143], which presumably opens the door for further applications via integration on silicon. Additionally, further investigations of these structures will certainly help to gain a deeper understanding of their properties. This may pave the way for novel microchips that exchange data optically on the chip. In this context, a lot of affiliated investigations have already been performed [144–152] that may contribute to the realization of the concept of optical chips. In particular, the control and guidance of light in silicon is a necessary prerequisite for succeeding in that.

Semiconductor technology has had and still has an enormous impact on our life. Tremendous changes have been caused by the wide-spread availability and application of electronic devices as well as by the information technology. Nevertheless, the ongoing miniaturization of these devices is rapidly approaching the intrinsic limitations of today's ICs [153]. One way to overcome that problem could be the above mentioned optical chip [154]. However, the interplay of research and application will certainly lead to further foreseeable but also unforeseeable developments that may enrich and change everyday life.

Über Halbleiter soll man nicht arbeiten,
das ist eine Schweinerei, wer weiß,
ob es überhaupt Halbleiter gibt.

Wolfgang Pauli, 1931

Part I

One-Dimensional Resonant Fibonacci Quasicrystals

1 Introduction

For a time span of more than 200 years, the structure of crystals has been subject of investigations [63]. A result of these investigations has been the definition of *molécules intégrantes* [63] that build up the crystal. Later on, these findings have lead to the definition of a crystal as to be a periodic arrangement of smallest units, called unit cells [66, 67], according to space lattices [64, 65]. Such a periodic arrangement of unit cells results in a translationally invariant crystal lattice, i.e. shifting the periodic crystal as a whole by a lattice vector transforms the crystal into itself. The observation of the periodicity of crystals can be viewed as the foundation of crystallography. The periodicity of crystals has been confirmed by X-ray diffraction [155–160] and other experimental investigations. Moreover, theoretical studies have yielded such powerful and successfully applied tools as, e.g., the Bloch theorem or the Brillouin zone [66, 67] which rely on the periodicity of the crystal lattice. Hence, there has been no need to doubt that successfully used model of periodic crystals. As a consequence, the definition of a crystal to be periodic has not been questioned, though it has never been proven that it is the most general one. Clearly, the periodicity directly establishes perfect long-range order. On the short length scale, fixed nearest-neighbor distances are defined by the unit cell configuration. This unit-cell configuration together with the periodic arrangement of unit cells causes certain symmetries of the crystal lattice. These symmetries manifest themselves in the fourteen Bravais [65–67] lattices which represent all possible (allowed) configurations of periodic crystals.

This long accustomed picture was shaken by the experimental observation of quasicrystals which came into light via electron diffraction patterns with crystallographically forbidden symmetry [161]. Shortly after the experimental observation, a theoretical study [162] could explain the measurements based on the quasicrystal concept for which these crystal symmetries, disallowed in the old periodic model, are allowed. The term *quasicrystal* is an abbreviation for *quasiperiodic crystal* [162] and indicates that quasicrystals lack in the long established periodicity. Thus, the definition of a QC differs from the one of a periodic crystal. In a QC, there is a finite lower and a finite upper limit for the distance between any pair of nearest neighbors, which is also true for pe-

riodic crystals. Additionally, the QC has perfect long-range orientational order while it doesn't have to have periodic but quasi-periodic translational order [162–164]. I.e., in a mathematical description, the density functions of quasicrystalline structures have to be expandable into a finite countable number of plane waves [163, 165]. Still, there is some debate going on whether or not QCs necessarily have to have a symmetry that is forbidden in periodic crystals [165]. Since that claim of a forbidden symmetry is very restrictive and excludes structures with clearly quasiperiodic properties from the QC class, we adopt the view that a forbidden symmetry is not required for a QC. As a consequence, there are QCs also in one dimension, which is not true otherwise.

The so-given definition of a QC in fact also includes the periodic crystals as a subclass of QCs. The corresponding set of wave vectors used in the expansion of the density function can be spanned by a minimal set of wave vectors via integral linear combinations. If that minimal number of needed wave vectors equals the crystal dimension, the crystal is periodic. If it is larger than the crystal dimension, the crystal is quasiperiodic [165].

The introduction of the new quasicrystal concept has affected crystallography at its foundation. In consequence, a controversy about the existence of QCs has ensued. Partly, QCs have been doubted and complicated models have been developed to explain the observation of the forbidden symmetries using only periodic crystals [166, 167]. These attempts to save the old picture of a crystal have been ruled out by further experimental and theoretical studies verifying the existence of QCs [168–173].

Finally, intense investigations of QCs have opened out in a new classification of a crystal being a *"solid having an essentially discrete diffraction diagram"* [174]. This definition includes both the periodic and the quasiperiodic crystals. While the new definition of a crystal has been given from necessity, there have been further suggestions [175, 176] of how to improve the definition of a crystal, meanwhile.

While QCs have been subject of investigations for 25 years, only recently a structurally almost perfect natural QC has been observed in a museum specimen that has formed under geologic conditions [177]. Before that, QCs have been exclusively produced in laboratories. In particular, QCs have initially been found in a rapidly quenched alloy of Al and Mn [161]. Therefore, the subsequent search for further quasicrystalline materials has focused on similar alloys containing Al. Besides others, quasicrystalline structures could thus have been established e.g. in Al-Cu-M with M=Li, Mn, Fe, Co, Ni, V, Cr [178–182]. Today, QC phases have been found in more than 100 combinations of different elements. Apart from the Al systems, further QCs have also been obtained in systems such as e.g. of Ga-Mg-Zn [183, 184], Zn-Mg-(Gd,Tb,Dy,Ho,Er) [185], and Ni-Cr [186].

While the first studied QCs have been metastable, also stable QC phases have been established [187], later on. Investigations on QCs have revealed intriguing quasicrystalline properties which could have been studied in detail with these stable QC phases at hand. For example, observed properties of Al-alloy-based QCs [188, 189] are extreme hardness [190, 191], poor electrical [192–194] and thermal conductivity, low friction [195, 196]

and low adhesion [197, 198], as well as strong resistance against oxidation [199, 200]. In the year 2000, the better understanding and improved fabrication resulted in a first commercial application in form of a non-stick frying pan [201]. In addition, QCs show intriguing features in catalysis [202] and are supposed to have strong impact in this field soon. For a more detailed discussion of possible applications, see e.g. Refs. [188, 189].

The basis of bringing QCs to application is a good understanding of the QC systems, both experimentally and theoretically. Deeper understanding has in particular been gained with the help of artificial QCs. In the production of artificial QCs, the QC structure serves as an input and is enforced. That enforced structure is in contrast to alloy-based QCs which form during a thermalization process. Therefore, the artificial QC structures have allowed to concentrate on the purely quasicrystalline properties while studies on alloy-based QCs initially have mainly focused on the determination of the atomic alloy structure.

Today, there exist several ways of producing artificial QCs. Two-dimensional QCs can be established e.g. by a respective assembly of dielectric cylinders [203–205] or tuning forks [206]. Also the production of films on appropriate surfaces [199, 207–209] yields two-dimensional QC systems. Similarly, optical lattices [210], created by combinations of several monochromatic waves to form a quasiperiodic interference pattern [211–215], allow for realization of QC structures. Moreover, QCs can be found in polymeric systems [216] or can be produced by electron-beam lithography [217]. It is even possible to realize artificial three-dimensional QCs [146, 218]. In particular, one-dimensional QCs can most easily be grown, e.g. by MBE or MOVPE.

From the theory point of view, there are many different ways to model QCs of either dimension. One may use the dual grid method [164, 219], the cut or cut-and-project method [220–223], or deflation and inflation techniques as known from the Penrose tilings [224–226] – see also Refs. [163, 227, 228]. The one thing all the different models have in common is the appearance of irrational numbers causing the aperiodic nature of the QCs. In fact, very often that irrational number is the golden mean [162–164, 177, 182, 187–189, 206–209, 218, 227–230].

The golden mean, $\tau = 0.5+\sqrt{1.25} \approx 1.618\ldots$, is a famous number known already from ancient and medieval architecture and arts [231]. It is often found in nature (sunflowers, daisies, pineapples, ...), and it is intimately related to the Fibonacci numbers [232]. As discussed in more detail in Sec. 2.1, the Fibonacci numbers and the Fibonacci sequence, $LSLSLLSLLSLLS\ldots$, are connatural. In particular, the observation of the Fibonacci sequence is often cited as evidence of the presence of a quasicrystalline structure [164, 195, 196, 208, 213, 214, 229, 230]. Moreover, the one-dimensional Fibonacci sequence is the textbook example of QCs [163, 188, 227, 228]. That is because *one*-dimensional QCs are the most instructive QCs due to their low dimensionality and clear arrangement. Additionally, they are easier to produce than alloy-based or higher-dimensional QCs. The Fibonacci sequence is the most elementary and concise one-dimensional QC.

As a consequence, one-dimensional Fibonacci QCs have been studied intensively, which has lead to the observation of many quasicrystalline features. Already shortly after the discovery of quasicrystals [161], the first MBE grown one-dimensional Fibonacci superlattice has been subject of investigations [233, 234]. The established GaAs-AlAs

superlattice has revealed the typical quasicrystalline dense set of diffraction vectors in X-ray experiments [233] as well as a certain robustness of the detected diffraction peaks against disorder in layer thicknesses [234]. Sharp quasicrystalline diffraction peaks and self-similar spectra have been observed [233]. Additionally, such multifractal spectral properties have been verified experimentally in one-dimensional Fibonacci lattices for phonons and electrons [235], ultrasonic waves [236], and third sound [237] which is a wave in thin films of superfluid liquid helium. Similar predictions for the optical range [238–240] have been confirmed experimentally as well [241–243]. Moreover, optical nonlinear effects such as second- [244, 245] and third-harmonic [245, 246] generation, making use of quasi-phase matching [247] with the help of the dense set of reciprocal vectors, have been investigated. Later on, symmetry effects have been observed [248] and light propagation has been studied [249].

However, attention has been drawn to optically active resonant Fibonacci QCs, realized in form of aperiodically spaced – that is Fibonacci-spaced – QWs, only recently. A first theoretical study has introduced the generalized Bragg condition for the resonant Fibonacci QCs [250]. Since then, only few theoretical investigations have been performed using a constant background refractive index and QW susceptibilities of Lorentzian form. Attempts to grow such resonant Fibonacci-spaced InGaAs/GaAs QWs [251] have resulted in surface gratings, that have been fostered by the non-uniform spacing and have prevented from the observation of the theoretically predicted spectral features [250]. These difficulties could have been overcome by using GaAs/AlGaAs Fibonacci-spaced QWs [252].

Investigations of quasiperiodically spaced QWs are the natural extension of the work performed on the traditional periodic QW structures which are already well understood. Studying periodic MQW structures, investigations have among others been performed on excitonic luminescence [84–86, 253], on the transition from excitonic to polaritonic behavior [254], and on light propagation in MQWs [255], as well as on quantum beats [256, 257], and Rabi flopping [258]. In addition, the optical Stark effect [259–261] screening and band filling effects [88, 89, 262, 263], adiabatic following [264], well-size effects [265], as well as photon echos [266] have been studied. Moreover, Rabi oscillations [264, 267–269], optical superlattices and radiative coupling effects in Bragg and anti-Bragg geometry [93, 257, 270–275], as well as Coulomb memory effects [276] have been subject of investigation. Furthermore, THz radiation can be used to manipulate and/or monitor low-energy excitations and/or quasi-particle states [78, 277–281].

For MQWs put into a cavity [77], the transition from the weak to the strong coupling regime has been studied [282]. Under strong coupling conditions, normal-mode coupling (NMC) which is the solid-state analog of the atomic vacuum-Rabi splitting has been observed [282–284]. For stronger pumps in the nonlinear regime, a saturation of NMC has been found [285, 286]. Moreover, Rabi oscillations [287] and effects of carrier-carrier scattering on these oscillations [288] as well as effects caused by structural disorder [289] have been investigated.

As discussed above, periodically arranged MQW structures have already been studied very intensively. Consequently, many applications also rely on MQW structures. Nevertheless, there is a lot of ongoing research on periodic MQW structures still today.

The subject of this first part of the thesis are *One-Dimensional Resonant Fibonacci Quasicrystals* realized in form of quasiperiodically arranged QWs. Hence, this work directly affiliates to recent investigations that initiated the research of resonant Fibonacci MQW QCs [250–252]. In addition, it is intimately related to the studies on periodically spaced MQW structures. In particular, quasiperiodic MQW structures stand in between periodic and disordered MQW structures due to the deterministic but aperiodic arrangement. Thus, it is interesting to see in how far effects known from periodic MQW structures can be found in MQW QCs or not.

The presentation of the investigated subjects is structured as follows. After the setup of the investigated system as well as its microscopic theoretical modeling is introduced in Chap. 2, the Semiconductor Bloch Equations which describe the system dynamics are discussed in Chap. 3. Then, the applied transfer-matrix method is discussed in Chap. 4. These tools enable theory-experiment comparisons presented in Chap. 5. Further, purely numerical studies of the origin of the observed optical properties are subject of Chap. 6. Finally, the findings are summarized in Chap. 7.

Most of the results on resonant Fibonacci QCs have been published in Ref. [290]. *Therefore, when presenting and discussing the respective results in Chaps. 5 and 6, the line of argumentation is kept close to the presentation in that paper.*

2 Investigated System

In this chapter, we will establish the basis of the investigations on resonant Fibonacci QCs. Starting from the properties and the construction of the Fibonacci numbers and the Fibonacci sequence, we will next recall the description of resonant Fibonacci QCs [250]. Then, the detailed structure of the investigated samples is introduced, which is followed by modeling these structures in the framework of a microscopic theory. That will lead us to the Semiconductor Bloch Equations which are discussed in Chap. 3 and which allow for numerical simulations of the samples.

2.1 Fibonacci Quasicrystals

2.1.1 Definition and Construction

The Fibonacci sequence has inherited its name from the Fibonacci numbers [232] which are constructed in a very similar way: Originally, the Fibonacci numbers $1, 1, 2, 3, 5, 8, 13, ...$ have been defined from a mathematical exercise known as "Fibonacci's rabbit problem" [291]. A generic form of that problem is defined on the basis of a large building block L and a small building block S. The problem deals with the number of occurrence of the two elements L and S in different strings that consist of these elements. The initial string contains only a single S block. The subsequent strings are obtained by repeatedly applying the substitution rules

$$S \rightarrow L\,, \tag{2.1}$$
$$L \rightarrow LS\,, \tag{2.2}$$

see left side of Fig. 2.1. The Fibonacci sequence is the infinitely long string which is gained by infinitely often application of the above substitution rules. Though the construction of that sequence starts from a single S block, the Fibonacci sequence begins with a L as a consequence of the substitution Eq. (2.1). Additionally, the building blocks L and S are concatenated aperiodically. Nevertheless, the structure is deterministic as a consequence of the substitution rules.

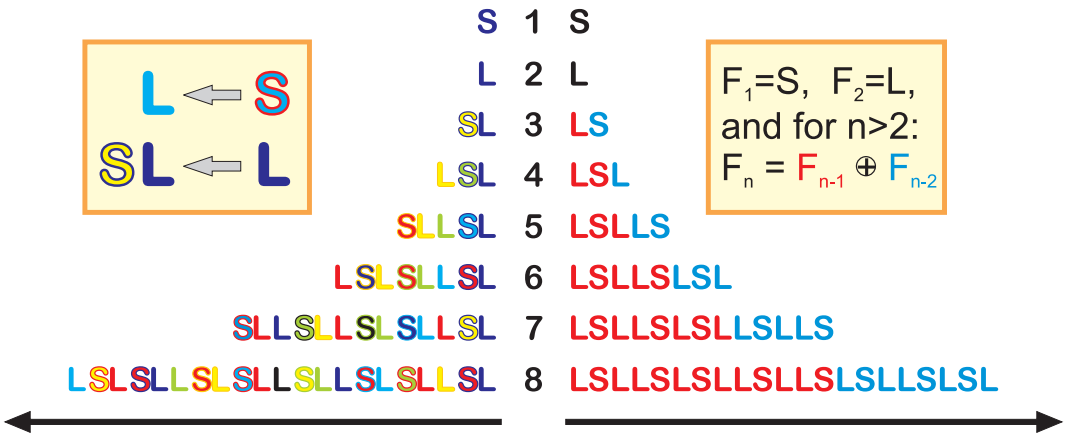

Figure 2.1: The Fibonacci sequence: The number of string generations is given in the center column. The left part of the figure should be read from right to left. It indicates the construction of the Fibonacci sequence according to the substitution rule [291]. The substitution is indicated in the left box with the help of a color code, where the rim of a small building block is colored like the large block it originates from. The color of a large block corresponds to the face color of the small block it stems from. The correspondence between the left and the right half is gained by mirroring. The latter side is to be read from left to right. There, the Fibonacci sequence is constructed by concatenating two successive Fibonacci generations in order to obtain the adjacent generation, see the right box.

The substitutes of both, L and S, contain one L block each. Hence, the number of L blocks in the n^{th} Fibonacci string F_n equals the total number of blocks in the $(n-1)^{th}$ string F_{n-1}. Additionally, every S block in F_n stems from a L block in F_{n-1}. The number of these L blocks corresponds in turn to the total number of blocks in the $(n-2)^{th}$ string F_{n-2}. If the number of building blocks in F_n is given by F_n[1], we therefore find $F_n = F_{n-1} + F_{n-2}$ if $n > 2$ and with $F_1 = 1$ and $F_2 = 1$, which is the definition of the Fibonacci numbers.

For large n, the ratio of consecutive Fibonacci numbers tends towards the golden mean, $\tau = 0.5 + \sqrt{1.25} \approx 1.618\ldots$, which is an irrational number [232]. Consequently, the ratio of the frequencies of occurrence of L and S blocks equals τ in the limit $n \to \infty$. As can be seen from Fig. 2.2, that ratio is converging very fast towards τ. In particular, already the ratio $F_7/F_6 = 13/8$ deviates less than a percent from the golden mean. Likewise, already finite sequences of sufficiently large numbers of building blocks show properties akin to the ones of the infinite Fibonacci sequence. Moreover, such finite sequences can be described in good approximation with the help of a theory that has been developed for the infinite Fibonacci sequence. That theory is subject of Sec. 2.1.2.

The aperiodicity of the Fibonacci sequence is caused by the irrationality of the golden mean. This can be nicely seen in another method of constructing this sequence. The

[1]Note the difference between the number F_n and the string F_n of building blocks

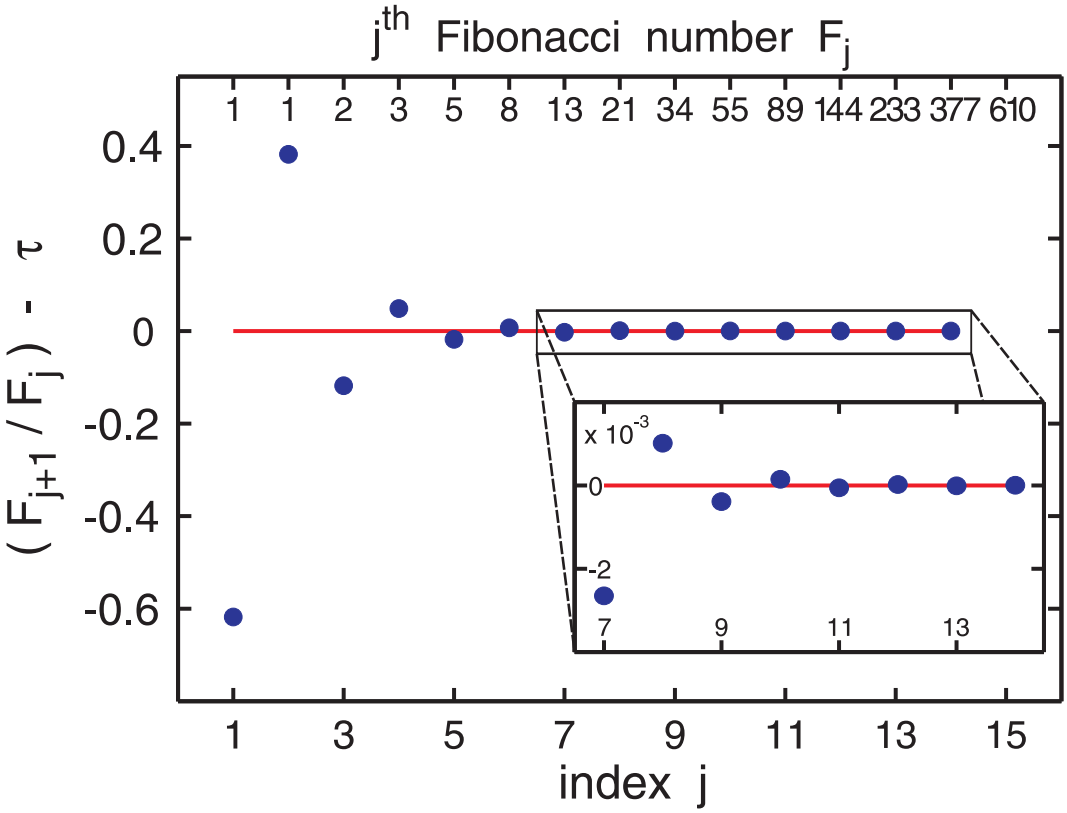

Figure 2.2: The ratio of subsequent Fibonacci numbers F_j, which are given in the upper x-axis, tends towards the golden mean $\tau = 0.5 + \sqrt{1.25} \approx 1.618\ldots$.

cut-and-project method, see Refs. [163, 220–223, 292] and appendix A, projects lattice points of a higher-dimensional lattice to a lower-dimensional subspace. Only selected points that are located within a certain volume around that subspace are taken into consideration in the projection. In order to construct the one-dimensional Fibonacci sequence, one uses a two-dimensional lattice and projects certain lattice points onto a line $\mathcal{L}$ that has a slope which is irrational. The projected points are all located within a strip the borders of which are parallel to $\mathcal{L}$, see Fig. A.1. As a consequence of that slope being irrational, the lattice and the line $\mathcal{L}$ are incommensurate and have only one common point. Thus, the projection cannot be periodic.

More insight into the arrangement of the building blocks in the Fibonacci sequence can be gained from yet another construction method. Figure 2.1 shows that the sequence can alternatively be constructed via the concatenation $\mathrm{F}_n = \mathrm{F}_{n-1} \oplus \mathrm{F}_{n-2}$ if $n > 2$ with $\mathrm{F}_1 = S$ and $\mathrm{F}_2 = L$. That concatenation means positioning F_{n-2} right of F_{n-1}, which is equivalent to the constructions discussed before. The definition of the concatenation additionally shows the kinship of the Fibonacci sequence with the Fibonacci numbers. Due to that concatenation, the finite partial strings of the Fibonacci sequence occur repeatedly in the infinitely long Fibonacci string. In particular, any substring of the Fibonacci sequence can be found infinitely often in the infinitely long string, $\mathrm{F}_{n\to\infty}$. Nevertheless,

the occurrence of these partial sequences is not periodic; in fact, the Fibonacci sequence has aperiodic, or better to say quasiperiodic translational order.

Concerning the further properties that identify a QC, the minimal and maximal distances between nearest neighbors are guaranteed by the two building blocks L and S. Thus, the Fibonacci sequence indeed forms a one-dimensional quasicrystal. In the one-dimensional case, these two conditions, long-range order and the existence of minimal and maximal nearest-neighbor distances, are sufficient for the identification of a quasicrystal as there is no analog of orientational order in one dimension.

2.1.2 Properties and Formulae

While the position of the m^{th} lattice point of a one-dimensional periodic lattice with lattice constant d and orientation in z direction is simply given by $z_m = z_0 + md$, where z_0 is a shift of the whole lattice, it is not straightforward to define the position of the m^{th} lattice point in a quasicrystal. Nevertheless, the deterministic structure of the infinitely long Fibonacci sequence allows for the definition of the lattice-point positions via

$$z_m \;=\; z_0 + m\bar{d} + r(m), \tag{2.3}$$

where z_0 is again a shift of the whole lattice, the mean period of the lattice is given by $\bar{d}$, and $r(m)$ is a modulation function. This form of defining the lattice point positions is well known from the one-dimensional incommensurate chains [293, 294] with building blocks S and L. In general, the modulation function $r(m)$ has the form

$$r(m) = \Delta \left\{ \frac{m}{t} + \varphi \right\} \,, \tag{2.4}$$

where in general $\{x\}$ determines the fractional part of x and the modulation strength is given by Δ. In case of rational t, the structure becomes periodic with a compound unit cell. In terms of the cut-and-project method, the line $\mathcal{L}$ of rational slope t is then commensurate with the lattice. In general, an irrational t leads to aperiodically structured crystals [163]. In particular, if one claims a crystallographically forbidden symmetry for QCs, there are no QCs in one dimension. Rather, in one dimension, then there are incommensurately modulated crystals which posses a crystallographically allowed symmetry. Since we do not postulate that forbidden symmetry, we do not need to distinguish between modulated crystals and QCs. Finally, the remaining structure parameter φ determines the initial phase of the modulation function $r(m)$, which defines the sequence of the intervals L and S within the chain.

In the infinitely long string, the mean period of the lattice is given by

$$\bar{d} \;\equiv\; l_S \left(\frac{\varrho - 1}{t} + 1 \right) , \tag{2.5}$$

where we introduced the ratio, $\varrho \equiv l_L / l_S$, of the lengths l_L and l_S of the building blocks L and S, respectively. Thus, the modulation strength is defined as

$$\Delta \;\equiv\; l_S - l_L \;=\; l_S(1 - \varrho) \,. \tag{2.6}$$

Note that the quasiperiodicity ($t \notin \mathbb{Q}$) of the sequence in general does not depend on ϱ [164, 233], except $\varrho = 1$ where $l_L = l_S$ are degenerate. The ratio of frequencies of occurrence of large intervals, N_L, and small intervals, N_S, depends on the irrational number t and is given by

$$\frac{N_L}{N_S} = \frac{1}{t-1}\,. \tag{2.7}$$

This ratio is independent of φ showing that φ only effects on the arrangement of the building blocks, not on their number.

The optical properties of such a sequence are determined by the structure factor that describes how incident radiation is scattered by the structure which the radiation is shined on. The structure factor reads

$$f(q) \equiv \lim_{N\to\infty} \frac{1}{N} \sum_{m=1}^{N} \exp(i2qz_m)\,. \tag{2.8}$$

In the limit $N \to \infty$, the structure factor of a quasicrystal [164, 220] consists of δ-peaks which correspond to the Bragg diffractions and densely fill the reciprocal space,

$$f(q) = \sum_{h,h'=-\infty}^{\infty} \delta_{2q,G_{h,h'}} f_{h,h'}\,, \tag{2.9}$$

where the diffraction vector,

$$G_{h,h'} = \frac{2\pi}{\bar{d}} \left(h + \frac{h'}{t} \right)\,, \tag{2.10}$$

equals a reciprocal-lattice vector that is identified by two integer numbers h and h' [163, 295]. For t being irrational and ϱ different from 1, one finds the intensity of the peaks given by

$$f_{h,h'} = \frac{\sin S_{h,h'}}{S_{h,h'}} \exp(i\Theta_{h,h'})\,, \tag{2.11}$$

with the abbreviations

$$\Theta_{h,h'} = (z_0 + \Delta\{\varphi\})G_{h,h'} + S_{h,h'}\,, \tag{2.12}$$

$$S_{h,h'} = \frac{\pi\Delta h}{\bar{d}} + \pi h' \left(1 + \frac{\Delta}{t\bar{d}} \right) = \pi h' + \frac{\Delta}{2} G_{h,h'}\,, \tag{2.13}$$

for otherwise arbitrary choice of $\bar{d}$, ϱ, t, and φ [290].

The Fibonacci sequence [164] is obtained if $t = \tau$ and $\varphi = 0$, c.f. appendix A. In particular, the *canonical* Fibonacci sequence corresponds to $\varrho = \tau$. This case is special in that each inflation step, i.e. each new generation of a string F_{n+1}, always enlarges the length of a string F_n by a factor of τ because it holds $l_L = \tau l_S$ and $l_{LS} = l_L + l_S =$

$(1+\tau^{-1})l_L = \tau l_L$. Hence, the different generations are self-similar, which is no necessary prerequisite of a QC but an additional property of the canonical Fibonacci sequence. If $t = \tau$ and $\varphi = 0$ while $\varrho \neq \tau$ and $\varrho \neq 1$, one obtains the noncanonical Fibonacci quasicrystals. Another prominent case is $\varrho = 1$ so that the quasiperiodic sequence is turned into the periodic crystal, $l_S = l_L$, so that $\Delta = 0$. In that sense, the periodic crystals are a subclass of quasicrystals.

In periodic crystals, the resonant Bragg condition is obtained by equalizing the reciprocal lattice vectors with the double light wave vector. In analogy, using the reciprocal lattice vectors, Eq. (2.10), the resonant Bragg condition for Fibonacci quasicrystals [250] reads

$$q(\omega_0)\bar{d} \;=\; \pi\left(h + \frac{h'}{\tau}\right), \tag{2.14}$$

where the resonance frequency is given by ω_0. Equation (2.14) accounts only for a uniform dielectric environment with constant index of refraction. However, the nontrivial dispersion of a QW as well as a structured dielectric environment lead to modifications of that Bragg condition, in analogy with periodically spaced multiple QWs [270]. Since a rigorous analytical generalization for such more complicated structures cannot be given, we overcome this difficulty by using the concept of the optical path length.

In particular, we assume the index of refraction to be constant within each material layer. The optical path length of a layer is then defined as the product of the physical thickness of a layer and it's index of refraction. With the help of that concept, the propagation of an electromagnetic wave through a complicated dielectric environment consisting of several material layers with different refractive indices can be described in a uniform way. Particularly, making use of the optical path length allows for a comparison of layer properties in terms of the vacuum wavelength, which provides a more intuitive insight into the sample lengths and to wave propagation through the sample.

In the physical sample, additional effects like multiple reflections of the wave at the several layer interfaces take place, which is not taken into account by the concept of the optical path length. We discuss the inclusion of these effects in Chap. 4. Rather, the concept of the optical wavelength is useful in the design of a sample, where interference effects have to be considered and hence distances have to be treated in a uniform and comparable way. Thus, one may use Eq. (2.14) in case of a complicated sample structure, if the average spacing $\bar{d}$ is replaced by the average of the optical path lengths of the spacings,

$$D \;=\; o_S\left(\frac{\rho - 1}{t} + 1\right), \tag{2.15}$$

where ρ is now defined as the ratio $\rho = o_L/o_S$ of the optical path lengths o_L and o_S corresponding to the respective spacings L and S. The wave vector is then given by $q(\omega_0) = \omega_0/c \equiv 2\pi/\lambda$, where c is the velocity of light and λ is the vacuum wavelength.

In the canonical case, Eqs. (2.8)–(2.14) provide the strongest resonances for pairs (h, h') with large coefficients $|f_{h,h'}|$, which is the case if h and h' are successive Fibonacci

numbers (F_n, F_{n+1}) [164]. Thus, the n^{th} Bragg resonance, obtained from the generalized Bragg condition, is identified by the pair of Fibonacci numbers (F_{n-1}, F_n). If $\rho = 1$, Eq. (2.14) reproduces the well-known result for periodic crystals, i.e. the two integers h and h' reduce to just a single one.

2.2 Sample Setup

In this work, we investigate one-dimensional resonant Fibonacci quasicrystals realized in form of MQW structures with two different QW-QW distances. These QW-QW distances range from the center of one QW to the center of a neighboring QW and correspond to the two building blocks L and S of the Fibonacci sequence. In order to achieve a resonant Fibonacci QC, the QWs are arranged such that the QW-QW distances form the Fibonacci sequence. Such structures have been investigated for the first time theoretically in Ref. [250] and experimentally in Ref. [252].

In particular, the experimental data that will be discussed in the theory-experiment comparisons has been taken from the same samples that have been studied in Ref. [252]. In addition to the investigations on such canonical Fibonacci QCs, a purely numerical study of similar noncanonical resonant Fibonacci QCs is performed as well. Concerning the design of such samples, the structure parameters of resonant MQW QCs with exciton resonance frequency ω_{1s} can directly be obtained from the resonant Bragg condition Eq. (2.14). Once the average QW spacing D is fixed, the choice of ρ establishes the large and small spacers L and S. Aiming at the modeling of a realistic MQW structure, we also include barrier, adjuster, and buffer layers besides the QWs and spacers. Such structures can be realized [296] by growing a stack of layers of different materials e.g. by MBE. The physical thicknesses of the respective layers have to be chosen such that the correct optical lengths o_L and o_S of the large and small building blocks are obtained.

The structure of the investigated samples is shown in Fig. 2.3. In the middle of that figure, the detailed sequence of material layers is depicted. A color code is used to distinguish the different types of layers and thus to indicate the intricate setup of the samples. At the top, the Fibonacci sequence of large (L, red) and small (S, blue) structural units is shown. The correspondence of the Fibonacci sequence with the detailed sequence of the different material layers is established by dashed red lines ending at the centers of the QWs which are plotted in dark blue. The large (L) and small (S) building blocks are grown such that the Fibonacci sequence is obtained in direction from the sample-air interface (left) towards the substrate (right). In particular, each structural unit L or S contains (from left to right) half a QW followed by a barrier, an adjuster, a spacer, and another barrier layer as well as half of the neighboring QW. The only difference between the large and the small units is the physical thickness of the respective spacer layer included in L or S. The thicknesses of the QW, barrier, and adjuster layers are identical in each case. Later on, when varying D or ρ, only the thicknesses of the spacer layers are adjusted according to the corresponding optical path lengths.

The composition of the large and the small building blocks is shown in more detail in the bottom part of the figure. At the left hand side, the large (red area) and small

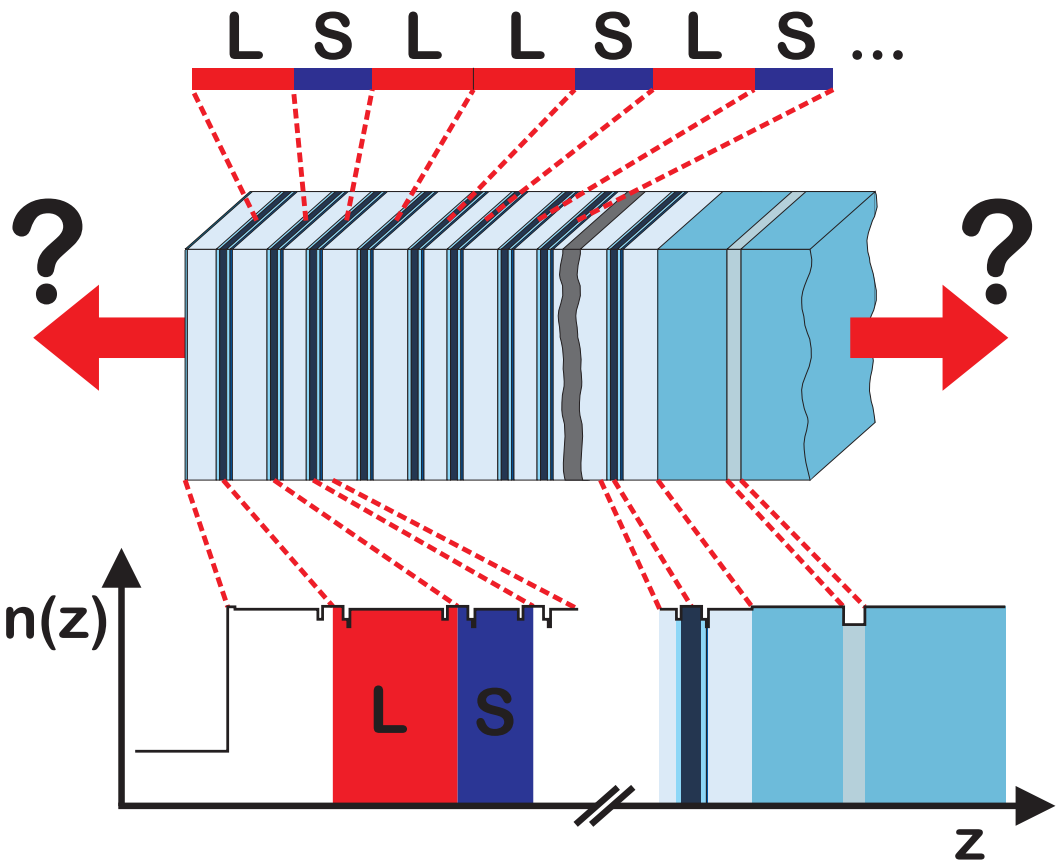

Figure 2.3: The samples consist of stacks of material layers grown by MBE (middle). Each sample is grown on a GaAs substrate (right) and has a GaAs-air interface (left). The QWs are separated by large building blocks L and small building blocks S. The sequence of these structural units follows the Fibonacci sequence, $LSLLSLSL$..., in direction towards the substrate (top). These L and S building blocks consist of different material layers with differing refractive indices, as indicated in the lower left part. The color code of the material layers is connected with the refractive index profile $n(z)$ in the lower right part of the figure.

(blue area) structural units are indicated within the refractive-index profile of the sample showing the intricate substructure of these building blocks. At the right hand side, the refractive-index profile is set in relation to the different material layers using the color code. Again, the correspondence to the layer sequence (middle) is given by the dashed red lines.

The number of material layers within a sample ranges from ten layers in case of a single QW (SQW) up to 275 layers in case of 54QWs. In the entirely numerical investigations, samples with even higher layer numbers have been studied. Altogether, the appearing layers can be categorized into only seven types. A single set of parameters for these seven

	periodic Bragg, $\rho = 1$			canonical Fibonacci, $\rho = \tau$		
j	D/λ	o_S/λ	o_L/λ	D/λ	o_S/λ	o_L/λ
1	0.5000	0.5000	0.5000	0.5000	0.3618	0.5854
2	1.0000	1.0000	1.0000	0.8090	0.5854	0.9472
3	1.5000	1.5000	1.5000	1.3090	0.9472	1.5326

Table 2.1: Comparison of sample parameters for the periodic Bragg spacing ($\rho = 1$) and for the canonical Fibonacci spacing ($\rho = \tau$) for the first three Bragg resonances, $j = 1, 2, 3$.

layer types is used in all computations. The specific sample details such as the layer thicknesses, the refractive indices, and the particular sequence of the different layers are given in appendix B. Some typical sample parameters – D, L, and S – corresponding to the investigated system class are shown in Tab. 2.1 for the periodic spacing, $\rho = 1$, as well as for the canonical Fibonacci spacing, $\rho = \tau$.

2.3 Total Hamiltonian

In order to appropriately describe such systems and their optical response, one needs to know the respective Hamilton operator that contains the system properties. In particular, a microscopic description of the carrier system and its internal interactions as well as its interaction with light fields is necessary. Since the derivation of that Hamilton operator is well known, only the corresponding result shall be given here while further details can be found e.g. in Refs. [69–71].

The strength of Coulomb interaction scales with the inverse of the carrier separation. As the QW-QW separation is in the order of the wavelength corresponding to the 1s-exciton resonance, interactions among carriers being located in different QWs are negligible compared to the interaction of carriers located within the same QW. Therefore, we consider only carrier-carrier interactions within one and the same QW and consequently assume the QWs to be only radiatively coupled. The radiative coupling will be modeled with the help of the transfer-matrix approach, Chap. 4, which makes it sufficient to formulate the microscopic description of the system for a SQW, only.

The corresponding full Hamilton operator reads

$$H \;=\; H_0 + H_C + H_I \;. \tag{2.16}$$

The free, non-interacting carrier system is described by H_0 which includes the effects from the background potential of the lattice of ions. The Coulomb interaction among these carriers is given by H_C. Interactions between a coherent light field and the QW material are described by H_I. These three parts of the Hamilton operator will be introduced in more detail in the following sections.

2.3.1 Carrier System

In a quantum-mechanical description in second quantization, the carrier system can be described with the help of field operators $\psi^\dagger(\mathbf{r})$ [$\psi(\mathbf{r})$] which create [annihilate] an electron at position $\mathbf{r}$. These field operators may be expanded into single-particle wave functions $\phi_{\nu,\mathbf{k}}(\mathbf{r})$,

$$\psi^\dagger(\mathbf{r}) = \sum_{\nu,\mathbf{k}} a^\dagger_{\nu,\mathbf{k}} \phi^\star_{\nu,\mathbf{k}}(\mathbf{r}) \qquad \text{and} \qquad \psi(\mathbf{r}) = \sum_{\nu,\mathbf{k}} a_{\nu,\mathbf{k}} \phi_{\nu,\mathbf{k}}(\mathbf{r}) \;, \tag{2.17}$$

where the expansion coefficients $a^\dagger_{\nu,\mathbf{k}}$ ($a_{\nu,\mathbf{k}}$) are operators that create (annihilate) an electron with momentum $\mathbf{k}$ in band ν. The electron creation and annihilation operators have to obey the fermionic anti-commutation relations

$$\begin{aligned} \left[a_{\nu,\mathbf{k}}, a^\dagger_{\mu,\mathbf{k}'}\right]_+ &= \delta_{\nu,\mu}\delta_{\mathbf{k},\mathbf{k}'} \;, \\ \left[a^\dagger_{\nu,\mathbf{k}}, a^\dagger_{\mu,\mathbf{k}'}\right]_+ &= \left[a_{\nu,\mathbf{k}}, a_{\mu,\mathbf{k}'}\right]_+ = 0 \;. \end{aligned} \tag{2.18}$$

The single-particle wave functions $\phi_{\nu,\mathbf{k}}(\mathbf{r})$ are solutions of the time-independent Schrödinger equation

$$\left(-\frac{\hbar^2}{2m}\nabla^2 + \mathrm{V}_L(\mathbf{r})\right)\phi_{\nu,\mathbf{k}}(\mathbf{r}) = \varepsilon^\nu_{\mathbf{k}}\phi_{\nu,\mathbf{k}}(\mathbf{r}) \;, \tag{2.19}$$

with the lattice-periodic potential $\mathrm{V}_L(\mathbf{r})$ and the band structure $\varepsilon^\nu_{\mathbf{k}}$. In particular, $V_L(\mathbf{r})$ contains the sample geometry, say the stacked sample structure in z-direction and the large extensions of all layers in the x-y plane. The carriers are located in the QWs which are quasi two-dimensional systems due to a strong confinement potential in z-direction. In particular, we assume sinusoidal eigenfunctions $\zeta_\nu(z)$ in confinement direction that do not penetrate the neighboring barrier layers. Hence, we assume the carriers to be entirely confined to the QW layer, which corresponds to the problem of a particle in a box [34] with infinitely large potential energy outside the box. In contrast to the z-direction, the carriers do not suffer any confinement in the QW plane. Thus, their in-plane propagation is free and can be described by plane waves. As a consequence, it is convenient to split the position and momentum vectors into the in-plane and the z coordinates, $\mathbf{r} = (\mathbf{r}_\parallel, z)$ and $\mathbf{k} = (\mathbf{k}_\parallel, k_z)$, respectively. In the envelop approximation [69, 297], the single-particle wave functions $\phi_{\nu,\mathbf{k}}(\mathbf{r})$ may then be written in the form

$$\phi_{\nu,\mathbf{k}}(\mathbf{r}) = \zeta_\nu(z)\frac{1}{\sqrt{A}}e^{i\mathbf{k}_\parallel\mathbf{r}_\parallel}w_\nu(\mathbf{r}) \;, \tag{2.20}$$

where the plane waves are given by $\sqrt{A^{-1}}\exp(i\mathbf{k}_\parallel\mathbf{r}_\parallel)$ with the quantization area A, and the lattice-periodic Bloch function given by $w_\nu(\mathbf{r})$. As a result of the carrier confinement, there is no translational invariance in z-direction [36]. k_z is no good quantum number anymore and the confinement function $\zeta(z)$ appears in Eq. (2.20) instead of a

plane wave $\sqrt{Z^{-1}}\exp(ik_z z)$ with the quantization length Z. Additionally, the confinement in z direction results in quantized eigenenergies which yield a set of subbands. These eigenenergies scale with the QW width Δw like $E \propto 1/\Delta w^2$. Consequently, the energetic separation of neighboring subbands becomes the larger the narrower the QW is. The investigated QWs consist of the direct semiconductor GaAs. The fundamental optical transitions therefore take place at the Γ-point. While bulk GaAs has degenerate light-hole and heavy-hole valence bands at the Γ-point, this degeneracy is lifted by the confinement in z-direction in QWs [69]. Due to that and due to the large energetic distance among bands in narrow QWs, we may restrict ourselves to a two-band model considering only one valence band and one conduction band. Since the typical photon momenta corresponding to the optical transitions are small in comparison to typical carrier momenta, the energy range of interest is in the vicinity of the fundamental band edge. Near the Γ-point, the band structure may be described by parabolic bands in good approximation [115]. This leads to the dispersion of free electrons, where the effective electron masses of the respective bands have to be used.

With these assumptions, the Hamiltonian of the free and non-interacting carriers is obtained as

$$H_0 = \sum_{\mathbf{k}_\parallel} \left(\varepsilon^c_{\mathbf{k}_\parallel} a^\dagger_{c,\mathbf{k}_\parallel} a_{c,\mathbf{k}_\parallel} + \varepsilon^v_{\mathbf{k}_\parallel} a^\dagger_{v,\mathbf{k}_\parallel} a_{v,\mathbf{k}_\parallel} \right) , \tag{2.21}$$

where we introduced the index c (v) for the conduction (valence) band operators and single-particle energies. The latter ones are defined via

$$\varepsilon^c_{\mathbf{k}_\parallel} = E_g + \frac{\hbar^2 \mathbf{k}_\parallel^2}{2m_c} \qquad \text{and} \qquad \varepsilon^v_{\mathbf{k}_\parallel} = \frac{\hbar^2 \mathbf{k}_\parallel^2}{2m_v} , \tag{2.22}$$

where E_g denotes the non-renormalized band-gap energy, $\hbar$ denotes Planck's constant divided by 2π, and the effective electron mass in the conduction (valence) band is given by m_c (m_v).

The carrier-carrier interaction is described by the Coulomb Hamilton operator

$$\begin{aligned} H_C = \frac{1}{2} \sum_{\mathbf{k}_\parallel, \mathbf{k}'_\parallel} \sum_{\mathbf{k}''_\parallel \neq 0} V_{\mathbf{k}''_\parallel} & \left(a^\dagger_{v,\mathbf{k}_\parallel + \mathbf{k}''_\parallel} a^\dagger_{v,\mathbf{k}'_\parallel - \mathbf{k}''_\parallel} a_{v,\mathbf{k}'_\parallel} a_{v,\mathbf{k}_\parallel} \right. \\ & + a^\dagger_{c,\mathbf{k}_\parallel + \mathbf{k}''_\parallel} a^\dagger_{c,\mathbf{k}'_\parallel - \mathbf{k}''_\parallel} a_{c,\mathbf{k}'_\parallel} a_{c,\mathbf{k}_\parallel} \\ & \left. + 2 a^\dagger_{c,\mathbf{k}_\parallel + \mathbf{k}''_\parallel} a^\dagger_{v,\mathbf{k}'_\parallel - \mathbf{k}''_\parallel} a_{v,\mathbf{k}'_\parallel} a_{c,\mathbf{k}_\parallel} \right) . \end{aligned} \tag{2.23}$$

These combinations of four electron creation and annihilation operators describe processes where two carriers with initial in-plane momenta $\mathbf{k}_\parallel$ and $\mathbf{k}'_\parallel$ exchange the in-plane momentum $\mathbf{k}''_\parallel$. Repulsive intraband scattering takes place between two valence-band carriers (first line) or two conduction-band carriers (second line). Interband scattering is obtained among conduction- and valence-band carriers (third line), which is an attractive interaction between conduction-band electrons and valence-band holes, i.e. missing

electrons. The prefactor $\frac{1}{2}$ prevents from double counting and the interaction strength is given by the quasi-two-dimensional Coulomb matrix element

$$V_{\mathbf{k}_\parallel} = \frac{e^2}{2\epsilon_0 \left|\mathbf{k}_\parallel\right|} \int g(z)g(z')e^{-\left|\mathbf{k}_\parallel\right||z-z'|}\mathrm{d}z\,\mathrm{d}z' \,, \tag{2.24}$$

where the electron charge is given by e and the electric permeability is given by ϵ_0. The confinement functions of the conduction band, $\zeta_c(z)$, and of the valence band, $\zeta_v(z)$, are taken into account via $g(z) = \zeta_c(z)\zeta_v^\star(z) = \zeta_v(z)\zeta_c^\star(z) \equiv |\zeta(z)|^2$, assuming identical confinement functions for both bands.

2.3.2 Light-Matter Interaction

One of the characteristic features of a semiconductor is its band gap. The band gap energy E_g is the energy difference between the lowest conduction-band state and the highest valence-band state. Typically, the band gap energy corresponds to wavelengths in the optical (or infrared) range. In consequence, a photon carrying an energy $\hbar\omega > E_g$ may excite an electron from the valence band into the conduction band. If the semiconductor is excited by laser light, a classical treatment of the light field is sufficient. For the description of the interaction of such optical fields with the above discussed carrier system, we use a semi-classical approach via the light-matter interaction Hamiltonian in dipole approximation

$$H_I = -\sum_{\mathbf{k}_\parallel,\mathbf{q}_\parallel} \left(\mathbf{E}(\mathbf{q}_\parallel,t)\cdot\mathbf{d}_{cv}(\mathbf{k}_\parallel)a^\dagger_{c,\mathbf{k}_\parallel}a_{v,\mathbf{k}_\parallel-\mathbf{q}_\parallel} + h.c.\right) \,, \tag{2.25}$$

where $h.c.$ denotes the Hermite conjugate. Here, the light field

$$\mathbf{E}(\mathbf{q}_\parallel,t) = \int \mathrm{d}z g(z)\mathbf{E}(\mathbf{q}_\parallel,z,t) \,, \tag{2.26}$$

with the in-plane photon momentum $\mathbf{q}_\parallel$ and with

$$\mathbf{E}(\mathbf{q}_\parallel,z,t) = \int \mathrm{d}\mathbf{r}_\parallel\, e^{i\mathbf{q}_\parallel\cdot\mathbf{r}_\parallel}\,\mathbf{E}(\mathbf{r}_\parallel,z,t) \,, \tag{2.27}$$

is treated classically while a quantized description is applied for the matter part. The excited conduction-band electron is created ($a^\dagger_{c,\mathbf{k}_\parallel}$) in a state with the carrier momentum $\mathbf{k}_\parallel$ and the initial valence-band electron is annihilated ($a_{v,\mathbf{k}_\parallel-\mathbf{q}_\parallel}$) from a state with carrier momentum $\mathbf{k}_\parallel - \mathbf{q}_\parallel$. The strength of this transition of the electron from the valence to the conduction band is governed by the dipole matrix element

$$\mathbf{d}_{cv}(\mathbf{k}_\parallel) = \int_U \mathrm{d}\mathbf{r}\, w_c^\star(\mathbf{r})e\mathbf{r}w_v(\mathbf{r}) \tag{2.28}$$

where the integral is taken over the unit-cell volume U.

The annihilation of the valence-band electron can also be viewed as the creation of a positively charged hole. Therefore, the excitation process directly yields a pair of oppositely charged carriers and thus introduces a microscopic interband polarization to the semiconductor system. The corresponding creation and annihilation operators, $P^\dagger_{\mathbf{k}_\parallel}(\mathbf{q}_\parallel)$ and $P_{\mathbf{k}_\parallel}(\mathbf{q}_\parallel)$, of that microscopic polarization are given by

$$P^\dagger_{\mathbf{k}_\parallel}(\mathbf{q}_\parallel) \;=\; a^\dagger_{c,\mathbf{k}_\parallel} a_{v,\mathbf{k}_\parallel-\mathbf{q}_\parallel} \qquad \text{and} \qquad P_{\mathbf{k}_\parallel}(\mathbf{q}_\parallel) \;=\; a^\dagger_{v,\mathbf{k}_\parallel-\mathbf{q}_\parallel} a_{c,\mathbf{k}_\parallel}\;, \quad (2.29)$$

respectively. As known from optics, it is the macroscopic polarization $\mathbf{P}$ that acts as a source of the electromagnetic field. The corresponding relation is given by the wave equation

$$\left[\nabla^2 - \frac{n^2(z)}{c^2}\frac{\partial^2}{\partial t^2}\right]\langle \mathbf{E}(\mathbf{r},t)\rangle \;=\; -\mu_0 \frac{\partial}{\partial t}\mathbf{P}(\mathbf{r},t)\;, \quad (2.30)$$

and has to be solved for the stacked QW structure [298]. The connection between the microscopic and the macroscopic polarization is established via

$$\mathbf{P}(\mathbf{r},t) \;=\; \sum_{\mathbf{q}_\parallel} \mathbf{P}(\mathbf{q}_\parallel,z,t) e^{-i\mathbf{q}_\parallel\cdot\mathbf{r}_\parallel} \quad (2.31)$$

with

$$\mathbf{P}(\mathbf{q}_\parallel,z,t) \;=\; \frac{1}{A}\sum_{\mathbf{k}_\parallel}\left(\mathbf{d}^\star_{cv} P^\dagger_{\mathbf{k}_\parallel}(\mathbf{q}_\parallel) + \mathbf{d}_{cv} P^\dagger_{\mathbf{k}_\parallel}(-\mathbf{q}_\parallel)\right) g(z)^2\;, \quad (2.32)$$

where A is the quantization area.

In order to obtain the material response to optical excitations and/or the emission characteristics, one now has to self-consistently solve the dynamics of the microscopic polarizations and the wave equation, Eqs. (2.29–2.32). Therefore, we will introduce the tools, needed for a self-consistent microscopic theory, in Sec. 2.4. Based on that, we develop the equations of motion of the relevant quantities describing a single QW in Chap. 3. In Chap. 4, we then introduce the transfer-matrix approach with the help of which the Fibonacci MQW samples can finally be modeled.

2.4 Hierarchy Problem and Cluster Expansion

In general, the dynamics of the expectation value of any operator $\mathcal{O}$ can be obtained from the Heisenberg's equation of motion

$$i\hbar\frac{\partial}{\partial t}\langle\mathcal{O}\rangle \;=\; \langle[\mathcal{O},H]_-\rangle\;. \quad (2.33)$$

Evaluating the corresponding equation of motion of an electron creation operator, one finds that an electron creation (annihilation) operator is coupled to two (one) electron creation and one (two) electron annihilation operators due to the Coulomb interaction,

$$i\hbar\frac{\partial}{\partial t}a^\dagger_{\nu,\mathbf{p}_\parallel}\Big|_{H_c} \;=\; -\sum_{\mathbf{k}_\parallel,\lambda}\sum_{\mathbf{k}''_\parallel\neq 0} V_{\mathbf{k}''_\parallel} a^\dagger_{\mu,\mathbf{p}_\parallel+\mathbf{k}''_\parallel} a^\dagger_{\lambda,\mathbf{k}_\parallel-\mathbf{k}''_\parallel} a_{\lambda,\mathbf{k}_\parallel}\;. \quad (2.34)$$

Following the definition of an expectation value of an N-particle operator to consist of N electron creation and N electron annihilation operators

$$\langle N \rangle \;=\; \langle a^\dagger_{\mu_1,\mathbf{k}_{\parallel 1}} \ldots a^\dagger_{\nu_N,\mathbf{k}_{\parallel N}} a_{\mu_N,\bar{\mathbf{k}}_{\parallel N}} a_{\mu_1,\bar{\mathbf{k}}_{\parallel 1}} \rangle \,, \tag{2.35}$$

Coulomb interaction establishes that in general N-particle expectation values couple not only to further N-particle expectation values but to $N+1$ particle expectation values as well

$$i\hbar \frac{\partial}{\partial t} \langle N \rangle \;=\; T\left[\langle N \rangle\right] + V\left[\langle N+1 \rangle\right]. \tag{2.36}$$

The functionals T and V follow directly from evaluating the right-hand side of Eq. (2.33). In particular the functional V follows from the Coulomb interaction H_C (more generally speaking from the many-body interaction) while the functional T is mainly governed by the single-particle part $H_0 + H_I$. In order to get to know the dynamics of $\langle N \rangle$, one consequently needs to know the dynamics of the $\langle N+1 \rangle$ expectation values, that in turn couple to $\langle N+2 \rangle$ expectation values and so on. This coupling scheme states the well-known problem of an infinite hierarchy of equations of motion in many-body physics [69, 73].

One way to overcome this hierarchy problem is to apply a consistent systematical truncation scheme provided by the so-called (coupled) cluster expansion. The cluster expansion has been developed and successfully employed in the field of chemistry [299–303]. Its basic idea is to approximate the N-electron wave function of an atom or molecule by the N non-interacting constituents and different levels of correlations among them.

In first approximation, the N-electron wave function is then described by an appropriately anti-symmetrized product of single-electron wave functions (singlets), which is the well-known Slater determinant of the Hartree-Fock approximation. The inclusion of particle-particle interactions is achieved by considering M-particle correlations up to a desired level $M \leq N$ where the electrons are coupled in pairs ($M = 2$, doublets), in triplets ($M = 3$), quadruplets ($M = 4$), and so on. The N-electron wave function is then obtained as the sum of all possible, correctly anti-symmetrized products of coupled clusters up to order M.

If $M = N$, the cluster-expansion truncation scheme yields the full N-electron wave function without approximation. In contrast, if $M < N$, the approximation consists of neglecting correlations of order $M+1$ and higher. That is, any N-electron wave function is described consistently using at most M-electron coupled clusters, which allows for the reduction of computational effort and, as we will see in the following, for the truncation of the hierarchy problem.

However, having in mind semiconductors instead of atoms or molecules, a wave-function approach is clearly not possible since the semiconductor carriers tremendously outnumber the atom or molecule electrons. Nevertheless, this cluster-expansion approach may be used in a similar fashion to truncate the infinite hierarchy of N-particle

expectation values, Eq. (2.36), and has been successfully applied to the description of semiconductor many-body correlations as well as to quantum optics [70, 71, 76, 78, 82, 113, 114, 119, 253, 304–307]. The recursively defined clusters are obtained [308] according to

$$\begin{aligned}
\langle 1\rangle &= \langle 1\rangle_S && (2.37)\\
\langle 2\rangle &= \langle 2\rangle_S + \Delta\langle 2\rangle && (2.38)\\
\langle 3\rangle &= \langle 3\rangle_S + \langle 1\rangle\Delta\langle 2\rangle + \Delta\langle 3\rangle && (2.39)\\
\langle 4\rangle &= \langle 4\rangle_S + \langle 2\rangle_S\Delta\langle 2\rangle + \Delta\langle 2\rangle\Delta\langle 2\rangle + \langle 1\rangle\Delta\langle 3\rangle + \Delta\langle 4\rangle && (2.40)\\
&\vdots &&\\
\langle N\rangle &= \langle N\rangle_S + \langle N-2\rangle_S\Delta\langle 2\rangle + \langle N-4\rangle_S\Delta\langle 2\rangle\Delta\langle 2\rangle + \ldots &&\\
&\quad +\Delta\langle N\rangle\ , && (2.41)
\end{aligned}$$

where the singlet part $\langle N\rangle_S$ corresponds to the Hartree-Fock factorization. Correlations are indicated by a Δ put in front of the expectation value so that $\Delta\langle N\rangle$ is the entirely correlated part of the N-particle expectation value $\langle N\rangle$. On the right hand side of the Eqs. (2.37)–(2.41), all possible ways to distribute the creation and annihilation operators among the clusters have to be taken into account. As a consequence of the semi-classical treatment of light-matter interaction, we have to consider only fermionic creation and annihilation operators. Therefore, the right hand side of the cluster expansion has to be correctly anti-symmetrized, here. In general, the cluster expansion can be applied to any system no matter if fermionic, bosonic, or mixed [308], which allows for the treatment of a quantized light field or of phonons as well [71].

The singlet (S), doublet (D), triplet (T), and so on level can then be defined via

$$\begin{aligned}
\langle N\rangle_S &= \langle N\rangle_{HF} && (2.42)\\
\langle N\rangle_D &= \langle N-2\rangle_S\Delta\langle 2\rangle + \langle N-4\rangle_S\Delta\langle 2\rangle\Delta\langle 2\rangle + \ldots && (2.43)\\
\langle N\rangle_T &= \langle N-3\rangle_{S,D}\Delta\langle 3\rangle + \langle N-6\rangle_{S,D}\Delta\langle 3\rangle\Delta\langle 3\rangle + \ldots && (2.44)\\
\langle N\rangle_Q &= \langle N-4\rangle_{S,D,T}\Delta\langle 4\rangle + \langle N-8\rangle_{S,D,T}\Delta\langle 4\rangle\Delta\langle 4\rangle + \ldots && (2.45)\\
&\vdots &&\\
\langle N\rangle_M &= \langle N-M\rangle_{S,\ldots,M-1}\Delta\langle M\rangle + \langle N-2M\rangle_{S,\ldots,M-1}\Delta\langle M\rangle\Delta\langle M\rangle + \ldots && (2.46)\\
\langle N\rangle_N &= \Delta\langle N\rangle\ , && (2.47)
\end{aligned}$$

where we have used

$$\langle N\rangle_{S,\ldots,M} = \sum_{l=1}^{M}\langle N\rangle_l\ . \qquad (2.48)$$

The truncation of the hierarchy is thus achieved by taking into account only correlations of at most M particles, $\langle N\rangle|_M = \langle N\rangle_{S,\ldots,M}$. Due to the consistent description of all expectation values at the M-particle-correlation level, the corresponding set of equations of motion is closed and the hierarchy is truncated. The cluster expansion is schematically illustrated for single- up to four-particle expectation values in Fig. 2.4.

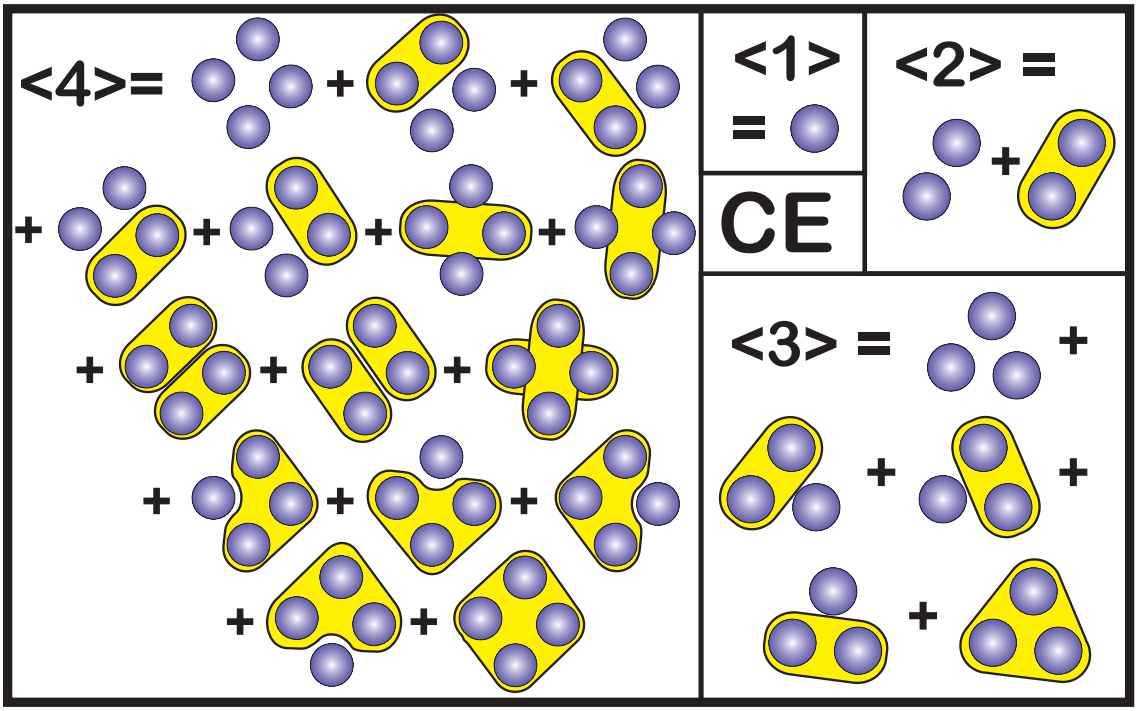

Figure 2.4: Schematic drawing of the cluster expansion for single-, two-, three- and four-particle expectation values. Single particle operators are drawn as balls. Correlations among particles are indicated by yellow areas enclosing the correlated particles. Thus, the order of correlation corresponds to the number of entirely enclosed balls.

3 Semiconductor Bloch Equations

In the ground state, the valence band of a semiconductor is completely filled with electrons while the conduction band is empty. A resonant optical excitation of the semiconductor can be achieved e.g. using laser light, entirely incoherent light, squeezed light, or light of any other quantum statistics, resonant to the semiconductor band gap. Moreover, the excitation state of a semiconductor can be altered by shining e.g. THz radiation on the sample. However, we restrict our investigations to the coherent excitation regime, which corresponds to the situation after resonant laser excitation. Then, the central quantity describing the system is the coherent polarization, Eq. 2.32. It contains all information about the optical excitation process as it is directly created by the light field, Eqs. (2.25), and as it is in turn the only source to the electrical field, Eq. (2.30), in the investigated scenario. The interband polarization is described by a conduction-band-electron creation operator and a valence-band-electron annihilation operator. Hence, the polarization directly drives the dynamics of electron (e) and hole (h) occupations

$$f^e_{\mathbf{k}_\parallel} = \langle a^\dagger_{c,\mathbf{k}_\parallel} a_{c,\mathbf{k}_\parallel} \rangle \quad , \qquad f^h_{\mathbf{k}_\parallel} = 1 - \langle a^\dagger_{v,\mathbf{k}_\parallel} a_{v,\mathbf{k}_\parallel} \rangle \quad , \tag{3.1}$$

in the conduction and valence band, respectively.

In the following, we will achieve a microscopic description of the QW-system dynamics with the help of the Heisenberg's equation of motion. That microscopic description is provided by a set of equations of motion for single- and two-particle quantities. Specifically, we assume in the derivation of the so-called Semiconductor Bloch Equations [69, 71, 309] that the system is homogeneously excited by an external light field which propagates perpendicularly to the QW plane. As a consequence, the single-particle quantities such as the interband polarizations as well as the carrier occupations are diagonal in the carrier momentum. Thus, the rotating wave approximation (RWA) becomes exact.

In the following, we recall the equations of motion of these system observables at the singlet-doublet level [71]. We will see later on, that this allows e.g. for the inclusion of carrier-carrier scattering, which results in excitation-induced dephasing (EID) [286, 298, 310–312].

As a simplification, we approximate $g(z) \approx \delta(z_{QW})$ in Eqs. (2.32) and (2.26), which is justified since the optical wavelength corresponding to the excitonic resonance is much larger than the QW extension in z-direction so that $g(z)$ effectively picks the QW position z_{QW} in a δ-function-like fashion.

3.1 Equations of Motion

The dynamics of the microscopic interband polarization is then given by

$$i\hbar\frac{\partial}{\partial t}P_{\mathbf{k}_\parallel} = \left(\tilde{\epsilon}^c_{\mathbf{k}_\parallel} - \tilde{\epsilon}^v_{\mathbf{k}_\parallel}\right) P_{\mathbf{k}_\parallel} - (1 - f^e_{\mathbf{k}_\parallel} - f^h_{\mathbf{k}_\parallel})\Omega_{\mathbf{k}_\parallel} + \Gamma^{v,c}_{\mathbf{k}_\parallel}, \tag{3.2}$$

where we find the renormalized electron and hole energies

$$\tilde{\epsilon}^c_{\mathbf{k}_\parallel} = \epsilon^c_{\mathbf{k}_\parallel} - \sum_{\mathbf{p}_\parallel \neq \mathbf{k}_\parallel} V_{\mathbf{p}_\parallel - \mathbf{k}_\parallel} f^e_{\mathbf{p}_\parallel} \qquad \text{and} \qquad \tilde{\epsilon}^v_{\mathbf{k}_\parallel} = \epsilon^v_{\mathbf{k}_\parallel} + \sum_{\mathbf{p}_\parallel \neq \mathbf{k}_\parallel} V_{\mathbf{p}_\parallel - \mathbf{k}_\parallel} f^h_{\mathbf{p}_\parallel} \ . \tag{3.3}$$

The renormalized Rabi frequency reads

$$\Omega_{\mathbf{k}_\parallel} = d_{cv}(\mathbf{k})E(t) + \sum_{\mathbf{p}_\parallel \neq \mathbf{k}_\parallel} V_{\mathbf{p}_\parallel - \mathbf{k}_\parallel} P_{\mathbf{p}_\parallel} \ . \tag{3.4}$$

It includes the driving external field $E(t)$ as well as the renormalization of that field due to the internal dipole field. The Rabi frequency is weighted with the so-called phase-space filling factor, $1 - f^e - f^h$. The strength of the phase-space-filling factor depends on the level of excitation of the semiconductor. For low densities, the phase-space-filling factor is close to unity. In addition, it may suffer a sign change at elevated carrier densities, which manifests the fermionic effect of Pauli blocking. For densities above the transparency point at which the phase-space-filling factor vanishes, the Coulomb interaction thus enters the equation of motion of the interband polarization with a different sign. This inhibits electron-hole pairs to be bound. In contrast, discrete excitonic resonances below the band gap result from that Coulomb sum for low enough densities. These resonances may be obtained as the eigenvalues of a generalized Wannier equation. That equation is obtained if one takes only the polarization-dependent terms into account in Eq. (3.2).

Finally, the remaining contribution to the dynamics of the microscopic polarization ,

$$\Gamma^{v,c}_{\mathbf{k}_\parallel} = \sum_{\mu,\mathbf{k}',\mathbf{p}\neq 0} V_{\mathbf{p}} \left\{ c^{\mathbf{p},\mathbf{k}',\mathbf{k}}_{v,\mu;\mu,c} - \left(c^{\mathbf{p},\mathbf{k}',\mathbf{k}}_{c,\mu;\mu,v} \right)^\star \right\} , \tag{3.5}$$

describes effects of Coulomb-induced carrier scattering via the two-particle correlations

$$c^{\mathbf{p},\mathbf{k}',\mathbf{k}}_{\lambda,\mu;\nu,\sigma} = \Delta\langle a^\dagger_{\lambda,\mathbf{k}_\parallel} a^\dagger_{\mu,\mathbf{k}'_\parallel} a_{\nu,\mathbf{k}'_\parallel - \mathbf{p}_\parallel} a_{\sigma,\mathbf{k}_\parallel + \mathbf{p}_\parallel} \rangle \ . \tag{3.6}$$

Similar correlations may also be found in the Coulomb-induced scattering contributions to the dynamics of electron and hole occupations which are given by

$$i\hbar\frac{\partial}{\partial t}f^e_{\mathbf{k}} = -2i\,\mathcal{I}m\left[\Omega_{\mathbf{k}_\parallel}\,(P_{\mathbf{k}})^\star - \sum_{\mu,\mathbf{k}',\mathbf{p}\neq 0} V_{\mathbf{p}}\,c^{\mathbf{p},\mathbf{k}',\mathbf{k}}_{c,\mu;\mu,c}\right], \tag{3.7}$$

$$i\hbar\frac{\partial}{\partial t}f^h_{\mathbf{k}} = -2i\,\mathcal{I}m\left[\Omega_{\mathbf{k}_\parallel}\,(P_{\mathbf{k}})^\star + \sum_{\mu,\mathbf{k}',\mathbf{p}\neq 0} V_{\mathbf{p}}\,c^{\mathbf{p},\mathbf{k}',\mathbf{k}}_{v,\mu;\mu,v}\right]. \tag{3.8}$$

In addition, the carrier dynamics is driven by the polarization. The influence of the correlated part (second term in the parentheses in Eqs. (3.7) and (3.8), respectively) is discussed in more detail below. Before heading to the explicit form of these correlations, we next review some of their general properties. Inspecting the band-index combination $(\lambda,\mu;\mu,\lambda)$ that is found in the carrier-occupation dynamics, it holds

$$\sum_{\mathbf{k}_\parallel}\mathcal{I}m\left[\sum_{\mu,\mathbf{k}'_\parallel,\mathbf{p}_\parallel\neq 0} V_{\mathbf{p}_\parallel}\,c^{\mathbf{p}_\parallel,\mathbf{k}'_\parallel,\mathbf{k}_\parallel}_{\lambda,\mu;\mu,\lambda}\right] = 0\,, \tag{3.9}$$

which can be shown by index shifts in the $\mathbf{k}_\parallel$ and $\mathbf{k}'_\parallel$ summation and writing $\mathcal{I}m[\ldots]$ explicitly. Thus, the correlation contributions do not cause a change of the total carrier population

$$i\hbar\frac{\partial}{\partial t}n^\lambda_{\mathrm{tot}}\big|_{\mathrm{corr.}} = i\hbar\frac{\partial}{\partial t}\sum_{\mathbf{k}_\parallel} f^\lambda_{\mathbf{k}_\parallel}\big|_{\mathrm{corr.}} = 0\,, \tag{3.10}$$

with $\lambda = e,h$. In consequence, the build-up of the carrier occupations is solely driven by the polarization so that $n^e_{\mathrm{tot}} = n^h_{\mathrm{tot}} \equiv n$. In particular, the Coulomb-induced scattering leads to a redistribution of the carriers, i.e. the Coulomb scattering drives the carriers towards their thermal (quasi-)equilibrium distributions.

Similarly, one may show for the correlation contributions to the dynamics of the microscopic polarization, where the band index combinations $(\lambda,\mu,\mu,\bar{\lambda})$ have to be considered, that

$$\sum_{\mu,\mathbf{k}_\parallel,\mathbf{k}'_\parallel,\mathbf{p}\neq 0} V_{\mathbf{p}_\parallel}\,c^{\mathbf{p}_\parallel,\mathbf{k}'_\parallel,\mathbf{k}_\parallel}_{\lambda,\mu;\mu,\bar{\lambda}} = \sum_{\mu,\mathbf{k}_\parallel,\mathbf{k}'_\parallel,\mathbf{p}\neq 0} V_{\mathbf{p}_\parallel}\left[c^{\mathbf{p}_\parallel,\mathbf{k}'_\parallel,\mathbf{k}_\parallel}_{\bar{\lambda},\mu;\mu,\lambda}\right]^\star, \tag{3.11}$$

which is equivalent to

$$\sum_{\mathbf{k}_\parallel}\Gamma^{v,c}_{\mathbf{k}_\parallel} = 0\,. \tag{3.12}$$

Consequently, these correlations do not cause a decay of the macroscopic polarization, either. Rather, microscopic polarizations are redistributed due to the Coulomb scattering events.

Generally speaking, it is the treatment of correlation contributions – which describe the many-body effects due to Coulomb interaction, phonons, or disorder – that defines the accuracy of the modeling used. As discussed above, Coulomb effects are described microscopically at the singlet-doublet level in this work. The basis of that microscopic treatment is the system Hamiltonian, Eq. (2.16). Since the Hamiltonian does not account for lattice vibrations (phonons) nor for the unavoidable disorder, a microscopic treatment of the corresponding effects is not possible at that level of description. Instead, we introduce a phenomenological dephasing constant γ to take the dephasing of the polarization caused by disorder and interaction with phonons into consideration,

$$i\hbar\frac{\partial}{\partial t}P_{\mathbf{k}_\parallel}\big|_{\text{phon.,dis.}} \approx -i\gamma P_{\mathbf{k}_\parallel} . \tag{3.13}$$

3.2 Carrier Scattering

While a detailed discussion of the correlations, Eq. (3.6), is given in Refs. [71, 304], only a brief review of their essential properties shall be given here. The dynamics of these two-particle correlations is obtained by setting up Heisenberg's equation of motion for the respective full two-particle expectation values. Applying the cluster expansion, the dynamics of the truly correlated part is obtained as

$$\begin{aligned} i\hbar\frac{\partial}{\partial t}c^{\mathbf{p}_\parallel,\mathbf{k}'_\parallel,\mathbf{k}_\parallel}_{\lambda,\mu;\nu,\sigma} &= \left(\tilde{\epsilon}^{\sigma}_{\mathbf{k}_\parallel-\mathbf{p}_\parallel}+\tilde{\epsilon}^{\nu}_{\mathbf{k}'_\parallel+\mathbf{p}_\parallel}-\tilde{\epsilon}^{\mu}_{\mathbf{k}'_\parallel}-\tilde{\epsilon}^{\lambda}_{\mathbf{k}_\parallel}\right)c^{\mathbf{p}_\parallel,\mathbf{k}'_\parallel,\mathbf{k}_\parallel}_{\lambda,\mu;\nu,\sigma} \\ &+\left\{S^{\mathbf{p}_\parallel,\mathbf{k}'_\parallel,\mathbf{k}_\parallel}_{\lambda,\mu;\nu,\sigma}\right\}_1+\left\{D^{\mathbf{p}_\parallel,\mathbf{k}'_\parallel,\mathbf{k}_\parallel}_{\lambda,\mu;\nu,\sigma}\big|_{\text{coh.}}\right\}_2+\left\{D^{\mathbf{p}_\parallel,\mathbf{k}'_\parallel,\mathbf{k}_\parallel}_{\lambda,\mu;\nu,\sigma}\big|_{\text{inc.}}\right\}_3+\left\{c^{\mathbf{p}_\parallel,\mathbf{k}'_\parallel,\mathbf{k}_\parallel}_{\lambda,\mu;\nu,\sigma}\big|_{\text{T}}\right\}_4 . \end{aligned} \tag{3.14}$$

The first term $\{S\}_1$ in the second line of Eq. (3.14) includes the singlet contributions that lead to the spontaneous built-up of two-particle correlations once carriers are present in the system. The second term $\{D\}_2$ describes coherent two-particle correlations of the form $c_{\lambda,\lambda;\lambda,\bar{\lambda}}$ as well as $c_{\lambda,\lambda;\bar{\lambda},\bar{\lambda}}$. These quantities include density-assisted polarizations and bi-excitons. In analogy, the third term $\{D\}_3$ represents incoherent two-particle correlations of the form $c_{\lambda,\lambda;\lambda,\lambda}$ describing intraband carrier correlations and $c_{\lambda,\bar{\lambda};\lambda,\bar{\lambda}}$ describing exciton populations. The discrimination of two-particle correlations follows from an inspection of the respective source terms. $\{D\}_2$ is driven by coherent polarization $P_{\mathbf{k}_\parallel}$ while $\{D\}_3$ is driven by the incoherent carrier occupations $f^{\lambda}_{\mathbf{k}_\parallel}$. The truly correlated three-particle quantities are collected in the remaining term $\{c\}_4$ which is formally neglected and replaced by a phenomenological dephasing constant δ at the singlet-doublet level. For more details of the form of the respective terms see the references given above.

A full description of the system dynamics at the singlet-doublet level demands solving the dynamics of microscopic polarizations, Eq. (3.2), of carrier occupations, Eqs. (3.7) and (3.8), as well as of the dynamics of density-assisted polarizations, carrier correlations and exciton correlations, Eq.(3.14). The solution of that set of coupled equations of motion displays a numerically challenging task since large memory and long computation times are needed, which makes such computations very demanding and at least max out if not exceed current computer powers. Therefore, a simplifying modeling is necessary

that describes the essential effects of the correlation contributions correctly and allows for practicable computations. In the following, we will develop such simplifications and we will discuss how to include the effects of dephasing, energy renormalization, screening, and relaxation towards thermal (quasi-)equilibrium provided by these correlations. Particularly, after a discussion of a typical pump-probe scenario, the relevant contributions are identified and some so-motivated approximations are applied.

The pump-probe experiment is a well-established standard method [313–315] to investigate the opto-electronic properties of a semiconductor heterostructure. In a pump-probe experiment, the coherent polarization as well as the population dynamics are probed. In semiconductors, the typical dephasing time of the polarization is in the picosecond range or below. Therefore, a time-resolved study of the corresponding dynamics needs a time resolution finer than the dephasing time. The ability to create laser pulses with durations in the femtosecond time scale [314–316] allows for such studies of the semiconductor many-body system [78, 285–287, 317–320]. To do so, one exposes the investigated sample to two subsequent laser pulses. The so-called pump pulse excites the sample and thus prepares a certain excitation state. That state in general depends on the exact properties of the pump pulse, e.g. its quantum statistics, intensity and so on. The subsequent probe pulse tests the quantum state of the excited system.

In accordance with Refs. [286, 311], we now make the following assumptions. If the probe pulse is weak enough, one may assume that the system remains unaffected by the probe. Similarly, a weak probe pulse also allows for the assumption that only terms linear in the polarization contribute significantly to the detected signal. Therefore, we keep only terms linear in $P_{\mathbf{k}_\parallel}$.

Given a sufficiently long delay time of the probe pulse, carrier-carrier and carrier-phonon scattering lead to a quasi-equilibration of the system (c.f. Eqs. (3.10) and (3.12) for carrier-carrier scattering) on a sub-picosecond time scale. Hence, one may assume the carriers to be Fermi-Dirac distributed. Consequently, the pump-induced carrier distribution is defined by an appropriate carrier density n and carrier temperature T so that one does not have to solve Eqs. (3.7) and (3.8). Instead, different excitation conditions are described by different carrier densities and temperatures. If additionally the carrier density and temperature are not too small, one may assume the carrier-occupation contributions to dominate the carrier-carrier-correlation and exciton-population contributions [99, 304, 321, 322]. Thus, we may drop the incoherent part $\{D\}_3$. Similarly, we omit the coherent contribution $\{D\}_2$ assuming that this source term decays on a timescale faster than the one of the associated $\{D\}_2$-induced build-up of the correlations, Eq. (3.14). Hence, omitting the two- and three-particle correlations, we compensate for the thus missing screening contributions, described by these correlations, by replacing the bare Coulomb potential with the Lindhard-screened Coulomb potential [69],

$$V_{\mathbf{k}_\parallel} \;\rightarrow\; W_{\mathbf{k}_\parallel} \;=\; \frac{V_{\mathbf{k}_\parallel}}{1 - V_{\mathbf{k}_\parallel} \sum_{\mathbf{k}'_\parallel,\mu=c,v} (f^\mu_{\mathbf{k}'_\parallel-\mathbf{k}_\parallel} - f^\mu_{\mathbf{k}'_\parallel}) / (\epsilon^\mu_{\mathbf{k}'_\parallel-\mathbf{k}_\parallel} - \epsilon^\mu_{\mathbf{k}'_\parallel})} \,. \tag{3.15}$$

Doing so and evaluating the steady-state result corresponds to applying a second-Born

approximation for the two-particle correlations contributing to the dynamics of microscopic polarizations. Then, the equation of motion of these correlations reads

$$i\hbar\frac{\partial}{\partial t}c^{\mathbf{p}_\parallel,\mathbf{k}'_\parallel,\mathbf{k}_\parallel}_{\lambda,\mu;\nu,\sigma} = \left(\tilde{\epsilon}^{\sigma}_{\mathbf{k}_\parallel-\mathbf{p}_\parallel} + \tilde{\epsilon}^{\nu}_{\mathbf{k}'_\parallel+\mathbf{p}_\parallel} - \tilde{\epsilon}^{\mu}_{\mathbf{k}'_\parallel} - \tilde{\epsilon}^{\lambda}_{\mathbf{k}_\parallel} - i\delta\right) c^{\mathbf{p}_\parallel,\mathbf{k}'_\parallel,\mathbf{k}_\parallel}_{\lambda,\mu;\nu,\sigma} + \tilde{S}^{\mathbf{p}_\parallel,\mathbf{k}'_\parallel,\mathbf{k}_\parallel}_{\lambda,\mu;\nu,\sigma} \quad , \tag{3.16}$$

where the simplified singlet source term $\tilde{S}$ is linear in the polarization and contains the screened Coulomb matrix elements, Eq. (3.15). Equation (3.16) can formally be solved with the help of a Markov approximation. The two-particle correlations then enter the polarization dynamics in form of a scattering matrix $\Gamma_{\mathbf{k}_\parallel,\mathbf{k}'_\parallel}$ [298, 311], so that we are left with the linear equation in $P_{\mathbf{k}_\parallel}$,

$$i\hbar\frac{\partial}{\partial t}P_{\mathbf{k}_\parallel} = \left(\tilde{\epsilon}^{c}_{\mathbf{k}_\parallel} - \tilde{\epsilon}^{v}_{\mathbf{k}_\parallel} - i\gamma\right) P_{\mathbf{k}_\parallel} - (1 - f^{e}_{\mathbf{k}_\parallel} - f^{h}_{\mathbf{k}_\parallel})\Omega_{\mathbf{k}_\parallel} + \sum_{\mathbf{k}'_\parallel}\Gamma_{\mathbf{k}_\parallel,\mathbf{k}'_\parallel}P_{\mathbf{k}'_\parallel} \, . \tag{3.17}$$

3.3 Optical Susceptibility

Due to the structure of Eq. (3.17), one now has direct access to the linear optical susceptibility via the relation

$$\chi(\omega) \equiv \frac{P(\omega)}{E(\omega)} = d_{cv}\sum_{\mathbf{k}_\parallel}\frac{P_{\mathbf{k}_\parallel}(\omega)}{E(\omega)} \equiv \sum_{\mathbf{k}_\parallel}\chi_{\mathbf{k}_\parallel}(\omega) \, . \tag{3.18}$$

The frequency dependence of the polarization is accessed by the Fourier transform of Eq. (3.17) with respect to time and by expressing the resulting equation in the format of a matrix equation

$$\sum_{\mathbf{k}'_\parallel}\Lambda_{\mathbf{k}_\parallel,\mathbf{k}'_\parallel}(\omega)P_{\mathbf{k}'_\parallel} = (1 - f^{e}_{\mathbf{k}_\parallel} - f^{h}_{\mathbf{k}_\parallel})d_{cv}E(\omega) \, . \tag{3.19}$$

The matrix Λ is then given by

$$\Lambda_{\mathbf{k}_\parallel,\mathbf{k}'_\parallel}(\omega) \equiv (\tilde{\epsilon}^{c}_{\mathbf{k}} - \tilde{\epsilon}^{v}_{\mathbf{k}} - \hbar\omega - i\gamma)\,\delta_{\mathbf{k}_\parallel,\mathbf{k}'_\parallel} - (1 - f^{e}_{\mathbf{k}} - f^{h}_{\mathbf{k}})V_{\mathbf{k}'_\parallel-\mathbf{k}_\parallel} \, . \tag{3.20}$$

Consequently, the microscopic optical susceptibility $\chi_{\mathbf{k}_\parallel}(\omega)$ can be obtained by the inversion of the matrix equation

$$\sum_{\mathbf{k}'_\parallel}\Lambda_{\mathbf{k}_\parallel,\mathbf{k}'_\parallel}(\omega)\chi_{\mathbf{k}'_\parallel} = (1 - f^{e}_{\mathbf{k}_\parallel} - f^{h}_{\mathbf{k}_\parallel})|d_{cv}|^2\mathbf{1} \, , \tag{3.21}$$

and $\chi(\omega)$ is obtained according to Eq. (3.18). Having solved the QW response in the frequency domain, corresponds to the situation of an initial excitation which is probed by a weak second pulse. Hence, that is consistent with the assumptions made in the description of the scattering contributions.

4 Transfer Matrix Approach

In realistic samples, the QW layer is often embedded in a sophisticated dielectric environment. Typical structures consist of barrier, spacer, and adjuster layers as well as eventually concentration-gradient layers, anti-reflection coatings (ARC), distributed Bragg reflectors, and cavities. As already discussed in Sec. 2.2, the investigated samples display such intricate setups as well. The different optical properties of the dielectric layers that build up the sample may strongly influence the propagation of the light field as well as the coupling of a QW to external fields [116, 117, 120]. In order to consistently describe these effects of the QW environment on the sample reflection, transmission, and absorption properties, we apply the so-called transfer-matrix method [70, 323, 324].

4.1 Passive Dielectric Structures

To introduce the basic concept, let us first of all consider the case of an entirely passive structure that does not include optically active layers such as e.g. QWs. In that case, we have to take into account only effects caused by the refractive indices of the different materials. Without a source to the electrical field, we therefore have to consider pure reflection, transmission and propagation effects only. The electrical field is described by Eq. (2.30) which due to the missing polarization simplifies to

$$\left[\nabla^2 - \frac{n^2(z)}{c^2}\frac{\partial^2}{\partial t^2}\right]\langle \mathbf{E}(\mathbf{r},t)\rangle \;=\; 0\,. \tag{4.1}$$

For z within a certain material layer, labeled by j and reaching from z_j to z_{j+1}, the refractive index $n(z) = n_j$ is constant. Hence, the solutions of the homogeneous wave equation are plane waves within each layer. They have the form

$$U_{j,\mathbf{q}_\parallel,q_\perp}(z,t) \;=\; u_{j,q_\perp,j}(z)e^{in_j\mathbf{q}_\parallel\mathbf{r}_\parallel}e^{\pm i\omega_\mathbf{q}t} \tag{4.2}$$

with the frequency $\omega_q = c|\mathbf{q}|/n$ and the z-component $q_\perp = \sqrt{n^2\mathbf{q}^2 - \mathbf{q}_\parallel^2}$ of the wave vector $\mathbf{q} = (\mathbf{q}_\parallel, q_\perp)$. The angle of incidence α_j in layer j, measured relative to the normal

to the layers, yields the z-component of the wave vector $q_{\perp,j} = n_j|\mathbf{q}|\cos(\alpha_j)$ within that layer, where the absolute value of the wave vector is given by $|\mathbf{q}|$. In addition, the in-plane component $\mathbf{q}_\parallel = n_j|\mathbf{q}|\sin(\alpha_j)$ is the same in all layers due to Snell's law. One then has to solve the equation

$$\left[\frac{\partial^2}{\partial z^2} + n^2(z)\mathbf{q}^2 - \mathbf{q}_\parallel^2\right] u_{q_\perp}(z) \;=\; 0\,. \tag{4.3}$$

Thus, the stationary mode functions in z-direction read

$$u_{j,q_\perp,j}(z) \;=\; A_j\, e^{+in_j q_{\perp,j} z} + B_j\, e^{-in_j q_{\perp,j} z}\,, \tag{4.4}$$

within layer j, where the coefficients A_j and B_j contain the effects resulting from the sample setup. These plane waves have to fulfill the boundary conditions following from Maxwell's equations at the material-layer interfaces. In particular, the j^{th} interface is found at the position z_j. For only two dielectric layers, which corresponds to the simplest case of a single interface, that leads to the reflection and transmission coefficients [70, 325, 326]

$$R_j^{s-} \;=\; \frac{q_{\perp,j-1} - q_{\perp,j}}{q_{\perp,j-1} + q_{\perp,j}} \quad,\quad T_j^{s-} \;=\; \frac{2q_{\perp,j-1}}{q_{\perp,j-1} + q_{\perp,j}}\,, \tag{4.5}$$

$$R_j^{s+} \;=\; \frac{q_{\perp,j} - q_{\perp,j-1}}{q_{\perp,j-1} + q_{\perp,j}} \quad,\quad T_j^{s+} \;=\; \frac{2q_{\perp,j}}{q_{\perp,j-1} + q_{\perp,j}}\,, \tag{4.6}$$

for s-polarized light as well as to

$$R_j^{p-} \;=\; \frac{\kappa_j q_{\perp,j} - q_{\perp,j-1}/\kappa_j}{\kappa_j q_{\perp,j-1} + q_{\perp,j}/\kappa_j} \quad,\quad T_j^{p-} \;=\; \frac{2q_{\perp,j-1}}{\kappa_j q_{\perp,j-1} + q_{\perp,j}/\kappa_j}\,, \tag{4.7}$$

$$R_j^{p+} \;=\; \frac{q_{\perp,j-1}/\kappa_j - \kappa_j q_{\perp,j}}{\kappa_j q_{\perp,j-1} + q_{\perp,j}/\kappa_j} \quad,\quad T_j^{p+} \;=\; \frac{2q_{\perp,j}}{\kappa_j q_{\perp,j-1} + q_{\perp,j}/\kappa_j}\,, \tag{4.8}$$

for p-polarized light, where $\kappa_j = n_{j-1}/n_j$. The superscripts '+' and '−' indicate the propagation direction of the light field. Referring to Fig. 4.1, we denote light initially traveling from left to right (right to left) as (counter-)propagating and label it by '−' ('+'). The coefficients A_j, B_j and A_{j+1}, B_{j+1} of neighboring layers are then related via the matrix equation

$$\begin{pmatrix} A_{j+1} \\ B_{j+1} \end{pmatrix} \;=\; \mathrm{M}_j^\varsigma \begin{pmatrix} A_j \\ B_j \end{pmatrix}\,. \tag{4.9}$$

For ς-polarized light (ς =s,p) the transfer matrix M_j^ς of the layer interface j reads

$$\mathrm{M}_j^\varsigma \;=\; \frac{1}{T_j^{\varsigma+}} \begin{pmatrix} (T_j^{\varsigma+}T_j^{\varsigma-} - R_j^{\varsigma+}R_j^{\varsigma-})e^{\theta_j} & R_j^{\varsigma+}e^{-\theta_j} \\ -R_j^{\varsigma-}e^{\theta_j} & e^{-\theta_j} \end{pmatrix}\,, \tag{4.10}$$

with $\theta_j = iq_{\perp,j}n_j(z_{j+1} - z_j)$. Iterative application of the matrices M_j^ς,

$$\begin{pmatrix} A_{j+1} \\ B_{j+1} \end{pmatrix} \;=\; \mathrm{M}_j^\varsigma \mathrm{M}_{j-1}^\varsigma \cdots \mathrm{M}_2^\varsigma \mathrm{M}_1^\varsigma \begin{pmatrix} A_0 \\ B_0 \end{pmatrix} \;=\; \mathcal{M}_j^\varsigma \begin{pmatrix} A_0 \\ B_0 \end{pmatrix}\,, \tag{4.11}$$

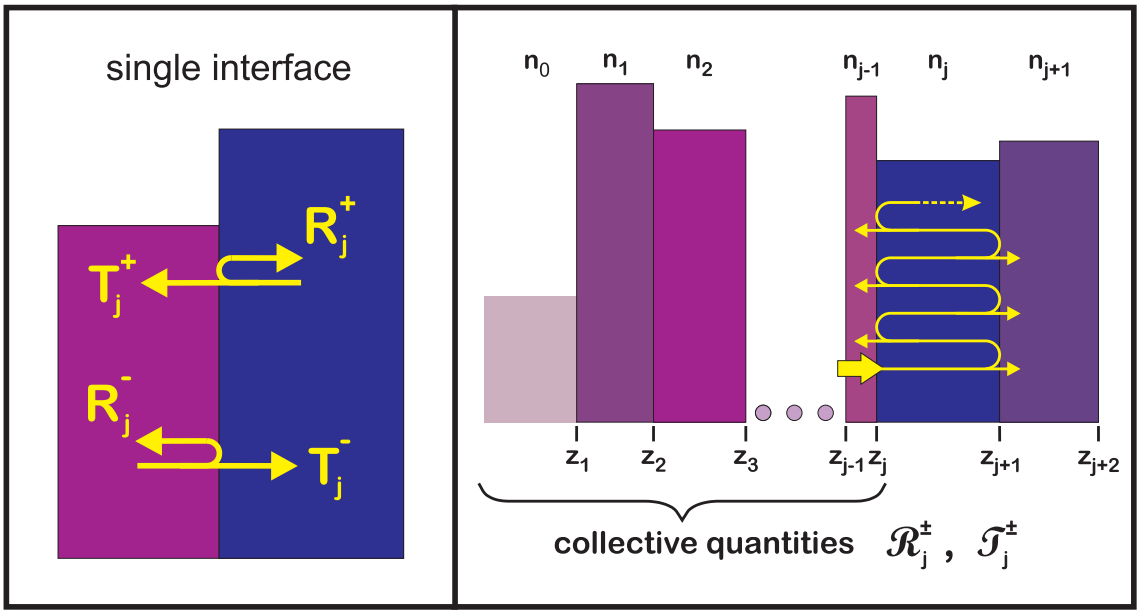

Figure 4.1: Reflection (R) and transmission (T) coefficients of propagating (−) and counter-propagating (+) light defined for a single layer interface (left) allow for the computation of collective reflection ($\mathcal{R}$) and transmission ($\mathcal{T}$) coefficients (right). The reflection, transmission and propagation effects introduced by each single constituent material layer are collected into effective reflection and transmission coefficients of a subset of layers by successively adding one layer after the other until the whole sample structure is taken into account.

allows to directly trace back any coefficients A_j, B_j to the wave outside the structure, A_0 and B_0, via the matrix

$$\mathcal{M}_j^{\varsigma} = \frac{1}{\mathcal{T}_j^{\varsigma+}} \begin{pmatrix} (\mathcal{T}_j^{\varsigma+}\mathcal{T}_j^{\varsigma-} - \mathcal{R}_j^{\varsigma+}\mathcal{R}_j^{\varsigma-})e^{\theta_j} & \mathcal{R}_j^{\varsigma+}e^{-\theta_j} \\ -\mathcal{R}_j^{\varsigma-}e^{\theta_j} & e^{-\theta_j} \end{pmatrix} , \tag{4.12}$$

which is defined with the help of new collective transmission $\mathcal{T}_j^{\varsigma\pm}$ and reflection $\mathcal{R}_j^{\varsigma\pm}$ coefficients. These coefficients are defined in analogy to the ones of a single barrier but they contain the collective reflection and transmission properties resulting from the interplay of the first j interfaces. In the most simple case of only one interface, they reduce to Eqs. (4.7) and (4.8).

For more complicated setups, these collective reflection and transmission coefficients can be computed recursively starting from a single interface and successively adding further interfaces one by one. Taking into account all possible paths of light propagation within a layer, that are caused by multiple reflections at the layer interfaces, via

$$\Pi_j^{\varsigma} = \sum_{m=0}^{\infty} \left(e^{\theta_j} R_{j+1}^{\varsigma-} e^{\theta_j} \mathcal{R}_j^{\varsigma+}\right)^m = \frac{1}{1 - R_{j+1}^{\varsigma-}\mathcal{R}_j^{\varsigma+}e^{2\theta_j}} , \tag{4.13}$$

the collective coefficients for propagating light read

$$\mathcal{R}_{j+1}^{\varsigma-} = \mathcal{R}_j^{\varsigma-} + \mathcal{T}_j^{\varsigma-}\Pi_j^{\varsigma}e^{\theta_j}R_{j+1}^{\varsigma-}e^{\theta_j}\mathcal{T}_j^{\varsigma+}\,, \tag{4.14}$$

$$\mathcal{T}_{j+1}^{\varsigma-} = \mathcal{T}_j^{\varsigma-}\Pi_j^{\varsigma}e^{\theta_j}T_{j+1}^{\varsigma-}\,. \tag{4.15}$$

Similarly, one obtains for the counter-propagating light

$$\mathcal{R}_{j+1}^{\varsigma+} = R_{j+1}^{\varsigma+} + T_{j+1}^{\varsigma+}\Pi_j^{\varsigma}e^{\theta_j}\mathcal{R}_j^{\varsigma+}e^{\theta_j}T_{j+1}^{\varsigma-}\,, \tag{4.16}$$

$$\mathcal{T}_{j+1}^{\varsigma-} = T_{j+1}^{\varsigma+}\Pi_j^{\varsigma}e^{\theta_j}\mathcal{T}_j^{\varsigma+}\,. \tag{4.17}$$

Again, the polarization direction is given by $\varsigma = s, p$. Once all layers of a sample are taken into account, these collective coefficients contain the full optical properties of the optically passive structure. In particular, the collective reflection and transmission coefficients of the entire structure are needed to define the initial conditions for the computation of the mode coefficients A_j and B_j which define the mode functions. When initially counter-propagating light has passed all interfaces of the sample, it is entirely traveling to the left. Therefore, left of the first interface, the counter-propagating light has the mode coefficients

$$A_0^+ = 0\,, \tag{4.18}$$

$$B_0^+ = \mathcal{T}_m^+\,, \tag{4.19}$$

where the total number of interfaces is given by m. Similarly, light that has initially been propagating, is only traveling to the right after having passed all interfaces. Consequently, the mode coefficient B_m has to vanish, which can be satisfied by the initial conditions for propagating light

$$A_0^- = 1\,, \tag{4.20}$$

$$B_0^- = \mathcal{R}_m^-\,. \tag{4.21}$$

Using these mode coefficients, $A_0^\pm$ and $B_0^\pm$, one can compute the mode functions in all layers of the sample.

4.2 Quantum Wells in a Dielectric Environment

To describe samples containing QWs, the remaining task is to join the description of QWs and the propagation of light through the dielectric environment of the QWs. In particular, a self-consistent treatment of light-matter interaction is needed. In this study, we will only investigate light propagating perpendicular to the QWs and thus perpendicular to all layers so that $\mathbf{q}_\parallel = 0$. As a consequence [298], Eq. (2.30) simplifies to

$$\left[\frac{\partial^2}{\partial z^2} - \frac{n^2(z)}{c^2}\frac{\partial^2}{\partial t^2}\right]E(z,t) = -\mu_o\frac{\partial^2}{\partial t^2}P(z,t)\,. \tag{4.22}$$

The influence of the QW on the light field can be attributed to two effects. First, the QW material differs from the material of the surrounding layers. Consequently, a possible difference in the respective indices of refraction causes reflection and transmission effects as described in the previous section. Hence, that effect can be modeled by an appropriate refractive index n_{QW} of the QW layer and application of the transfer matrix as discussed above. Such reflections at the QW-barrier interfaces may cause that light travels through the QW layer back and forth several times. In particular, the width of the QW layer becomes important in the description of these multiple transits of light. Hence, the QW cannot be assumed to be infinitely thin though it's extension is small compared to the spacer layers.

Second, the light-matter interaction leads to absorption and re-emission of light, which is described by the dynamics of the coherent polarization. The corresponding optical response of the QW can be described by the QW susceptibility.

The self-consistent description may be achieved if one solves Eq. (4.22) assuming a constant refractive index $n = n_{QW}$ in a QW of finite extension, which corresponds to the discrimination of the QW effects into the background-refractive-index contribution and the polarization contribution. With the help of the dimensionless quantity

$$\xi(\omega) \equiv \frac{1}{2}\frac{\omega}{n_{QW}c}\chi(\omega)\,, \tag{4.23}$$

which directly follows from the QW susceptibility, one then obtains the linear transmission and reflection coefficients of the QW as

$$T(\omega) = \frac{1}{1-i\xi(\omega)} \tag{4.24}$$

$$R(\omega) = \frac{i\xi(\omega)}{1-i\xi(\omega)}\,. \tag{4.25}$$

For more details of the derivation of these coefficients, it is referred to Refs. [71, 298]. While the consideration of the QW background refractive index and of the QW width is straight forward, the task is to include the effects of light-matter interaction given by Eqs. (4.24) and (4.25).

Technically, this can be done as discussed below. Starting from a transfer-matrix calculation in which only the QW background refractive index and the finite QW width are considered, one may split the QW layer into two identical parts. The so created additional interface does not change the resulting spectra since an interface between two identical layers provides full transmission and vanishing reflection. Nevertheless, it is that artificially introduced interface that allows for an inclusion of the entire QW properties. In particular, the previously neglected effects of many-body interactions may be included by adopting the respective QW transmission and reflection probabilities following from Eqs. (4.24) and (4.25) for this artificial interface. Under that assumption, the QW is emitting (at the interface position) into two adjacent layers of identical refractive index n_{QW}, which was assumed in the derivation of the QW transmission and reflection coefficients, Eqs. (4.24) and (4.25). Moreover, reflections caused by the

QW-barrier interfaces are fully included via the transfer matrices. In addition, this approach allows to simulate arbitrarily many QWs embedded in a dielectric environment. Particularly, this self-consistent approach fully includes a microscopic description of radiative dephasing of the QW polarization.

5 Theory vs. Experiment

With the discussed microscopic theory for a SQW and the transfer-matrix method at hand, we are able to describe the Fibonacci MQW samples appropriately. In particular, the microscopic theory including the carrier-carrier scattering allows for the investigation of nonlinear effects such as EID. The transfer-matrix method ensures a consistent treatment of the QWs and of the propagation of light through the dielectric environment. Hence, the theory in principle is capable of describing experiments realistically. The basis of a theory-experiment comparison is an adequate description of the sample and of the experimental conditions. Therefore, we first of all have to find an appropriate and reasonable set of sample parameters that is suitable to reproduce the experimental findings. These parameters have been determined by matching theoretical results with data obtained from measurements in the linear-response regime.

5.1 Linear Spectra

Of course, an appropriate description of a representative SQW is crucial for a correct description of MQW samples. Hence, we start the investigations with a study of an experimentally taken SQW linear spectrum shown as shaded area in Fig. 5.1(a). In the reflection spectrum of that 10-layer SQW sample (FIB10), we observe asymmetric line shapes of both, the heavy-hole (hh) and the light-hole (lh) resonance. Such line shapes are known from disorder and phonon investigations [327–333]. To account for these line shapes, we refine the phenomenological treatment of phonon and disorder contributions, Eq. (3.13), by introducing an additional frequency dependence to the phenomenological dephasing constant

$$\gamma(\omega) \;=\; \frac{\gamma}{\exp(-(\hbar\omega - E_x + \Delta E_{\mathrm{cut}})/C) + 1}\,. \tag{5.1}$$

In particular, for the hh (lh) 1s resonance, positioned at E_x, the dephasing constant $\gamma = 0.163\mathrm{meV}$ ($0.110\mathrm{meV}$) and a cut-off energy of $\Delta E_{\mathrm{cut}} = 0.25\mathrm{meV}$ together with the constant $C = 0.1\mathrm{meV}$ have been chosen. In the corresponding computations of

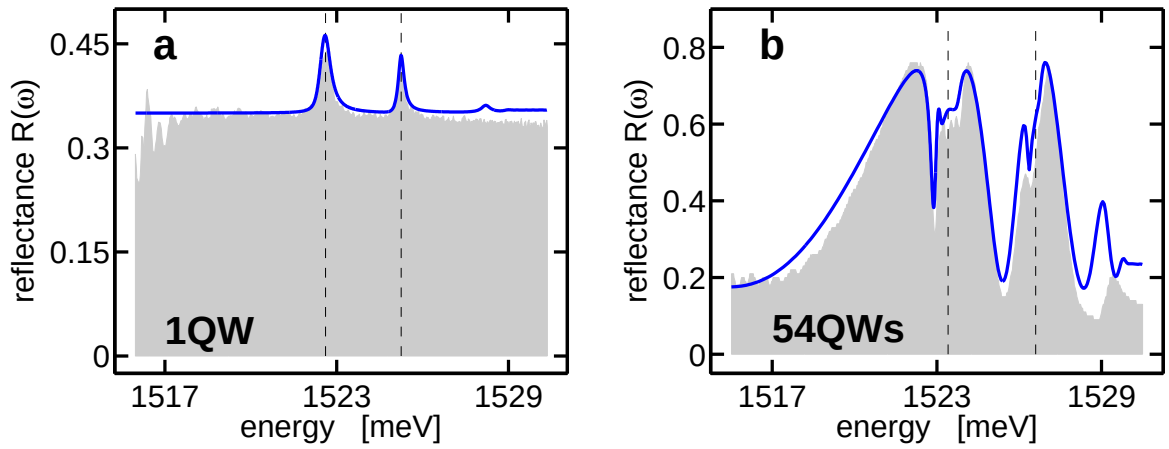

Figure 5.1: Linear fits to experimental [296] reflectance spectra. With a single set of parameters, all spectral features are well reproduced for a SQW (a) as well as for 54 Fibonacci-spaced QWs (b).

the QW susceptibility [334], hh and lh dipole-matrix elements of $d_{cv} = e \cdot 0.78\text{nm}$ and $d_{cv} = e \cdot 0.5\text{nm}$, respectively, are used which are obtained from a separate band-structure calculation [335]. Assuming a carrier density of $n = 1 \times 10^9 \text{cm}^{-2}$ in thermal quasi-equilibrium at a carrier temperature of $T = 40K$, one obtains the computed linear reflection spectrum which is plotted as a blue line in Fig. 5.1(a). Due to the two-band model separate computations are performed for the hh and the lh susceptibility which are combined to the full QW susceptibility. The above parameter choice yields a very good agreement of the experimentally observed asymmetric line shape of the SQW reflectance spectrum and the computed reflectance spectrum. The resonance positions are indicated by dashed vertical lines.

The used refractive indices of the different sample layers have been determined by a detailed parameter study. In particular, the exact refractive indices of the different material layers are not known, in contrast to the widths of these material layers which are experimentally known with high accuracy. The refractive indices of the respective bulk materials are tabulated. However, the refractive index within a narrow layer of either material differs from the bulk value. Nevertheless, the bulk refractive index may serve as a landmark in the search of the correct values. The used refractive indices have been chosen such that the computations are in accordance with the measured spectrum of a SQW. The so-obtained sample-parameter set is given in appendix B. In particular, the different material layers can be categorized into only seven layer types so that a set of only seven matching refractive indices has had to be found.

The validity of the parameters for the refractive indices and the asymmetric line shape used to match the measured SQW spectra by the theory can be verified from a simulation of a more complicated sample and comparison with experimental observations. Figure 5.1(b) shows the measured linear reflectivity spectrum of the Fibonacci-spaced 54 QW sample FIB13 as a shaded area together with the corresponding calculated reflectivity spectrum (blue line). The vertical dashed lines indicate the spectral positions

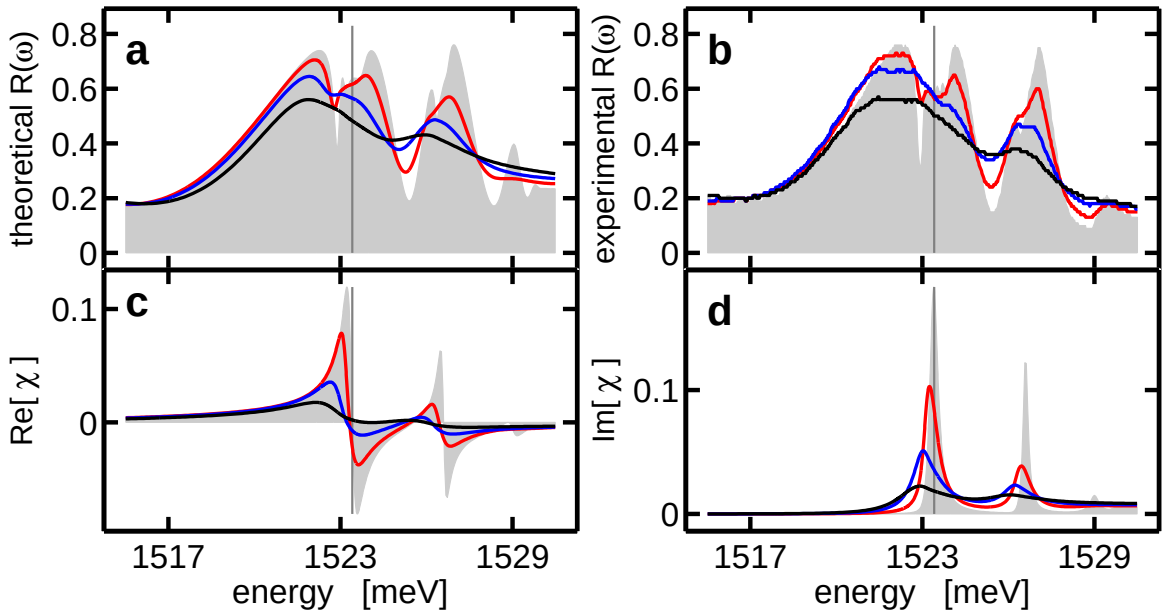

Figure 5.2: Very good agreement between (a) computed and (b) experimental [296] nonlinear reflectance is obtained for FIB13. Densities of $n = 1 \times 10^9 \mathrm{cm}^{-2}$ (shaded area), $n = 5 \times 10^9 \mathrm{cm}^{-2}$ (red line), $n = 2 \times 10^{10} \mathrm{cm}^{-2}$ (blue line), and $n = 5 \times 10^{10} \mathrm{cm}^{-2}$ (black line) have served as an input to the theory while pump powers of 76.6μW (shaded area), 871μW (red line), 3.7mW (blue line), and 11.1mW (black line) have been used in the single-beam experiments. The real part (c) and the imaginary part (d) of the QW susceptibility show broadening and bleaching with increasing carrier densities.

of the hh and the lh resonance. In accordance with the observations in Refs. [250, 252], the measured reflectance spectrum shows detailedly structured dips near the resonance positions. Particularly, a very pronounced deep dip is observed below the hh resonance. All spectral features are very well reproduced by the theory using the same parameter set as for the SQW. That best-matching set of parameters refers to an average QW spacing of $D_0 = 0.5016\lambda$ and a ratio of large to small spacing of $\rho_0 = 1.643$, which are close to the aimed values $D = 0.5\lambda$ and $\rho = \tau \approx 1.618$.

Especially, in the simulation of the sample FIB13, the reflectance spectrum has proved to be very sensitive to variations of the refractive indices, which can be attributed to the high number of 275 dielectric layers that have to be considered in the calculations. Spectral changes caused by refractive-index variations have been found to be the stronger the more often the respective layer type was found in the sample. Therefore, the used set of fit parameters, reproducing the spectral features that well, may be considered an appropriate basis for further investigations. In the following, we will particularly focus on the spectral region in the vicinity of the hh resonance.

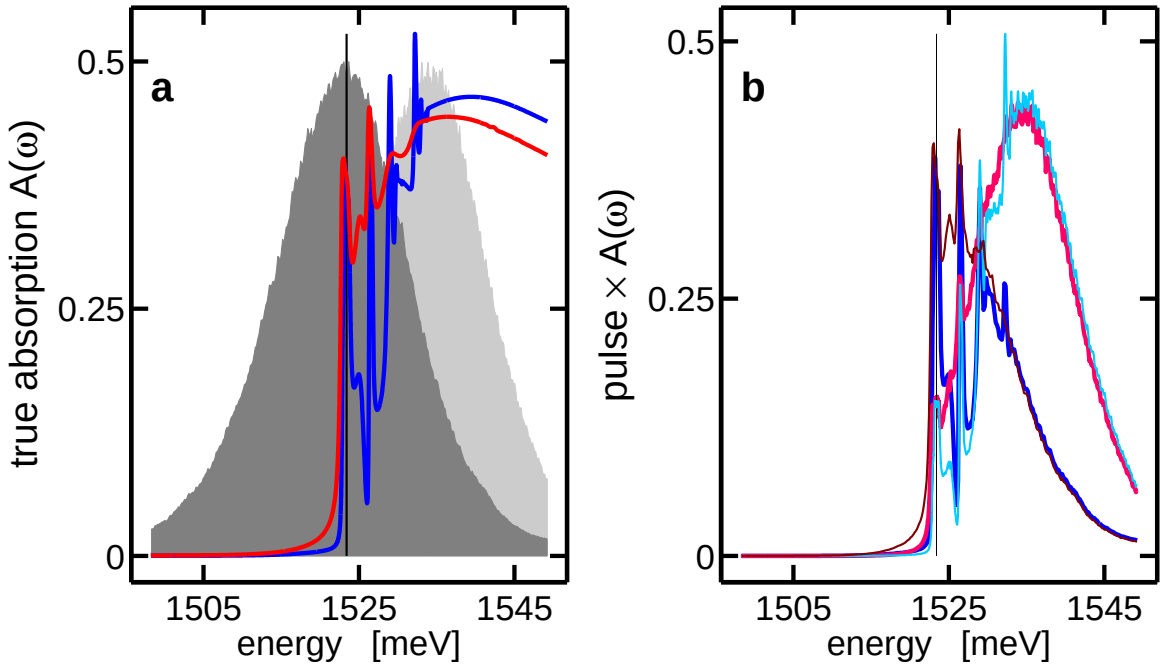

Figure 5.3: (a) The spectra of the experimentally applied pulses (shaded areas) [296] are shown together with the computed true-absorption probability $A(\omega) = 1 - R(\omega) - T(\omega)$ for low (blue line) and high (red line) excitation. (b) The corresponding true absorption is plotted for on-resonance and above-resonance excitation, showing that in both cases most of the absorption generates free carriers. The hh resonance position is indicated by a vertical line.

5.2 Nonlinear Reflectance Spectra

Equipped with the well-working parameter assignment obtained from the linear evaluations, one may thus draw attention to the analysis of nonlinear effects. Experimental nonlinear reflectance spectra taken after single-beam excitation of FIB13 are shown in Fig. 5.2(b). The different spectra have been obtained with pump powers of 76.6μW (shaded area), 871μW (red line), 3.7mW (blue line), and 11.1mW (black line). Since these different pump powers yield different carrier densities in the sample, we assume elevated carrier densities, which are in thermal quasi-equilibrium, in order to match the experimental findings and the simulations. In the calculations of nonlinear spectra, Fig. 5.2(a), a carrier temperature of 40K and carrier densities of $n = 1\times10^{9}\mathrm{cm}^{-2}$ (shaded area), $n = 5 \times 10^{9}\mathrm{cm}^{-2}$ (red line), $n = 2 \times 10^{10}\mathrm{cm}^{-2}$ (blue line), and $n = 5 \times 10^{10}\mathrm{cm}^{-2}$ (black line) have been assumed.

The corresponding real and imaginary part of the QW susceptibility used in the calculations are shown in the same figure, frames (c) and (d). For higher excitation levels, the susceptibility suffers more and more EID, i.e. an increasing bleaching and broadening of the hh and lh resonances is observed with increasing carrier density. Consequently,

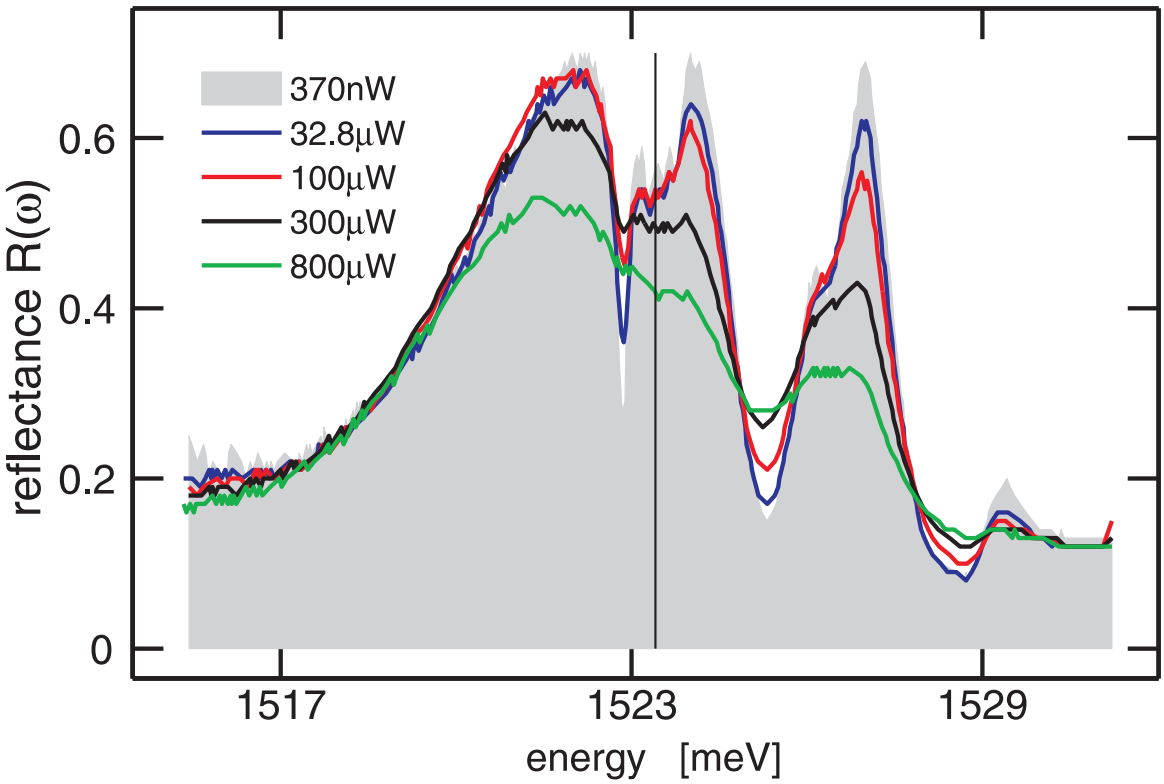

Figure 5.4: Nonlinear reflectance spectra obtained by above-band pump experiments [296] look very similar to those obtained by resonant pumping, compare for Fig. 5.2.

the pronounced deep dip below the hh exciton resonance gradually disappears from the spectra once the excitation level is risen. Comparison between the measured and calculated reflectance spectra shows excellent agreement. Specifically, the observed overall peak and valley structure is nicely reproduced.

5.3 Excitation Conditions

In this section, we will address the question why the single-beam experiments are so nicely matched by calculations from a theory based on the assumption of pump-probe conditions. To do so, we compare resonant and above-band excitation conditions. In particular, we start that inspection by an examination of the absorption properties of the sample FIB13.

Figure 5.3(a) shows the scaled spectra of experimentally applied pulses for resonant (dark gray) and above-band (light gray) excitation as shaded areas. The calculated true-absorption probabilities $A(\omega) = 1 - R(\omega) - T(\omega)$ for low excitation (blue line) and high excitation (red line), where the reflection [transmission] probability is given by $R(\omega)$ [$T(\omega)$], are plotted in the same frame. The respective true absorption resulting from

the multiplication of the pulse spectrum with the true-absorption probability is plotted in Fig. 5.3(b) for low and high excitation levels after both, resonant and above-band excitation. The reddish curves correspond to high excitation and the bluish ones to low excitation. Specifically, the light colored lines refer to spectra for above-band pump while the darker colored lines refer to spectra for on-resonance pump, respectively.

As one can see, considerable absorption is observed in a wide spectral range for all excitation conditions. In particular, resonant and above-band excitation yield very similar absorption spectra. Moreover, most of the absorption generates free carriers under both excitation conditions due to the strong continuum-absorption contributions. In consequence, the experimental spectra obtained by above-band excitations, Fig. 5.4, look very similar to the spectra obtained after resonant excitation, Fig. 5.2(b), when the respective pump powers are comparable.

That similarity can be understood as follows. From pulsed nonlinear experiments of QWs one has learned that carriers which have been created by the near band edge absorption of 100fs pulses can be adequately described by an equilibrium carrier distribution with a carrier temperature of $40 - 50$K. Especially, only negligible cooling or redistribution of these carriers occurs within 100fs. Hence, the excited system can be described by an appropriately chosen carrier density and temperature for above-band excitation conditions.

In particular, the difference that originates from the two different excitation schemes is a creation of coherent polarization by the resonant pump while the above-band excitation generates carriers incoherently. Nevertheless, the microscopic treatment of the carrier-carrier scattering guarantees an appropriate description of the density-dependent QW nonlinearity, and thus of the EID. Moreover, the self-consistent treatment of light-matter interactions ensures the correct inclusion of the corresponding broadening of the spectral features which change only relatively slowly with the density, as the simulations show.

Under above-band excitation conditions, the effect of the carriers, generated incoherently by the non-resonant pump, on resonant spectral features is monitored by the weak resonant part of the pulse. That resonant tail of the off-resonant pulse serves here as the probe pulse that is assumed in the theory, which establishes the link between theory and non-resonant conditions. As we have seen previously, spectra obtained by non-resonant excitation are very similar to spectra after resonant excitation due to similar absorption characteristics. Thus, the very good agreement between theory and resonant-pump experiments can be understood. At the same time, one has to remark that a detailed comparison of the exact carrier densities becomes meaningful only once the excitation conditions are modeled closer to the experiment.

6 Numerical Studies

The very good agreement of our theory with the experimental results found in the linear as well as in the nonlinear regime confirms an appropriate modeling of the investigated samples and thus the predictive power of the theory. Therefore, further entirely numerical studies shall now deepen the understanding of the spectral properties of the Fibonacci-spaced MQW samples. In particular, investigation of effects and conditions that cannot be achieved or that are at least very difficult to achieve in experiments can be performed by numerical simulations in an easy way. The same sample parameters which have successfully been used in the previously discussed theory-experiment comparisons are used in all following computations unless the usage of deviating parameters is stated.

Specifically, the focus of the investigations will be on the sharp minimum in the linear reflectance spectrum. Sharp spectral features like the observed reflectance minimum are possible candidates for optical applications. For instance, the optical Stark effect [336] can be used to shift the entire spectrum in a short time so that the present sample, i.e. the sharp dip, could be used as a high-speed optical switch [337–339]. The dip also has possible applications to slow light similar to the case of interference fringes observed in the spectral stopband of a very large number of slightly detuned excitonic Bragg periodic QWs [340, 341]. Thus, we will now aim at an understanding of the properties as well as of the origin of that reflectance minimum.

6.1 Origin of Sharp Reflectance Minimum

In order to study the origin or the pronounced, sharp minimum in the reflectance spectrum close to the 1s hh-resonance, a switch-off analysis of the QW susceptibility is performed. Since that reflectance minimum is most pronounced in the linear spectrum of FIB13, we focus on that case. Therefore, we show as a shaded area in Fig. 6.1 the already discussed linear reflectance spectrum obtained from the full calculation. That reflectance spectrum is compared to the results of identical computations except that either the real part of the QW susceptibility (blue line), or its imaginary part (red line),

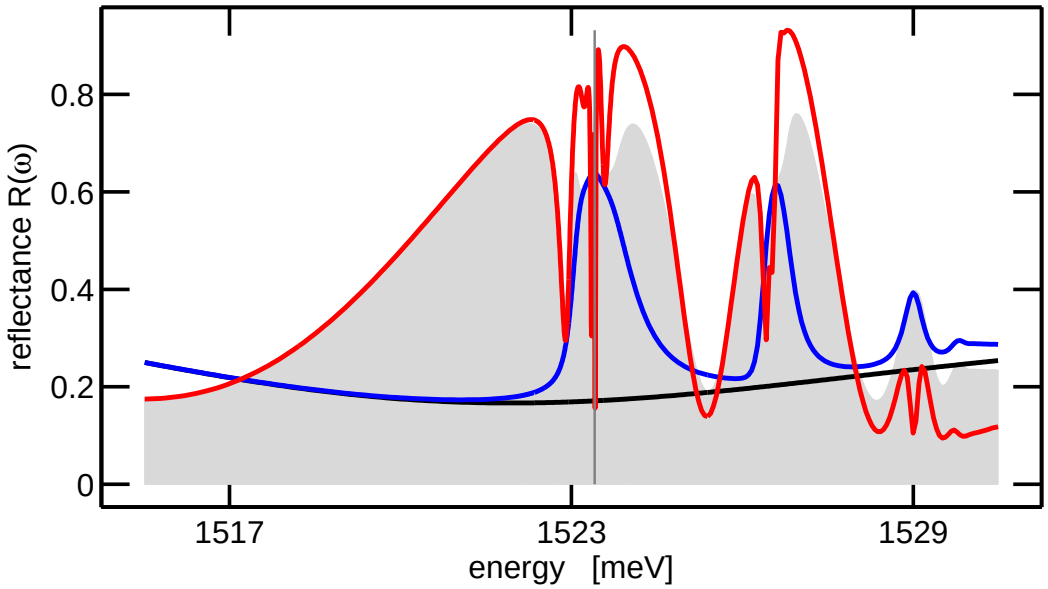

Figure 6.1: A switch-off analysis shows a disappearance of the stopbands with entirely switched-off QW susceptibility (black line). While the inclusion of only the imaginary part of the susceptibility (blue line) reveals a smoothly peaked spectrum, the corresponding real part (red line) almost completely reproduces the highly structured spectrum of the full simulation (shaded area) of FIB13 in the linear regime.

or the whole QW susceptibility (black line) is artificially set to zero. If the QW susceptibility is neglected completely, the stopbands disappear and the remaining almost constant reflectance originates only from the array of dielectric layers. In particular, the reflection of light at the sample-air interface strongly contributes to the observed total reflectance of the sample in the whole spectral range if there is no ARC added to that interface.

Switching on the imaginary part of the QW susceptibility, one finds that additional absorption peaks are introduced to the reflectance. These peaks are located at the resonance positions and are additive to the spectrum obtained with vanishing QW susceptibility. The observed spectral shape clearly differs from the full computation.

In contrast, all the main spectral features of the full computation agree with the spectrum obtained when only the real part of the QW susceptibility is considered. In particular, the stopbands as well as the valley between the hh and the lh resonance originate from the real part of the susceptibility. Moreover, the spectral shape of the full computation is completely matched in the spectral region energetically below the sharp reflectance minimum. In addition, even the spectral shape of that reflectance minimum is observed to be in nice agreement with the spectrum from the full computation as well.

Close to the resonance positions, a number of additional very sharp peaks and dips is observed. In the full computation, the imaginary part causes some of these extremely sharp features to smear out. At the same time, the imaginary part of the QW suscep-

tibility reduces the strength of some of the stopbands. In conclusion, the performed switch-off analysis reveals the main spectral features to have their origin in the real part of the QW susceptibility. Thus, the spectral properties mainly stem from cavity-like effects.

6.2 Sensitivity of Spectra to Average Spacing and Ratio of QW-QW separations

The influence of the Fibonacci spacing on the spectral properties in the vicinity of the 1s hh resonance shall now be investigated. Particular attention is drawn to the strong reflectance minimum. Since the Fibonacci spacing is entirely defined by the average QW spacing D and the ratio ρ of the two spacers, we vary either D or ρ and keep the other variable constant. The respective dependence of the spectrum on these structural variations is quantified with the help of the deviation

$$\epsilon = \frac{\int_{\omega_{1s,hh}-\vartheta}^{\omega_{1s,hh}+\vartheta} |R(\omega) - R_0(\omega)| \mathrm{d}\omega}{\int_{\omega_{1s,hh}-\vartheta}^{\omega_{1s,hh}+\vartheta} R_0(\omega) \mathrm{d}\omega} , \tag{6.1}$$

where $\hbar\omega_{1s,hh} = 1523.4\mathrm{meV}$ and $\hbar\vartheta = 1.5\mathrm{meV}$. In particular, we use the calculated linear spectrum $R_0(\omega)$ of the 54QW sample FIB13 as a reference and detune the average spacing D and the layer-thickness ratio ρ away from the corresponding reference parameters $D_0 = 0.5016\lambda$ and $\rho_0 = 1.643$. The integrated absolute spectral deviations are normalized with respect to the integrated reference spectrum $R_0(\omega)$. When varying the thicknesses of the building blocks L or S, all refractive indices as well as all layer thicknesses except the thickness of the spacer layer are kept unchanged at all times.

For fixed $\rho = \rho_0 = 1.643$, the computed deviation ϵ is plotted as a function of average spacing D in Fig. 6.2(a). A variation of D within a range of $\pm 1\%$ around the reference value D_0 already results in 25% changes, which indicates a very strong sensitivity of the reflectance spectrum to the average spacing. Based on the generalized Bragg condition, Eq. (2.14), this strong dependence on D can easily be understood. The Bragg condition directly defines a certain average spacing $\bar{D}$ associated with the resonance condition for a given frequency $\bar{\omega}$. Therefore, the detuning of the average spacing away from that $\bar{D}$ to $\bar{D}'$ yields a new Fibonacci structure that has a different resonance frequency $\bar{\omega}'$. Consequently, the initially resonant frequency $\bar{\omega}$ corresponding to $\bar{D}$ is off-resonant for the detuned $\bar{D}'$. Hence, it is obvious that the spectrum should have that strong dependence on the average spacing D.

In particular, the local minimum of the reflectance spectrum is present in the spectra within a narrow range from $D = 0.5000\lambda$ up to $D = 0.503\lambda$ for the Fibonacci spacing. In an analogical investigation for the same average spacing $D = D_0$ but for a periodic structure with $\rho = 1$ instead, a similar reflectance minimum has been obtained. For the periodic structure, the local minimum is present in the spectra within a similarly narrow range from $D = 0.501\lambda$ up to $D = 0.503\lambda$. This observation already gives a hint to that the spectral reflectance dip is not just related to the explicit Fibonacci spacing but to

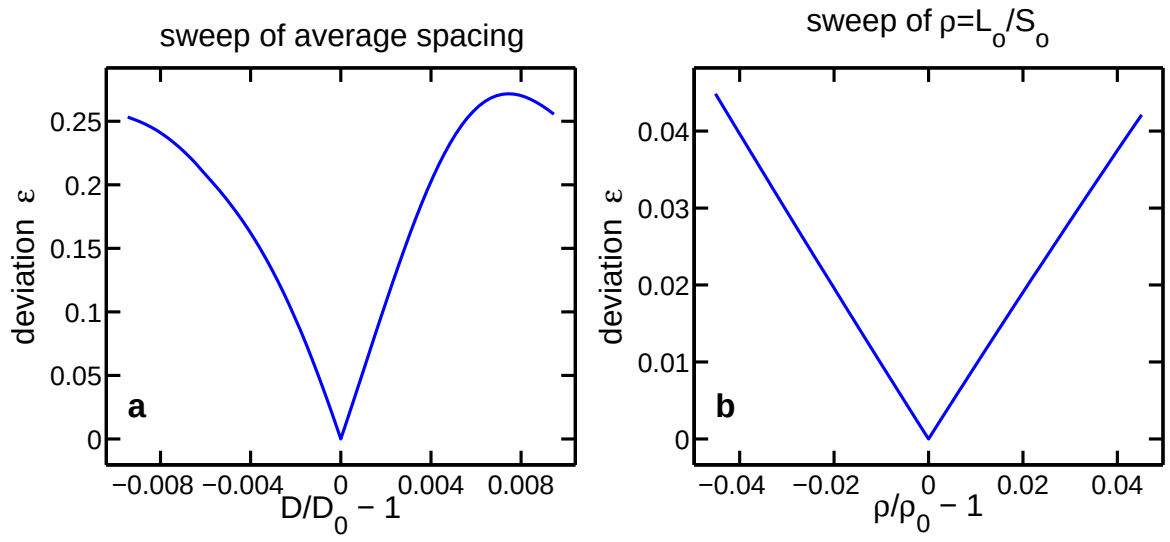

Figure 6.2: Deviations of 54QW reflectance spectra from the fit spectrum ($D_0 = 0.5016\lambda$ and $\rho_0 = 1.643$) are shown in dependence of (a) the average distance D and (b) the ratio of the layer thicknesses $\rho = o_L/o_S$. A strong sensitivity to changes in D is found while a certain robustness against changes in ρ is observed.

the accuracy of fulfilling the Bragg condition as well. This issue will be studied in more detail later on in Secs. 6.3 and 6.4.

Additionally, an investigation of the deviation ϵ has been performed for constant average spacing $D_0 = 0.5016\lambda$ and a variation of the ratio ρ of the optical path lengths of the two building-block types. In Fig. 6.2(b), the deviation ϵ is plotted as a function of ρ. It can be seen that the spectra are only weakly affected by a variation of ρ when the average spacing is unchanged. More specifically, though ρ/ρ_0 was changed almost an order of magnitude more than D/D_0 in Fig. 6.2(a), the obtained maximum deviation is smaller by a factor of five compared to the deviation observed when varying D. In contrast to the strong sensitivity to D, the Fibonacci features thus show a certain robustness of the spectrum to changes in ρ.

The observed stopbands, the pronounced dips near the hh and lh resonances in the reflection spectra, as well as the strong sensitivity of the spectra to matching the resonance condition are in accordance with findings from calculations for constant background refractive index and Lorentzian susceptibilities [250] as well as with experiments on resonant Fibonacci QCs [252]. The robustness against variations in the ratio of spacer thicknesses is to be seen in analogy to the similar findings in Ref. [233] for X-ray studies on passive one-dimensional Fibonacci QCs.

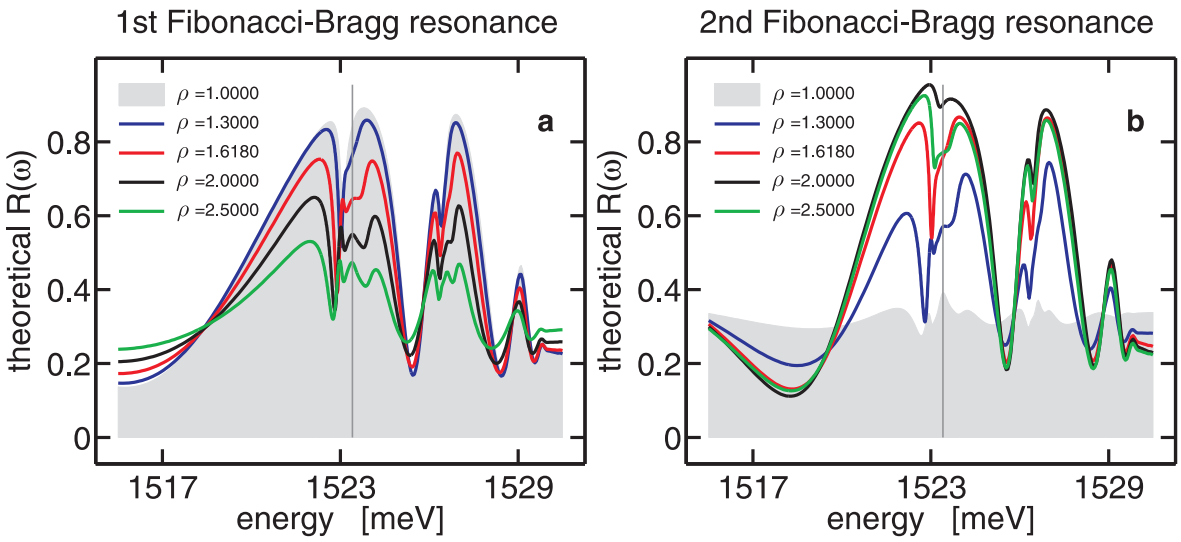

Figure 6.3: For (a) the first Bragg resonance with $(h, h') = (F_1, F_0) = (1, 0)$ as well as an average spacing $D_0 = 0.5016\lambda$, and (b) for the second Bragg resonance with $(h, h') = (F_2, F_1) = (1, 1)$ as well as $D = 0.8115\lambda$, the reflectance is shown for different ratios of the optical lengths $\rho = o_L/o_S$, while the respective average spacing is kept constant.

6.3 Fibonacci vs. Periodic Spacing

A natural extension of the study presented in Fig. 6.2(b) is the variation of the ratio ρ in a larger range. In particular, this allows to tune the sample setup from the periodic arrangement to any non-canonical ($\rho \neq \tau$) or to the canonical ($\rho = \tau$) Fibonacci spacing while the average spacing D remains constant. The so-obtained reflectance spectra for the first Fibonacci Bragg resonance, i.e. $j = 1$ with $(h, h') = (F_1, F_0) = (1, 0)$, are plotted in Fig. 6.3(a). In analogy, the reflectance spectra computed for the second Fibonacci Bragg resonance with $j = 2$ so that $(h, h') = (F_2, F_1) = (1, 1)$ are plotted in Fig. 6.3(b). In both cases, the ratio ρ is tuned from the well-known [75] periodic case, $\rho = 1$, via $\rho = 1.300$ to the canonical Fibonacci spacing, $\rho = \tau$, as well as to even larger values of ρ such as $\rho = 2.000$ and $\rho = 2.500$. At the same time, the respective average spacing D is kept constant.

For the first Fibonacci-Bragg resonance, an average spacing of $D_0 = 0.5016\lambda$ has been used in the computations. This average spacing follows from the previously used sample parameters and differs slightly from the ideal one of $D = 0.5\lambda$. Among the spectra obtained with the above set of values for ρ, the maximal reflection is observed for the periodic case, $\rho = 1$. In addition, a monotonic decrease of the overall reflectance is found as ρ is increased. That is, the reflection gets weaker and weaker the more the large and small building blocks differ from each other. Below the hh resonance energy, there is a reflectance minimum for any chosen ρ. The most pronounced, i.e. the narrowest and deepest reflectance dip is observed for $\rho = \tau$.

Structures arranged according to the second Fibonacci Bragg resonance display a

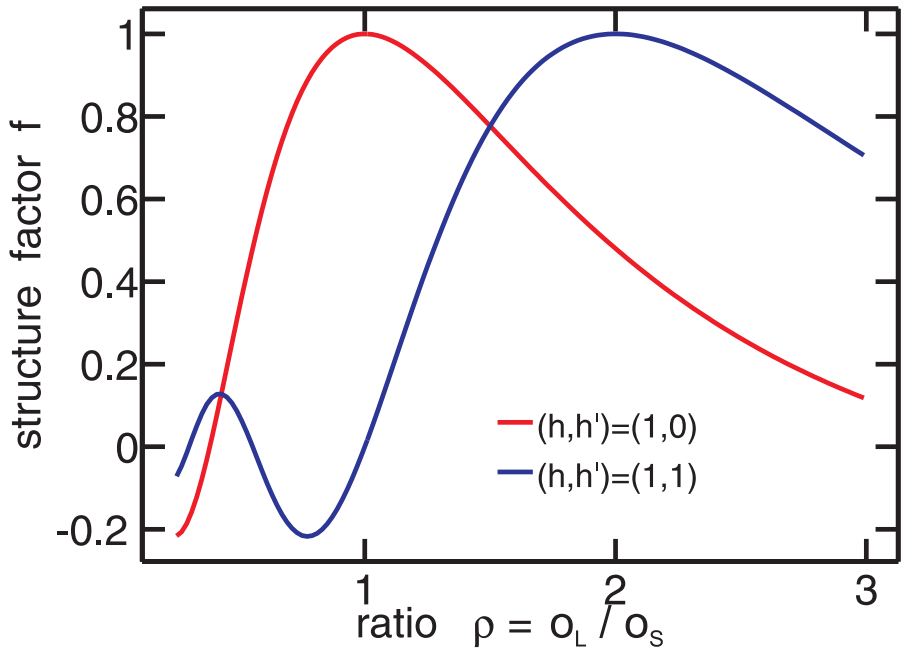

Figure 6.4: Structure factors for the first two Bragg resonances $(h, h') = (F_1, F_0) = (1, 0)$ plotted in red and $(h, h') = (F_2, F_1) = (1, 1)$ plotted in blue.

different behavior of the reflectance when ρ is varied in the same way. In contrast to the case of $j = 1$, the weakest reflectance is observed in the periodic arrangement with $\rho = 1$. With increasing ρ, the reflectance increases until its maximum is reached at $\rho = 2$. Then, the reflectance decreases again if the ratio ρ is further increased to $\rho = 2.500$. In analogy to the first Fibonacci Bragg resonance, a reflectance minimum is observed below the hh exciton resonance for any choice of ρ. Again, the narrowest and deepest reflectance minimum is found for $\rho = \tau$. But, for $j = 2$, there is a stronger variation in the shape of that minimum than in case of $j = 1$.

The behavior of the reflectance is in agreement with the respective structure factor of the corresponding Fibonacci sequence plotted in Fig. 6.4. Assuming sample parameters that exactly satisfy the Fibonacci Bragg condition, the structure factor is plotted in red (blue) for the first (second) Fibonacci Bragg resonance. In contrast to the first resonance ($j = 1$) where the ideal average spacing is $D = 0.5\lambda$, the second resonance ($j = 2$) defines an average spacing of $D = 0.8090\lambda$. In general, one observes complete constructive interference when the QWs are separated by integer multiples of 0.5λ. Therefore, a ratio of $\rho = 1$ yields a maximum of the structure factor if $j = 1$ since $D = o_L = o_S = 0.5\lambda$. In contrast, the same ratio ρ applied to the second Fibonacci Bragg resonance, $D = 0.8090\lambda$, results in $D = o_L = o_S = 0.8090\lambda = 0.5\tau\lambda$. This causes destructive interference in the reflectance because the QWs are separated by irrational fractions of the hh-resonance wavelength λ. Consequently, the structure factor vanishes at $\rho = 1$ if $j = 2$. For the second Fibonacci Bragg resonance, the maximum of the structure factor is found at $\rho = 2$. Then, the optical thicknesses of the two building

blocks are $o_S = 0.5\lambda$ and $o_L = 1.0\lambda$, which follows directly from Eq. (2.15) and which displays constructive interference.

Comparing these structure factors with the respective reflectance spectra plotted in Fig. 6.3, we observe the same trends in the magnitude of the reflectance. That is the case, even though the average spacings used in the computations of these spectra slightly differ from the ideal ones used computing the structure factors. Thus, the structure factor indicates the strength of the overall reflectance even if the Bragg condition is not exactly satisfied.

It is well-known from the periodic MQWs that the specific reflectance results from interference effects which are governed by the QW arrangement. As a result of the quasiperiodic arrangement, the average spacings corresponding to the Fibonacci Bragg resonances of order $j > 1$ differ from the Bragg spacings know from the periodic MQWs. Moreover, the fact that the local reflectance minimum below the hh-resonance position is most pronounced if $\rho = \tau$ for both Fibonacci Bragg resonances indicates that the strength of this minimum may be directly related with the quasiperiodic arrangement.

6.4 Influence of the Dielectric Environment

To gain even more insight into the origin and the nature of the local reflectance minimum below the hh resonance energy, we investigate the influence of the dielectric environment on the dip next. Figure 6.5(a) shows the calculated linear reflectivity spectrum of the sample FIB13 as a shaded area. Additionally, the reflectivity spectrum of the same sample to which an ARC is added is plotted as a red line. Clearly, the ARC removes the background reflection as expected because it is designed to prevent reflections from the sample-air interface. However the stopband and dip structure remains intact after adding the ARC. Hence, interference effects originating from the sample-air interface do not cause the reflectance dip.

To check for propagation effects inside the sample, we simplify the 275 layers within the sample in the most drastic way by giving them a uniform background refractive index of $n = n_{QW}$. In order to keep the optical lengths unchanged we compensate for the changes in the refractive indices by adjusting the respective layer thicknesses such that the corresponding original optical length is preserved. Doing so, we remove all additional reflections occurring at the internal layer interfaces. Thus, we are left with the pure interplay of the Fibonacci-spaced QWs to which reflections at the sample-air interface are superimposed since the ARC is removed again. The corresponding spectrum is plotted as a blue line in which the main spectral features are intact as well. Consequently, the internal reflections do not cause any additional spectral features while they rather contribute to the relative reflection strength. In conclusion, the minimum in the reflectance must be caused by the QW arrangement, not by light-interference effects due to the structure of the dielectric environment.

Therefore, another variation of the sample FIB13 has been simulated in that the average spacing has been kept constant while the ratio of the spacer thicknesses has been tuned to the periodic case. The corresponding spectrum is depicted as a black

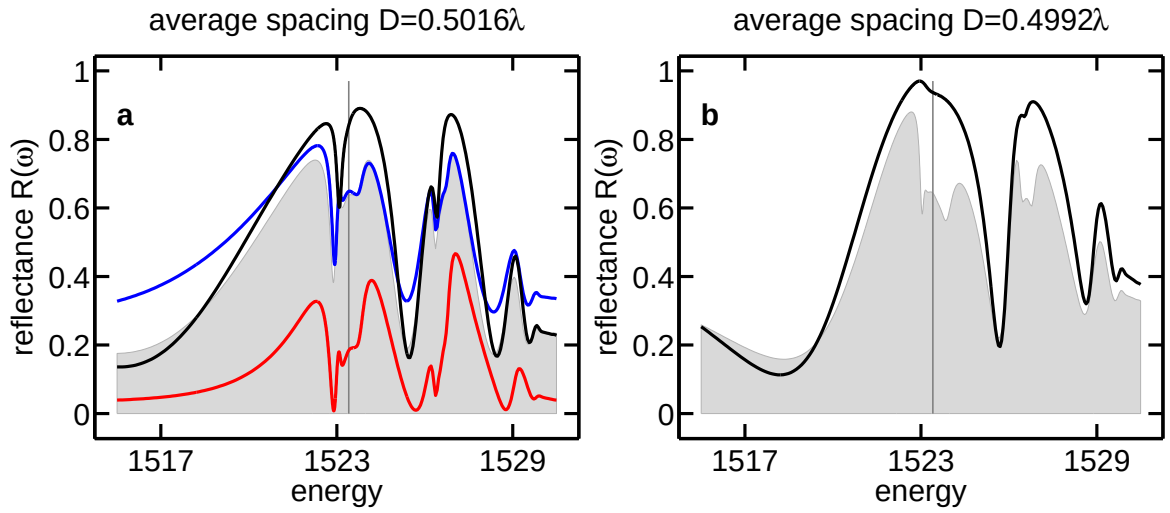

Figure 6.5: (a) Calculated reflectance spectra for the sample FIB13 (shaded area), for the sample FIB13 with an additional ARC (red line), and for constant refractive index within the material where the optical path lengths have been kept according to FIB13 (blue line) are plotted together with the spectrum obtained for a periodic structure with the same average spacing as FIB13 (black line). (b) Calculated reflectance spectra for a periodic (black line) and a Fibonacci-spaced (shaded area) 54 QW sample with parameters similar to FIB13, but $D = 0.4992\lambda$.

line. One again observes a spectrum similar to the original one (shaded area) with a pronounced dip below the 1s hh resonance (vertical line).

To complete this analysis, the influence of the average spacing D on the reflectance minimum is investigated. Thus, in Fig. 6.5(b), the reflectance calculated for a periodic (black line) and a Fibonacci-spaced (shaded area) 54QW sample with the same average spacing of $D = 0.4992\lambda$ is plotted. In particular, the average spacing is negatively detuned with respect to the ideal average spacing $D = 0.50\lambda$ for the first Bragg resonance. The reason for that is the real part of the QW susceptibility which corresponds to an additional refractive index contribution. This contribution is not taken into account in the Bragg condition, Eq. (2.14), which considers only the background refractive index. Hence, this neglect can be compensated by such a negative detuning. The negative detuning is chosen so that the reflectance of the periodic structure has one single maximum, i.e. there is no minimum.

While the reflectance of the periodic sample thus does not have a dip below the hh resonance position, the dip is still present for the Fibonacci spacing. The difference of the reflectance in the minimum and in the reflectance maximum energetically below the minimum has become only slightly smaller due to the variation of the average spacing. But, the reflectance contrast between the minimum and the neighboring energetically higher reflectance maximum is much smaller. Therefore, one can conclude that the

pronounced reflectance minimum observed in Fig. 6.5(a) is partially caused by the detuning of the average spacing D away from the exact Bragg condition. Nevertheless, the Fibonacci structure additionally leads to the formation of a dip as well due to the quasiperiodic arrangement. The interplay of these two effects leads to a narrower and deeper minimum for the Fibonacci structure, c.f. figs. 6.3 and 6.5.

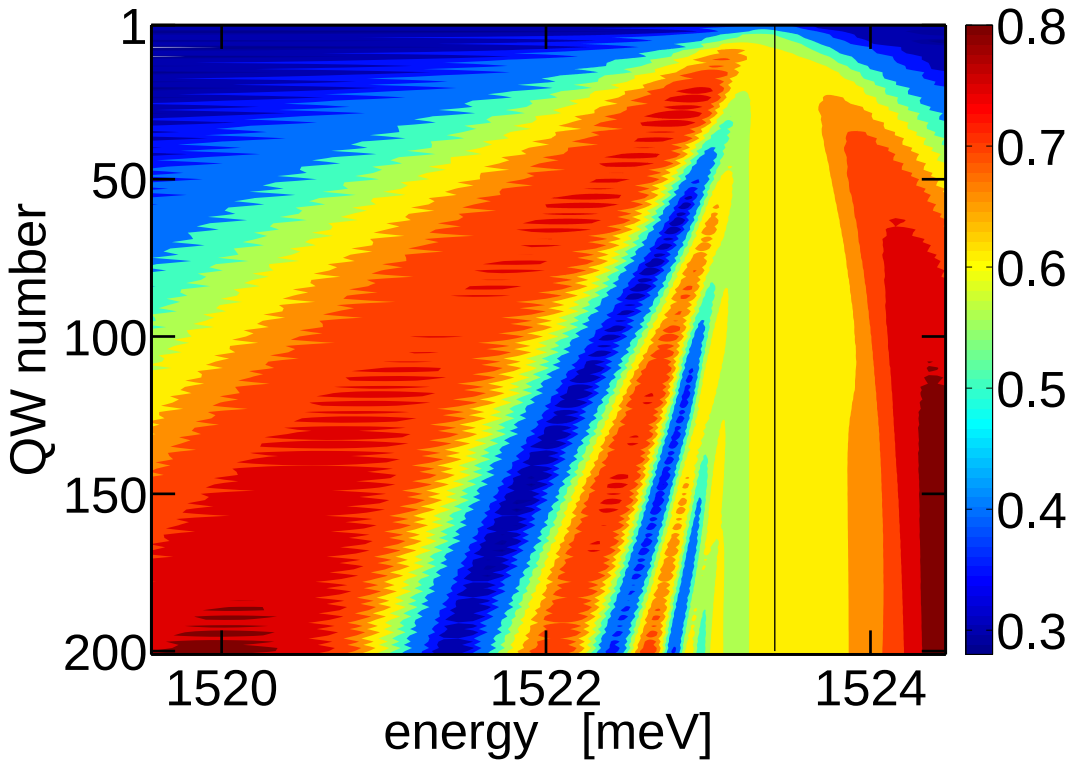

Figure 6.6: Reflectance in the vicinity of the 1s hh resonance as a function of QW number and frequency. Sample parameters correspond to FIB13.

6.5 Dependency on Quantum-Well number

The reflectance minimum may additionally be affected by the number of QWs present in the sample as well. Therefore, the reflectance spectra of Fibonacci spectra computed for different numbers of QWs are presented in Fig. 6.6 as function of energy and QW number. In each simulation, the same parameters as used in the linear fit to FIB13 have been used, Sec. 5.1, except that the QW number has been varied. The figure shows a zoom to the vicinity of the 1s hh resonance which is indicated by a black line. For small QW numbers, the spectrum consists of only one single peak positioned at the 1s hh exciton energy. With increasing QW number, the peak splits into two which correspond to the stopbands discussed before. At the same time, the investigated dip emerges slightly below the 1s hh resonance position. With further increasing QW number, this dip broadens and shifts to lower energies while simultaneously new dips emerge from the

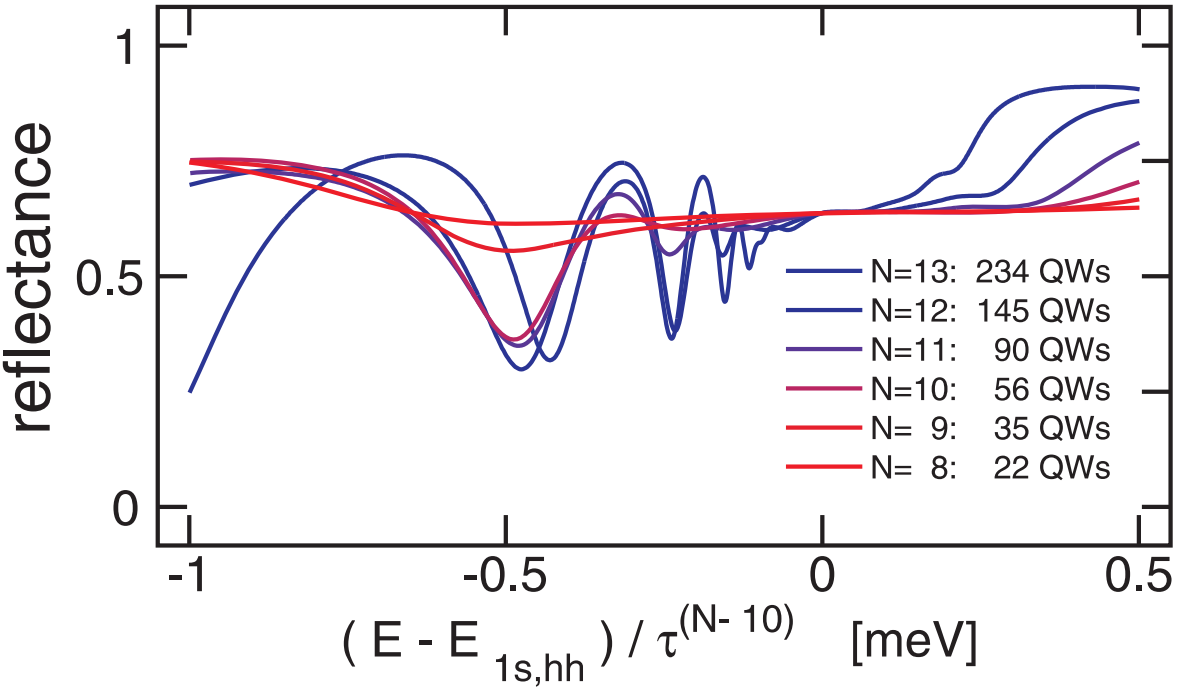

Figure 6.7: If the QW number is larger by one than a Fibonacci number, the sequence of building blocks L and S corresponds to the canonical sequences obtained by the substitution rules, Eqs.(2.1) and (2.2). Reflectance spectra for the Fibonacci numbers F_N with $8 \leq N \leq 13$ are plotted. The energy axis is scaled according to $(E - E_{1s,hh})/\tau^{N-10}$ such that the given energy scale corresponds to 56QWs ($N = 10$), which is comparable to the previous investigations with 54QWs. One finds that the spectra are self-similar with coinciding reflectance maxima and minima if energy axis is scaled by the golden mean τ.

wiggly structure near the hh resonance. This behavior is found in all sample structures investigated in Fig. 6.5(a) so that it has to be attributed to the QW spacing as well.

No special spectral features are observed when the QW number passes the Fibonacci numbers. However, if the QW number is larger than a Fibonacci number by one, the respective finite subsequence of building blocks L and S of the Fibonacci sequence can directly be obtained by the substitutions, Eq. (2.1) and (2.2). Thus, the N^{th} Fibonacci string F_N corresponds to $F_N + 1$ QWs. Figure 6.7 shows the reflectance spectra for QW numbers $F_N + 1$ where $8 \leq N \leq 13$, which corresponds to QW numbers between 22QWs and 234QWs. The latter sample consists of 1174 material layers. The energy is given relative to the 1s hh exciton position $E_{1s,hh}$ and is scaled by powers of the golden mean. In particular, the given energy scale corresponds to the case $N = 10$ with 56QWs, which is comparable with the previously investigated sample FIB13 including 54QWs. Consequently, the energy scaling factor reads $1/\tau^{N-10}$. The so-scaled reflectance spectra reveal coinciding reflectance maxima and minima. These coincidences manifest the self-

similarity of the reflectance spectra. Thus, in form of self-similarity, a typical feature of Fibonacci sequences [239, 342, 343] could be observed as well. Moreover, the re-scaling according to the self-similarity identifies the pronounced dip as well as the wiggles that appear in the vicinity of the hh resonance position to be a fingerprint of the Fibonacci spacing of the QWs.

7 Summary and Outlook

In the present work, the optical properties of resonant Fibonacci QCs have been studied. These resonant Fibonacci QCs are MQW structures in which the QW-QW distances are given either by a large spacer L or by a small spacer S. In particular, the QWs are arranged so that the structure constitutes the Fibonacci sequence $LSLLSLSL...$ in growth direction. As a consequence, the QW assembly represents a one-dimensional QC and thus stands in between the periodic and the spacially entirely disordered MQW structures due to the deterministic but aperiodic arrangement. Specifically, the average spacing satisfies a generalized Bragg condition.

In this work, for the first time, a microscopic theory has been applied to describe such resonant Fibonacci MQW QCs . According to the laser excitation employed in the experiments, a semi-classical theory in the framework of the well-known Semiconductor Bloch Equations has been used to model the QWs. That theory allows for the microscopic description of many-body effects such as excitation-induced dephasing caused by Coulomb scattering of carriers. Here, disorder and phonon effects are considered only phenomenologically. A transfer-matrix approach is used to describe propagation, transmission, and reflection effects caused by the dielectric environment of the QWs.

Based on an appropriate single set of fixed sample parameters, the theory provides reflectance spectra that are in excellent agreement with the corresponding measured linear and nonlinear spectra. In particular, experimentally observed highly similar reflectance spectra for on-resonance and above-resonance excitation can be attributed to very similar absorption properties with a considerable absorption in a wide spectral range. As a consequence, the spectra calculated with the pump-probe-based theory are in that excellent agreement with the resonant-pump measurements.

A pronounced sharp reflectivity minimum is found in the vicinity of the heavy-hole resonance both in the measured as well as in the calculated linear 54-QW spectra. Such sharp spectral features are suitable for application as optical switches or for slow-light effects. Hence, their properties have been studied in detail. For elevated carrier densities, that sharp spectral feature bleaches due to excitation-induced dephasing. The measured overall peak and valley structure is excellently matched by the calculations at

all excitation levels.

The spectral shape of the reflectance is found to be caused by refractive-index effects governed by the QW arrangement. For the investigated samples, the Fibonacci spacing as well as a slight detuning away from the exact Bragg condition cause the sharp dip in the reflectance spectra. Particularly, the spectral shape is highly dependent on the average spacing of the QWs while it is quite robust against moderate variations in the ratio of the optical path lengths $\rho = o_L/o_S$ of the large and small building blocks L and S, respectively, around the golden mean $\rho \approx \tau$. Thus, similar spectra are observed for the canonical $\rho = \tau$ as well as for the noncanonical $\rho \neq \tau$ structures if the ratio ρ is not changed too much. The overall reflectance follows the structure factor of the Fibonacci QCs. The pronounced dip in the reflectance spectrum in turn shifts to lower energies and becomes broader if the QW number increases. At the same time, new dips of similar behavior emerge. Specifically, self-similarity among reflection spectra corresponding to QW numbers that exceed a Fibonacci number by one is observed, which identifies the dips as true fingerprints of the Fibonacci spacing.

Further insight and better understanding of the optical properties of resonant Fibonacci QCs can be gained with the help of an improved modeling. A dynamic simulation of the excitation process is necessary to obtain a modeling that is still closer to the investigated experimental conditions, which is numerically challenging due to large memory demand and long computation times.

Similarly, the Semiconductor Luminescence Equations may eventually be applied to investigate the Fibonacci-QC photoluminescence, which is clearly different from the periodic-Bragg-MQW photoluminescence. Here, the numerical effort is even larger than in the coherent case since the coherent quantities vanish and the non-vanishing incoherent quantities of lowest level are already much more intricate and thus more memory extensive. Hence, the presented first microscopic investigations are a first steps towards a better theoretical understanding of the optical properties of resonant Fibonacci QCs and further work may follow as outlined above. Especially, it may be checked whether or not effects known from periodic MQWs can be found in resonant Fibonacci QCs as well, and if so, in how far they are influenced or changed by the quasicrystalline setup of the samples.

Part II

Resonant Tunneling of Light in Silicon Nanostructures

8 Introduction

In the second part of this thesis, we turn away from quantum-well structures and focus on the resonant tunneling of light in silicon nanostructures. The tunnel effect is one of the most famous consequences of quantum mechanics. Being a pure quantum phenomenon, there is no classical analog of tunneling. The tunneling problem deals with a potential barrier which a classical particle cannot penetrate while a quantum object can. That well-understood problem is part of any lecture on quantum mechanics and it is a standard textbook example of quantum effects [323, 344, 345].

Initially, the tunneling of particles such as the electrons has been studied [346]. Small sample sizes of the order of the de Broglie wave length of the particle are generally necessary to observe quantum effects. Hence, the tunnel effect has been observed for electrons in p-n junctions [12], in GaAs/AlGaAs heterostructures [347, 348], and in resonant-tunneling diodes [349–353]. As can bee seen from the latter example, tunneling is already used in applications as well. Another outcome of the studies of the tunnel effect is the tunneling microscope [354], where electrons tunnel through the gap between the sample under investigation and the tip of the microscope. Tunneling processes are also of fundamental importance as they e.g. could explain the radioactive decay [355].

In the course of the investigations on particle tunneling, there has been some discussion about how to define the corresponding tunneling times [356–360]. Depending on the studied system, different quantities have been defined for the tunneling time and it has been shown that these different quantities have one common contribution while they may differ otherwise [358] so that no unique tunneling time can be defined. In contrast to these difficulties in defining tunneling times in particle tunneling, the tunneling time of light can directly be determined.

Moreover, analogies between electrons and photons have lead to the generalization of the electronic band structure and band gap to the photonic band structure and the photonic band gap [116, 117], which has lead to new fields of investigation and to new applications. Similarly, the analogy [356] of photon tunneling [361] and electron tunneling [362] has been used to investigate the tunnel effect on an easier manageable structure. In the tunneling of light, the total-internal-reflection geometry is used. Classically, the light cannot penetrate the interface between a high and a low-refractive index material,

if the angle of incidence is above the critical angle, and total reflection occurs. However, an evanescent wave can be found in the low-refractive-index region that adjoins the respective material interface, though. It is this evanescent wave that mediates the tunneling process as will be explained later on in more detail.

The frustrated total internal reflection of light was proposed for filtering applications in 1947 [363], but the focus was clearly on filtering and not on investigations of the tunneling of light at that time. Meanwhile, numerous studies of photon tunneling have been performed. The simplest setup is provided by a double prism [356, 364], where the barrier is given by the air gap between the two prisms. Concerning applications, this effect of photon tunneling can be used e.g. to couple light from one waveguide to another and it allows for the scanning near-field microscopy [365].

However, we will focus on a special tunneling phenomenon which is called resonant tunneling. Resonant tunneling is characterized by a complete transmission at certain resonance energies. In order to observe resonant tunneling of light, the simple double-prism setup can be extended by putting additional material layers in between the prisms. In particular, these additional material layers provide regions where light propagation is allowed, i.e. the wave vector is entirely real valued. For appropriately chosen materials and layer thicknesses, the resonant tunneling of light can be observed [366, 367].

Apart from the double-prism setup, (resonant) tunneling of light has also been studied in superlattices and negative refractive index materials [368, 369], metals [370, 371], and photonic crystals [372–374] as well as in semiconductor heterostructures [375, 376] and absorbing barriers [377]. Superluminal light velocities [361], all-optical switches [378], and filters [379] have been achieved using photon tunneling. Additionally, all-optical switches [375, 376], as well as memory devices [375], and superlenses [366, 380] have been realized based on the *resonant* tunneling of light as well.

In the present work, that resonant tunneling of light in silicon samples is investigated. Due to the large difference in the refractive indices of silicon and air, for example silicon-based wave guides can easily be produced. Here, that contrast is used to create resonant-tunneling structures where air gaps are introduced to the silicon and the refractive-index contrast promotes total internal reflection. Besides the study of the fundamental resonant-tunneling properties as well as of the dependency of the optical properties on the sample geometry, the choice of silicon-based samples is also motivated from a bigger context. While the electronic ICs approach the fundamental material limits that provide from further miniaturization, an alternative is seen in the optical properties of semiconductors which govern the field of photonics that is supposed to overcome the limitations of electronics.

Hence, one aim of today's research is the development and the production of optical chips which unify the common properties of silicon-based electronics and of the (mainly III-V-compound-based) optical devices [154, 381, 382]. Therefore, the control of light [149, 152] in silicon structures as well as alternative silicon-based light sources [129–137] or the transfer and inclusion of III-V compound knowledge to the silicon systems [138–143] are needed. A lot of work has already been performed in that field of research. Silicon waveguides have been produced [150, 383], and silicon-based mirrors [384] and cavities [385] have been built. Additionally, all-silicon optical modulators [386] and

all-optical switches based on silicon have been realized [147, 387, 388]. Moreover, a mechanical nanocavity has been constructed to control the trapped light [389]. Slow light has been achieved in silicon-based photonic-crystal waveguides [390–392] and on-chip applications such as e.g. a gas detector [393] and an optical spectrometer [394] have been established. Even all-optical transistors have been proposed [148].

Effects caused by the resonant tunneling may eventually contribute to the needed control of light as well. Hence, a detailed study of the influence of the sample geometry on the optical properties of the sample has been performed. The presentation of that study is structured as follows. The setup of the investigated samples as well as the corresponding nomenclature is introduced together with a discussion of the theoretical description of these samples in Chap. 9. Based on that theoretical description, the effect of resonant tunneling is discussed in detail in Chap. 10. Then, the results of numerical simulations of tunneling and resonant tunneling structures are presented in Chap. 11. The obtained findings are summarized in Chap.12 where also an outlook to further work is given.

9 Investigated System and Theory

In this chapter, the investigated system shall be introduced. Particularly, the setup of the studied tunneling and resonant-tunneling structures is presented first, which is followed by a discussion of how to describe these systems as well as their optical properties theoretically. In the theory, previous results and methods obtained in Part I of this thesis can be used and will be recalled briefly. Moreover, some additional helpful quantities will be introduced in preparation of the discussion of the resonant tunneling of light.

9.1 Sample Setup

The basic shape of all investigated samples is a cuboidal block of bulk silicon. The specific sample design is obtained by working a number of N air gaps in the silicon from above, which in practice can be done by etching [58, 395] or sputtering [61, 62]. That way, an alternating sequence of silicon layers and air gaps is created. Specifically, the so-arisen silicon-air interfaces are arranged parallel to each other.

To describe the sample geometry more accurately, a Cartesian coordinate system is introduced such that the normal to these interface planes is identified with the z-axis. Consequently, the silicon-air interfaces are spanned by the x-y-axes. A topview of the samples is obtained if one looks in $-y$-direction. Such a topview of the setup is shown in the right column of Fig. 9.1 for the cases of (a) one, (b) two, and (c) three air gaps (white areas) worked in the silicon (gray areas). The particular focus of the investigations is on light propagation through such structures. Specifically, the propagation direction of light inside the first silicon layer shall be parallel to the longest edge of the silicon cuboid. Due to the parallel layer interfaces and Snell's law, the propagation direction is identical in all silicon layers. That direction of light propagation is indicated by a blue line in Fig. 9.1. As a result, the light propagation can in general be characterized via the angle of incidence α (blue) relative to the normal (black line) to the silicon-air interfaces inside the silicon. That angle thus is defined by and can be adjusted via the orientation of the air gaps within the silicon cuboid (red line and angle α).

The corresponding side view of the samples along the $-x$-direction is shown in the left

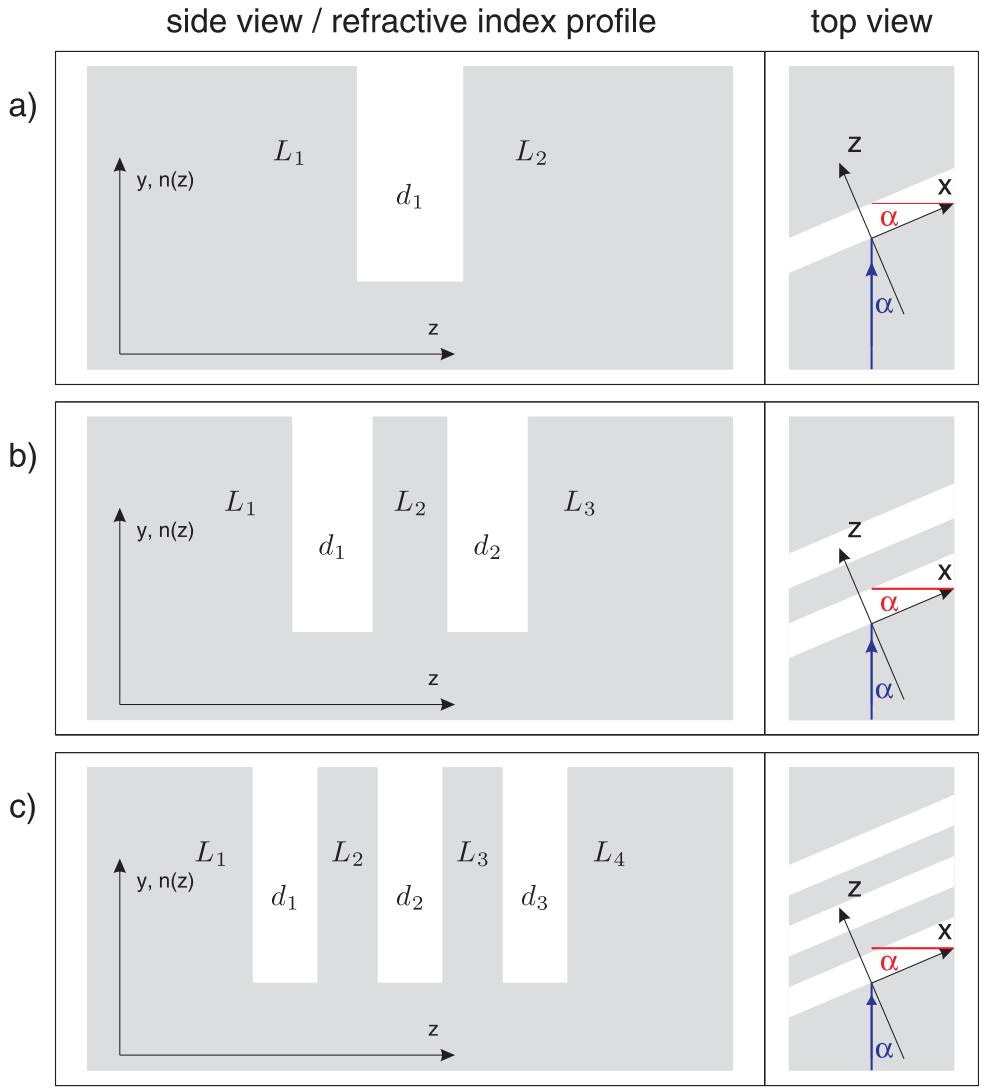

Figure 9.1: Typical (resonant-)tunneling samples based on silicon. Parallel grooves worked in a block of silicon yield alternating layers of silicon (gray area) and air (white). The left column shows a side view looking along the grooves. That side view indicates the sequence of silicon ($n_{Si} = 3.471$) and air ($n_{air} = 1.000$) layers and is scaled such that the height corresponds to the refractive index profile $n(z)$. Light is propagating in the upper part while the lower continuous silicon serves as structural connection. From left to right, silicon (air) layers are labeled by L_1, L_2, L_3,... (d_1, d_2, d_3,...). Tunneling structures with (a) no, (b) one (L_2), and (c) two (L_2 and L_3) silicon wells inside the air barrier are shown. The right column shows top views of these structures. Light is propagating in vertical direction (blue line) under an angle of incidence α with respect to the normal to the layer interfaces (diagonal black line). α is fixed via the groove orientation (red angle α).

column of Fig. 9.1. Silicon material is depicted as gray area and the white regions correspond to air. While the lower continuous silicon part provides the structural connection of the silicon layers, light propagation takes place in the upper part of the structure where the alternating sequence of silicon and air is found. Besides the structural information, the gray area provides additional information about the refractive-index profile. On that purpose, the gray area is scaled according to the refractive index profile $n(z)$. That is, the height of the silicon layers corresponds to the refractive index of silicon n_{Si} and the height of the lower, continuous silicon, that connects the silicon layers and that is found below the air layers, corresponds to the refractive index of air n_{air}.

The thicknesses of the silicon layers are in z-direction given by L_1, L_2, L_3, ... while the thicknesses of the air gaps are denoted by d_1, d_2, d_3, ... Hence, the structural type of the samples can be defined as, e.g. $L_1 - d_1 - L_2$ or $L_1 - d_1 - L_2 - d_2 - L_3$ which are the two most simple structures. Unless the opposite is stated, we will always investigate symmetric samples. That is, the thicknesses of corresponding layers are identical, e.g. $L_1 = L_3$, $d_1 = d_2$, and $L_2 = arb.$ for the structure $L_1 - d_1 - L_2 - d_2 - L_3$. Moreover, we assume the face silicon-layers to have infinite extension to $+\infty$ or $-\infty$, respectively, in the direction of light propagation. Thus, we do not take into account coupling of light into/out of the silicon-cuboid structure and solely focus on the effects of the internal interfaces.

Due to the large refractive-index contrast between silicon ($n_{Si} = 3.471$) and air/vacuum ($n_{air} = 1.000$) a strong influence of the detailed sample structure on the light propagation can be expected since each interface leads to partial reflection and transmission of light. Concerning the nomenclature, we will refer to silicon layers surrounded by air layers as 'silicon wells' or for short 'wells' opposed to the already mentioned face layers.

9.2 Transfer Matrix Method

The propagation of light through such layered structures can be described with the help of the transfer-matrix method which has already been introduced and used in Part I of this thesis. In particular, it is assumed that there is no optically active medium in the investigated samples so that one has to deal with the pure propagation, reflection and transmission properties, only. Furthermore, a constant refractive index $n_{Si} = 3.471$ within all silicon layers independent of the thickness of the layers is taken into account. Neglecting the frequency dependence of the refractive index of silicon serves as a simplification by which a better understanding of the fundamental effects shall be achieved. Thus, the transfer-matrix formalism can be used as derived in Sec. 4.1. Therefore, the central features of that formalism will only be briefly recalled and adapted to the present scenario.

Nevertheless, some notational conventions shall be given again to avoid ambiguities. Owing to the one-dimensional stacked structure of the samples, it is convenient to define the position $\mathbf{r} = (\mathbf{r}_\parallel, z)$ and momentum vector $\mathbf{q} = (\mathbf{q}_\parallel, q_\perp)$ with the help of the in-plane components indicated by a subscript $\parallel$ and the perpendicular components z and $q_\perp$, respectively. In the first silicon layer, the parallel component of the momentum vector

is defined from a given angle of incidence α_0 relative to the normal to the first silicon-air interface according to $\mathbf{q}_\parallel = n_{Si}|\mathbf{q}|\sin(\alpha_0)$, where $|\mathbf{q}|$ defines the absolute value of the wave vector. It follows from Snell's law that this parallel component is constant throughout the whole sample. As a result, the electrical field can be written in the form

$$\begin{aligned} E(\mathbf{r},t) &= E(z)e^{i\mathbf{q}_\parallel \mathbf{r}_\parallel - i\omega t} = E(z)e^{in(z)|\mathbf{q}|\sin(\alpha)\mathbf{r}_\parallel - i\omega t} \\ &= E(z)e^{in_{Si}|\mathbf{q}|\sin(\alpha_0)\mathbf{r}_\parallel - i\omega t}, \end{aligned} \tag{9.1}$$

where, in the first line, the respective index of refraction and the angle of incidence has to be chosen according to the z position while the constancy of the parallel component of the wave vector has been used in the second line so that $\mathbf{q}_\parallel$ is given independently of the z-position [356]. As a consequence, the Helmholtz equation Eq. (4.1) can be written in the simplified form

$$\left[\frac{\partial^2}{\partial z^2} + \frac{\omega^2}{c^2}\left(n^2(z) - n_{si}^2\sin^2(\alpha_0)\right)\right] E(z) = 0, \tag{9.2}$$

where $\omega = c|\mathbf{q}|$ and where $n(z)$ takes one of the two values n_{Si} and n_{air} depending on the z-position. In particular, the direction of light propagation and the sample geometry enter via α_0 which defines the orientation of the air layers and thus the propagation direction as well as via the z dependence of the refractive index. Equation (9.2) is equivalent to Eq. (4.3) and is adapted to the specific structure of the silicon samples.

The stationary mode functions in z-direction can be computed with the help of the transmission and reflection coefficients, $T_j^{\varsigma\pm}$ and $R_j^{\varsigma\pm}$, of the j^{th} interface for (counter-) propagating light, $-(+)$, with polarization ς =s,p , see Eqs. (4.5)–(4.8). Specifically, the mode coefficients, Eq. (4.4), are gained from recursively defined matrices, Eq. (4.12), which in turn include the collective reflection and transmission coefficients, $\mathcal{T}_j^{\varsigma\pm}$ and $\mathcal{R}_j^{\varsigma\pm}$, of the first j interfaces where the same sub- and superscripts are used as before, see Eqs. (4.14)–(4.17). These collective coefficients can be computed from the coefficients of the single interfaces, $T_j^{\varsigma\pm}$ and $R_j^{\varsigma\pm}$. In general, the computations are formally in full analogy to the ones performed in Part I. Thus, it is referred to the discussion in Chap. 4 for more detailed information about the transfer-matrix method. In the following, we will focus on s-polarized light while the lines of argumentation also hold for p-polarized light for which different transmission and reflection properties of the single barriers have to be considered yielding different but analogous results.

9.3 Partial Collective Transmission and Reflection Coefficients

The sample materials and the sample structure are chosen with intent to investigate the (resonant) tunneling of light. As already mentioned, the same transfer-matrix method as used in Part I of this thesis can be applied to simulate the propagation of light through these structures as well as to investigate the (resonant) tunneling of light. However, in preparation of the discussion of the resonant tunneling of light, which is subject of

Chap. 10, some additional collective quantities shall be defined that will be helpful in the discussion of that effect.

While the previously discussed collective transmission and reflection coefficients, $\mathcal{T}_j^{\varsigma\pm}$ and $\mathcal{R}_j^{\varsigma\pm}$, account for the interplay of the first j interfaces, the transmission (reflection) through (by) any single layer within the entire sample shall be described by a separate quantity as well. In order to do so, the effects of the corresponding two layer interfaces and all possible paths of propagation through that layer have to be taken into account. Consequently, the reflection $\bar{\mathcal{R}}_j^{\varsigma\pm}$ caused by that single layer contains the direct reflection from the first interface as well as the reflection from the second interface. The latter is accompanied by two transmission processes through the first interface of the layer (to and fro) as well as by all possible multiple reflections within the layer. Thus, one obtains for the different propagation paths in the single layer

$$\bar{\Pi}_j^{\varsigma} \;=\; \sum_{m=0}^{\infty} \left(e^{\theta_j} R_{j+1}^{\varsigma-} e^{\theta_j} R_j^{\varsigma+}\right)^m \;=\; \frac{1}{1 - R_{j+1}^{\varsigma-} R_j^{\varsigma+} e^{2\theta_j}} \tag{9.3}$$

in analogy to Eq. (4.13) and with $\theta_j = iq_{\perp,j} n_j (z_{j+1} - z_j)$. Hence, the reflection (transmission) of propagating light by (through) the layer j is given by

$$\bar{\mathcal{R}}_j^{\varsigma-} \;=\; R_j^{\varsigma-} + T_j^{\varsigma-} \bar{\Pi}_j^{\varsigma} e^{\theta_j} R_{j+1}^{\varsigma-} e^{\theta_j} T_j^{\varsigma+} \;=\; R_j^{\varsigma-} + R_{j+1}^{\varsigma-} \frac{T_j^{\varsigma-} T_j^{\varsigma+} e^{2\theta_j}}{1 - R_{j+1}^{\varsigma-} R_j^{\varsigma+} e^{2\theta_j}} \,, \tag{9.4}$$

$$\bar{\mathcal{T}}_j^{\varsigma-} \;=\; T_j^{\varsigma-} \bar{\Pi}_j^{\varsigma} e^{\theta_j} T_{j+1}^{\varsigma-} \;=\; \frac{T_j^{\varsigma-} T_{j+1}^{\varsigma-} e^{\theta_j}}{1 - R_{j+1}^{\varsigma-} R_j^{\varsigma+} e^{2\theta_j}} \,, \tag{9.5}$$

while one obtains for counter-propagating light

$$\bar{\mathcal{R}}_j^{\varsigma+} \;=\; R_{j+1}^{\varsigma+} + T_{j+1}^{\varsigma+} \bar{\Pi}_j^{\varsigma} e^{\theta_j} R_j^{\varsigma+} e^{\theta_j} T_{j+1}^{\varsigma-} \;=\; R_{j+1}^{\varsigma+} + R_j^{\varsigma+} \frac{T_{j+1}^{\varsigma+} T_{j+1}^{\varsigma-} e^{2\theta_j}}{1 - R_{j+1}^{\varsigma-} R_j^{\varsigma+} e^{2\theta_j}} \,, \tag{9.6}$$

$$\bar{\mathcal{T}}_j^{\varsigma+} \;=\; T_{j+1}^{\varsigma+} \bar{\Pi}_j^{\varsigma} e^{\theta_j} T_j^{\varsigma+} \;=\; \frac{T_j^{\varsigma+} T_{j+1}^{\varsigma+} e^{\theta_j}}{1 - R_{j+1}^{\varsigma-} R_j^{\varsigma+} e^{2\theta_j}} \,. \tag{9.7}$$

The alternating sequence of air and silicon layers results in the following symmetry relations for the single layer under investigation,

$$\begin{aligned} R_j^{\varsigma-} \;=\; R_{j+1}^{\varsigma+} \quad , \quad R_{j+1}^{\varsigma-} \;=\; R_j^{\varsigma+} \quad , \quad R_j^{\varsigma+} \;=\; R_{j+1}^{\varsigma-} \quad , \\ \text{and} \quad T_j^{\varsigma-} \;=\; T_{j+1}^{\varsigma+} \quad , \quad T_{j+1}^{\varsigma-} \;=\; T_j^{\varsigma+} \end{aligned} \tag{9.8}$$

so that one can identify

$$\bar{\mathcal{R}}_j^{\varsigma} \;=\; \bar{\mathcal{R}}_j^{\varsigma-} \;=\; \bar{\mathcal{R}}_j^{\varsigma+} \;=\; |\bar{\mathcal{R}}_j^{\varsigma}| \, \exp(i\Phi_R) \,, \tag{9.9}$$

and

$$\bar{\mathcal{T}}_j^{\varsigma} \;=\; \bar{\mathcal{T}}_j^{\varsigma-} \;=\; \bar{\mathcal{T}}_j^{\varsigma+} \;=\; |\bar{\mathcal{T}}_j^{\varsigma}| \, \exp(i\Phi_T), \tag{9.10}$$

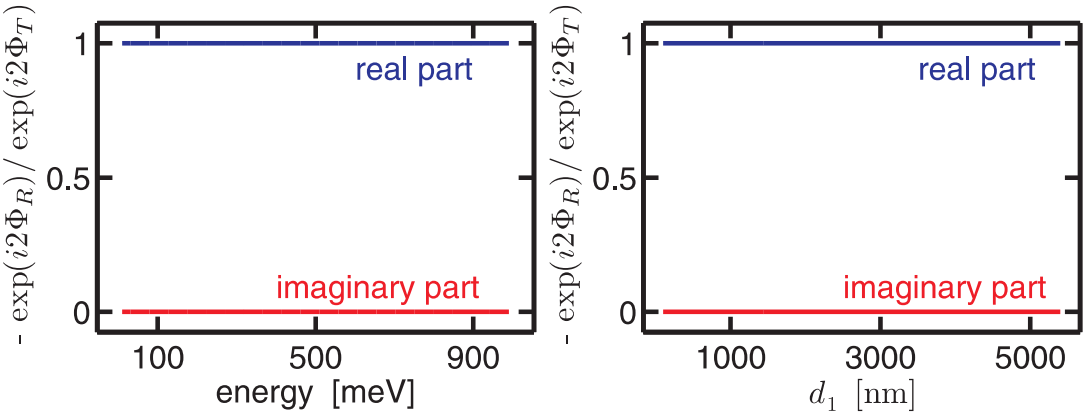

Figure 9.2: Illustration of the phase relation $\exp(i2\Phi_R) = -\exp(i2\Phi_T)$ for (a) a fixed layer thickness $d_1 = 450\text{nm}$ and (b) for a fixed energy $E = 827\text{meV}$.

where the phase Φ_R (Φ_T) is associated with the reflection (transmission) by (through) that layer. The phases corresponding to reflection and transmission fulfill the relation

$$\frac{(\bar{\mathcal{R}}_j^{\varsigma})^2}{|\bar{\mathcal{R}}_j^{\varsigma}|^2} = \exp(i2\Phi_R) = -\exp(i2\Phi_T) = -\frac{(\bar{\mathcal{T}}_j^{\varsigma})^2}{|\bar{\mathcal{T}}_j^{\varsigma}|^2}\,, \tag{9.11}$$

which can be shown in general and which is exemplified in Fig. 9.2.

Fig. 9.2(a) shows a spectral scan of the ratio $-\exp(i2\Phi_R)/\exp(i2\Phi_T)$ for a fixed layer thickness $d_1 = 450\text{nm}$. Similarly, the effect of a variation of the layer thickness d_1 on that ratio is studied in Fig. 9.2(b), where the energy of the investigated light is kept constant at $E = 827\text{meV}$.

In general, more complicated situations in which the investigated layer – either silicon or air – is surrounded by arrangements of several silicon and air layers can be studied in the same fashion as well. Specifically, the interfaces that have been considered in the transmission and reflection coefficients of the single layer may represent even a whole set of bordering layers.

Applying such a substitution of a subset of layers by a single interface, the correct optical properties of the structure are guaranteed if the reflection and transmission properties of the new interface are given by the collective reflection and transmission coefficients of the substituted layer group. If the optical properties of an entire sample are computed, this method of determining these optical properties yields the same results as they are obtained when considering the different layers one by one in the order of their arrangement, c.f. Sec. 4.1.

The advantage of the above introduced way of computation is in the focus on one special layer. In particular, the optical properties of the sample (or a subset of layers) are obtained in a format in which the structural properties of that layer enter explicitly while the influence of all other layers enters via collective reflection and transmission coefficients. Thus, one may study the detailed dependence of the collective optical properties of the entire sample on the specific properties of that single layer. Before

doing so, another quantity describing the sample shall be introduced first.

9.4 Phase Time and Quality Factor

A measure of the time which light needs to propagate through the structure can be gained from the transmission coefficient $\mathcal{T}^{\varsigma\pm}$. The transmission coefficient includes all possible paths of light-propagation and thus accounts for the traveling time of light [357, 358]. Specifically, the phase of the light carries that temporal information. Hence, we determine the phase time τ via

$$\tau^{\varsigma\pm}(\omega) \;=\; \frac{1}{i\mathcal{T}^{\varsigma\pm}}\,\frac{\partial}{\partial\omega}\,\mathcal{T}^{\varsigma\pm}\,. \tag{9.12}$$

For the following discussion, it is necessary to give some prerequisites and properties of resonant tunneling in anticipation of a detailed inspection of resonant tunneling: When resonant tunneling of light shall be studied, the angle of incidence α has to be larger than a certain critical angle α_c, which causes the air layers to be classically forbidden regions for light propagation. Real-valued wave vectors and thus truly (counter-) propagating light is found only in the silicon layers. In contrast, the light passes the air layers via tunneling, which is related to purely imaginary wave vectors. For now, these facts may be taken for granted since the detailed discussion is presented in the following Chap. 10.

A resonant tunneling structure with N silicon wells includes $N+1$ air layers. Specifically, the face layers, given by the first L_1 and the last L_{N+2} silicon layer in the sample, influence the optical properties of the sample only via their refractive index which determines the reflection and transmission coefficient of the respective layer interface. Thus, the optical properties of the entire sample depend on all layer interfaces as well as on the thicknesses of all layers except the face layers.

In order to inspect that dependence in more detail, a cuboidal block of bulk silicon which has an infinite extension in direction of light propagation shall be considered. Inside that continuous silicon block, light does not suffer any reflections. If now such a resonant tunneling structure with N wells is created out of that silicon block, $N+1$ air layers have to be introduced. In the following, we abandon the physical structure of a real sample for a while and take a more fundamental approach. That is, we disregard the structural connection of the silicon layers and consider these layers to be independent structural objects that can be moved freely. The only restriction is that they must be oriented parallel to each other. The continuous silicon block may be considered to consist of the semi-open face layers L_1 and L_{N+2} as well as of further layers $L_2, \ldots, L_{N+1}$ of finite extension. These layers directly adjoin each other without air layers in between. The propagation time of light through the array of finite silicon layers is given by

$$t_0 = \frac{n_{Si}\,\sum_{i=2}^{N+1} L_i}{\cos(\alpha)\,c_0}\,, \tag{9.13}$$

where the propagation direction is considered via the angle of incidence α which is measured relative to the normal to the pseudo-layer-interfaces.

A resonant tunneling structure is achieved when the silicon layers do not adjoin each other anymore. Hence, there are air layers of finite extension $d_1, \ldots, d_{N+1}$ in between the silicon layers. Due to the difference in the refractive indices of silicon and air, light suffers (multiple) reflections. Specifically, cavity-like effects can be expected. Due to the semi-infinite face layers, the computed transmission coefficient $\mathcal{T}^{\varsigma\pm}$ contains a phase information which refers to the propagation of light from the first towards the last layer interface. The phase of light does not change during tunneling events which take place in the air layers. Hence, that phase time and the propagation time t_0 allow for the definition of a quality factor according to

$$Q^{\varsigma\pm}(\omega) \;=\; \tau^{\varsigma\pm}(\omega)/t_0 \,. \tag{9.14}$$

That quality factor is a measure for the cavity-like properties of the sample. In particular, it measures the propagation time of light between leaving the first face layer until penetrating the end face layer in case of a resonant tunneling structure. Specifically, that measure is defined relative to the propagation time in case of pure (counter-) propagation through directly adjoining silicon layers that correspond to the silicon wells in the resonant tunneling structure.

With these definitions at hand, we may now proceed to a discussion of what tunneling and resonant tunneling of light is, which is presented in Chap. 10. That discussion is followed by numerical studies of the tunneling effects in Chap. 11.

10 Resonant Tunneling

In this chapter, the resonant tunneling of light shall be discussed. Following Ref. [356], the well-known case of particle tunneling such as electron tunneling shall be used below to show analogies and correspondences between particle tunneling and tunneling of light.

10.1 Tunnel Effect – Electrons vs. Light

In the usual tunneling problem, which shall briefly be recalled first, there is a potential barrier of square shape. That is, for $-L/2 \leq z \leq L/2$, the potential $V(z)$ takes the value V_0 and it vanishes otherwise. Classically, a particle can only pass the barrier if the particle energy is larger than V_0. The non-classical tunneling needs to be described by a quantum-mechanical treatment of the particle which is based on the stationary Schrödinger equation

$$\left(-\frac{\hbar^2}{2m}\frac{\partial^2}{\partial z^2} + V(z)\right)\Psi(z) \;=\; E\Psi(z)\;. \tag{10.1}$$

The particle wave function is given by $\Psi(z)$ and E is the particle energy. The particle mass is given by m and $\hbar$ corresponds to Planck's constant divided by 2π. The Schrödinger equation can be re-arranged to

$$\left(\frac{\partial^2}{\partial z^2} + \frac{2m}{\hbar^2}(E - V(z))\right)\Psi(z) \;=\; 0\;, \tag{10.2}$$

where one may identify the familiar corresponding wave vector

$$k \;=\; \sqrt{\frac{2m}{\hbar^2}(E - V(z))}\;. \tag{10.3}$$

The wave function is proportional to $\exp(ikz)$ within the different regions of constant potential. In the regions where $E < V(z)$, the wave vector becomes entirely imaginary, i.e. $k = ia$ with $a \in \mathbb{R}$. Hence, there exists a wave function in the classically forbidden

region $-L/2 \leq z \leq L/2$ though $E < V_0$, but the wave function is decaying exponentially $\exp(ikz) = \exp(-az)$. However, the wave function may eventually become propagating again behind the barrier where $E > V(z)$. Thus, the particle described by the wave function may tunnel through the barrier. The strength of the tunnel efficiency depends on the width and the height of the barrier which determine how much the wave function has decayed after passing the barrier.

Now, these familiar findings shall be transferred to the tunneling of light with the help of analogy observations [356]. For that reason, the Eqs. (9.2) and (10.2) are opposed to each other,

$$\left[\frac{\partial^2}{\partial z^2} + \frac{\omega^2}{c^2}\left(n^2(z) - n_{Si}^2 \sin^2(\alpha_0)\right)\right] E(z) = 0\,, \tag{10.4}$$

$$\left[\frac{\partial^2}{\partial z^2} + \frac{2m}{\hbar^2}(\,E \quad - \quad V(z) \quad)\right] \Psi(z) = 0\,, \tag{10.5}$$

and a comparison reveals the same structure of the equations. Specifically, a permeability $\mu = 1$ is assumed for all layers in Eq. (10.4) so that the electrical field and thus $E(z)$ as well as the magnetic field are continuous across the interfaces. As a consequence, the same boundary conditions are found in Eqs. (10.4) and (10.5). Moreover, one can identify the equivalent terms

$$\frac{2m}{\hbar^2}(E - V(z)) = \frac{\omega^2}{c^2}\left(n^2(z) - n_{Si}^2 \sin^2(\alpha_0)\right)\,, \tag{10.6}$$

which represent the square of the wave vector. While the electron wave vector is real as long as $E \geq V(z)$, the photon wave vector is real valued when $n^2(z) \geq n_{Si}^2 \sin^2(\alpha_0)$. The potential $V(z)$ takes one of the two values 0 and V_0 which correspond to the refractive indices of silicon n_{Si} and air n_{air}. Consequently, the energy E is in analogy with the angle α. The non-classical behavior is connected with the imaginary wave vector obtained for energies E below a critical energy $E_c = V_0$. Similarly, the critical angle is given by

$$\alpha_c = \arcsin(n_{air}/n_{Si}) \approx 16.74^o\,, \tag{10.7}$$

which follows from Snell's law and corresponds to the onset of total internal reflection. For angles $\alpha > \alpha_c$, light is often said to be entirely reflected at the silicon→air interface. However, in analogy to the imaginary electron wave vector, the imaginary wave vector of the light results in an evanescent wave within the air layer. That evanescent wave has to exist due to the continuity of the electrical field. If the air layer is narrow enough, that wave may penetrate the next silicon layer and become propagating again, which is called frustrated total internal reflection [325] and which is the analog to electron tunneling. The tunneling efficiency decays with increasing barrier height and barrier thickness, i.e. with increasing angle and air-layer thickness.

10.2 Resonant Tunneling

A special kind of tunneling phenomenon is called *resonant tunneling* and can be observed if the barrier region which is classically forbidden contains further classically allowed

regions. In a different view, this corresponds to the situation when tunneling takes place not only through a single barrier but through several barriers which are placed side by side. The remarkable and characteristic feature of resonant tunneling (through multiple barriers) is a transmission resonance with a transmission probability of 1, though the tunneling probability through any single barrier is smaller than 1. In the following discussion of resonant tunneling, we will refer to the most simple structure in which that effect occurs. That structure contains two barriers and is depicted in Fig. 9.1(b).

The structural setup is given by $L_1 - d_1 - L_2 - d_2 - L_3$, where the two air layers, d_1 and d_2, correspond to the barriers. For simplicity, we assume again a symmetric structure so that $L_1 = L_3$ and $d_1 = d_2$. Consequently, the two barriers are identical due to identical thicknesses and the same neighboring materials. Moreover, the optical properties of these air layers embedded in the silicon can be described with the help of the collective transmission $\bar{\mathcal{T}}_j^{\varsigma\pm}$ and reflection coefficients $\bar{\mathcal{R}}_j^{\varsigma\pm}$ which have been defined in Sec. 9.3. Due to the symmetry of the structure, the respective collective quantities for propagating and counter-propagating light are identical and Eqs. (9.9) and (9.10) hold. Therefore, the superscript $\pm$ can be dropped. Additionally, the subscript $j = air$ is used to identify the coefficients that describe the transmission through and reflection by the air layers.

With these collective coefficients at hand, the transmission through the entire sample $L_1 - d_1 - L_2 - d_2 - L_3$ can be described in a more simple way [357]. The partial collective reflection and transmission coefficients, see Sec. 9.3, allow to replace the air layer by a single interface. This new interface is surrounded by silicon at either side according to the layers L_1 and L_2 or to the layers L_2 and L_3. Instead of complete transmission, which is usually obtained for such an interface within one and the same material, the partial collective reflection and transmission coefficients $\bar{\mathcal{T}}_{air}^{\varsigma}$ and $\bar{\mathcal{R}}_{air}^{\varsigma}$ are applied for the interface, because it represents the air layer embedded in the silicon.

In analogy to the air layer, such collective transmission and reflection coefficients can be defined for the middle silicon layer L2 as well. Again, the symmetry of the sample structure yields identical coefficients for propagating and counter-propagating light. The total collective reflection of the sample is thus given by

$$\bar{\mathcal{R}}_{tot}^{\varsigma} = \bar{\mathcal{R}}_{air}^{\varsigma} + \bar{\mathcal{R}}_{air}^{\varsigma} \frac{(\bar{\mathcal{T}}_{air}^{\varsigma})^2 e^{2\theta_{L_2}}}{1 - (\bar{\mathcal{R}}_{air}^{\varsigma})^2 e^{2\theta_{L_2}}}, \tag{10.8}$$

where $\theta_{L_2} = iq_{\perp,L_2} n_{Si} L_2$ with the z component $q_{\perp,L_2}$ of the wave vector in the silicon layer L_2. Similarly, the total transmission probability follows from

$$\bar{\mathcal{T}}_{tot}^{\varsigma} = \frac{(\bar{\mathcal{T}}_{air}^{\varsigma})^2 e^{\theta_{L_2}}}{1 - (\bar{\mathcal{R}}_{air}^{\varsigma})^2 e^{2\theta_{L_2}}}. \tag{10.9}$$

Following Ref. [357], the resonant-tunneling effect can be shown with the help of the phases Φ_R and Φ_T for reflection and transmission, respectively, Eqs. (9.9) and (9.10). Writing the absolute values and phase factors of the reflection and transmission coeffi-

cients of the air layer explicitly in the fractions in Eqs. (10.8) and (10.9), one obtains

$$\bar{\mathcal{R}}^{\varsigma}_{tot} = \bar{\mathcal{R}}^{\varsigma}_{air} + \bar{\mathcal{R}}^{\varsigma}_{air} \frac{|\bar{\mathcal{T}}^{\varsigma}_{air}|^2 e^{2i\Phi_T} e^{2iq_{\perp,L_2} n_{Si} L_2}}{1 - |\bar{\mathcal{R}}^{\varsigma}_{air}|^2 e^{2i\Phi_R} e^{2iq_{\perp,L_2} n_{Si} L_2}} , \tag{10.10}$$

$$\bar{\mathcal{T}}^{\varsigma}_{tot} = \frac{|\bar{\mathcal{T}}^{\varsigma}_{air}|^2 e^{2i\Phi_T} e^{2iq_{\perp,L_2} n_{Si} L_2}}{1 - |\bar{\mathcal{R}}^{\varsigma}_{air}|^2 e^{2i\Phi_R} e^{2iq_{\perp,L_2} n_{Si} L_2}} \, e^{-iq_{\perp,L_2} n_{Si} L_2}. \tag{10.11}$$

Using the relation Eq.(9.11) yields

$$\bar{\mathcal{R}}^{\varsigma}_{tot} = \bar{\mathcal{R}}^{\varsigma}_{air} - \bar{\mathcal{R}}^{\varsigma}_{air} \frac{|\bar{\mathcal{T}}^{\varsigma}_{air}|^2 e^{2i\Phi_R + 2iq_{\perp,L_2} n_{Si} L_2}}{1 - |\bar{\mathcal{R}}^{\varsigma}_{air}|^2 e^{2i\Phi_R + 2iq_{\perp,L_2} n_{Si} L_2}} . \tag{10.12}$$

Claiming the resonant-tunneling condition

$$2q_{\perp,L_2} n_{Si} L_2 + 2\Phi_R = 2m\pi , \tag{10.13}$$

where $m \in \mathbb{N}_0$, the reflection simplifies further to

$$\bar{\mathcal{R}}^{\varsigma}_{tot} = \bar{\mathcal{R}}^{\varsigma}_{air} - \bar{\mathcal{R}}^{\varsigma}_{air} \frac{|\bar{\mathcal{T}}^{\varsigma}_{air}|^2}{1 - |\bar{\mathcal{R}}^{\varsigma}_{air}|^2} . \tag{10.14}$$

Due to the identity $1 = |\bar{\mathcal{T}}_{air}|^2 + |\bar{\mathcal{R}}_{air}|^2$, the reflection is found to be vanishing

$$\bar{\mathcal{R}}^{\varsigma}_{tot} = \bar{\mathcal{R}}^{\varsigma}_{air} - \bar{\mathcal{R}}^{\varsigma}_{air} = 0 , \tag{10.15}$$

at an energy

$$E^m_{RT} = \hbar c_0 |\mathbf{q}| = \frac{\hbar c_0 q^m_{\perp,L_2}}{\cos(\alpha)} , \tag{10.16}$$

defined by the wave vector $q^m_{\perp,L_2}$ that solves Eq. (10.13).

As a consequence, complete transmission is observed at the same energy, which can be seen by applying

$$\begin{aligned}
\bar{\mathcal{T}}^{\varsigma}_{tot} &= \frac{|\bar{\mathcal{T}}^{\varsigma}_{air}|^2 e^{2i\Phi_T + 2iq_{\perp,L2} n_{Si} L2}}{1 - |\bar{\mathcal{R}}^{\varsigma}_{air}|^2 e^{2i\Phi_R + 2iq_{\perp,L_2} n_{Si} L_2}} \, e^{-iq_{\perp,L_2} n_{Si} L_2} \\
&= -\frac{|\bar{\mathcal{T}}^{\varsigma}_{air}|^2 e^{2i\Phi_R + 2iq_{\perp,L_2} n_{Si} L_2}}{1 - |\bar{\mathcal{R}}^{\varsigma}_{air}|^2 e^{2i\Phi_R + 2iq_{\perp,L_2} n_{Si} L_2}} \, e^{-iq_{\perp,L_2} n_{Si} L_2} \\
&= -\frac{|\bar{\mathcal{T}}^{\varsigma}_{air}|^2}{1 - |\bar{\mathcal{R}}^{\varsigma}_{air}|^2} \, e^{-iq_{\perp,L_2} n_{Si} L_2} \\
&= -e^{-iq_{\perp,L_2} n_{Si} L_2} ,
\end{aligned} \tag{10.17}$$

so that

$$|\bar{\mathcal{T}}^{\varsigma}_{tot}|^2 = 1 . \tag{10.18}$$

Therefore, Eq. (10.13) indeed manifests the resonant-tunneling condition and implies a series of resonances of order m at the same time.

11 Simulations

11.1 Tunneling Through a Single Air Gap

Non-tunneling transmission through the given structure $L_1-d_1-L_2$ with $n_{Si} = 3.471$ and $n_{air} = 1.000$ is classically allowed for angles $\alpha < \alpha_c \approx 16.74^o$. Figure 11.1(a) shows the transmission probability for light propagating through that structure with $d_1 = 450$nm as a function of energy and angle of incidence. In the calculations, a transmission maximum with complete transmission probability is observed at $E = 1378$meV for $\alpha = 0^o$. That resonance is related to the thickness of the d_1 layer which selects the resonance according to $d_1 = \lambda/2$ in the air layer so that the theoretically expected energy is $E = 1378.7$meV. At elevated angles smaller than the critical angle, the resonance shifts to higher energies. That is due to the fact that the z-projection of half of the wavelength has to match d_1 so that

$$d_1 = \frac{\lambda/2}{\cos(\alpha')} = \frac{\lambda/2}{\cos(\arcsin(\frac{n_{Si}}{n_{air}}\sin(\alpha)))} , \tag{11.1}$$

where the projection of the wavelength from its propagation direction within the air layer on the z direction is taken into account by the factor $1/\cos(\alpha')$. Here, α' is the angle of refraction in the air layer which is obtained from Snell's law. As a result, the energetic position of the resonance is given by

$$E_{res}(\alpha) = 1378.7\text{meV}\,\frac{1}{\cos(\arcsin(\frac{n_{Si}}{n_{air}}\sin(\alpha)))} . \tag{11.2}$$

In Fig. 11.1(a), $E_{res}(\alpha)$ is plotted as a dashed black line. Very good agreement between the numerical simulation and the analytic formula is found.

Additionally, the critical angle α_c is plotted as a horizontal solid black line in Fig. 11.1(a). Obviously, there is no significant transmission for angles larger than the critical angle. Figure 11.1(b) shows the transmission probability at angles of $\alpha = 17^o$, $\alpha = 20^o$, $\alpha = 40^o$, and $\alpha = 60^o$, which are all above the critical angle, in a semi-logarithmic plot. A weak

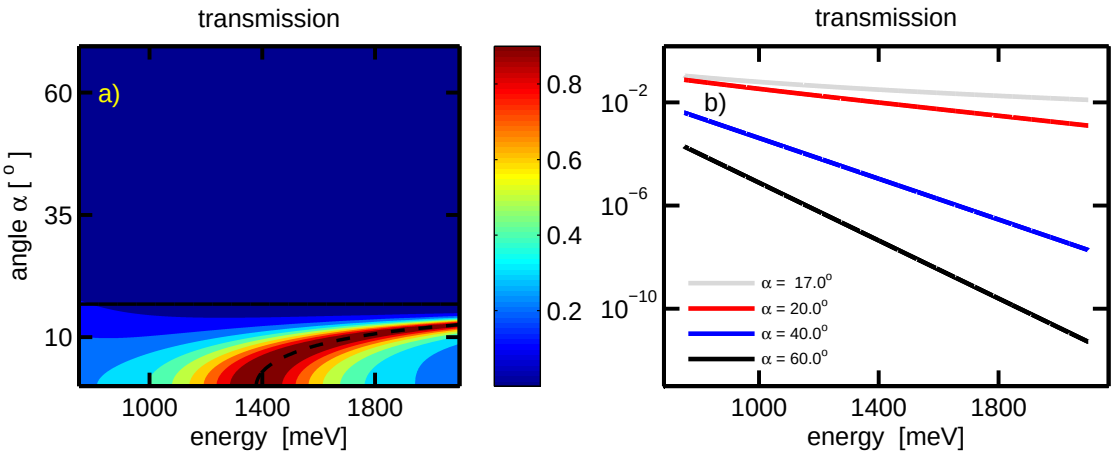

Figure 11.1: Transmission probability of the structure $L_1 - d_1 - L_2$ with $d_1 = 450$nm. (a) For angles $\alpha < \alpha_c$, 100% transmission is obtained at transmission resonances that shift to higher energies with increasing α. (b) For $\alpha > \alpha_c$, tunneling of light takes place and the transmission probability decreases strongly with increasing α.

but finite transmission through the air layer is observed. Specifically, the transmission probability decreases with increasing angle of incidence. These observations correspond to the previously discussed effect of frustrated total internal reflection, i.e. tunneling of light.

Figure 11.2 shows the transmission properties of an analogous structure with fixed angle $\alpha = 45^o$ and a varied thickness d_1 of the air layer. In comparison to the electron-tunnel barrier, a thicker air layer corresponds to a thicker tunneling barrier. Consequently, one would expect the tunneling efficiency to drop with increasing thickness of the barrier respectively of the air layer. Indeed, strong transmission is observed for thin air layers and the transmission probability rapidly drops for elevated air-layer thicknesses. A continuous scan of the transmission probability with respect to the thickness d_1 is presented in frame (a). Specifically, the transmission decreases the faster the shorter the wavelength of the light is. Considerable transmission is still observed at long wavelengths for thicknesses d_1 of the air layer at which the transmission has effectively already vanished at shorter wavelengths. However, the transmission probability nevertheless drops at larger wavelengths, anyway, though the dropping is slower. That fact is illustrated with the help of transmission-probability spectra in frame (b) as well, where the quantitative decrease of transmission can be seen better.

The observed transmission properties for $\alpha \leq \alpha_c$ have successfully been explained by a resonance phenomenon. For $\alpha > \alpha_c$ the transmission properties furthermore agree with the expectations drawn from the analogies with electron tunneling, both with respect to the observation of tunneling of light as well as with respect to the dependence of the tunneling strength on the barrier thickness. Thus, the correct description of light propagation as well as of the frustrated total internal reflection which is nothing else

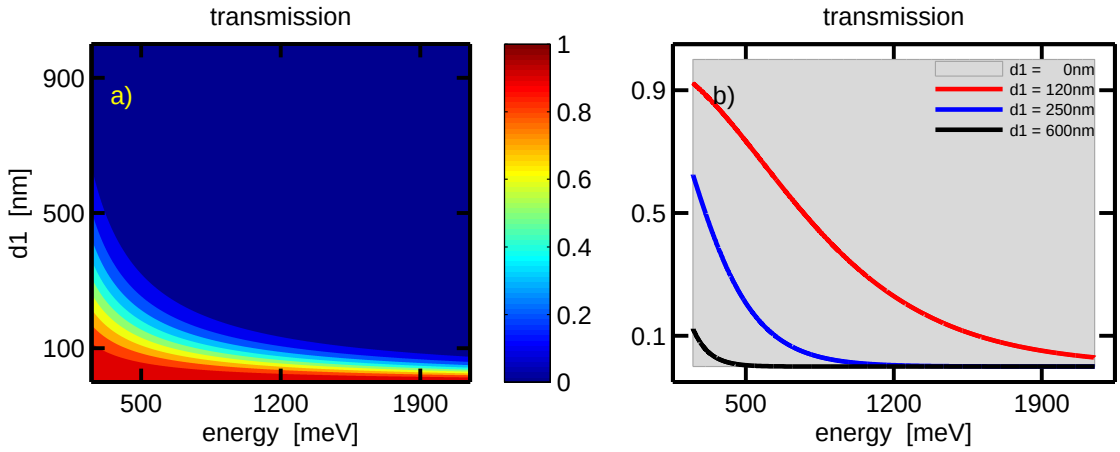

Figure 11.2: Transmission probability of the structure $L_1 - d_1 - L_2$ with fixed angle $\alpha = 45^o$ for different thicknesses d_1. (a) Transmission as a function of air-layer thickness d_1 and energy. (b) Selected transmission spectra. With increasing thickness d_1 of the air layer, the transmission probability decreases.

but the tunneling of light through a single barrier can be ascertained. After tunneling of light through a single air barrier has been inspected, more complicated structures shall be studied now as well.

11.2 Resonant Tunneling Structures

As discussed in Sec. 10.2, additional silicon wells positioned in the air barrier of a structure of type $L_1 - d_1 - L_2$ enable complete transmission through the sample at certain resonance energies. In order to gain more insight into the resonant tunneling, numerical simulations of resonant-tunneling samples have been performed and the results are discussed below.

11.2.1 Single-Well Structures

Samples of the structure $L_1 - d_1 - L_2 - d_2 - L_3$ are the most simple resonant-tunneling structures, c.f. Fig. 9.1(b). Thus, it is natural to begin inspecting resonant-tunneling phenomena by investigating the features of these structures. In Fig. 11.3(a), the resonant propagating (solid blue line) and counter-propagating mode function (dashed red line) of a sample with the layers $d_1 = d_2 = 300$nm and $L_2 = 140$nm are plotted. The mode functions are scaled to fit into the refractive-index profile of the sample (gray area) which also corresponds to the sequence of silicon and air layers. The propagation direction as well as the maximum intensity of the mode function are indicated in the figure using the same color in which the respective mode function is plotted. Due to the symmetry of the structure, the two mode functions are identical. The highest light intensity is observed in the L_2 layer. In particular, the light is concentrated in an area which is smaller than

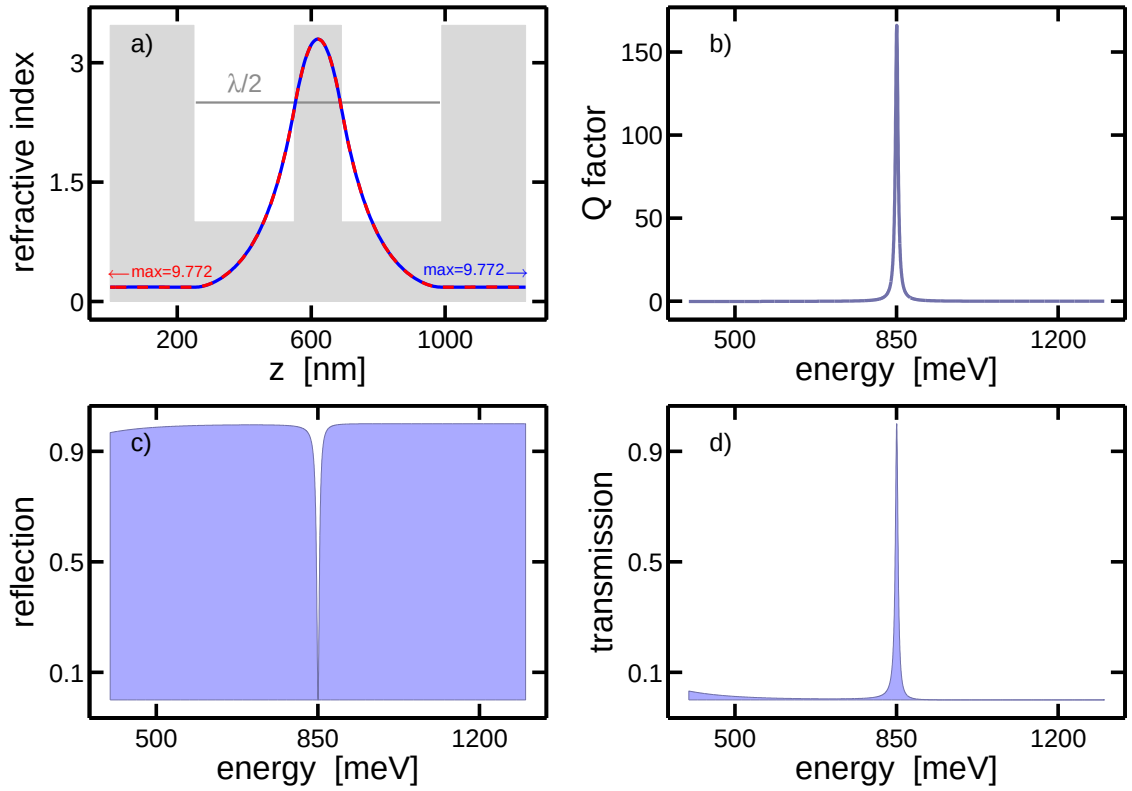

Figure 11.3: (a) Refractive-index profile and scaled resonant (counter-)propagating mode of the resonant-tunneling structure $L_1 - d_1 - L_2 - d_2 - L_3$ with $d_1 = d_2 =$ 300nm and $L_2 = 140$nm. The light is concentrated in the L_2 layer. The respective strength of the mode maximum is denoted in the figure. For comparison, the dark gray bar represents half the resonance wavelength. (c) Light is almost completely reflected in a wide spectral range. (d) Only at an energy of 850meV, one can observe resonant tunneling with a transmission probability of 100%. (b) The corresponding quality factor Q is peaked at the resonance with a maximum of about 170, which indicates that the resonant mode is captured in the sample.

half the resonance wavelength which in turn is indicated by the dark gray horizontal bar.

Resonant tunneling takes place at a resonance energy of 850meV, where the characteristic transmission probability of 100% is observed, frame (d). The transmission probability drops strongly with detuning away from the resonance energy. Consequently, light is almost completely reflected at energies other than the tunneling-resonance energy, frame (c). The corresponding quality factor is plotted in frame (b). The quality factor is peaked at the tunneling resonance and reaches a maximum of about 170, which indicates that the light is captured in the structure for some time at resonance.

In order to gain a better understanding of the resonant-tunneling structures, the influence of the sample geometry on the optical properties shall be studied next. Figure 11.4

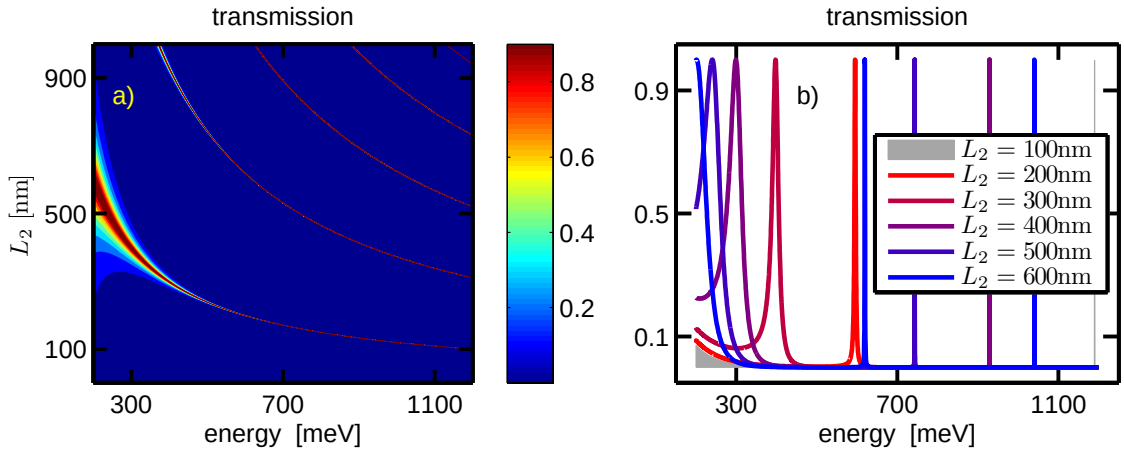

Figure 11.4: (a) Transmission probability of $L_1-d_1-L_2-d_2-L_3$ structures as a function of energy and thickness L_2 of the silicon well which is surrounded by the two air gaps. (b) Selected transmission spectra for different values of L_2. Resonances with complete transmission $T = 1$ are observed in the resonant-tunneling structures. Specifically, the resonances shift to lower energy with increasing width L_2 of the silicon well and they become broader at the same time.

shows the corresponding numerically calculated transmission probabilities as a function of energy and silicon-well thickness L_2. In frame (a), a transmission resonance is observed within the investigated spectral range once L_2 exceeds a thickness of 100nm. Moreover, even a set of transmission resonances is found for layer thicknesses $L_2 > 300$nm. Each of these resonances is associated with complete transmission as can be seen from the spectra plotted in frame (b). For a fixed layer thickness L_2, the different resonances can be labeled by increasing integers m beginning at the energetically lowest resonance $m = 0$. With increasing order m and thus with increasing resonance energy, the widths of the resonances decrease strongly. Furthermore, the spectral positions of the resonances shift when the well thickness L_2 is changed. Specifically, the resonances shift to the red with increasing layer width L_2. As a consequence, the resonances become broader with increasing thickness of the silicon layer L_2, which is in analogy to the different peak widths observed for resonances of different order m.

The numerically obtained set of transmission resonances can be used to test the accuracy of the analytic expressions derived in the course of the discussion of resonant tunneling in Sec. 10.2. The Eqs. (10.13) and (10.16) provide direct analytic access to the spectral resonance position once the phase Φ_R has been determined. The predictive power of these relations can be tested by comparison of the predicted resonance positions $E^m_{RT}|_{m>0}$ against the numerical results. The phase Φ_R may be determined from a fit using the lowest resonance branch $m = 0$ of the numerically computed spectra as an input. The resonance energy defines a corresponding z component of the wave vector $q^{(m=0)}_{\perp,L_2}$ according to Eq. (10.16). Φ_R can then directly be determined from Eq. (10.13) as

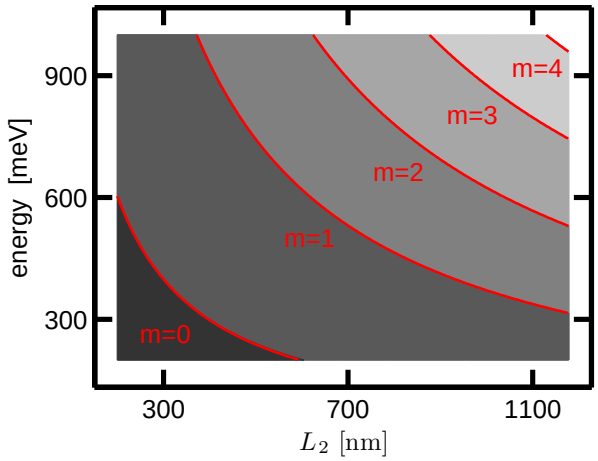

Figure 11.5: The energy at which resonant tunneling is observed is plotted as a function of the layer thickness L_2 for the first five resonance branches. Analytic predictions (shaded areas) are in excellent agreement with numerical computations (red lines).

a function of the well thickness L_2. That phase enters the computation of the positions of higher order resonances, $m > 0$, and thus provides the spectral resonance position E_{RT}^m in dependence of the silicon-well thickness.

The so-obtained dependence of the energetic resonance position on the well width is plotted in form of shaded areas for the resonances $m = 0$ up to $m = 4$ in Fig. 11.5. The numerically determined equivalents of these energy - well-width pairs are identified from Fig. 11.4(a) by localizing the transmission maxima. The respective numerically obtained resonance energies are plotted as a function of layer thickness L_2 in Fig. 11.5 as well (red lines). The analytic predictions are in excellent agreement with the numerical simulations.

For structures of the type $L_1 - d_1 - L_2 - d_2 - L_3$, the study of the influence of the sample geometry on the optical sample properties is completed by an inspection of the influence of the thickness of the air layers $d_1 = d_2$. Figure 11.6(a) shows transmission spectra obtained from a uniform sweep of the air-layer thicknesses. For small air layers with $d_1 = d_2 = 20nm$, strong transmission is observed in the full spectral range. With increasing barrier thickness $d_1 = d_2$, the overall transmission drops significantly except at the resonant-tunneling resonances where complete transmission is observed. When the thickness of the air layers is increased, the resonance peaks become narrower and they slightly shift to lower energies. As a general finding, a resonance of order m' is narrower and thus stronger peaked than a resonance of order m if $m < m'$. In Fig. 11.6(b), this relation is shown for the resonances $m = 0$ and $m' = 1$.

As a consequence of the peaked transmission probability, the quality factor is peaked at the transmission-resonance energies as well. Frame (b) shows the quality factor as a function of energy where the spectral position of the quality-factor peaks is given relative to the respective resonance energy $E_{RT}^{(m)}$ for the first $m = 0$ (left) and the second

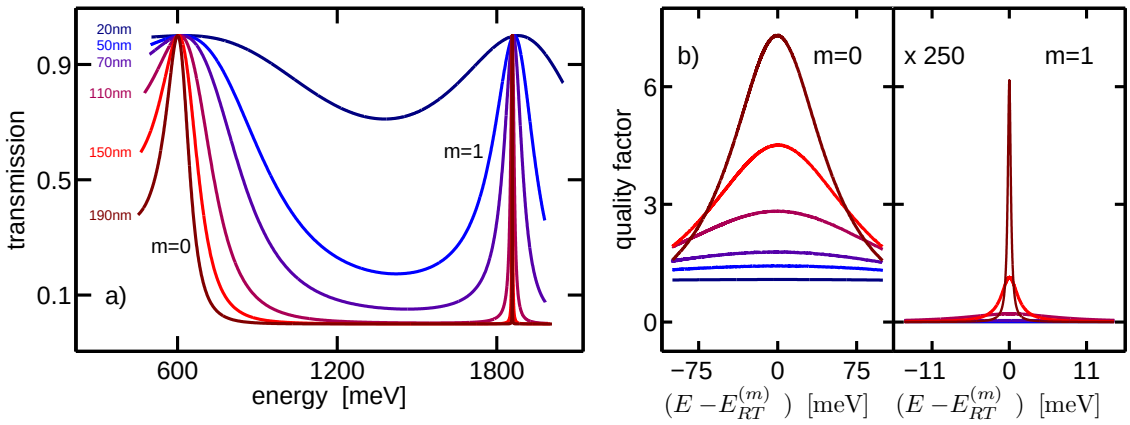

Figure 11.6: Influence of the air-layer thickness $d_1 = d_2$ in a single-well structure. (a) The transmission-resonance peaks become sharper with increasing air-barrier widths $d_1 = d_2$. The second order resonance $m = 1$ is much narrower than the first order one $m = 0$. In addition, both resonances slightly shift to lower energies with increasing $d_1 = d_2$. (b) The quality factor is peaked at the transmission resonances (same color code as used in frame (a)) and increases with increasing thickness of the air layers.

resonance $m = 1$ (right). The same color code is used as in frame (a). With the transmission peak getting narrower and thus with increasing $d_1 = d_2$, the maximum of the quality factor increases and the quality-factor peak becomes narrower. In particular, an exponential increase of the quality-factor peak height taken at the resonance position as well as an exponential decrease of the full width at half maximum (FWHM) of the corresponding peak is observed, Fig. 11.7.

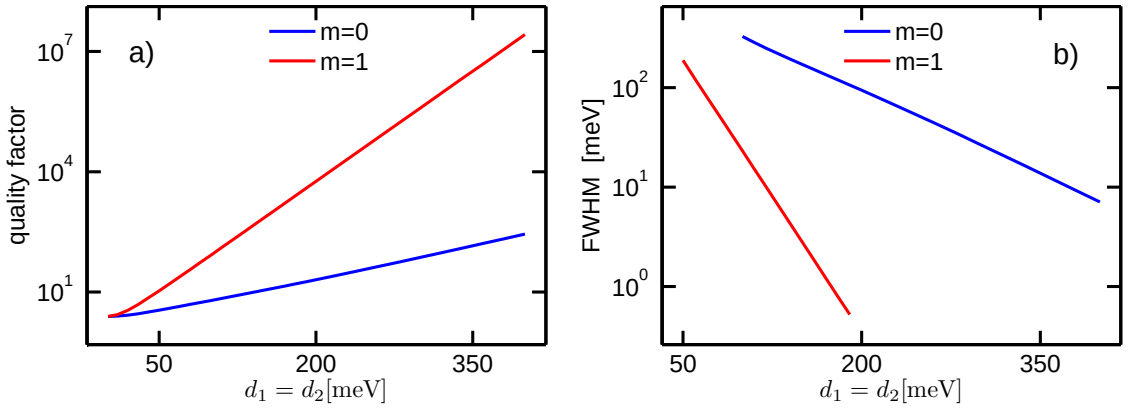

Figure 11.7: Dependence of (a) the maximum and (b) the FWHM of the quality factor on the thickness of the air layers $d_1 = d_2$ for the first two resonances $m = 0$ and $m = 1$, respectively. With increasing $d_1 = d_2$ the peak height of the quality factor increases while its width decreases. In general, these effects are the stronger the higher the order of the resonance is.

11.2.2 Double-Well Structures

The next level of structural complexity is obtained if an additional silicon well is added to the system. The system can then be characterized by the layer sequence $L_1 - d_1 - L_2 - d_2 - L_3 - d_3 - L_4$ which is again assumed to be symmetric so that $L_2 = L_3$, $d_1 = d_3$, and $d_2 = arb.$ unless the opposite is stated. The optical properties of such double-well structures are subject of investigation in the present section. In particular, the focus will be on the energetically lowest resonance branch $m = 0$ which provides the broadest resonances and is thus of most practical importance and easier to observe.

As can be seen in Fig. 11.8(d), the transmission probability of the double-well structure is double peaked. Figure 11.8(a) shows the setup of the respective sample together with the (counter-)propagating mode functions that correspond to these two tunneling resonances. Due to the symmetric sample setup, the propagating and counter-propagating modes are identical for a specific resonance. In the figure, the mode functions are scaled to fit into the refractive-index profile (gray area). The respective propagation directions and mode intensities are indicated in the figure and correspondences are ascertained by a color code. In particular, the modes are peaked at the positions of the two silicon wells. Hence, the light is concentrated in these silicon layers, in analogy to the single-well structure. For comparison, the horizontal bar indicates again half the wavelength corresponding to the lower-energetic resonance. Obviously, the light is concentrated within regions smaller than the corresponding wavelength. The obtained four mode functions that correspond to the two resonances and the two propagation directions are very similar to each other and they differ only in the region of the middle air layer d_2. That is because of the small energetic difference between the two resonance positions. In general, there can be stronger differences in the form of the mode functions as well if the transmission resonances are energetically further apart from each other.

In particular, the second transmission maximum cannot be attributed to the second order $m = 1$ resonance which eventually could have come close to the first order $m = 0$ resonance. Rather, it appears as a consequence of the additional silicon well. Since the two wells are identical, each of these silicon wells would yield the same resonant-tunneling behavior if either well was taken into account separately. The transmission properties of the entire structure are a result of the single-well properties and of the coupling among them provided by the common barrier d_2. Similar to the coupling of two identical electric eigenstates, a splitting of the resonance is observed and two transmission peaks occur. As a result, the reflection probability shows two sharp minima, frame (c). Analogously, the double-peak structure is also observed in the quality factor, frame (b). The two quality-factor peaks have maxima of about 1000. Moreover, these peaks are not identical, either, like the mode functions.

In the following, the influence of the sample setup on the spectral properties is investigated. Specifically, the above discussed structure with the layer widths $d_1 = d_3 = 429$nm, $L_2 = L3 = 152$nm, and $d_2 = 600$nm is taken as a reference structure. That is, while one parameter (pair) is varied, the other parameters are kept according to that structure.

If the thicknesses of the two air barriers $d_1 = d_3$ are varied uniformly, resonant tunnel-

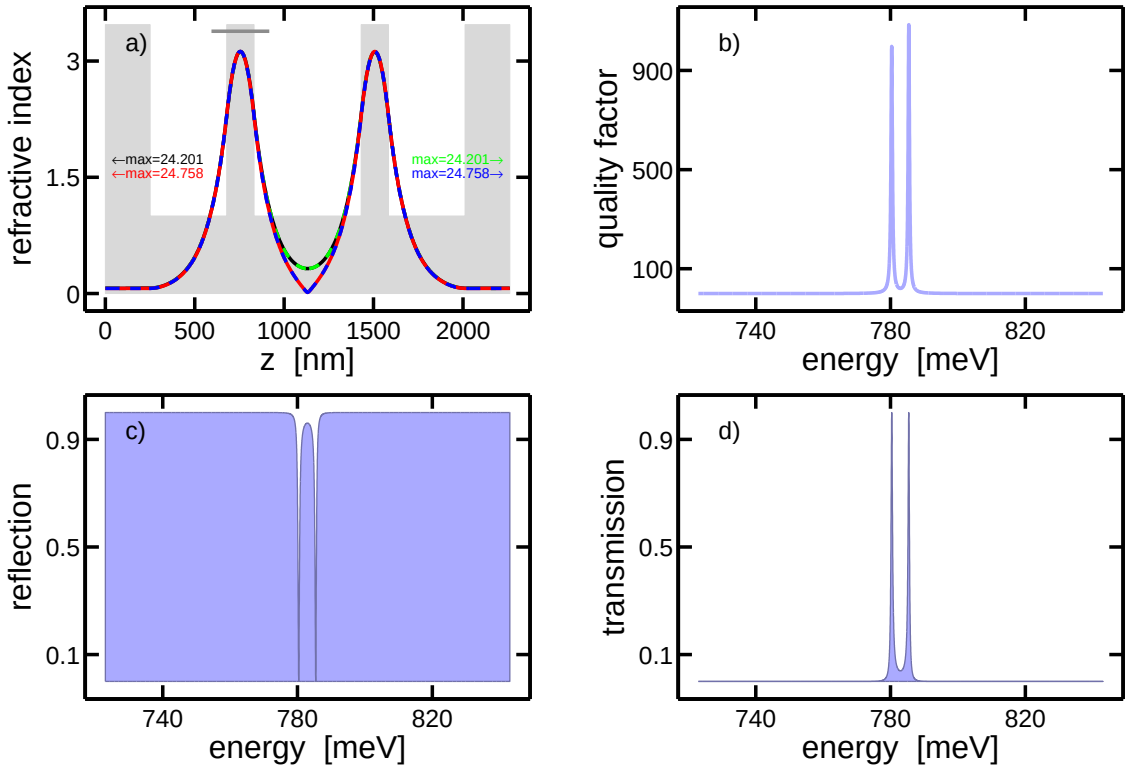

Figure 11.8: Typical double-well resonant-tunneling structure. (a) The refractive-index profile is shown together with the (counter-)propagating modes at the resonance energies. The maximum intensity of the scaled mode functions as well as their propagation direction are indicated in the figure using the same color in which the mode function is plotted. The horizontal bar indicates half of the wavelength corresponding to the lower resonance energy. (d) Two sharp transmission peaks with 100% transmission probability are observed. Consequently, light is entirely reflected except at the resonance energies, frame (c). (b) The transmission peaks are associated with sharp peaks in the quality factor.

ing occurs at about the same spectral position as in the reference structure. However, for small thicknesses $d_1 = d_3$, only a single resonance is obtained, gray area and blue line in Fig. 11.9(a), which is broad and does not reach full transmission, i.e. $|\mathcal{T}|^2 < 100\%$. As can be seen in frame (b), the spectral position of that single resonance shifts and approaches the center of the resonance positions corresponding to the reference structure with increasing air-layer thicknesses $d_1 = d_2$. At the same time the transmission peak becomes stronger and narrower, frame (a). Above a threshold thickness of $d_1 = d_3 = 290$nm that single resonance splits into two resonances, reddish lines in frame (a). In Fig. 11.9(b), the energetic position of the lower resonance peak is plotted in blue and the one of the energetically higher resonance is plotted in red. Obviously, the splitting saturates for larger air-layer widths $d_1 = d_3$. That splitting of the resonance goes along with a strong reduction of the FWHM of the resonance(s), Fig. 11.9(a). As

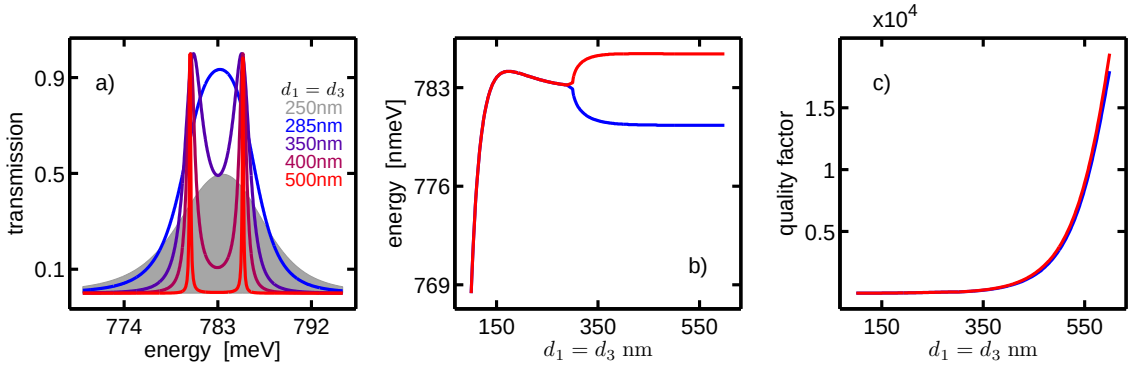

Figure 11.9: Influence of the air barriers $d_1 = d_3$ on (a) the transmission spectra, (b) the energetic position of the lower (blue) and the upper (red) resonance peak, and on (c) the quality factor of the two peaks. With increasing $d_1 = d_3$, the initial single resonance splits and the emerging two resonance peaks become narrower and larger. At the same time, the quality factor increases.

a consequence, the phase time and thus the quality factor increases with increasing air-barrier thickness, Fig. 11.9(c). Therefore, the layers d_1 and d_3 can be used to adjust the quality factor and the resonance width without considerably shifting the resonance position spectrally, if the thicknesses $d_1 = d_3$ are in the saturation regime of the splitting.

The strength of the splitting of the two tunneling resonances can be controlled via the middle air barrier d_2 as can be seen in Fig. 11.10. Specifically, there is no splitting for a large enough thickness of that air layer. Moreover, if the thickness d_2 is too large, the transmission resonance gradually disappears, frame (a). If instead the thickness d_2

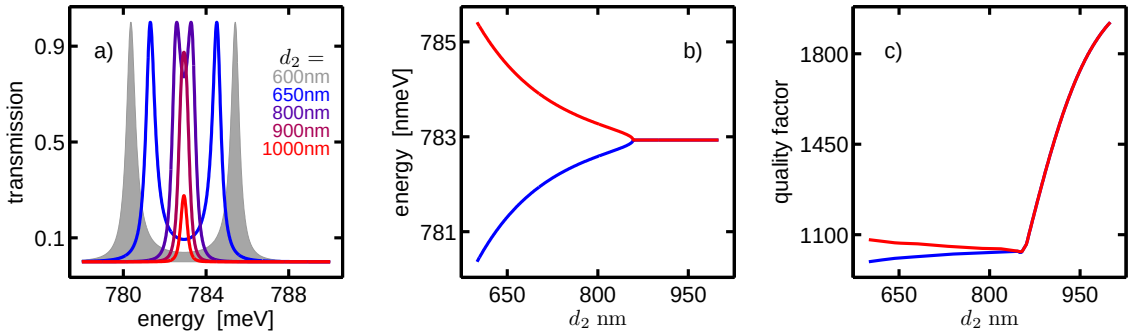

Figure 11.10: Influence of the air barrier d_2 on (a) the transmission spectra, (b) the energetic position of the lower (blue) and the upper (red) resonance peak, and (c) on the quality factor of the two peaks. For large d_2, only a single tunneling resonance is observed which splits into two transmission peaks when d_2 decreases (a). That splitting increases strongly with decreasing thickness of the middle air barrier (b). With increasing d_2, the quality factor of the lower (higher) resonance grows (drops) weakly until a single peak with strongly increasing quality factor is obtained, frame (c).

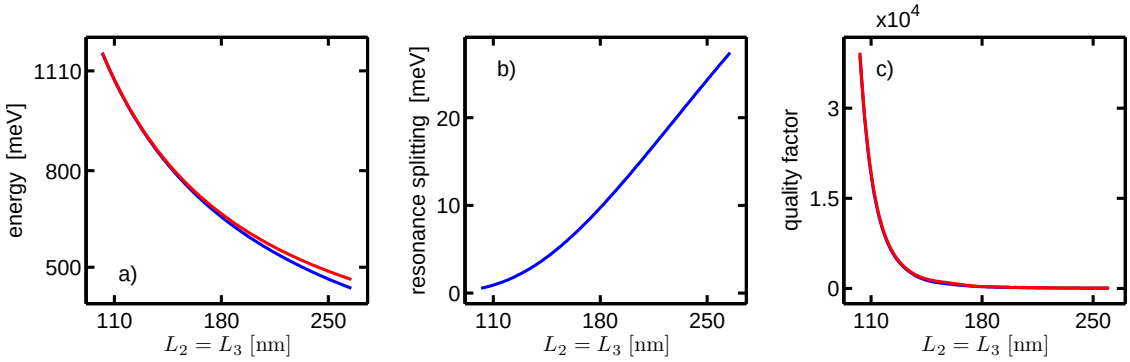

Figure 11.11: Influence of the thickness of the silicon wells $L_2 = L_3$ on the transmission spectrum. (a) energetic position of the transmission resonances, (b) strength of the resonance splitting, and (c) quality factor of the two transmission peaks. In frames (a) and (c), the red (blue) line belongs to the energetically higher (lower) resonance. With increasing thickness of the silicon wells $L_2 = L_3$, the transmission resonances shift to lower energies (a) and the resonance splitting increases (b). At the same time, the quality factor decreases (c).

is diminished, the already observed splitting sets in and the strength of the splitting increases with decreasing thickness d_2 of the middle barrier, frame (b). The quality factor is largest for large d_2. When the air barrier d_2 becomes narrower, the quality factor drops strongly. Once the resonance splitting is established, the quality factor of the higher energetic resonance is slightly increasing again with decreasing thickness of the layer d_2 while the quality factor of the lower energetic resonance decreases further, frame (c).

With the exceptions of too narrow outer air layers $d_1 = d_3$ as well as of a too large middle air barrier d_2, transmission spectra with two resonance peaks have been observed. The individual spectral positions of these two transmission peaks depend on the thicknesses of the air layers d_1, d_2, and d_3. Additionally, these tunneling resonances occur around a center energy that is hardly dependent on either air-barrier thickness. Rather, that center energy is determined by the silicon-well thicknesses $L_2 = L_3$. In particular, the overall spectral position of the resonances shifts to lower energies with increasing well thickness, Fig. 11.11(a). At the same time, the splitting of the two transmission resonances shows an additional dependence on the silicon-well width as that splitting increases with increasing thickness $L_2 = L_3$, Fig. 11.11(b). That behavior is accompanied by a strong decrease of the quality factor when the silicon wells become thicker, Fig. 11.11(c).

As a first conclusion, the spectral positions of the transmission resonances can be controlled by the sample geometry. The overall position, i.e. the center energy of the resonances is determined by the silicon-well thickness $L_2 = L_3$. Once that is fixed, the splitting of the resonances may be adjusted by an appropriately chosen width of the air

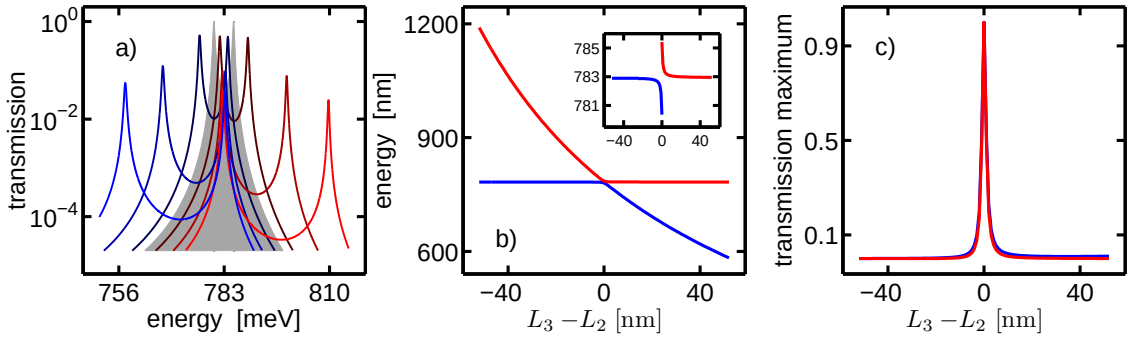

Figure 11.12: Influence of a difference in the thicknesses of the silicon wells L_2 and L_3. (a) Transmission spectra in a semi-logarithmic scale. Double-peaked complete transmission (gray area) is observed if $L_2 = L_3$. If $L_2 < L_3$ (bluish lines) or $L_2 > L_3$ (reddish lines), the transmission intensity drops with increasing difference of these thicknesses. At the same time, one of the peaks slightly shifts towards an energy of 783meV while the other strongly shifts away from that energy. (b) The spectral position of the lower-(higher-)energetic transmission peak is plotted as blue (red) line. The anti-crossing of the two resonances is shown in the inset. (c) The transmission probability at the transmission peaks is plotted as function of the thickness variation $L_3 - L_2$ using the same color code as in frame (b). With increasing difference of the thicknesses L_2 and L_3, the transmission decreases strongly.

barrier d_2. The widths of the resonances and thus the strength of the quality factor are controllable via the outer air barriers d_1 and d_3.

11.3 Asymmetric Double-Well Structures

Up to now, only symmetric samples have been studied in this thesis. Hence, asymmetric samples shall be investigated next. Figure 11.12 shows the optical properties of a double-well structure $L_1 - d_1 - L_2 - d_2 - L_3 - d_3 - L_4$ in which the outer air layers $d_1 = d_3$ are identical while the silicon wells L_2 and L_3 differ. In particular, the thickness of the layer L_2 is kept at the reference value of 152nm and the thickness of the second silicon well L_3 is varied. Some typical transmission spectra are shown in Fig. 11.12(a) in a semi-logarithmic scale.

The spectrum of the symmetric reference structure is plotted as a gray shaded area. Spectra where $L_2 < L_3$ are plotted using bluish lines while the reddish lines correspond to structures with $L_2 > L_3$. Once $L_2 \neq L_3$, only one of the two transmission resonances is found near the center energy of the two peaks obtained for the reference structure. The other energy shifts away from that center energy the stronger the larger the difference of the two silicon-well widths becomes. That shifting of the energetic resonance positions is shown as a function of silicon-well-thickness difference $L_3 - L_2$ in Fig. 11.12(b). The position of the energetically higher (lower) resonance is plotted as a red (blue) line. Apart

from the distinction of the energetically lower and higher resonance, one clearly observes one transmission resonance at an almost fixed spectral position of about 783meV while the other one is shifting strongly to lower energies with increasing layer thickness of the silicon-well L_3.

If one considers the two silicon wells separately, the fixed thickness of the layer L_2 defines a fixed transmission-resonance energy. On the contrary, the variation of the well thickness L_3 results in a shift of the corresponding spectral resonance position, c.f. Sec. 11.2.1. Specifically, these two resonances of separate wells would cross for $L_2 = L_3$ when the wells are identical so that the structure is symmetric. Hence the observed behavior of the resonance positions can be attributed to the different silicon-well thicknesses. Due to the coupling of the two resonances, an anti-crossing of the resonances is observed as can be seen in the inset of Fig. 11.12(b). Therefore the energetically lower resonance shifts hardly and the higher energetic one shifts strongly for $L_2 > L_3$. As a consequence of the anti-crossing, these roles are changed when $L_2 < L_3$ where the energetically lower resonance is shifting to lower energies and the energetically higher resonance is pinned.

Moreover, the transmission strength taken at the resonance-peak maxima considerably differs from the complete transmission that is found in the symmetric structure. The maximum transmission is strongly dependent on whether the thicknesses of the silicon wells L_2 and L_3 agree or not, frame (a). In Fig. 11.12(c), the transmission strength obtained at the spectral position of the energetically lower (higher) resonance is plotted as a blue (red) line. In general, the transmission becomes smaller with increasing deviation $|L_2 - L_3|$ of the layer widths of the two silicon wells. Thus, the transmission maximum reveals a sharp peak at equal silicon-well thicknesses $L_2 = L_3$, frame (c).

Similarly, the effect of deviating thicknesses of the outer air layers d_1 and d_3 on the transmission characteristics of the sample can be studied. Figure 11.13 shows the corresponding results for (a) the transmission spectra, (b) the spectral transmission-resonance positions, and (c) for the transmission maximum observed at the transmission-peak positions. The thickness of the air barrier d_3 is varied while the reference value of 429nm is used for the thickness of the air barrier d_1.

For an air barrier d_3 narrower than 288nm, a single peak is observed (gray area and dark blue line in Fig. 11.13(a)). With increasing thickness d_3 the peak maximum shifts slightly to lower energies and a shoulder emerges at the high-energy tail. This shoulder develops to a second maximum so that the single peak splits into the already previously observed two transmission-resonance peaks for $d_3 > 288$nm. That behavior is also shown in Fig. 11.13(b) where the position of the energetically lower (higher) resonance is plotted as a blue (red) line. In case of air-layer thicknesses d_3 that are much larger than the air-layer thickness d_1, a saturation of the splitting is observed. The initial single transmission peak, as well as its splitting into two peaks, and the saturation of that splitting for a large layer thickness d_3 are in analogy to the findings obtained for uniform variation of the air-layer thicknesses d_1 and d_3, Fig. 11.9(a) and (b).

However, the differences between these two situations shall be addressed next. In

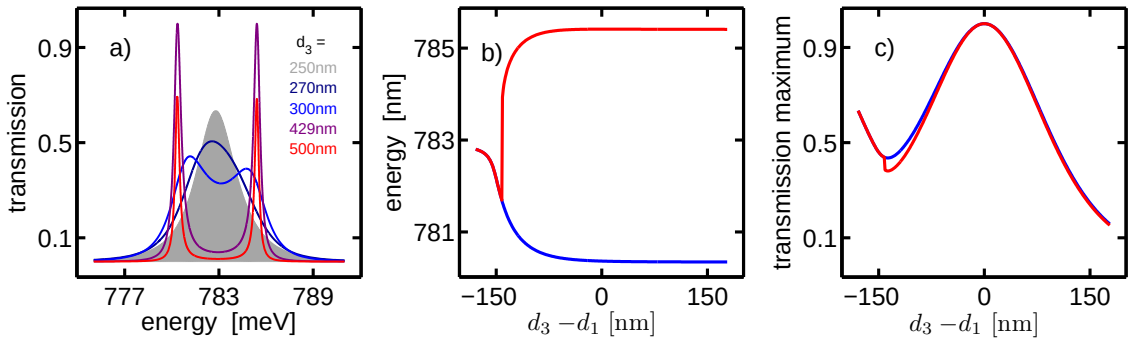

Figure 11.13: Transmission properties of a double-well structure with differing thicknesses of the air layers d_1 and d_3. (a) Transmission spectra vs. energy; (b) resonance positions and (c) maximal transmission probability at the resonances as function of air-layer-thickness difference $d_3 - d_1$.

Fig. 11.13(a), one observes that the maximal transmission probability of the single transmission-resonance peak decreases with increasing air-layer thickness d_3, in contrast to the case of uniform variation of $d_1 = d_3$. When the air-layer thickness d_3 is just above the splitting threshold, the transmission probability is clearly below 1, frame (a). With increasing barrier width d_3, the transmission probability taken at the resonance positions increases again until complete transmission is obtained for the symmetric structure with $d_1 = d_3 = 429nm$ (purple line). If the thickness of the air barrier d_3 exceeds the thickness of the barrier d_1, the transmission efficiency decreases again (red line).

In Fig. 11.13(c), the transmission maxima of the resonance peaks are plotted as a function of the layer-thickness difference $d_3 - d_1$. After the initial decrease of these transmission-probability maxima, the transmission-probability maxima of the two split resonances increase again and reach their highest level for $d_3 - d_1 = 0$. In particular, a broad peak centered at $d_3 - d_1 = 0$ is obtained if the maximum transmission probabilities of the two resonances are plotted in dependence of the layer-thickness difference $d_3 - d_1$.

If the dependence of the transmission maxima on deviations in the air-layer thicknesses d_1 and d_3, Fig. 11.13(c), is compared against the respective dependence of the maximum transmission on the silicon-well thicknesses L_2 and L_3, Fig. 11.12(c), one observes that the transmission maxima are less sensitive to deviations of the air-layer thicknesses d_1 and d_3 than on deviations of L_2 and L_3. In particular, the FWHM of the transmission-maximum peak as a function of $d_3 - d_1$ is about 200nm while the FWHM with respect to $L_3 - L_2$ is only about 2nm. The observed sensitivity to the structural symmetry is of practical importance in the production of such resonant-tunneling samples and is studied in more detail in Sec. 11.3.2. Before that, more complicated resonant-tunneling structures with more than two silicon wells are studied in the following Sec. 11.3.1.

11.3.1 Multiple-Well Structures

Now that the optical properties of single- and double-well resonant-tunneling structures are understood, attention is drawn to structures including even higher numbers of silicon

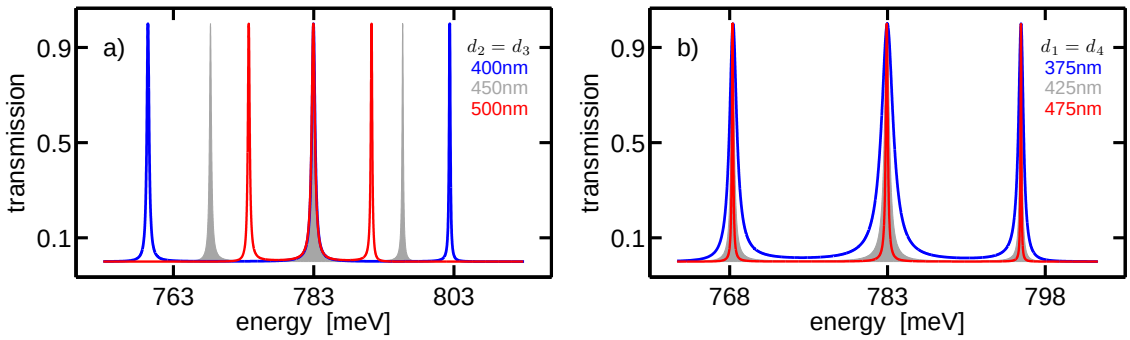

Figure 11.14: Transmission spectra of a triple-well structure. (a) The thicknesses of the air barriers $d_2 = d_3$ determine the energetic separation of the three transmission peaks. (b) The FWHM of the transmission peaks is controlled by the thicknesses of the air barriers $d_1 = d_4$.

wells. In the study of these multiple-well structures, the thicknesses of the silicon wells are kept uniform since it has already been observed that there is a strong sensitivity of the transmission efficiency on deviations of these thicknesses. For now, only ideal, symmetric structures shall be investigated.

Figure 11.14 shows the transmission spectra obtained from a triple-well structure $L_1 - d_1 - L_2 - d_2 - L_3 - d_3 - L_4 - d_4 - L_5$. In the calculations, a reference structure with $L_2 = L_3 = L_4 = 152$nm and $d_1 = d_4 = 425$nm as well as $d_2 = d_3 = 450$nm has been chosen. The respective reference spectra are plotted as a gray area. According to the three silicon wells, three transmission peaks are observed. The center energy of the spectral positions of these peaks is determined by the silicon-well thickness. If the widths of the layers d_2 and d_3 are varied uniformly, the spectral positions of the energetically lowest and highest resonance are affected. In contrast, the spectral position of the center peak remains unaffected. The energetically lower and higher peak shift away from (towards) the center peak when the air-barrier thicknesses $d_2 = d_3$ are diminished (enlarged), see blue (red) line in Fig. 11.14(a). As can be seen in Fig. 11.14(b), there is no influence of the air barriers d_1 and d_4 on the spectral peak positions. Rather, the FWHM of the peaks increases with decreasing air-layer thicknesses $d_1 = d_4$ (blue line), while the peaks become narrower if these thicknesses increase (red line).

If a fourth silicon well is added to the system, an additional transmission resonance can be observed in the transmission spectra of that quad-well sample, Fig. 11.15. In that figure, the spectrum corresponding to the chosen reference structure is plotted as gray area. That structure contains layers with the thicknesses $L_2 = L_3 = L_4 = L_5 = 152$nm, $d_1 = d_5 = 350$nm, $d_2 = d_4 = 350$nm, and $d_3 = 450$nm. The width of the transmission peaks can be adjusted with the help of the layer pair d_1 and d_5, frame (a). With increasing layer thicknesses $d_1 = d_5$, the peaks become narrower.

Among these four transmission-resonance peaks, two pairs of peaks can be identified. One pair is formed by the two energetically lowest resonances, the other one by the energetically highest resonances. The spectral separation of these two pairs of resonances

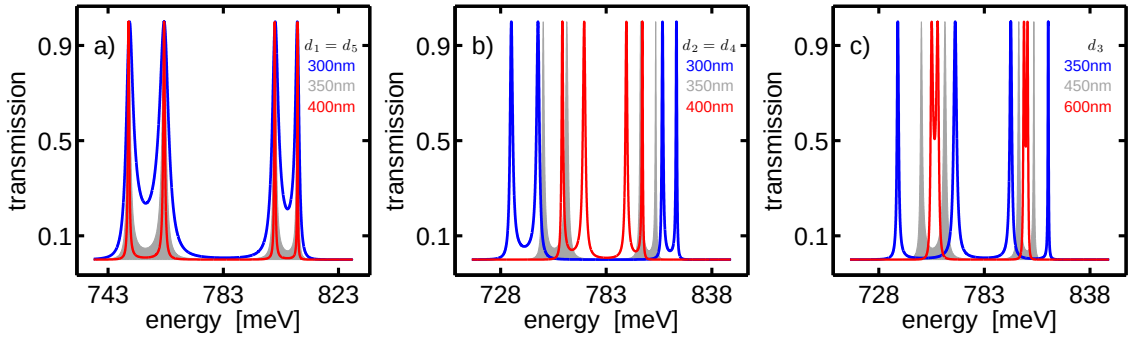

Figure 11.15: Transmission spectra of a quad-well structure.(a) The air-barrier thicknesses $d_1 = d_5$ define the FWHM of the transmission peaks. (b) The energetic separation of the lower-energetic and the higher-energetic pair of transmission resonances is governed by the layers $d_2 = d_4$. (c) The energetic distance of the two peaks of such a resonance pair is controlled by the layer thickness d_3.

is governed by the air barriers d_2 and d_4. If these air layers are narrow, the resonance pairs are energetically more separated from each other. They come closer to each other when the thickness of the air layers grows, Fig. 11.15(b). Similarly, the spectral separation of the two peaks within each of these resonance pairs is determined by the thickness of the air barrier d_3. With increasing layer thickness d_3, the spectral positions of the two peaks of a resonance pair approach each other, frame (c).

As a general finding, the uniform thicknesses of the silicon wells determine the overall spectral position of the resonant-tunneling transmission peaks. The number of wells corresponds to the maximal number of transmission peaks that can be obtained. The relative positions of these peaks among each other as well as their FWHM can be controlled by adjusting the air-barrier thicknesses. The respective influence of the different air barriers on the spectral properties depends on the number of silicon wells. However, with an appropriate choice of the layer thicknesses, the resonant tunneling structures can be designed at will. Specifically, sharp transmission peaks can be achieved which allow for selective filters or the peaks can be merged to form a transmission band.

For a quad-well structure some specific cases are shown in Fig. 11.16 to illustrate how the sample design may possibly be used. In frame (a), the transmission probability is plotted. For silicon wells of thickness 152nm, the air layers are chosen such that the four peaks either merge to form a broad transmission band with a transmission probability of at least 75% (red line), or such that two separate transmission bands exist (gray area). Moreover, four distinct narrow transmission peaks may be achieved as well (blue line). These spectra and any cases in between may be designed according to the specific needs, which may focus either at the transmission properties as discussed above or at the quality factor.

The corresponding quality factors are plotted in Fig. 11.16(b) using the same color code as in frame (a). For the broad transmission band consisting of four merged res-

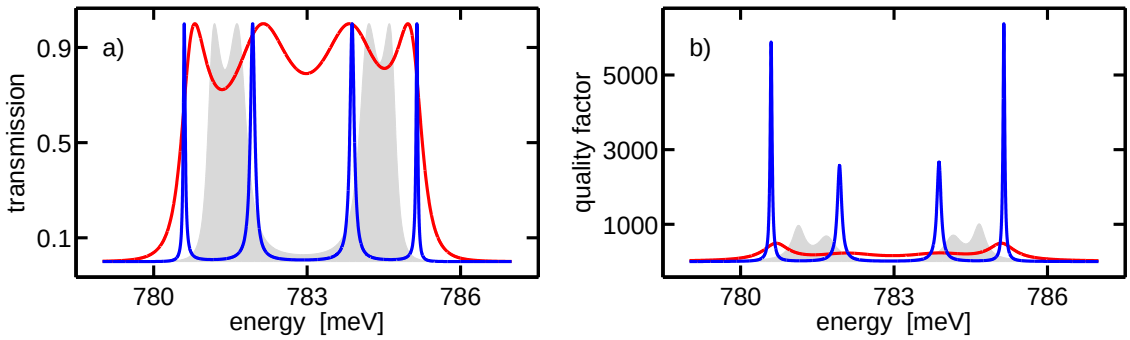

Figure 11.16: (a) Transmission spectra and (b) quality factors of three quad-well resonant-tunneling structures designed with different emphasis on the transmission and quality factor properties. Broad and/or multiple transmission bands can be formed by merging several transmission resonances. Alternatively, sharp single transmission resonances can be obtained as well. At the same time, the quality factor can be tuned in a wide range.

onances (red line), the quality factor is smallest and ranges from 200 to 400 at the resonance positions. A somewhat larger quality factor is obtained for the two small transmission bands (blue line), where the quality factor scales from 400 to 900 in the band regions. The largest quality factor is obtained for the sharp single resonances. While the quality factor ranges from 6000 to 6500 for the two outer resonances, the two middle resonance have a smaller quality factor of about 2500. These large quality factors make the resonant tunneling structures interesting candidates for studying slow light. The variety in the achievable properties of the transmission and/or of the quality factor can be increased by using more silicon layers. Hence, these structures have a high potential for optical application.

11.3.2 Towards Sample Production

If such samples shall be produced, the limitations of the fabrication process have to be taken into account. Since the air layers cannot be created by MBE or MOVPE, other techniques such as etching, sputtering, or milling have to be applied. Therefore, certain stronger fluctuations in the layer widths cannot be avoided. Consequently, one has to consider the strong dependence of the transmission efficiency on deviations in the thicknesses of the silicon wells carefully. For illustration, a double-well resonant-tunneling structure shall be studied, which is the simplest example in which that problem occurs as the sample consists of two silicon wells.

In particular, the thickness of the first silicon well L_2 is again set to the reference value of 152nm while the thickness L_3 of the second well is varied. That situation has already been studied in Fig. 11.12 where a sharp peak of the maximum transmission as a function of silicon-well-thickness detuning $L_3 - L_2$ has been observed at $L_3 - L_2 = 0$. Specifically, a FWHM of that peak of 2nm has been obtained. A realistic estimate of the fluctuations of the layer thicknesses L_2 and L_3 is in the order of $|L_3 - L_2| \geq 5$nm.

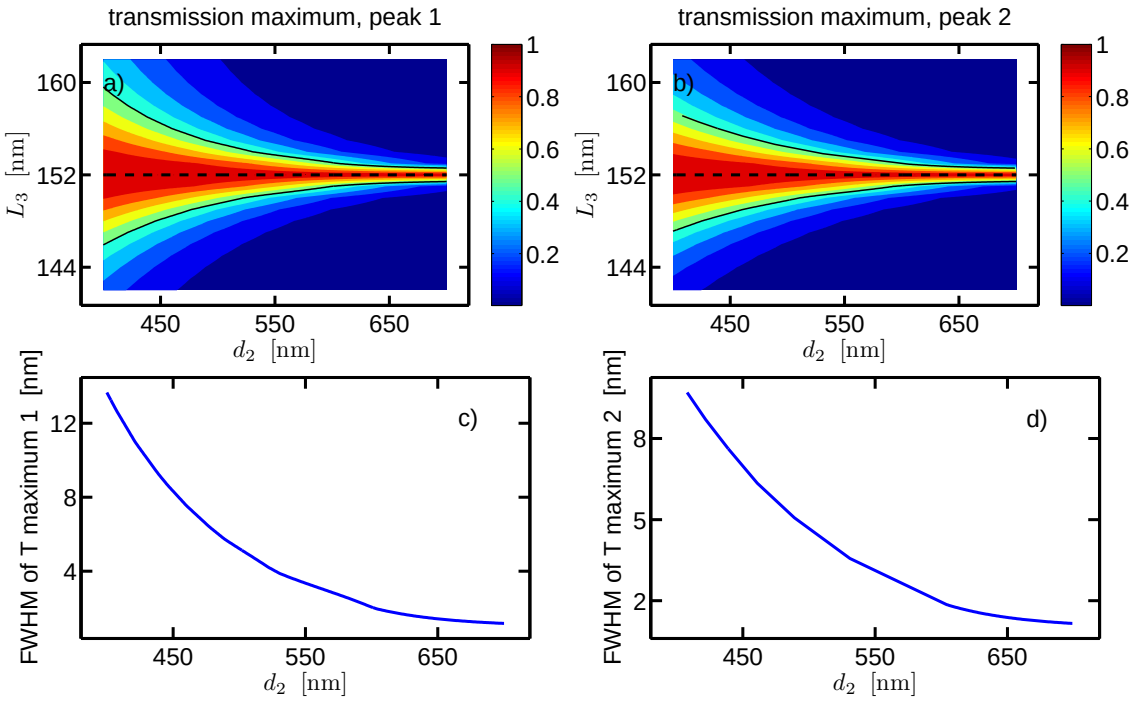

Figure 11.17: Transmission maxima for (a) the lower-energetic and (b) the higher-energetic transmission peak of a double-well structure in dependence of air-layer thickness d_2 and silicon-well thickness L_3, where $L_2 = 152$nm is kept constant. The sensitivity of the transmission peaks to differences of the silicon-well thicknesses L_2 and L_3 decreases with decreasing thickness of the air layer d_2, frames (c) and (d).

Therefore, the task is to identify a sample geometry in which that fluctuation is taken into account and which nevertheless guarantees the observation of resonant tunneling with a high enough transmission efficiency.

As a lower limit of the transmission peak intensity, we chose 50% transmission. Thus, we need to identify conditions in which the FWHM of the transmission peak is larger than 10nm. On that purpose, the thickness of the middle air barrier d_2 is also varied while the remaining air barriers are kept at a thickness of $d_1 = d_3 = 429$nm. The Figs. 11.17(a) and (b) show the obtained maximum transmission at the first and at the second transmission-resonance peak, respectively, as a function of the silicon-layer thickness L_3 and of the air-barrier thickness d_2. For large air barriers, the structures are very sensitive to deviations of the silicon-well thicknesses, which can be seen by the narrow peak of the maximum transmission at both transmission resonances, frames (a) and (b). The ideal case of identical silicon wells is indicated by the dashed black line. In the area between the two solid black lines, the obtained transmission probability at the resonant-tunneling resonances is larger than 50%. One can see that the FWHM of the maximum-transmission peak becomes larger if the air-barrier d_2 becomes smaller. That FWHM is plotted in Fig. 11.17(c) for the energetically lower resonance and in

Fig. 11.17(d) for the energetically higher resonance. The lower resonance is found to be slightly less sensitive to the deviations of L_2 and L_3. However, for the chosen target silicon-well thickness and for the outer air barriers d_1 and d_3, the thickness of the center air layer d_2 should be chosen below 400nm to guarantee a transmission probability of at least 50%. In contrast to the predictions in Ref. [396], clear resonant-tunneling peaks can be observed in the transmission spectra if the sample design is chosen appropriately. Nevertheless, the choice of a minimum transmission larger than 50% displays a more restrictive condition. The target range, given by the area between the solid black lines in Figs. 11.17(a) and (b), becomes the narrower the higher the minimum transmission is chosen. Consequently, an even larger air barrier d_2 would have to be chosen to achieve the desired minimum transmission efficiency despite the due inaccuracies of the silicon-well widths.

According to the above procedure, silicon-based double-well resonant-tunneling structures have been designed and produced. First experiments are currently under way so that theory-experiment comparisons should be possible soon, in which probably some improvements of how to treat the silicon layers may become necessary. In particular the inclusion of the frequency dependence of the refractive index of silicon as well as taking into account the absorption by the silicon layers are straightforward improvements of the present theoretical modeling of the samples.

12 Summary and Outlook

Resonant tunneling of light in stacked structures consisting of alternating parallel layers of silicon and air have been studied theoretically. While usually total internal reflection is expected for light shined on a silicon→air interface under an angle larger than the critical angle, light may tunnel through the air barrier due to the existence of evanescent waves inside the air layers if the neighboring silicon layer is close enough.

This tunneling of light is in analogy to the well-known tunneling of a quantum particle through a potential barrier. In particular, the wave equation and the stationary Schrödinger equation are of the same form. Consequently, the resonant tunneling of light can be understood in analogy to the resonant tunneling of e.g. electrons as well.

The characteristic feature of resonant tunneling is a complete transmission through the barrier at certain resonance energies. The transmission, reflection, and propagation properties of the samples have been determined numerically using a transfer-matrix method and assuming a uniform constant refractive index in all silicon layers. Moreover, analytical expressions for the energetic resonance positions have been found to be in excellent agreement with the numerical simulations for both, tunneling and resonant tunneling of light.

Special attention has been drawn to the lowest resonance out of a series of resonant-tunneling resonances. At that resonance, light has been observed to be concentrated within silicon layers the extension of which is smaller than the corresponding wavelength of the light. Specifically, the quality factor is large at the resonance energies, which indicates that the resonant light leaves the sample delayed compared to propagation in bulk silicon of the same size, which in turn allows for the study of slow light.

A detailed investigation of how the sample geometry influences the optical properties of the sample has been presented. In particular, it has been outlined how to design a sample to obtain certain desired optical properties. Well-separated single resonances, near-by resonances, or even bands consisting of several merged resonances can be achieved. Moreover, the width of these resonances can be adjusted. In the course of designing the transmission properties, the properties of the quality factor can be designed at the same time due to its direct connection to the total transmission coefficient of the samples.

The optical properties that are related to the resonant tunneling strongly rely on the (mirror-)symmetry of the samples. If asymmetries – especially of the silicon wells inside the air barrier – are present in the sample setup, the resonant-tunneling efficiency is diminished. Such asymmetries are unavoidable in the production of the samples. Therefore, a parameter range has been identified in which reasonable transmission above a transmission probability of 50% can be expected taking typical fluctuations caused by the production process into account.

Silicon-based resonant-tunneling structures of a setup proposed by the presented theory have already been fabricated and first experiments are under way. This will allow for theory-experiment comparisons. To achieve a more realistic description of the samples, the inclusion of the frequency dependence of the refractive index as well as the inclusion of the absorption by the silicon layers might have to be taken into consideration. These additional effects can be included in a straight-forward way and have previously been neglected to simplify the model system. Additionally, slow light effects can be studied in detail. The use of the investigated silicon-material system may also lead to applications in the context of light-control on optical chips where the samples could serve as filters or delay lines.

Zusammenfassung

Die vorliegende Arbeit beschäftigt sich mit den 'optischen Eigenschaften quasiperiodisch angeordneter Halbleiternanostrukturen'. Dieser eher allgemein gehaltene Titel der Arbeit liegt darin begründet, dass die optischen Eigenschaften zweier recht verschiedener Halbleitersysteme untersucht worden sind. So wurden einerseits eindimensionale resonante Fibonacci Quasikristalle und andererseits das resonante Tunneln von Licht durch Silizium-Luft Schichtstrukturen untersucht. Demzufolge gliedert sich die Arbeit auch in zwei Teile, die nach einem kurzen Überblick über die Halbleiterphysik und -technologie zusammenfassend beschrieben werden.

Allgemeines zur Halbleitertechnologie Unser heutiges Alltagsleben ist stark durch die Halbleitertechnologie geprägt, was in der Erfindung des Transistors [1–3] seinen Ursprung hat. Diese Erfindung ermöglichte kostengünstige, effiziente und robuste logische Schaltungen, die in den integrierten Schaltkreisen [4–6], mit denen die heutigen elektronischen Geräte gesteuert werden, Anwendung finden. Aufgrund der Vielseitigkeit und Effizienz der Halbleiterbauelemente kommen diese in (Mobil)Telefonen und Haushaltsgeräten, Fernsehern und Taschenrechnern, Satelliten und Autos, industriellen Fertigungsanlagen, Digitalkameras und vielen weiteren Anwendungen zum Einsatz. Insbesondere basieren auch Computer auf eben diesen integrierten Schaltkreisen, die im Laufe der Zeit immer weiter miniaturisiert werden konnten [7].

Neben den oben genannten elektronischen Eigenschaften, werden auch die optischen Eigenschaften der Halbleiter in Anwendungen genutzt. Leuchtdioden [16–18], Solarzellen [19–21], optische Detektoren [22–24], und Laserdioden [27–30] sind nur einige Beispiele. Von besonderer Bedeutung sind die Laser, die zumeist aus Mehrfachquantenfilmstrukturen bestehen und z.B. in CD und DVD Spielern und Rekordern [37–39], in Laserpointern [40], Barcodelesegeräten [41], Laserdruckern, sowie in Projektoren [42, 43], in der Holographie [44] und als Pumplaser [45, 46] eingesetzt werden.

Die Grundlage der Entwicklung dieser Anwendungen der Halbleitertechnik sind und waren ein immer tiefergreifendes Verständnis der Festkörper [63–67] im Allgemeinen und

insbesondere der Halbleitermaterialien [35, 68–77] wie auch verbesserte Fabrikationsverfahren [48–62]. Wurde die Halbleiterphysik in den 1920er und 1930er Jahren noch als 'Schweinerei' [47] bezeichnet, so entwickelte sie sich rasant zu einer Kerntechnologie.

Heute können Halbleiterstrukturen höchster Präzision und Reinheit hergestellt werden. Es ist möglich, verschiedene Materialien aufeinander zu wachsen, wobei Genauigkeiten von bis zu einer Atomlage erzielt werden. Die Fähigkeit, vordefinierte Halbleiterstrukturen mit dieser Genauigkeit herzustellen, ist die Grundlage für viele Anwendungen, die auf dem speziellen Design der Bauelemente basieren, da die Eigenschaften des Halbleitermaterials durch die Probengeometrie beeinflusst und gesteuert werden können [115–120].

Der gezielte Einsatz von Quantisierungseffekten [35, 83] eröffnete somit die Möglichkeit der Untersuchung von zweidimensionalen Quantenfilmen [34, 84–103], eindimensionalen Quantendrähten [104–107], und nulldimensionalen Quantenpunkten [108–114]. Der gewählte Probenaufbau kann dabei speziell auf den anwendungsbezogenen Einsatz der Halbleitereigenschaften oder aber auf die optimalen Bedingungen zur Untersuchung noch unverstandener Eigenschaften abgestimmt werden. Halbleiterstrukturen dienen somit als ideale kleine Labore [121] der Halbleiterforschung. Ein grundlegendes Verständnis der Vorgänge innerhalb der Proben konnte auf mikroskopischer Ebene durch Messungen im linearen Regime erzielt werden. Außerdem wurden und werden noch heute Einblicke in die Vielteilchenwechselwirkungen durch intensive Forschung an nichtlinearen Probeneigenschaften [71, 78–82] gewonnen. Das Verständnis dieser Vorgänge ist die Grundlage zukünftiger Anwendungen, sodass auch die Forschung durch den Anwendungsbedarf gefördert und gefordert wird. Fortschritte in Forschung und Anwendung sind daher eng miteinander verknüpft.

So führte beispielsweise der Bedarf an höheren Datenübertragungsraten in der Telekommunikationsindustrie zum Einsatz von Glasfaserkabeln [125]. Für diese mussten wiederum passende elektro-optische Kopplungen entwickelt werden, die durch neue Laserstrukturen [126–128] realisiert werden konnten. In Zuge der an diesem Beispiel verdeutlichten Spezialisierung entwickelte sich die auf dem indirekten Silizium basierende Elektronik relativ unabhängig von der auf direkten Materialien der III-V-Halbleiter basierenden Halbleiteroptik. Es wäre allerdings wünschenswert Optik und Elektronik auf einem Chip vereinen zu können, um kleinere Abmessungen, größere Robustheit und kostengünstigere Herstellung zu erzielen. Außerdem eröffnete dies ein weites Feld neuer Anwendungsmöglichkeiten. Die Realisierung des Laserbetriebs galt im indirekten Halbleiter Silizium jedoch lange Zeit als nahezu unmöglich, konnte aber in den vergangenen Jahren umgesetzt werden [129–134]. Ebenso wird versucht, die III-V Halbleiter in die Siliziumchips zu integrieren [135–137], wobei die Problematik in den verschiedenen Gitterkonstanten der Materialien liegt. Mittels des indirekten III-V Halbleiters GaP kann dieses Problem überwunden werden [138, 139] und GaP-basierende Laser konnten ebenfalls hergestellt werden [140–143], sodass diese prinzipiell auf Silizium gewachsen werden können. Dies steht insbesondere im Zusammenhang mit Versuchen, die an ihre Grenzen [153] stoßenden elektronischen Schaltkreise durch optische Schaltkreise [154] abzulösen, was ein Feld intensiver Forschung darstellt [144–152], in dem es auf die Kontrolle und Führung des Lichtes sowie auf geeignete Lichtquellen ankommt.

Mit den resonanten Fibonacci Quasikristallen wird im ersten Teil dieser Arbeit eine erst wenig untersuchte Mehrfachquantenfilmstruktur untersucht, die einerseits als Lichtquelle und andererseits als optisch aktives Element der Kontrolle von Licht dienen kann. Neben den Anwendungsmöglichkeiten ist hier aber auch das fundamentale Verständnis dieser Strukturen von Bedeutung. Die im zweiten Teil der Arbeit betrachteten Siliziumnanostrukturen können ebenfalls als Filter oder als optische Verzögerungslinien der Lichtkontrolle dienen. Nachfolgend werden nun die jeweiligen Untersuchungen diskutiert.

Resonante Fibonacci Quasikristalle Der bekannte Teil der Bezeichnung 'resonante Fibonacci Quasikristalle' ist der 'Kristall'. Kristalle und ihr Aufbau werden seit mittlerweile mehr als 200 Jahren untersucht [63]. Durch Röntgenuntersuchungen [155–160] wurde der periodische Aufbau der Kristalle festgestellt, aus dem sich vierzehn mögliche Raumgitter ergeben, nach denen sich die Kristallatome anordnen können [64–67].

Quasikristalle [161–163, 165, 227, 228] wurden erst vor 25 Jahren entdeckt, als Messungen an metallischen Legierungen Beugungsgitter lieferten, die nicht mit der Periodizität der Kristalle in Einklang zu bringen waren, wohl aber mit dem Quasikristallkonzept. Im Gegensatz zu Kristallen sind Quasikristalle zwar deterministisch aber nicht periodisch, sondern eben quasiperiodisch angeordnet. Ebenso wie Kristalle besitzen auch sie langreichweitige Ordnung und der Abstand zweier Nächster-Nachbaratome ist nach unten und oben beschränkt und endlich. Damit stehen sie zwischen periodischen und ungeordneten Strukturen. Die Entdeckung der Quasikristalle rüttelte an den Grundfesten der Kristallographie, sodass zunächst teilweise versucht wurde, durch komplizierte Modelle, die jedoch durch experimentelle Befunde und theoretische Studien widerlegt werden konnten [168–173], die experimentellen Befunde zu erklären und das Bild des periodischen Kristalls zu retten [166, 167]. Somit wurde eine Neudefinition des kristallinen Zustands erforderlich [174], durch die die periodischen Kristalle zu einer speziellen Unterklasse der Quasikristalle wurden.

Infolge der Entdeckung der Quasikristalle in einer Legierung wurden Quasikristalle in Laboren aus einer Vielzahl weiterer Legierungen hergestellt [161, 178–186]. Diese Quasikristalle zeigten im Vergleich zu Kristallen außergewöhnliche Eigenschaften [188–200, 202], die hohes Potential für Anwendungen haben [188, 189, 201]. Ein natürlich entstandener Quasikristall wurde jedoch erst kürzlich in einer Gesteinsprobe eines Museums entdeckt [177].

Große Fortschritte bezüglich des Verständnisses der fundamentalen Eigenschaften der Quasikristalle konnten durch Untersuchungen an Quasikristallen aus künstlich hergestellten Materialsystemen erzielt werden, bei denen sich der quasikristalline Zustand nicht wie bei den Legierungen aus der Schmelze heraus ergab sondern aufgeprägt wurde [146, 199, 203–209, 211–218]. Zur Modellbildung von Quasikristallen können der Duale Grid [164, 219], Projektionsmethoden [220–223], oder Deflations- und Inflationstechniken, wie man sie von Penrose Tilings [224–226] kennt, genutzt werden. Die Gemeinsamkeit aller Modelle ist das Auftreten irrationaler Zahlen. In vielen Fällen handelt es sich bei dieser irrationalen Zahl um den Goldenen Schnitt [162–164, 177, 182, 187–189, 206–209, 218, 227–230].

Der Goldene Schnitt, $\tau = 0.5 + \sqrt{1.25} \approx 1.618\ldots$, ist eine aus Kunst und Architektur bekannte Zahl [231], die auch in natürlichen Strukturen gefunden werden kann und unmittelbar mit den Fibonacci Zahlen verwandt ist [232]. Letztere können aus der Fibonacci Sequenz, $LSLSLLSLLSLLS\ldots$, abgeleitet werden [291], deren Auftreten wiederum oft als Indiz für das Vorliegen einer quasikristallinen Struktur gewertet wird [164, 195, 196, 208, 213, 214, 229, 230]. Insbesondere ist die eindimensionale Fibonacci Sequenz das Standardbeispiel eines Quasikristalls [163, 188, 227, 228]. Aufgrund ihrer einfachen und übersichtlichen Struktur wurden eindimensionale Fibonacci Quasikristalle intensiv untersucht [233–246, 248, 249].

Resonante Fibonacci Quasikristalle, die aus quasiperiodisch angeordneten Mehrfachquantenfilmstrukturen bestehen, wurden jedoch erst vor kurzem zunächst theoretisch behandelt [250]. Daraufhin erfolgten Versuche der experimentellen Realisierung dieser Strukturen [251] sowie erste Untersuchungen ihrer optischen Eigenschaften [252]. Diese Studien quasiperiodisch angeordneter Mehrfachquantenfilmstrukturen können als natürliche Erweiterung der Untersuchen an periodischen Mehrfachquantenfilmstrukturen betrachtet werden, deren Eigenschaften bereits sehr gut verstanden werden [77, 78, 84–86, 88, 89, 93, 253–289] und die heute dennoch Gegenstand intensiver Forschung sind.

Somit knüpft auch die im ersten Teil dieser Arbeit vorgestellte Untersuchung GaAs-basierter resonanter Fibonacci Quasikristalle sowohl an Untersuchungen periodischer Mehrfachquantenfilmstrukturen als auch an die bislang durchgeführten Studien resonanter Fibonacci Quasikristalle an. In diesen eindimensionalen Quasikristallen sind die Abstände zwischen benachbarten Quantenfilmen entweder durch eine große Barriere L oder durch eine kleine Barierre S gegeben, die entsprechend der Fibonacci Sequenz angeordnet sind. Der gemittelte Abstand zweier Quantenfilme erfüllt dabei eine für Quasikristalle verallgemeinerte Bragg Bedingung. Zur Beschreibung des Quantenfilmmaterials in resonanten Fibonacci Quasikristallen wird hier zum ersten Mal eine mikroskopische Theorie genutzt. Mit den semiklassischen Halbleiter Bloch Gleichungen ist es möglich, die kohärente Anregung der Quantenfilme zu simulieren. Dabei wird die Ladungsträger-Ladungsträgerstreuung mikroskopisch berücksichtigt, sodass anregungsinduziertes Dephasieren von der Theorie beschrieben werden kann. Unordnungseffekte und Wechselwirkungen mit Phononen werden hingegen phänomenologisch behandelt. Um die Propagations-, Transmissions- und Reflexionseffekte zu beschreiben, wird ein Transfermatrixverfahren verwendet, was einer Probe-Antwort Messgeometrie entspricht.

Alle Simulationen basieren auf einem einzigen Satz an Materialparametern. Die so berechneten Reflexionsspektren sind in exzellenter Übereinstimmung mit den gemessenen linearen und nichtlinearen Spektren. Die experimentell beobachtete große Ähnlichkeit der nach resonanter und nicht resonanter Anregung erhaltenen Reflexionsspektren kann auf sehr ähnliche Absorptionseigenschaften bei beiden Anregungen zurückgeführt werden, die zu namhafter Absorption in einem breiten spektralen Bereich führt. Dies ist auch der Grund für die hohe Übereinstimmung der mit einer Probe-Antwort basierenden Theorie berechneten Spektren mit den nach resonanter Anregung gemessenen Spektren.

Sowohl in den berechneten als auch in den gemessenen Reflexionsspektren einer aus 54 Quantenfilmen bestehenden Probe ist ein ausgeprägtes scharfes Reflexionsminimum zu finden. Derart scharfe spektrale Eigenschaften können als optische Schalter oder für die

Erzeugung langsamen Lichts genutzt werden, sodass dieses Minimum eingehend untersucht wurde. Wenn höhere Ladungsträgerdichten vorliegen, bleicht dieses Reflexionsminimum infolge des anregungsinduzierten Dephasierens aus. Eine sehr gute Entsprechung der gemessenen und berechneten Reflexionsmaxima und -minima kann im gesamten spektralen Bereich bei allen Anregungsintensitäten beobachtet werden.

Insbesondere kann die Form des Reflexionsspektrums auf Brechungsindexeffekte zurückgeführt werden, die durch die Quantenfilmanordnung bestimmt werden. Als Ursache des scharfen Reflexionsminimums konnte dabei einerseits die quasikristalline Anordnung der Quantenfilme und andererseits eine leichte Abweichung des mittleren Quantenfilmabstands von der idealen Bragg Bedingung identifiziert werden. Die Form der Spektren ist stark vom mittleren Quantenfilmabstand beeinflusst, während sie relativ robust gegenüber Änderungen des Längenverhältnisses ρ der beiden Quantenfilmabstände L und S um den Goldenen Schnitt $\rho \approx \tau$ ist. Daher werden ähnliche Spektren für die kanonischen $\rho = \tau$ und die nicht kanonischen $\rho \neq \tau$ Proben beobachtet, solange dieses Längenverhältnis nicht zu sehr geändert wird. Allgemein folgt die Stärke der Reflexion dem entsprechenden Strukturfaktor der Fibonacci Quasikristalle.

Wenn die Quantenfilmanzahl erhöht wird, verschiebt sich die spektrale Position des Reflexionsminimums zu niedrigeren Energien und das Minimum wird breiter. Gleichzeitig prägen sich neue Minima mit ähnlichem Verhalten nahe der Schwerlochresonanz aus. Für Strukturen, deren Quantenfilmanzahl eine Fibonacci Zahl um eins übertrifft, können selbstähnliche Spektren beobachtet werden, was die Reflexionsminima als eine Folge der quasikristallinen Anordnung ausweist.

Ein tiefergehendes Verständnis der optischen Eigenschaften der untersuchten Strukturen kann durch eine verbesserte Modellierung dieser Strukturen erreicht werden. So wäre eine dynamische Simulation des Anregungsprozesses notwendig, um die experimentellen Bedingungen bei resonanter Anregung exakter zu beschreiben. Aufgrund des damit verbundenen wesentlich größeren Speicherbedarfs und längerer Rechenzeiten stellt dies allerdings eine numerische Herausforderung dar.

Die Halbleiter Lumineszenz Gleichungen könnten genutzt werden, um die Lumineszenz der resonanten Fibonacci Quasikristalle zu untersuchen, die sich deutlich von der der periodischen Mehrfachquantenfilmstrukturen unterscheidet. Auf diese Weise könnte auch hier der Einfluss der quasikristallinen Anordnung auf die spektralen Eingenschaften bestimmt werden. Der dazu notwendige numerische Aufwand ist allerdings noch größer als der für die dynamische Simulation resonanter Anregung anfallende. Dies liegt darin begründet, dass unter inkohärenten Bedingungen die in dieser Arbeit zur Beschreibung verwendeten kohärenten Größen verschwinden und die einfachsten nicht verschwindenden Größen bereits von erheblich komplizierterer Struktur sind.

Die vorgestellten mikroskopischen Untersuchungen resonanter Fibonacci Quasikristalle sind somit als ein Schritt auf dem Weg zu einem besseren theoretischen Verständnis der optischen Eigenschaften dieser Strukturen zu verstehen, dem wie zuvor dargelegt weitere folgen mögen. Insbesondere können weitere Untersuchungen darauf abzielen zu untersuchen, welche von periodischen Mehrfachquantenfilmen bekannte Effekte ebenfalls in resonanten Fibonacci Quasikristallen auftreten und inwiefern diese Effekte durch die quasikristalline Anordnung beeinflusst bzw. verändert werden.

Resonantes Tunneln von Licht Im zweiten Teil dieser Arbeit wurde resonantes Tunneln von Licht in Siliziumnanostrukturen untersucht. Der Tunneleffekt ist eine der bekanntesten Konsequenzen der Quantenmechanik. Da es sich bei diesem Effekt um ein reines Quantenphänomen handelt, gibt es dazu kein klassisches Analogon. Beim Tunnelproblem wird eine Barriere betrachtet, die ein klassisches Teilchen nicht passieren kann, während die Barriere von einem Quantenteilchen durchdrungen werden kann. Dieses wohlverstandene Problem ist Teil jeder Quantenmechanikvorlesung und ein Standardbeispiel für Quanteneffekte [323, 344, 345].

In ersten Tunnelexperimenten wurde das Tunneln von Teilchen wie z.B. Elektronen untersucht [346]. Probenabmessungen in der Größenordnung der de Broglie Wellenlänge des untersuchten Teilchens sind im Allgemeinen nötig, um Quantenphänomene beobachten zu können. Demzufolge wurde das Tunneln von Elektronen auch an p-n Übergängen [12], in GaAs/AlGaAs Heterostrukturen [347, 348] sowie in resonanten Tunneldioden beobachtet [349–353]. Wie das letzte Beispiel zeigt, kommt der Tunneleffekt bereits gezielt zur Anwendung. Ein weiteres Ergebnis der Untersuchungen des Tunneleffektes ist die Anwendung im Tunnelmikroskop [354], bei dem Elektronen von der Probe in die Spitze des Mikroskops tunneln und der Tunnelstrom gemessen wird. Ferner sind Tunnelprozesse auch von fundamentaler Bedeutung, da sie beispielsweise den radioaktiven Zerfall erklären können [355].

Im Rahmen der Untersuchungen von Tunnelprozessen ist eine Debatte über die Definition der zugehörigen Tunnelzeit aufgekommen [356–360]. Abhängig vom untersuchten System wurden verschiedene Größen zur Bestimmung der Tunnelzeit definiert, die jedoch nur *eine* allen gemeinsame Komponente haben [358] und sich ansonsten unterscheiden. Im Gegensatz dazu ist die Tunnelzeit für Licht klar definiert.

Mit Analogieschlüssen von Elektronen auf Photonen wurde das Konzept der elektronischen Bandstruktur und Bandlücke auf die photonische Bandstruktur und die photonische Bandlücke übertragen [116, 117], was zu neuen Forschungsgebieten und Anwendungen geführt hat. Auf ähnliche Weise ist die Analogie [356] zwischen dem Tunneln von Photonen [361] und dem Tunneln von Elektronen [362] genutzt worden, um den Tunneleffekt an einem besser handhabbaren System zu untersuchen. Insbesondere sind die Wellengleichung für eindimensionale Schichtstrukturen und die eindimensionale Schrödingergleichung von gleicher Form. Beim Tunneln von Licht wird die Geometrie für Totalreflexion genutzt. Klassisch kann das Licht die Grenzschicht zwischen einem Material mit hohem und einem Material mit niedrigem Brechungsindex nicht passieren, wenn der Einfallswinkel größer als der Grenzwinkel ist. Dennoch existiert in dem Material mit dem niedrigeren Brechungsindex eine exponentiell abfallende evaneszente Welle. Aufgrund dieser evaneszenten Welle kann auch ein Tunneln von Licht beobachtet werden, wenn sich in ausreichender Nähe hinter dem Material mit niedrigem wieder Material mit hohem Brechungsindex befindet.

Diese verhinderte Totalreflexion des Lichts wurde schon 1947 zu Filterzwecken vorgeschlagen [363], wobei zu dieser Zeit das Augenmerk auf der praktischen Anwendung und nicht auf dem Tunneleffekt lag. Mittlerweile sind jedoch zahlreiche Untersuchungen des Tunnelns von Licht durchgeführt worden [356, 364], die wiederum in Anwendungen resultierten [365].

In dieser Arbeit wird jedoch das *resonante* Tunneln von Licht betrachtet, das durch vollständige Transmission des Lichtes an bestimmten Resonanzenergien charakterisiert ist. Um resonantes Tunneln zu ermöglichen, muss in die Barrierenregion eine zusätzliche Materialschicht eingebracht werden, in der der Wellenvektor reell und somit die Propagation des Lichtes möglich ist [366, 367]. Tunneln bzw. resonantes Tunnel von Licht wurde bereits in verschiedenen Tunnelstrukturen beobachtet [368–377]. Während Überlichtgeschwindigkeit [361], rein-optische Schalter [378] sowie Filter [379] in Tunnelstrukturen realisiert werden konnten, konnten Speicher [375], Superlinsen [366, 380] und ebenfalls optische Schalter [375, 376] unter Benutzung des resonanten Tunnelns von Licht hergestellt werden.

In dieser Arbeit werden Siliziumnanostrukturen betrachtet. Aufgrund des großen Brechungsindexunterschieds zwischen Silizium und Luft eignet sich Silizium beispielsweise zur Herstellung von Wellenleitern. Im vorliegenden Fall wird dieser Brechungsindexunterschied genutzt, um unter Einbringen von Furchen in das Silizium die resonanten Tunnelstrukturen zu realisieren, da an den entstehenden Silizium-Luft Grenzschichten Totalreflexion herbeigeführt werden kann.

Diese resonanten Tunnelstrukturen ermöglichen die Untersuchung der fundamentalen Eigenschaften des resonanten Tunnelns wie auch der Abhängigkeit der optischen Eigenschaften dieser Strukturen vom Probenaufbau. Das gewählte Materialsystem Silizium ist darüberhinaus von besonderer Bedeutung. Während die elektronischen integrierten Schaltkreise sich den fundamentalen Grenzen weiterer Miniaturisierung nähern, werden die optischen Eigenschaften der Halbleiter, die in der sogenannten Photonik Anwendung finden, als die Alternative betrachtet, mit deren Hilfe man hofft, die Grenzen der Elektronik überwinden zu können.

Daher ist die Entwicklung und Herstellung optischer integrierter Schaltkreise, in denen die Eigenschaften der siliziumbasierten Elektronik und der hauptsächlich auf III-V Halbleitern basierenden Halbleiteroptik vereint werden sollen, ein Ziel heutiger Forschung [154, 381, 382]. Um dies zu erreichen, müssen die Kontrolle von Licht [149, 152] in Siliziumstrukturen wie auch alternative siliziumbasierte Lichtquellen [129–137] bzw. der Transfer und das Einbinden des Wissens um III-V Verbindungen auf/in Siliziumstrukturen [138–143] realisiert werden.

Auf diesem Forschungsgebiet ist bereits sehr viel Arbeit geleistet worden. So wurden Siliziumwellenleiter [150, 383] sowie siliziumbasierte Spiegel [384] und Kavitäten [385] hergestellt. Außerdem konnten optische Modulatoren [386] und rein-optische Schalter [147, 387, 388] in Siliziumstrukturen erzeugt werden. Ebenso wurde eine Nanokavität mit mechanischer Kontrolle über das eingeschlossene Licht hergestellt [389]. Langsames Licht konnte in Wellenleitern, die aus siliziumbasierten photonischen Kristallen bestehen, [390–392] erzeugt werden, und Anwendungen wie z.B. ein Gasdetektor [393] oder ein optisches Spektrometer [394] konnten in Siliziumchips integriert werden. Ferner sind Strukturen vorgeschlagen worden, in denen die Realisierung rein-optischer Transistoren vorhergesagt wird [148].

Auch Effekte, die auf dem resonanten Tunneln von Licht basieren, können eventuell zur Kontrolle von Licht beitragen. Außerdem sollen die grundlegenden Eigenschaften des resonanten Tunnelns von Licht in Siliziumnanostrukturen untersucht werden. Da-

her wurden detaillierte Untersuchungen der Probengeometrie auf die optischen Eigenschaften der Strukturen durchgeführt. Zur Beschreibung dieser Strukturen wurde die Transfermatrixmethode in numerischen Simulationen benutzt, wobei ein einheitlicher konstanter Brechungsindex für alle Siliziumschichten angenommen wurde. Außerdem wurden basierend auf demselben Zugang analytische Größen hergeleitet, die mit den numerischen Resultaten in exzellenter Übereinstimmung sind und mit deren Hilfe einige der optischen Eigenschaften verstanden werden können.

Insbesondere wurde die unterste Resonanz einer Siliziumtunnelstruktur genauer untersucht. Licht der entsprechenden Frequenz ist innerhalb der in der Barriere befindlichen Siliziumschichten konzentriert, deren Dicke kleiner als die Wellenlänge dieses Lichtes ist. An den Resonanzenergien wird ein großer Gütefaktor beobachtet, der zeigt, dass das resonante Licht mehr Zeit für die Propagation durch die Tunnelstruktur benötigt als für dieselbe Distanz in homogenem Silizium. Dies ermöglicht die Untersuchung langsamen Lichts.

Im Rahmen einer detaillierten Parameterstudie wurde gezeigt, wie die Probengeometrie genutzt werden kann, um bestimmte optische Eigenschaften der Struktur zu erreichen. So können klar separierte Resonanzen, nah benachbarte Resonanzen und zu ganzen Bändern verschmolzene Resonanzen realisiert werden. Außerdem kann die Breite der Resonanzen gezielt beeinflusst werden. Da der Gütefaktor direkt mit dem Transmissionskoeffizienten zusammenhängt, kann somit auch der Gütefaktor kontrolliert werden.

Die mit dem resonanten Tunneln von Licht verbundenen optischen Eigenschaften hängen stark von der (Spiegel-)Symmetrie der Probe ab. Wenn Asymmetrien – insbesondere in den Siliziumschichtdicken – vorliegen, ist die Tunneleffizienz stark herabgesetzt. Solche Asymmetrien können während der Probenherstellung nicht ganz vermieden werden. Daher wurde ein Strukturparameterbereich gesucht und gefunden, in dem eine ausreichende Transmissionswahrscheinlichkeit, $\geq 50\%$, besteht, auch wenn Fluktuationen in den Schichtdicken vorliegen.

Mit dieser theoretischen Modellierung wurde so eine Probengeometrie bestimmt, die bereits in einer entsprechenden Siliziumnanostruktur realisiert worden ist. Erste Experimente werden derzeit durchgeführt, sodass Theorie-Experiment Vergleiche bald möglich sein werden. Im Rahmen dieser Vergleiche kann eine realistischere Beschreibung dieser Struktur nötig werden, die durch Berücksichtigen der Frequenzabhängigkeit des Brechungsindexes sowie der Absorption von Licht im Silizium erreicht werden kann. Diese Verfeinerungen können direkt in die bestehende Theorie integriert werden und wurden zuvor vernachlässigt, um das Modellsystem zum besseren Verständnis der optischen Eigenschaften einfach zu halten. Bei geeignetem Probenaufbau kann des weiteren langsames Licht untersucht werden. Somit kann die vorgestellte Theorie auch zum Design von Filtern oder Verzögerungslinien mit erwünschten optischen Eigenschaften genutzt werden.

A

Basic Properties of One-Dimensional Fibonacci Sequences

There are several ways of constructing the Fibonacci sequence. Here, we will follow the geometrical approach according to the cut-and-project method [163, 220–223]. The reason for doing so is that several properties of the Fibonacci sequence can directly be seen from that construction method. While commonly the construction of the *canonical* Fibonacci sequence is presented, the more general derivation of canonical and *non*canonical Fibonacci sequences, for which the ratio of the building blocks differs from the golden mean, shall be presented in the following.

The basic idea is to obtain the one-dimensional Fibonacci sequence via a projection of selected points of a periodic two-dimensional lattice onto a line, Fig. A.1. Let this lattice be given by the lattice constants a and b, so that the lattice points are given by (na, mb) with integers $n, m \geq 0$. The line $\mathcal{L}$ is then defined by

$$y(x) = \tan(\theta)\, x \;, \tag{A.1}$$

with the angle θ given by

$$\theta \;=\; \arctan\left(\frac{a}{b}\tau\right) \;. \tag{A.2}$$

The properties of the constructed sequence are determined by the constant τ. For the Fibonacci sequence, this constant is the golden mean

$$\tau = 0.5 + \sqrt{1.25} \;\approx\; 1.618\ldots \tag{A.3}$$

which is an irrational number. For any irrational τ, the line $\mathcal{L}$ and the lattice are incommensurate, i.e. the origin of the coordinate system is the one and only common point of the line $\mathcal{L}$ and the lattice. One now defines a window that is limited by the lines

$$y'(x) \;=\; \tan(\theta)\,[x + a] \;, \tag{A.4}$$

$$y''(x) \;=\; \tan(\theta)x \,- b \;. \tag{A.5}$$

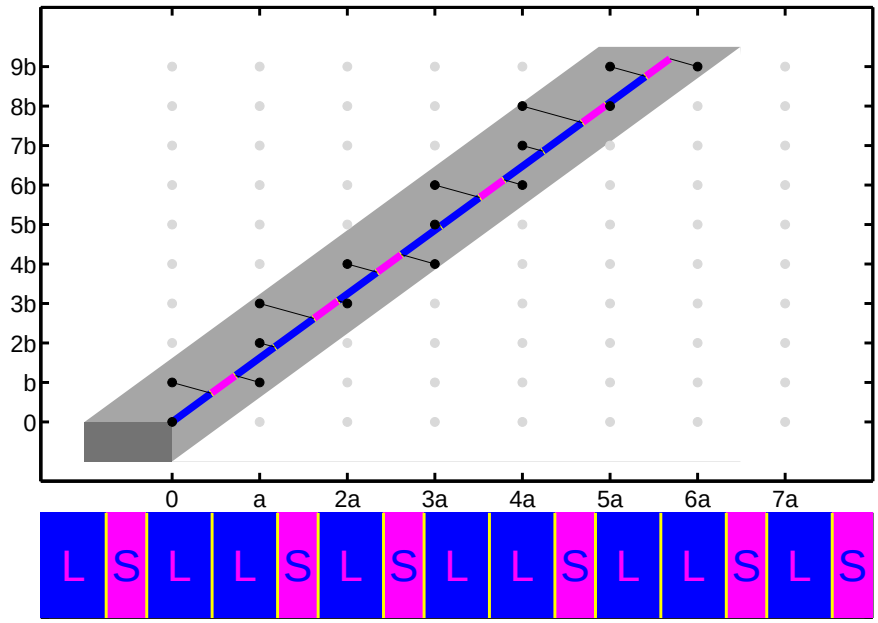

Abbildung A.1: Construction of the Fibonacci sequence $LSLLSLSLLSLLSLS\ldots$ with the help of the cut-and-project method. If the indicated rectangular $a \times b$ is moved along the line $\mathcal{L}$ of gradient $\tau a/b$ such that its orientation is kept and its upper right corner follows $\mathcal{L}$, a subspace (stripe) of the two-dimensional space is gained. All lattice points within that stripe are projected onto $\mathcal{L}$, which yields the Fibonacci sequence.

All lattice points within that window, which corresponds to the area covered by moving the rectangular $a \times b$ along the line $\mathcal{L}$, are projected onto the line $\mathcal{L}$, where the projection direction is perpendicular to that line. Due to the definition of the window, the distance in b-direction between the line $\mathcal{L}$ and the lower border of the window is

$$y(x = na) - y'(x = na) = b\,, \tag{A.6}$$

so that there is always exactly one lattice point in the selected window below the line $\mathcal{L}$ if $n > 0$. This point is given by

$$\begin{aligned} P_{n\downarrow} &= (na\,,\, \lfloor \frac{1}{b} y(na) \rfloor b) \\ &= (na\,,\, \lfloor n\tau \rfloor b)\,, \end{aligned} \tag{A.7}$$

where $\lfloor x \rfloor$ is the integer part of x. The distance of the upper window border to the line $\mathcal{L}$ is

$$y''(x = na) - y(x = na) = \tau b\,. \tag{A.8}$$

For the chosen τ, it holds $1 < \tau < 2$ so that one finds either one or two points above the

line $\mathcal{L}$ in the window. The coordinate of the uppermost point in that window reads

$$\begin{aligned} P_{n\uparrow} &= (na\,,\,\lfloor\frac{1}{b}y''(na)\rfloor b) \\ &= (na\,,\,\lfloor(n+1)\tau\rfloor b)\,. \end{aligned} \tag{A.9}$$

Hence, each point $P_{n\downarrow} = (na\,,\,\lfloor n\tau\rfloor b)$ within the chosen window that is located below the line $\mathcal{L}$ has two nearest neighbors that are within that window as well. These are $P_{n-1\uparrow} = ((n-1)a\,,\,\lfloor n\tau\rfloor b)$ and $P = (na\,,\,\lfloor n\tau+1\rfloor b)$. Therefore, the projection leads to two intervals along $\mathcal{L}$, namely the intervals L and S. As a consequence of the incommensurateness, the sequence of intervals L and S is non-periodic. The lengths l_L and l_S of these intervals are

$$l_L = b\,\sin(\theta)\,, \tag{A.10}$$

$$l_S = a\,\cos(\theta)\,. \tag{A.11}$$

The ratio of these interval lengths

$$\rho = \frac{l_L}{l_S} = \frac{b\sin(\theta)}{a\cos(\theta)} = \frac{b}{a}\tan(\theta) = \frac{b^2}{a^2}\tau \tag{A.12}$$

can be controlled by an appropriate choice of the lattice constants a and b,

$$\frac{a}{b} = \sqrt{\rho/\tau}. \tag{A.13}$$

The number of lattice points in the window with $x \le Na$ can be subdivided (c.f. Eqs. A.7 & A.9) as follows

position	number
any	$N_{\rm tot} = \sum_{n=0}^{N}\left[(\lfloor(n+1)\tau\rfloor - \lfloor n\tau\rfloor)+1\right] = N+1+\lfloor(N+1)\tau\rfloor$
below $\mathcal{L}$	$N_{\downarrow} = \sum_{n=0}^{N} 1 - 1 = N$
above $\mathcal{L}$	$N_{\uparrow} = \sum_{n=0}^{N}\left[\lfloor(n+1)\tau\rfloor - \lfloor n\tau\rfloor\right] = \lfloor(N+1)\tau\rfloor$
at $\mathcal{L}$	$N_{\mathcal{L}} = 1$

Since each point above (below) $\mathcal{L}$ results in an interval L (S), the ratio of the number N_L of intervals L and N_S of intervals S reads

$$\begin{aligned} \frac{N_L}{N_S} &= \frac{\lfloor(N+1)\tau\rfloor}{N} \\ &= \frac{(N+1)\tau}{N} - \frac{\{(N+1)\tau\}}{N} \\ &= \tau + \frac{1}{N}\tau - \frac{\{(N+1)\tau\}}{N} \\ &\xrightarrow[n\to\infty]{} \tau\,, \end{aligned} \tag{A.14}$$

where $\{x\}$ defines the non-integer part of x, i.e. $0 \leq \{x\} < 1$. With the help of that relation, we additionally find

$$\begin{aligned} \frac{N_{\mathrm{tot}}}{N_L} &= \frac{N_L + N_S}{N_L} \\ &\xrightarrow[n\to\infty]{} 1 + \frac{1}{\tau} \\ &= \tau \, . \end{aligned} \tag{A.15}$$

The average spacing d reads

$$\begin{aligned} d &= \frac{N_L l_L + N_S l_S}{N_{\mathrm{tot}}} \\ &= l_S \, \frac{N_L \rho + N_S}{N_{\mathrm{tot}}} \\ &= l_S \, \frac{N_L (\rho - 1) + N_{\mathrm{tot}}}{N_{\mathrm{tot}}} \\ &= l_S \left[\frac{N_L}{N_{\mathrm{tot}}} (\rho - 1) + 1 \right] \\ &\xrightarrow[n\to\infty]{} l_S \left[\frac{\rho - 1}{\tau} + 1 \right] \, . \end{aligned} \tag{A.16}$$

If the number of interval borders is given by n, there are $\lfloor n/\tau \rfloor$ large intervals L. Consequently, the number of small intervals S is given by $n - \lfloor n/\tau \rfloor - 1$. One has to subtract 1 since two interval borders are needed in order to obtain the first interval. Based on this, the position of the m^{th} interval border is given by

$$z_m = \left\lfloor \frac{m}{\tau} \right\rfloor l_L + \left(m - \left\lfloor \frac{m}{\tau} \right\rfloor - 1 \right) l_S \, , \tag{A.17}$$

which, with the help of the identity $x = \lfloor x \rfloor + \{x\}$ and with $l_L = \rho l_S$, can be written as

$$\begin{aligned} z_m &= l_S \left(\left\lfloor \frac{m}{\tau} \right\rfloor (\rho - 1) + m - 1 \right) \\ &= l_S \left(\frac{m}{\tau} (\rho - 1) - \left\{ \frac{m}{\tau} \right\} (\rho - 1) + m - 1 \right) \, . \end{aligned} \tag{A.18}$$

Rearranging this expression yields

$$\begin{aligned} z_m &= m \, l_S \left(\frac{\rho - 1}{\tau} + 1 \right) - l_S \left(\left\{ \frac{m}{\tau} \right\} (\rho - 1) + 1 \right) \\ &= m \, l_S \left(\frac{\rho - 1}{\tau} + 1 \right) + \left\{ \frac{m}{\tau} \right\} (l_S - l_L) - l_S \, , \end{aligned} \tag{A.19}$$

where one may identify the average spacing $d = l_S \left(\frac{\rho - 1}{\tau} + 1 \right)$, the modulation strength $\Delta = l_S - l_L$, and an overall shift of the whole lattice $z_0 = -l_S$, so that

$$z_m = z_0 + m \, \bar{d} + \Delta \left\{ \frac{m}{\tau} \right\} \, . \tag{A.20}$$

B

Parameters of Fibonacci Samples

The below table shows the layer widths and refractive indices, used in the analysis of the samples, as well as a classification of the appearing layer types. In addition, the building blocks of the samples, called groups, are identified.

type	layer	width [nm] FIB10	width [nm] FIB13	refractive index n	group
	vacuum	∞	∞	1.000	cap
7	GaAs cap	6.357	7.713	3.634	
3	$Al_{0.04}Ga_{0.96}As$ spacer	90.823	89.537	3.589	
5	$Al_{0.3}Ga_{0.7}As$ barrier	4.874	4.805	3.406	
6	GaAs QW	22.490	22.174	3.642	
5	$Al_{0.3}Ga_{0.7}As$ barrier	––	4.805	3.406	large spacer
4	GaAs adjuster	––	1.928	3.271	
3	$Al_{0.04}Ga_{0.96}As$ spacer	––	100.07	3.589	
5	$Al_{0.3}Ga_{0.7}As$ barrier	––	4.805	3.406	
6	GaAs QW	––	22.174	3.642	
5	$Al_{0.3}Ga_{0.7}As$ barrier	––	4.805	3.406	small spacer
4	GaAs adjuster	––	2.410	3.271	
3	$Al_{0.04}Ga_{0.96}As$ spacer	––	47.402	3.589	
5	$Al_{0.3}Ga_{0.7}As$ barrier	––	4.805	3.406	
6	GaAs QW	––	22.174	3.642	

type	layer	width [nm] FIB10	width [nm] FIB13	refractive index n	group
5	$Al_{0.3}Ga_{0.7}As$ barrier	4.874	4.805	3.406	buffer and substrate
4	GaAs adjuster	2.445	2.410	3.271	
3	$Al_{0.04}Ga_{0.96}As$ spacer	90.823	47.402	3.589	
1	GaAs	296.31	292.11	$3.634 + i0.07$	
2	AlAs/GaAs SL	22.62	22.32	3.310	
1	GaAs substrate and buffer	∞	∞	$3.634 + i0.07$	

The sample FIB10 which contains only a single QW consists of just “cap“ and “buffer and substrate“ layer groups while the sample FIB13 contains additional “large spacer“ and “small spacer“ layer groups, producing a Fibonacci-spaced chain of 54QWs. The AlAs/GaAs superlattice (SL) consists of six repetitions of 2 nm AlAs followed by 2 nm GaAs. The layers in both samples can be categorized into seven types indicated in the first column. All computations are performed based on this set of material parameters.

Literaturverzeichnis

[1] J. Bardeen and W. H. Brattain. The transistor, a semi-conductor triode. *Physical Review*, **74**:230–231, 1948.

[2] W. Shockley and G. L. Pearson. Modulation of Conductance of Thin Films of Semi-Conductors by Surface Charges. *Phys. Rev.*, **74**:232–233, 1948.

[3] W. Shockley, J. Bardeen, and W. H. Brattain. The electronic theory of the transistor. *Science*, **108**:678–679, 1948.

[4] J. S. Kilby. Miniaturized Self-Contained Circuit Modules and Method of Fabrication. U. S. Patent No. 3,138,744, filed on May 06, 1959. issued on June 23, 1964.

[5] R. N. Noyce. Semiconductor Device and Lead Structure. U. S. Patent No. 2,981,877, filed on July 30, 1959. issued on April 25, 1961.

[6] A. N. Saxena. Monolithic Concept and the Inventions of Integrated Circuits by Kilby and Noyce. In *NSTI-Nanotech 2007 – Technical Proceedings of the 2007 Nanotechnology Conference and Trade Show*, volume **3**, pages 460–474, 2007.

[7] G. E. Moore. Cramming more components onto integrated circuits. *Electronics*, **38**:114–117, 1965.

[8] W. S. Boyle and G. E. Smith. Charge coupled semiconductor devices. *Bell Syst. Tech. J.*, **49**:587–593, 1970.

[9] W. Schottky. Vereinfachte und erweiterte Theorie der Randschichtgleichrichter. *Z. Phys.*, **118**:539–592, 1942.

[10] K. B. Mc Afee, E. J. Ryder, W. Shockley, and M. Sparks. Observations of Zener Current in Germanium p-n Junctions. *Phys. Rev.*, **83**:650–651, 1951.

[11] S. L. Miller. Avalanche Breakdown in Germanium. *Phys. Rev.*, **99**:1234–1241, 1955.

[12] L. Esaki. New Phenomenon in Narrow Germanium p-n Junctions. *Phys. Rev.*, **109**:603–604, 1958.

[13] A. K. Jonscher. The physics of the tunnel diode. *Br. J. Appl. Phys.*, **12**:654–659, 1961.

[14] C. W. Bates Jr. Tunneling Current in Esaki Diodes. *Phys. Rev.*, **121**:1070–1071, 1961.

[15] D. R. Fredkin and G. H. Wannier. Theory of Electron Tunneling in Semiconductor Junctions. *Phys. Rev.*, **128**:2054–2061, 1962.

[16] H. Sugawara, M. Ishikawa, and G. Hatakoshi. High-efficiency InGaAlP/GaAs visible light-emitting diodes. *Appl. Phys. Lett.*, **58**:1010–1012, 1991.

[17] T. Kato, H. Susawa, M. Hirotani, T. Saka, Y. Ohashi, E. Shichi, and S. Shibata. GaAs/GaAlAs surface emitting IR LED with Bragg reflector grown by MOCVD. *J. Crystal Growth*, **107**:832–835, 1991.

[18] C.-C. Yang, C.-M. Lin, Y.-J. Chen, Y.-T. Wu, S.-R. Chuang, R.-S. Liu, and S.-F. Hu. Highly stable three-band white light from an InGaN-based blue light-emitting diode chip precoated with (oxy)nitride green/red phosphors. *Appl. Phys. Lett.*, 90:123503, 2007.

[19] D. M. Chapin, C. S. Fuller, , and G. L. Pearson. A New Silicon p-n Junction Photocell for Converting Solar Radiation into Electrical Power. *J. Appl. Phys.*, **25**:676–677, 1954.

[20] Zh. I. Alferov, V. M. Andreev, and V. D. Rumyantsev. Solar photovoltaics: Trends and prospects. *Semiconductors*, **38**:899–908, 2004.

[21] M. Bosi and C. Pelosi. The potential of III-V semiconductors as terrestrial photovoltaic devices. *Prog. Photovolt.: Res. Appl.*, **15**:51–68, 2007.

[22] T. Nakamura, K. Kiyohashi, and H. Suzuki. Light detector for camera using a $GaAs_{1x}P_x$ photo diode. *Solid-St. Electron.*, **22**:639–644, 1978.

[23] J.-C. Dousse and Ch. Rhême. The Si photodiode: An inexpensive though high-performing α detector. *Am. J. Phys.*, **51**:452–455, 1983.

[24] C. Brenner, S. Hoffmann, M. R. Hofmann, M. Salhi, M. Koch, A. Klehr, G. Erbert, G. Tränkle, J. T. Steiner, M. Kira, and S. W. Koch. Detection of THz radiation with semiconductor diode lasers. *Appl. Phys. Lett.*, **91**:101107, 2007.

[25] A. L. Schawlow and C. H. Townes. Infrared and Optical Masers. *Phys. Rev*, **112**:1940–1949, 1958.

[26] T. H. Maiman. Stimulated Optical Radiation in Ruby. *Nature*, **187**:493–494, 1960.

[27] R. N. Hall, G. E. Fenner, J. D. Kingsley, T. J. Soltys, and R. O. Carlson. Coherent Light Emission From GaAs Junctions. *Phys. Rev. Lett.*, **9**:366–368, 1962.

[28] Jr. N. Holonyak and S. F. Bevacqua. Coherent (visible) light emission from $Ga(As_{1x}P_x)$ junctions. *Appl. Phys. Lett.*, **1**:82–83, 1962.

[29] M. I. Nathan, W. P. Dumke, G. Burns, Jr. F. H. Dill, and Gordon Lasher. Stimulated emission of radiation from GaAs p-n junctions. *Appl. Phys. Lett.*, **1**:62–64, 1962.

[30] T. M. Quist, R. H. Rediker, R. J. Keyes, W. E. Krag, B. Lax, A. L. McWhorter, and H. J. Zeigler. Semiconductor Maser of GaAs. *Appl. Phys. Lett.*, **1**:91–92, 1962.

[31] H. Kroemer. A proposed class of heterojunction injection lasers. *Proc. IEEE*, 51:1782–1783, 1963.

[32] Zh. I. Alferov and R. F. Kazarinov. Semiconductor Laser with Electrical Pumping. U.S.S.R. Patent No. 181737, 1963.

[33] I. Hayashida, M. B. Panish, P. W. Foy, and S. Sumski. Junction Lasers Which Operate Continuously at Room Temperature. *Appl. Phys. Lett.*, **17**:109–111, 1970.

[34] R. Dingle. Confined Carrier Quantum States in Ultrathin Semiconductor Heterostructures. In H.-J. Queisser, editor, *Festkörperprobleme XV*, pages 21–48. Pergamon Vieweg, Braunschweig, 1975.

[35] C. Weisbuch and B. Vinter. *Quantum Semiconductor Structures: Fundamentals and Applications*. Academic Press, London, first edition, 1991.

[36] E. Hanamura. Rapid radiative decay and enhanced optical nonlinearity of excitons in a quantum well. *Phys. Rev. B*, **38**:1228–1234, 1988.

[37] C. M. Goldstein. Optical Disk Technology and Information. *Science*, **215**:862–868, 1982.

[38] K. A. Schouhamer Immink. The Compact Disk Story. *J. Audio Eng. Soc.*, **46**:458–465, 1998.

[39] J. Palmer. Optical data storage: Polarization and wavelength-resolved recording comes of age. *Laser Focus World*, **45**:22, 2009.

[40] J. Ting. Laser pointer. U. S. Patent No. D,403,451, filed on November 24, 1997.

[41] P. G. Howard. Hand held bar code reader with modulated laser diode and detector. U. S. Patent No. 4,694,182, filed on February 27, 1986.

[42] F. Brunner, E. Innerhofer, S. V. Marchese, T. Südmeyer, R. Paschotta, T. Usami, H. Ito, S. Kurimura, K. Kitamura, G. Arisholm, and U. Keller. Powerful red-green-blue laser source pumped with a mode-locked thin disk laser. *Opt. Lett.*, **29**:1921–1923, 2004.

[43] G. Zheng, B. Wang, T. Fang, H. Cheng, Y. Qi, Y. W. Wang, B. X. Yan, Y. Bi, Y. Wang, S. W. Chu, T. J. Wu, J. K. Xu, H. T. Min, S. P. Yan, C. W. Ye, and Z. D. Jia. Laser Digital Cinema Projector. *J. Display Technol.*, **4**:314–318, 2008.

[44] E. A. Barbosa and J. F. Cavalho. Surface analysis by two-diode laser photorefractive holography. *Appl. Phys. B*, **87**:417–423, 2007.

[45] A. R. Reinberg, L. A. Riseberg, R. M. Brown, R. W. Wacker, and W. C. Holton. GaAs: Si LED Pumped Yb-Doped YAG Laser. *Appl. Phys. Lett.*, **19**:11–13, 1971.

[46] J. Stone, C. A. Burrus, A. G. Dentai, and B. I. Miller. Single-crystal Nd: YAG fiber laser end-pumped CW with a light-emitting diode. *Opt. Commun.*, **18**:87–87, 1976.

[47] R. W. Cahn. The science of dirt. *Nature Mater.*, **1**:3–4, 2002.

[48] A. Y. Cho. Film Deposition by Molecular Beam Techniques. *J. Vacuum Science and Technol.*, **8**:S31–S38, 1971.

[49] A. Y. Cho and J. R. Arthur. Molecular beam epitaxy. *Prog. Solid State Chem.*, **10**:157–191, 1975.

[50] B. A. Joyce and C. T. Foxon. Growth and doping kinetics in molecular-beam epitaxy. *Japan. J. Appl. Phys.*, **16**:17–23, 1977.

[51] H. T. Grahn. *Semiconductor Superlattices – Growth and Electronic Properties.* World Scientific, Singapore, first edition, 1995.

[52] P. D. Dapkus. Metalorganic Chemical Vapor Deposition. *Annu. Rev. Materi. Sci.*, **12**:243–269, 1982.

[53] S. D. Hersee and J. P. Duchemin. Low-Pressure Chemical Vapor Deposition. *Annu. Rev. Materi. Sci.*, **12**:65–80, 1982.

[54] M. Theunissen, J. A. Appels, and W. Verkulyen. Application of preferential electrochemical etching of silicon to semiconductor device technology. *J. Electrochem. Soc.*, **117**:959–, 1970.

[55] G. Smolinsky, R. P. Chang, and T. M. Mayer. Plasma etching of III-V compound semiconductor materials and their oxides. *J. Vac. Sci. Technol.*, **18**:12–16, 1981.

[56] L. A. Nagahara, T. Thundat, and S. M. Lindsay. Nanolithography on semiconductor surfaces under an etching solution. *Appl. Phys. Lett.*, **57**:270–272, 1990.

[57] T. Ito and S. Okazaki. Pushing the limits of lithography. *Nature*, **406**:1027–1031, 2000.

[58] N. Chekurov, K. Grigoras, A. Peltonen, S. Franssila, and I. Tittonen. The fabrication of silicon nanostructures by local gallium implantation and cryogenic deep reactive ion etching. *Nanotechnology*, **20**:065307, 2009.

[59] S. J. Pearton. Ion implantation in III-V semiconductor technology. *Int. J. Mod. Phys. B*, **7**:4687–4761, 1993.

[60] J. S. Williams. Ion implantation of semiconductors. *Mater. Sci. Eng. A*, **253**:8–15, 1998.

[61] S. Reyntjens and R. Puers. A review of focused ion beam applications in microsystem technology. *J. Micromech. Microeng.*, **11**:287–300, 2001.

[62] A. A. Tseng. Recent developments in micromilling using focused ion beam technology. *J. Micromech. Microeng.*, **14**:R15–R34, 2004.

[63] R. J. Haüy. Les molécules intégrantes qui sont censées être les plus petits solides que l'on puisse extraire d'un minéral. in Observation sur la physique, 1782.

[64] A. M. Schönflies. *Kristallsysteme und Kristallstruktur*. Leipzig, first edition, 1891.

[65] M. A. Bravais. *On the Systems Formed by Points Regularly Distributed on a Plane or in Space*. Dover Publications, Mineola, New York, first edition, 2005. Translation by A. J. Shaler of the original *Mémoire sur les systèmes formés par des points distributés régulièrement sur un plan ou dans l'espace*, published in Paris in 1850 in *Journal de l'École Polytechnique, Cahier 33, Tome XIX, pages 1–128*.

[66] N. W. Ashcroft and D. N. Mermin. *Festkörperphysik*. Oldenbourg Verlag, München Wien, third edition, 2007.

[67] C. Kittel. *Einführung in die Festkörperphysik*. Oldenbourg Verlag, München Wien, 14th edition, 2005.

[68] F. Rossi. Coherent phenomena in semiconductors. *Semicond. Sci. Technol.*, **13**:147–168, 1998.

[69] H. Haug and S. W. Koch. *Quantum Theory of the Optical and Electronic Properties of Semiconductors*. World Scientific Publishing, Singapore, fifth edition, 2009.

[70] M. Kira, F. Jahnke, W. Hoyer, and S. W. Koch. Quantum theory of spontaneous emission and coherent effects in semiconductor microstructures. *Prog. Quantum Elec.*, 23:189–279, 1999.

[71] M. Kira and S. W. Koch. Many-body correlations and excitonic effects in semiconductor spectroscopy. *Prog. Quantum Elec.*, 30:155–296, 2006.

[72] T. Meier, P. Thomas, and S. W. Koch. *Coherent Semiconductor Optics – From Basic Concepts to Nanostructure Applications*. Springer, Berlin, first edition, 2006.

[73] W. Schäfer and M. Wegener. *Semiconductor optics and transport phenomena*. Springer, Berlin, first edition, 2002.

[74] K. H. Seeger. *Semiconductor Physics. An Introduction*. Springer, Berlin, seventh edition, 1999.

[75] E. L. Ivchenko. *Optical spectroscopy of semiconductor nanostructures*. Alpha Science International, Harrow, UK, 2005.

[76] M. Kira and S. W. Koch. Microscopic theory of optical excitations, photoluminescence, and therahertz response in semiconductors. *Eur. Phys. J. D*, 36:143–157, 2005.

[77] G. Khitrova, H. M. Gibbs, F. Jahnke, M. Kira, and S. W. Koch. Nonlinear optics of normal-mode-coupling in semiconductor microcavities. *Rev. Mod. Phys.*, 71:1591–1639, 1999.

[78] J. R. Danielson, Y.-S. Lee, J. P. Prineas, J. T. Steiner, M. Kira, and S. W. Koch. Interaction of Strong Single-Cycle Terahertz Pulses with Semiconductor Quantum Wells. *Phys. Rev. Lett.*, 99:237401, 2007.

[79] W. Hoyer, M. Kira, S. W. Koch, J. Hader, and J. V. Moloney. Coulomb effects on quantum-well luminescence spectra and radiative recombination times. *J. Opt. Soc. Am. B*, **24**:1344–1353, 2007.

[80] C. Lange, N. S. Köster, S. Chatterjee, H. Sigg, D. Chrastina, G. Isella, H. von Känel, M. Schäfer, M. Kira, and S. W. Koch. Ultrafast nonlinear optical response of photoexcited Ge/SiGe quantum wells: Evidence for a femtosecond transient population inversion. *Phys. Rev. B*, **79**:201306(R), 2009.

[81] G. Khitrova, H. M. Gibbs, M. Kira, and S. W. Koch ans A. Scherer. Vacuum Rabi splitting in semiconductors. *Nature Physics*, 2:81–90, 2006.

[82] L. Schneebeli, M. Kira, and S. W. Koch. Characterization of Strong Light-Matter Coupling in Semiconductor Quantum-Dot Microcavities via Photon-Statistics Spectroscopy. *Phys. Rev. Lett.*, **101**:097401, 2008.

[83] T. Ogawa and Y. Kanemitsu. *Optical properties of low-dimensional materials*. World Scientific, Singapore, first edition, 1995.

[84] B. Deveaud, F. Clérot, N. Roy, K. Satzke, B. Sermage, and D. S. Katzer. Enhanced radiative recombination of free excitons in GaAs quantum wells. *Phys. Rev. Lett.*, **67**:2355–2358, 1991.

[85] E. O. Göbel, H. Jung, J. Kuhl, and K. Ploog. Recombination Enhancement due to Carrier Localization in Quantum Well Structures. *Phys. Rev. Lett.*, **51**:1588–1591, 1983.

[86] J. Feldmann, G. Peter, E. O. Göbel, P. Dawson, K. Moore, C. Foxon, and R. J. Elliott. Linewidth dependence of radiative exciton lifetimes in quantum wells. *Phys. Rev. Lett.*, 59:2337–2340, 1987.

[87] D. A. B. Miller, D. S. Chemla, T. C. Damen, A. C. Gossard, W. Wiegmann, T. H. Wood, and C. A. Burrus. Electric field dependence of optical absorption near the band gap of quantum-well structures. *Phys. Rev. B*, **32**:1043–1060, 1985.

[88] S. Schmitt-Rink, D. S. Chemla, and D. A. B. Miller. Theory of transient excitonic optical nonlinearities in semiconductor quantum-well structures. *Phys. Rev. B*, **32**:6601–6609, 1985.

[89] D. S. Chemla and D. A. B. Miller. Room-temperature excitonic nonlinear-optical effects in semiconductor quantum-well structures. *J. Opt. Soc. Am. B*, **2**:1155–1173, 1985.

[90] S. Schmitt-Rink, C. Ell, and H. Haug. Many-body effects in the absorption, gain, and luminescence spectra of semiconductor quantum-well structures. *Phys. Rev. B*, **33**:1183–1189, 1986.

[91] T. Kuhn and F. Rossi. Analysis of coherent and incoherent phenomena in photo-excited semiconductors: A Monte Carlo approach. *Phys. Rev. Lett.*, **69**:977–980, 1992.

[92] F. Tassone, F. Bassani, and L. C. Andreani. Quantum-well reflectivity and exciton-polariton dispersion. *Phys. Rev. B*, **45**:6023–6030, 1992.

[93] E. L. Ivchenko, A. I. Nesvizhskii, and S. Jorda. Bragg reflection of light from quantum-well structures. *Phys. Solid State*, **36**:1156–1161, 1994.

[94] K.-C. Je, T. Meier, F. Rossi, and S. W. Koch. Theory of quasiequilibrium nonlinear optical absorption in semiconductor superlattices. *Appl. Phys. Lett.*, 67:2978–2980, 1995.

[95] M. Hübner, J. Kuhl, T. Stroucken, A. Knorr, S. W. Koch, R. Hey, and K. Ploog. Collective Effects of Excitons in Multiple-Quantum-Well Bragg and Anti-Bragg Structures. *Phys. Rev. Lett.*, **76**:4199–4202, 1996.

[96] S. Haacke, R. A. Taylor, R. Zimmermann, I. Bar-Joseph, and B. Deveaud. Resonant Femtosecond Emission from Quantum Well Excitons: The Role of Rayleigh Scattering and Luminescence. *Phys. Rev. Lett.*, **78**:2228–2231, 1997.

[97] G. R. Hayes, J. L. Staehli, U. Oesterle, B. Deveaud, R. T. Phillips, and C. Ciuti. Suppression of exciton-polariton light absorption in multiple quantum well Bragg structures. *Phys. Rev. Lett.*, **83**:2837–2840, 1999.

[98] G. Malpuech, A. Kavokin, W. Langbein, and J. M. Hvam. Resonant Rayleigh Scattering of Exciton-Polaritons in Multiple Quantum Wells. *Phys. Rev. Lett.*, **85**:650–653, 2000.

[99] S. Chatterjee, C. Ell, S. Mosor, G. Khitrova, H. M. Gibbs, W. Hoyer, M. Kira, S. W. Koch, J. P. Prineas, and H. Stolz. Excitonic Photoluminescence in Semiconductor Quantum Wells: Plasma versus Excitons. *Phys. Rev. Lett.*, **92**:067402, 2004.

[100] I. Kuznetsova, T. Meier, S. T. Cundiff, and P. Thomas. Determination of homogeneous and inhomogeneous broadening in semiconductor nanostructures by two-dimensional Fourier-transform optical spectroscopy. *Phys. Rev. B*, **76**:153301, 2007.

[101] M. Kira, F. Jahnke, and S. W. Koch. Microscopic Theory of Excitonic Signatures in Semiconductor Photoluminescence. *Phys. Rev. Lett.*, 81:3263–3266, 1998.

[102] M. Kira, F. Jahnke, and S. W. Koch. Quantum Theory of Secondary Emission in Optically Excited Semiconductor Quantum Wells. *Phys. Rev. Lett.*, 82:3544–3547, 1999.

[103] W. Hoyer, M. Kira, S. W. Koch, H. Stolz, S. Mosor, J. Sweet, C. Ell, G. Khitrova, and H. M. Gibbs. Entanglement between a Photon and a Quantum Well. *Phys. Rev. Lett.*, **93**:067401, 2004.

[104] F. Rossi and E. Molinari. Linear and nonlinear optical properties of realistic quantum-wire structures: The dominant role of Coulomb correlation. *Phys. Rev. B*, **53**:16462–16473, 1996.

[105] X.-L. Wang and V. Voliotis. Epitaxial growth and optical properties of semiconductor quantum wires. *J. Appl. Phys.*, **99**:121301, 2006.

[106] K.-D. Hof, C. Rossler, S. Manus, J. P. Kotthaus, A. W. Holleitner, D. Schuh, and W. Wegscheider. Dynamic photoconductive gain effect in shallow-etched AlGaAs/GaAs quantum wires. *Phys. Rev. B*, **78**:115325, 2008.

[107] Y. B. Yu. Effects of Electron-Phonon Interaction on Linear and Nonlinear Optical Absorption in Cylindrical Quantum Wires. *Commun. Theor. Phys.*, **49**:1615–1618, 2008.

[108] A. Wojs, P. Hawrylak, S. Fafard, and L. Jacak. Electronic structure and magneto-optics of self-assembled quantum dots. *Phys. Rev. B*, **54**:5604–5608, 1996.

[109] M. Brasken, M. Lindberg, D. Sundholm, and J. Olsen. Full configuration interaction calculations of electron-hole correlation effects in strain-induced quantum dots. *Phys. Rev. B*, **61**:7652–7655, 2000.

[110] O. I. Micic, J. R. Sprague, C. J. Curtis, K. M. Jones, J. L. Machol, A. J. Nozik, H. Giessen, B. Fluegel, G. Mohs, and N. Peyghambarian. Synthesis and Characterization of InP, GaP, and GaInP2 Quantum Dots. *J. Phys. Chem.*, **99**:7754–7759, 1995.

[111] J. P. Reithmaier, G. Sek, A. Loffler, C. Hofmann, S. Kuhn, S. Reitzenstein, L. V. Keldysh, V. D. Kulakovskii, T. L. Reinecke, and A. Forchel. Strong coupling in a single quantum dot-semiconductor microcavity system. *Nature*, **432**:197–200, 2004.

[112] T. Yoshie, A. Scherer, J. Hendrickson, G. Khitrova, H. M. Gibbs, G. Rupper, C. Ell, O. B. Shchekin, and D. G. Deppe. Vacuum Rabi splitting with a single quantum dot in a photonic crystal nanocavity. *Nature*, **432**:200–203, 2004.

[113] N. Baer, C. Gies, J. Wiersig, and F. Jahnke. Luminescence of a semiconductor quantum dot system. *Euro. Phys. J. B*, **50**:411–418, 2006.

[114] T. Feldtmann, L. Schneebeli, M. Kira, and S. W. Koch. Quantum theory of light emission from a semiconductor quantum dot. *Phys. Rev. B*, 73:155319, 2006.

[115] L. C. L. Y. Voon and M. Willatzen. *The k·p method: Electronic Properties of Semiconductors*. Springer, Berlin, first edition, 2009.

[116] E. Yablonovitch. Inhibited Spontaneous Emission in Solid-State Physics and Electronics. *Phys. Rev. Lett.*, **58**:2059–2062, 1987.

[117] S. John. Strong localization of photons in certain disordered dielectric superlattices. *Phys. Rev. Lett.*, **58**:2486–2489, 1987.

[118] D. Ammerlahn, B. Grote, S. W. Koch, J. Kuhl, M. Hubner, R. Hey, and K. Ploog. Influence of the dielectric environment on the radiative lifetime of quantum-well excitons. *Phys. Rev. B*, **61**:4801–4805, 2000.

[119] M. Kira, W. Hoyer, T. Stroucken, and S. W. Koch. Exciton Formation in Semiconductors and the Influence of a Photonic Environment. *Phys. Rev. Lett.*, 87:176401, 2001.

[120] M. Schafer, W. Hoyer, M. Kira, S.W. Koch, and J. V. Moloney. Influence of dielectric environment on quantum-well luminescence spectra. *J. Opt. Soc. Am.*, **B 25**:187–195, 2008.

[121] D. S. Chemla and J. Shah. Many-body and correlation effects in semiconductors. *Phys. Rev. Lett.*, **60**:1645–1648, 1988.

[122] S. M. Sze and K. N. G. Kwok. *Physics of semiconductor devices*. Wiley & Sons, 2006 edition, 2006.

[123] S. W. Koch and W. W. Chow. *Semiconductor Laser Fundamentals: Physics of the Gain Materials*. Springer, Berlin, first edition, 1999.

[124] W. W. Chow, S. W. Koch, and M. Sargent III. *Semiconductor-Laser Physics*. Springer, Berlin, first edition, 1994.

[125] K. C. Kao and G. A. Hockham. Dielectric fibre surface waveguides for optical frequencies. *Proc. IEEE*, **113**:1151–1158, 1966.

[126] T. R. Chen, W. Hsin, and N. Bar-Chaim. Very high power InGaAsP/InP distributed feedback lasers at 1550 nm wavelength. *Appl. Phys. Lett.*, **72**:1269–1271, 1998.

[127] B. Chen, W. Wang, X.-J. Wang, J.-Y. Zhang, and Z. Fan. A Novel 1.3-μm High T_0 AlGaInAs/InP Strained-Compensated Multi-Quantum Well Complex-Coupled Distributed Feedback Laser Diode. *Jpn. J. Appl. Phys.*, **38**:5096–5100, 1999.

[128] T. Kitatani, K. Nakahara, M. Kondow, K. Uomi, and T. Tanaka. A 1.3-μm GaInNAs/GaAs Single-Quantum-Well Laser Diode with a Hight Characteristic Temperature over 200 K. *Jpn. J. Appl. Phys.*, 39:L86–L87, 2000.

[129] O. Boyraz and B. Jalali. Demonstration of a silicon Raman laser. *Opt. Express*, **12**:5069–5273, 2004.

[130] H. Rong, A. Liu, R. Jones, O. Cohen, D. Hak, R. Nicolaescu, A. Fang, and M. Paniccia. An all-silicon Raman laser. *Nature*, **433**:292–294, 2005.

[131] H. Rong, R. Jones, A. Liu, O. Cohen, D. Hak, A. Fang, and M. Paniccia. A continuous-wave Raman silicon laser. *Nature*, **433**:725–728, 2005.

[132] S. G. Pavlov, U. Böttger, H.-W. Hübers, R. Kh. Zhukavin, K. A. Kovalevsky, V. V. Tsyplenkov, V. N. Shastin, N. V. Abrosimov, and H. Riemann. Low-threshold terahertz Si:As laser. *Appl. Phys. Lett.*, **90**:141109, 2007.

[133] X. Sun, J. Liu, L. C. Kimerling, and J. Michel. Direct gap photoluminescence of n-type tensile-strained Ge-on-Si. *Appl. Phys. Lett.*, **95**:011911, 2009.

[134] J. Liu, X. Sun, L. C. Kimerling, and J. Michel. Direct-gap optical gain of Ge on Si at room temperature. *Opt. Lett.*, **34**:1738–1740, 2009.

[135] H.-H. Chang, A. W. Fang, M. N. Sysak, H. Park, R. Jones, O. Cohen, O. Raday, M. J. Paniccia, and J. E. Bowers. 1310nm silicon evanescent laser. *Opt. Express*, **15**:11466–11471, 2007.

[136] B. R. Koch, A. W. Fang, O. Cohen, and J. E. Bowers. Mode-locked silicon evanescent lasers. *Opt. Express*, 15:11225–11233, 2007.

[137] M. N. Sysak, H. Park, A. W. Fang, J. E. Bowers, R. Jones, O. Cohen, O. Raday, and M. J. Paniccia. Experimental and theoretical thermal analysis of a Hybrid Silicon Evanescent Laser. *Opt. Express*, **15**:15041–15046, 2007.

[138] H. Yonezu. Control of structural defects in group III-V-N alloys grown on Si. *Semicond. Sci. Technol.*, **17**:762–768, 2002.

[139] I. Németh, B. Kunert, W. Stolz, and K. Volz. Heteroepitaxy of GaP on Si: Correlation of morphology, anti-phase domain structure and MOVPE growth conditions. *J. Crystal Growth*, **310**:1595–1601, 2008.

[140] B. Kunert, S. Reinhard, J. Koch, M. Lampalzer, K. Volz, and W. Stolz. First demonstration of electrical injection lasing in the novel dilute nitride Ga(NAsP)/GaP-material system. *Phys. Stat. Sol. c*, **3**:614–618, 2006.

[141] S. Borck, S. Chatterjee, B. Kunert, K. Volz, W. Stolz, J. Heber, W. W. Rühle, N. C. Gerhardt, and M. R. Hofmann. Lasing in optically pumped Ga(NAsP)/GaP heterostructures. *Appl. Phys. Lett.*, **89**:031102, 2006.

[142] B. Kunert, K. Volz, and W. Stolz. Dilute nitride Ga(NAsP)/GaP-heterostructures: toward a material development for novel optoelectronic functionality on Si-substrate. *Phys. Stat. Sol. b*, **244**:2730–2739, 2007.

[143] J. Chamings, A. R. Adams, S. J. Sweeney, B. Kunert, K. Volz, and W. W. Stolz. Temperature dependence and physical properties of Ga(NAsP)/GaP semiconductor lasers. *Appl. Phys. Lett.*, **93**:101108, 2008.

[144] S. John. Light control at will. *Nature*, **460**:337–337, 2009.

[145] K. Ishizaki and S. Noda. Manipulation of photons at the surface of three-dimensional photonic crystals. *Nature*, **460**:367–370, 2009.

[146] A. Ledermann, L. Cademartiri, M. Hermatschweiler, C. Toninelli, G. A. Ozin, D. S. Wiersma, M. Wegener, and G. von Freymann. Tree-dimensional silicon inverse photonic quasicrystals for infrared wavelengths. *Nature Mater.*, 5:942–945, 2006.

[147] V. R. Almeida, C. A. Barrios, R. R. Panepucci, and M. Lipson. All-optical control of light on a silicon chip. *Nature*, **431**:1081–1084, 2004.

[148] M. Soljačić, C. Luo, J. D. Joannopoulos, and S. Fan. Nonlinear photonic crystal microdevices for optical integration. *Opt. Lett.*, **28**:637–639, 2004.

[149] T. F. Krauss. Planar photonic crystal waveguide devices for integrated optics. *Phys, Stat. Sol. a*, 197:688–702, 2003.

[150] M. Tokushima, H. Kosaka, A. Tomita, and H. Yamada. Lightwave propagation through a 120° sharply bent single-line-defect photonic crystal waveguide. *Appl. Phys. Lett.*, **76**:952–954, 2000.

[151] J. C. Knight, J. Broeng, T. A. Birks, and P. St. J. Russell. Photonic Band Gap Guidance in Optical Fibers. *Science*, 282:1476–1478, 1998.

[152] J. D. Joannopoulos, P. R. Villeneuve, and S. Fan. Photonic crystals: putting a new twist on light. *Nature*, **386**:143–149, 1997.

[153] P. S. Peercy. The drive to miniaturization. *Nature*, **406**:1023–1026, 2000.

[154] B. Jalali. Can silicon change photonics? *Phys. Stat. Sol. a*, 205:213–224, 2008.

[155] W. Friedrich, P. Knipping, and M. Laue. Interferenzerscheinungen bei Röntgenstrahlen. *Ann. d. Phys.*, 41:971–988, 1913.

[156] P. Debye and P. Scherrer. Interference on inordinate orientated particles in roentgen light. *Physikalische Zeitschrift*, 17:277, 1916.

[157] W. L. Bragg. The diffraction of short electromagnetic waves by a crystal. *Proc. Camb. Phil. Soc.*, **17**:43–57, 1913.

[158] W. L. Bragg. The Structure of Some Crystals as Indicated by Their Diffraction of X-rays. *Proc. Roy. Soc. Lond.*, **A89**:248–277, 1913.

[159] W. H. Bragg and W. L. Bragg. The Structure of the Diamond. *Proc. Roy. Soc. Lond.*, **A89**:277–291, 1913.

[160] P. P. Ewald. Zur Begründung der Kristalloptik; Teil III: Die Kristalloptik der Röntgenstrahlen. *Ann. Phys.*, **54**:519–556, 1917.

[161] D. Shechtman, I. Blech, D. Gratias, and J. W. Cahn. Metallic Phase with Long-Range Orientational Order and No Translational Symmetry. *Phys. Rev. Lett.*, **53**:1951, 1984.

[162] D. Levine and P. J. Steinhardt. Quasicrystals: A New Class of Ordered Structures. *Phys. Rev. Lett.*, 53:2477–2480, 1984.

[163] C. Janot. *Quasicrystals. A Primer*. Clarendon Press, Oxford, UK, second edition, 1994.

[164] D. Levine and P. J. Steinhardt. Quasicrystals. I. Definition and structure. *Phys. Rev. B*, **34**:596–616, 1986.

[165] R. Lifshitz. Quasicrystals: A Matter of Definition. *Foundations of Physics*, **33**:1703–1711, 2003.

[166] L. Pauling. Apparent icosahedral symmetry is due to directed multiple twinning of cubic crystals. *Nature*, **317**:512–514, 1985.

[167] L. Pauling. Icosahedral Symmetry. *Science*, **239**:963–963, 1988.

[168] J. W. Cahn, D. Gratias, and D. Shechtman. Pauling's model not universally accepted. *Nature*, **319**:102–103, 1986.

[169] A. L. Mackay. Pauling's model not universally accepted. *Nature*, **319**:103–104, 1986.

[170] P. A. Bancel, P. A. Heiney, P. W. Stephens, and A. I. Goldman. Pauling's model not universally accepted. *Nature*, **319**:104–104, 1986.

[171] A. A. Berezin. Pauling's model not universally accepted. *Nature*, **319**:104–104, 1986.

[172] P. J. Steinhardt. Icosahedral Solids: A New Phase of Matter? *Science*, **238**:1242–1247, 1987.

[173] P. J. Steinhardt. Response: Icosahedral Symmetry. *Science*, **239**:963–964, 1988.

[174] International Union of Crystallography. Report of the executive committee for 1991. *Acta. Cryst. A*, **48**:922–946, see p. 928, 1992.

[175] N. D. Mermin. Copernican Crystallography. *Phys. Rev. Lett.*, **68**:1172–1175, 1992.

[176] R. Lifshitz. What is a crystal? *Z. Kristallogr.*, **222**:313–317, 2007.

[177] L. Bindi, P. J. Steinhardt, N. Yao, and P. J. Lu. Natural Quasicrystals. *Science*, **324**:1306–1309, 2009.

[178] B. Dubost, J.-M. Lang, M. Tanaka, P. Sainfort, and M. Audier. Large AlCuLi single quasicrystals with triacontahedral solidification morphology. *Nature*, **324**:48–50, 1986.

[179] A.-P. Tsai, A. Inoue, and T. Masumoto. A Stable Quasicrystal in Al-Cu-Fe System. *Jpn. J. Appl. Phys.*, **26**:L1505–L1507, 1987.

[180] A.-P. Tsai, A. Inoue, and T. Masumoto. New quasicrystals in $Al_{65}Cu_{20}M_{15}$ (M = Cr, Mn or Fe) systems prepared by rapid solidification. *J. Mater. Sci. Lett.*, **7**:322–326, 1988.

[181] L. X. He, Y. K. Wu, and K. H. Kuo. Decagonal quasicrystals with different periodicities along the tenfold axis in rapidly solidified $Al_{65}Cu_{20}M_{15}$ (M=Mn, Fe, Co or Ni). *J. Mater. Sci. Lett.*, **7**:1284–1286, 1988.

[182] A. R. Kortan, F. A. Thiel, H. S. Chen, A. P. Tsai, A. Inoue, and T. Masumoto. Stable tenfold faceted single-grain decagonal quasicrystals of $Al_{65}Cu_{15}Co_{20}$. *Phys. Rev. B*, 40:9397–9399, 1989.

[183] P. Villars, J. C. Phillips, and H. S. Chen. Icosahedral Quasicrystals and Quantum Structural Diagrams. *Phys. Rev. Lett.*, **57**:3085–3088, 1986.

[184] W. Ohashi and F. Spaepen. Stable Ga-Mg-Zn quasi-periodic crystals with pentagonal dedecahedral solidification morphology. *Nature*, **330**:555–556, 1987.

[185] A.-P. Tsai, A. Niikura, A. Inoue, and T. Masumoto. Highly Ordered Structure of Icosahedral Quasi-Crystals in Zn-Mg-RE (RE-Equivalent-to-Rare Earth Metals) Systems . *Phil. Mag. Lett.*, **70**:169–175, 1994.

[186] T. Ishimasa, H.-U. Nissen, and Y. Fukano. New Ordered State Between Crystalline and Amorphous in Ni-Cr Particles. *Phys. Rev. Lett.*, **55**:511–513, 1985.

[187] A.-P. Tsai. "Back to the future An account discovery of stable quasicrystals. *Acc. Chem. Res.*, **36**:31–38, 2003.

[188] J.-M. Dubois. *Useful Quasicrystals*. World Scientific, Singapore, first edition, 2005.

[189] Z. M. Stadnik. *Physical Properties of Quasicrystals*. Springer, Berlin, first edition, 1999.

[190] Y. Fu, L. Ana, F. Zhoua, Y. Zhaoa, D. Yanga, and Y. Gao. AlCuCr quasicrystalline coatings prepared by low power plasma spraying. *Surf. Coat. Technol.*, 202:4964–4970, 2008.

[191] J. Zhang, L. Peia, H. Dua, W. Lianga, C. Xua, and B. Lu. Effect of Mg-based spherical quasicrystals on microstructure and mechanical properties of AZ91 alloys. *J. Alloys Compd.*, **453**:309–315, 2008.

[192] S. J. Poon. Electronic properties of quasicrystals an experimental review. *Adv. Phys.*, **41**:303–363, 1992.

[193] K. Kimura and S. Takeuchi. Experimental Studies of Electronic Transport in Quasicrystals. In Ref. [227], pages 325–359.

[194] T. Klein and O. G. Symko. Formation of AlCuFe quasicrystalline thin films by solid state diffusion. *Appl. Phys. Lett.*, **64**:431–433, 1994.

[195] J. Y. Park, D. F. Ogletree, M. Salmeron, R. A. Ribeiro, P. C. Canfield, C. J. Jenks, and P. A. Thiel. High Frictional Anisotropy of Periodic and Aperiodic Directions on a Quasicrystal Surface. *Science*, **309**:1354–1356, 2005.

[196] J. Y. Park, D. F. Ogletree, M. Salmeron, R. A. Ribeiro, P. C. Canfield, C. J. Jenks, and P. A. Thiel. Tribological properties of quasicrystals: Effect of aperiodic versus periodic surface order. *Phys. Rev. B*, **74**:024203, 2006.

[197] J. Y. Park, D. F. Ogletree, M. Salmeron, R. A. Ribeiro, P. C. Canfield, C. J. Jenks, and P. A. Thiel. Adhesion properties of decagonal quasicrystals in ultrahigh vacuum. *Phil Mag.*, **86**:945–950, 2006.

[198] R. D. Diehl, W. Setyawan, and S. Curtarolo. Gas adsorption on quasicrystalline surfaces. *J. Phys.: Condens. Matter*, 20:314007, 2008.

[199] D. Rouxel and P. Pigeat. Surface oxidation and thin film preparation of AlCuFe quasicrystals. *Prog. Surf. Sci.*, **81**:488–514, 2006.

[200] D. Popovic, D. Naumovic, M. Bovet, C. Koitzsch, L. Schlapbach, and P. Aebi. Oxidation of AlPdMn quasicrystal surfaces . *Surf. Sci.*, **492**:294–304, 2001.

[201] D. J. Sordelet, S. D. Widener, Y. Tang, and M. F. Besser. Characterization of a commercially produced Al-Cu-Fe-Cr quasicrystalline coating. *Mater. Sci. Eng. A*, **294–296**:834–837, 2000.

[202] A.-P. Tsai and M. Yoshimura. Highly active quasicrystalline Al-Cu-Fe catalyst for steam reforming of methanol. *Appl. Catal. A*, **214**:237–241, 2001.

[203] Y. S. Chan, C. T. Chan, and Z. Y. Liu. Photonic Band Gaps in Two Dimensional Photonic Quasicrystals. *Phys. Rev. Lett.*, **80**:956–959, 1998.

[204] M. Hase, M. Egashira, N. Shinya, H. Miyazaki, K. M. Kojima, and S. Uchida. Optical transmission spectra of two-dimensional quasiperiodic photonic crystals based on Penrose-tiling and octagonal-tiling systems. *J. Alloys Comp.*, **342**:455–459, 2002.

[205] J. Feng, X. Zhang, Y. Wang, Z. Y. Li, B. Cheng, and D.-Z. Zhang. Negative refraction and imaging using 12-fold-symmetry quasicrystals. *Phys. Rev. Lett.*, 94:247402, 2005.

[206] S. He and J. D. Maynard. Eigenvalue Spectrum, Density of States, and Eigenfunctions in a Two-Dimensional Quasicrystal. *Phys. Rev. Lett.*, **62**:1888–1891, 1989.

[207] K. J. Franke, H. R. Sharma, W. Theis, P. Gille, Ph. Ebert, and K. H. Rieder. Quasicrystalline Epitaxial Single Element Monolayers on Icosahedral Al-Pd-Mn and Decagonal Al-Ni-Co Quasicrystal Surfaces. *Phys. Rev. Lett.*, **89**:156104, 2002.

[208] J. Ledieu, J. T. Hoeft, D. E. Reid, J. A.Smerdon, R. D. Diehl, T. A. Lograsso, A. R. Ross, and R. McGrath. Pseudomorphic Growth of a Single Element Quasiperiodic Ultrathin Film on a Quasicrystalline Substrate. *Phys. Rev. Lett.*, 92:135507, 2004.

[209] H. R. Sharma, M. Shimoda, A. R. Ross, T. A. Lograsso, and A. P. Tsai. Real-space observation of quasicrystalline Sn monolayer formed on the fivefold surface of icosahedral Al-Cu-Fe quasicrystal. *Phys. Rev. B*, **72**:045428, 2005.

[210] M. M. Burns, J. M. Fournier, and J. A. Golovchenko. Optical Matter: Crystallization and Binding in Intense Optical Fields. *Science*, **249**:749–754, 1990.

[211] L. Guidoni, C. Triché, P. Verkerk, and G. Grynberg. Quasiperiodic Optical Lattice. *Phys. Rev. Lett.*, **79**:3363–3366, 1997.

[212] B. Freedman, G. Bartal, M. Segev, R. Lifshitz, D. N. Christodoulides, and J. W. Fleischer. Wave and defect dynamics in nonlinear photonic quasicrystals. *Nature*, **440**:1166–1169, 2006.

[213] J. Mikhael, J. Roth, L. Helden, and C. Bechinger. Archimedean-like tiling on decagonal quasicrystalline surfaces. *Nature*, **454**:501–504, 2008.

[214] S. C. Glotzer and A. S. Keys. A tale of two tilings. *Nature*, **454**:420–421, 2008.

[215] M. Schmiedeberg and H. Stark. Colloidal Ordering on a 2D Quasicrystalline Substrate. *Phys. Rev. Lett.*, **101**:218302, 2008.

[216] K. Hayashida, T. Dotera, A. Takano, and Y. Matsushita. Polimeric Quasicrystal: Mesoscopic Quasicrystalline Tiling in ABC Star Polymers. *Phys. Rev. Lett.*, **98**:195502, 2007.

[217] A. Behrooz, M. J. Burns, H. Deckmann, D. Levine, B. Whitehead, and P. M. Chaikin. Flux Quantization on Quasicrystalline Networks. *Phys. Rev. Lett.*, **57**:368–371, 1986.

[218] W. Man, M. Megens, P. J. Steinhardt, and P. M. Chaikin. Experimental measurement of the photonic properties of icosahedral quasicrystals. *Nature*, **436**:993–996, 2005.

[219] P. Kramer and R. Neri. On Periodic and Non-periodic Space Fillings of E^m Obtained by Projection. *Acta cryst. A*, 40:580–587, 1984.

[220] R. K. P. Zia and W. J. Dallas. A simple derivation of quasi-crystalline spectra. *J. Phys. A: Math. Gen*, **18**:L341–L345, 1985.

[221] M. Duneau and A. Katz. Quasiperiodic Patterns. *Phys. Rev. Lett.*, **54**:2688–2691, 1985.

[222] V. Elser. The Diffraction Pattern of Projected Structures. *Acta. Cryst. A*, **42**:36–43, 1986.

[223] M. Holzer. Three classes of one-dimensional, two-tile Penrose tilings and the Fibonacci Kronig-Penney model as a generic case. *Phys. Rev. B*, **38**:1709–1720, 1988.

[224] R. Penrose. Pentaplexity. *Bull. Inst. Math. Appl.*, **10**:266–271, 1974.

[225] M. Gardner. Extraordinary nonperiodic tiling that enriches the theory of tiles. *Sci Amer.*, **236**:110–121, 1977.

[226] J. E. S. Socolar, P. J. Steinhardt, and D. Levine. Quasicrystals with arbitrary orientational symmetry. *Phys. Rev. B*, **32**:5547–5550, 1985.

[227] D. P. Di Vincenzo and P. J. Steinhardt. *Quasicrystals – The State of the Art*. World Scientific, Singapore, second edition, 1999.

[228] M. Senechal. *Quasicrystals and geometry*. Cambridge University Press, Cambridge, third edition, 2009.

[229] P. A. Thiel. Quasicrystal surfaces. *Annu. Rev. Phys. Chem.*, **59**:129–152, 2008.

[230] Ph. Ebert, K.-J. Chao, Q. Niu, and C. K. Shih. Dislocations, Phason Defects, and Domain Walls in a One-Dimensional Quasiperiodic Superstructure of a Metallic Thin Film. *Phys. Rev. Lett.*, **83**:3222–3225, 1999.

[231] P. J. Lu and P. J. Steinhardt. Decagonal and Quasi-Crystalline Tilings in Medieval Islamic Architecture. *Science*, **315**:1106–1110, 2007.

[232] A. Beutelspacher and B. Petri. *Der Goldene Schnitt*. Spektrum Akademischer Verlag, Heidelberg, second edition, 1996.

[233] R. Merlin, K. Bajema, R. Clarke, F. Y. Juang, and P. K. Bhattacharya. Quasiperiodic GaAs-AlAs Heterostructures. *Phys. Rev. Lett.*, **55**:1768–1770, 1985.

[234] J. Todd, R. Merlin, R. Clarke, K. M. Mohanty, and J. D. Axe. Synchroton X-Ray Study of a Fibonacci Superlattice. *Phys. Rev. Lett.*, **57**:1157, 1986.

[235] F. Nori and J. P. Rodriguez. Acoustic and electronic properties of one-dimensional quasicrystals. *Phys. Rev. B*, **34**:2207–2211, 1986.

[236] Y. Y. Zhu, N. B. Ming, and W. H. Jiang. Ultrasonic spectrum in Fibonacci acoustic superlattices. *Phys. Rev. B*, **40**:8536–8540, 1989.

[237] K. Kono, S. Nakada, Y. Narahara, and Y. Ootuko. Transmission spectra of 3rd sound in a Fibonacci lattice. *J. Phys. Soc. Jpn.*, 60:368–371, 1991.

[238] M. Kohmoto, B. Sutherland, and K. Iguchi. Localization of optics: Quasiperiodic media. *Phys. Rev. Lett.*, **58**:2436–2438, 1987.

[239] H. Miyazaki and M. Inoue. Theory of Self-Similarity in the Reflectivity Spectrum of a Fibonacci Superlattice. *Solid State Commun.*, **72**:241–244, 1989.

[240] X. Huang, Y. Wang, and C. Gong. Numerical investigation of light-wave localization in optical Fibonacci superlattices with symmetric internal structure. *J. Phys.: Condens. Matter*, **11**:7645–7651, 1999.

[241] W. Gellermann, M. Kohmoto, B. Sutherland, and P. C. Taylor. Localization of light waves in Fibonacci dielectric multilayers. *Phys. Rev. Lett.*, **72**:633–636, 1994.

[242] L. Chow and K. H. Guenther. Critical field patterns in optical Fibonacci multilayers. *J. Opt. Soc. Am. A*, **10**:2231–2235, 1993.

[243] T. Hattori, N. Tsurumachi, S. Kawato, and H. Nakatsuka. Photonic dispersion relation in a one-dimensional quasicrystal. *Phys. Rev. B*, **50**:4220–4223, 1994.

[244] Y. Y. Zhu and N. B. Ming. Second-harmonic generation in a Fibonacci optical superlattice and the dispersive effect of refractive index. *Science*, **42**:3676–3679, 1990.

[245] J. Feng, Y. Y. Zhu, and N. B. Ming. Harmonic generations in an optical fibonacci superlattice. *Phys. Rev. B*, 41:5578–5582, 1990.

[246] S. N. Zhu, Y. Y. Zhu, and N. B. Ming. Quasi-Phase-Matched Third-Harmonic Generation in a Quasi-Periodic Optical Superlattice. *Science*, **278**:843–846, 1997.

[247] J. A. Armstrong, N. Bloembergen, J. Ducuing, and P. S. Pershan. Interactions between Light Waves in a Nonlinear Dielectric. *Phys. Rev.*, **127**:1918–1939, 1962.

[248] R. W. Peng, X. Q. Huang, F. Qiu amd M. Wang, A. Hu, S. S. Jiang, and M. Mazzer. Symmetry-induced perfect transmission of light waves in quasiperiodic dielectric multilayers. *Appl. Phys. Lett.*, **80**:3063–3065, 2002.

[249] L. Dal Negro1, C. J. Oton, Z. Gaburro, L. Pavesi, P. Johnson, A. Lagendijk, R. Righini, M. Colocci, and D. S. Wiersma. Light Transport through the Band-Edge States of Fibonacci Quasicrystals. *Phys. Rev. Lett.*, 90:055501, 2003.

[250] A. N. Poddubny, L. Pilozzi, M. M. Voronov, and E. L. Ivchenko. Resonant Fibonacci quantum well structures in one dimension. *Phys. Rev. B*, **77**:113306, 2008.

[251] B. C. Richards, J. Hendrickson, J. Sweet, G. Khitrova, D. Litvinov, D. Gerthsen, B. Myer, S. Pau, D. Sarid, M. Wegener, E. L. Ivchenko, A. N. Poddubny, and H. M. Gibbs. Attempts to grow optically coupled Fibonacci-spaced InGaAs/GaAs quantum wells result in surface gratings. *Opt. Express*, **16**:21512–21521, 2008.

[252] J. Hendrickson, B. C. Richards, J. Sweet, G. Khitrova, A. N. Poddubny, E. L. Ivchenko, M. Wegener, and H. M. Gibbs. Excitonic polaritons in Fibonacci quasicrystals. *Opt. Express*, **16**:15382–15387, 2008.

[253] M. Schäfer, M. Werchner, W. Hoyer, M. Kira, and S.W. Koch. Quantum Theory of Luminescenence in Multiple-Quantum-Well Bragg structures. *Phys. Rev. B*, **74**:166315, 2006.

[254] T. Rappen, G. Mohs, and M. Wegener. Polariton dynamics in quantum wells studied by femtosecond four-wave mixing. *Phys. Rev. B*, **47**:9658–9662, 1993.

[255] T. Stroucken, A. Knorr, C. Anthony, A. Schulze, P. Thomas, S. W. Koch, M. Koch, S. T. Cundiff, J. Feldmann, and E. O. Göbel. Light Propagation and Disorder Effects in Semiconductor Multiple Quantum Wells. *Phys. Rev. Lett.*, **74**:2391–2394, 1995.

[256] E. O. Göbel, K. Leo, T. C. Damen, J. Shah, S. Schmitt-Rink, W.Schäfer, J. F. Müller, and K. Köhler. Quantum Beats of Excitons in Quantum Wells. *Phys. Rev. Lett.*, **64**:1801–1804, 1990.

[257] T. Stroucken, A. Knorr, P. Thomas, and S. W. Koch. Coherent dynamics of radiatively coupled quantum-well excitons. *Phys. Rev. B*, **53**:2026–2033, 1996.

[258] S. T. Cundiff, A. Knorr, J. Feldmann, S. W. Koch, E. O. Göbel, and H. Nickel. Rabi Flopping in Semiconductors. *Phys. Rev. Lett.*, **73**:1178–1181, 1994.

[259] A. Mysyrowicz, D. Hulin, A. Antonetti, A. Migus, W. T. Masselink, and H. Morkoc. "Dressed Excitonsïn a Multiple-Quantum-Well Structure: Evidence for an Optical Stark Effect with Femtosecond Response Time. *Phys. Rev. Lett.*, **56**:2748–2751, 1986.

[260] S. Schmitt-Rink and D. S. Chemla. Collective Excitations and the Dynamical Stark Effect in a Coherently Driven Exciton System. *Phys. Rev. Lett.*, **57**:2752–2755, 1986.

[261] D. Fröhlich, R. Wille, W. Schlapp, and G. Weimann. Optical Quantum-Confined Stark Effect in GaAs Quantum Wells. *Phys. Rev. Lett.*, **59**:1748–1751, 1987.

[262] N. Peyghambarian, H. M. Gibbs, J. L. Jewell, A. Antonetti, A. Migus, D. Hulin, and A. Mysyrowicz. Blue Shift of the Exciton Resonance due to Exciton-Exciton Interactions in a Multiple-Quantum-Well Structure. *Phys. Rev. Lett.*, **53**:2433–2436, 1984.

[263] Y. H. Lee, A. Chavez-Pirson, S. W. Koch, H. M. Gibbs, S. H. Park, J. Morhange, A. Jeffery, N. Peyghambarian, L. Banyai, A. C. Gossard, and W. Wiegmann. Room-Temperature Optical Nonlinearities in GaAs. *Phys. Rev. Lett.*, 57:2446–2449, 1986.

[264] R. Binder, S. W. Koch, M. Lindberg, and N. Peyghambarian. Ultrafast Adiabatic Following in Semiconductors. *Phys. Rev. Lett.*, **65**:899–902, 1990.

[265] D. Hulin, A. Mysyrowicz, A. Antonetti, A. Migus, W. T. Masselink, H. Morkoc, H. M. Gibbs, and N. Peyghambarian. Well-size dependence of exciton blue shift in GaAs multiple-quantum-well structures. *Phys. Rev. B*, **33**:4389–4391, 1986.

[266] M. D. Webb, S. T. Cundiff, and D. G. Steel. Observation of time-resolved picosecond stimulated photon echoes and free polarization decay in GaAs/AlGaAs multiple quantum wells. *Phys. Rev. Lett.*, **66**:934–937, 1991.

[267] A. Schülzgen, R. Binder, M. E. Donovan, M. Lindberg, K. Wundke, H. M. Gibbs, G. Khitrova, and N. Peyghambarian. Direct Observation of Excitonic Rabi Oscillations in Semiconductors. *Phys. Rev. Lett.*, **82**:2346–2349, 1999.

[268] T. Shih, K. Reimann, M. Woerner, T. Elsaesser, I. Waldmüller, A. Knorr, R. Hey, and K. H. Ploog. Nonlinear response of radiatively coupled intersubband transitions of quasi-two-dimensional electrons. *Phys. Rev. B*, **72**:195338, 2005.

[269] I. Waldmueller, W. W. Chow, and A. Knorr. Influence of radiative coupling on coherent Rabi intersubband oscillations in multiple quantum wells. *Phys. Rev. B*, **73**:035433, 2006.

[270] E. L. Ivchenko, M. M. Voronov, M. V. Erementchouk, L. I. Deych, and A. A. Lisyansky. Multiple-quantum-well-based photonic crystals with simple and compound elementary supercells. *Phys. Rev. B*, **70**:195106, 2004.

[271] D. S. Citrin. Exciton radiative decay and polaritons in multiquantum wells: quantum-well-to-superlattice crossover. *Solid State Commun.*, **89**:139–143, 1994.

[272] L. C. Andreani. Polaritons in Multiple Quantum Wells. *Phys. Stat. Sol. b*, **188**:29–42, 1995.

[273] M. Hübner, J. P. Prineas, C. Ell, P. Brick, E. S. Lee, G. Khitrova, H. M. Gibbs, and S. W. Koch. Optical Lattices Achieved by Excitons in Periodic Quantum Well Structures. *Phys. Rev. Lett.*, **83**:2841–2844, 1999.

[274] M. Hübner, J. Kuhl, T. Stroucken, A. Knorr, S. W. Koch, R. Hey, and K. Ploog. Collective Effects of Excitons in Multiple-Quantum-Well Bragg and Anti-Bragg Structures. *Phys. Rev. Lett.*, **76**:4199–4202, 1996.

[275] S. Haas T. Stroucken, M. Hübner, J. Kuhl, B. Grote, A. Knorr, F. Jahnke, S. W. Koch, R. Hey, and K. Ploog. Intensity dependence of superradiant emission from radiatively coupled excitons in multiple-quantum-well Bragg structures. *Phys. Rev. B*, **57**:14860–14868, 1998.

[276] C. Sieh, T. Meier, F. Jahnke, A. Knorr, S. W. Koch, P. Brick, M. Hübner, C. Ell, J. Prineas, G. Khitrova, and H. M. Gibbs. Coulomb Memory Signaturees in the Excitonic Optical Stark Effect. *Phys. Rev. Lett.*, **82**:3112–3115, 1999.

[277] D. Golde, M. Wagner, D. Stehr, H. Schneider, M. Helm, A. M. andrews, T. Roch, G. Strasser, M.'Kira, and S. W. Koch. Fano Signatures in the Intersubband Terahertz Response of Optically Excited Semiconductor Quantum Wells. *Phys. Rev. Lett.*, **102**:127403, 2009.

[278] C. W. Luo, K. Reimann, M. Woerner, T. Elsaesser, R. Hey, and K. H. Ploog. Phase-Resolved Nonlinear Response of a Two-Dimensional Electron Gas under Femtosecond Intersubband Excitation. *Phys. Rev. Lett.*, **92**:047402, 2004.

[279] R. Huber, F. Tauser, A. Brodschelm, M. Bichler, G. Abstreiter, and A. Leitenstorfer. How many-particle interactions develop after ultrafast excitation of an electronhole plasma. *Nature*, **414**:286–289, 1986.

[280] I. Galbraith, R. Chari, S. Pellegrini, P. J. Phillips, C. J. Dent, A. F. G. van der Meer, D. G. Clarke, A. K. Kar, G. S. Buller, C. R. Pidgeon, B. N. Murdin, J. Allam, and G. Strasser. Excitonic signatures in the photoluminescence and terahertz absorption of a $GaAsAl_xGa_{1x}As$ multiple quantum well. *Phys. Rev. B*, **71**:073302, 2005.

[281] A. Bonvalet, J. Nagle, V. Berger, A. Migus, J.-L. Martin, and M. Joffre. Femtosecond Infrared Emission Resulting from Coherent Charge Oscillations in Quantum Wells. *Phys. Rev. Lett.*, **76**:4392–4395, 1996.

[282] V. Savona andL. C. Andreani, P. Schwendimann, and A. Quattropani. Quantum well excitons in semiconductor microcavities: Unified treatment of weak and strong coupling regimes. *Solid State Commun.*, **93**:733–739, 1995.

[283] E. L. Ivchenko, M. A. Kaliteevski, A. V. Kavokin, and A. I. Nesvizhskii. Reflection and absorption spectra from microcavities with resonant Bragg quantum wells. *J. Opt. Soc. Am. B*, **13**:1061–1068, 1996.

[284] C. Weisbuch, M. Nishioka, A. Ishikawa, and Y. Arakawa. Observation of the Coupled Exciton-Photon Mode Splitting in a Semiconductor Quantum Microcavity. *Phys. Rev. Lett.*, **69**:3314–3317, 1992.

[285] J.-K. Rhee, D. S. Citrin, T. B. Norris, Y. Arakawa, and M. Nishioka. Femtosecond dynamics of semiconductor-microcavity polaritons in the nonlinear regime. *Solid State Commun.*, **97**:941–946, 1996.

[286] F. Jahnke, M. Kira, S. W. Koch, G. Khitrova, E. K. Lindmark, T. R. Nelson, D. V. Wick, J. D. Berger, O. Lyngnes, and H. M. Gibbs. Excitonic nonlinearities of semiconductor microcavities in the nonperturbative regime. *Phys. Rev. Lett.*, 77:5257–5260, 1996.

[287] T. B. Norris, J.-K. Rhee, C.-Y. Sung, Y. Arakawa, M. Nishioka, and C. Weisbuch. Time-resolved vacuum Rabi oscillations in a semiconductor quantum microcavity. *Phys. Rev. B*, **50**:14663–14666, 1994.

[288] O. Lyngnes, J. D. Berger, J. P. Prineas, S. Park, G. Khitrova, H. M. Gibbs, F. Jahnke, M. Kira, and S. W. Koch. Nonlinear emission dynamics from semiconductor microcavities in the nonperturbative regime. *Solid State Commun.*, **104**:297–300, 1997.

[289] C. Ell, J. Prineas, T. R. Nelson Jr., S. Park, H. M. Gibbs, G. Khitrova, S. W. Koch, and R. Houdré. Influence of Structural Disorder and Light Coupling on the Excitonic Response of Semiconductor Microcavities. *Phys. Rev. Lett.*, **80**:4795–4798, 1998.

[290] M. Werchner, M. Schafer, M. Kira, S. W. Koch, J. Sweet, J. D. Olitzky, J. Hendrickson, B. C. Richards, G. Khitrova, H. M. Gibbs, A. N. Poddubny, E. L. Ivchenko,

M. Voronov, and M. Wegener. One dimensional resonant Fibonacci quasicrystals: noncanonical linear and canonical nonlinear effects. *Opt. Express*, **17**:6813–6828, 2009.

[291] Leonardo da Pisa (called Fibonacci). *Liber Abaci*. historic, 1202.

[292] J. E. S. Socolar and P. J. Steinhardt. Quasicrystals. II. Unit-cell configurations. *Phys. Rev. B*, **34**:617–647, 1986.

[293] M. Y. Azbel. Energy spectrum of a conduction electron in a magnetic field. *Sov. Phys. JETP*, **19**:634, 1964.

[294] M. Y. Azbel. Quantum Particle in One-Dimensional Potentials with Incommensurate Periods. *Phys. Rev. Lett.*, **43**:1954–1957, 1979.

[295] J. M. Luck, C. Godreche, A. Janner, and T. Janssen. The nature of the atomic surfaces of quasiperiodic self-similar structures. *J. Phys. A*, **26**:1951–1999, 1993.

[296] The investigated samples have been grown by and the experiments have been performed in the group of Prof. H. M. Gibbs and Prof. G. Khitrova at the College of Optical Sciences, The University of Arizona, Tucson.

[297] G. Bastard. *Wave mechanics applied to semiconductor heterostructures*. Monographies de physique. Les éditions de physique, Les Ulis, first edition, 1988.

[298] F. Jahnke, M. Kira, and S. W. Koch. Linear and nonlinear optical properties of excitons in semiconductor quantum wells and microcavities. *Z. Phys. B*, 104:559–572, 1997.

[299] J. Čížek. On the Correlation Problem in Atomic and Molecular Systems. Calculation of Wavefunction Components in Ursell-Type Expansion Using Quantum-Field Theoretical Methods. *J. Chem. Phys.*, **45**:4256–4266, 1966.

[300] F. E. Harris, H. J. Monkhorst, and D. L. Freeman. *Algebraic and Diagrammatic Methods in Many-Fermion Theory*. Oxford University Press, New York, first edition, 1992.

[301] J. Paldus, J. Čížek, and I. Shavitt. Correlation Problems in Atomic and Molecular Systems. IV. Extended Coupled-Pair Many-Electron Theory and Its Application to the BH_3 Molecule. **5**:50–67, 1972.

[302] G. D. Purvis III and R. J. Bartlett. A full coupled-cluster singles and doubles model: The inclusion of disconnected trrples. *J. Chem. Phys.*, **76**:1910–1918, 1981.

[303] S. A. Kucharski and R. J. Bartlett. The coupled-cluster single, double, triple, and quadruple excitation method. *J. Chem. Phys.*, **97**:4284–4288, 1992.

[304] W. Hoyer, M. Kira, and S. W. Koch. Influence of Coulomb and phonon interaction on the exciton formation in semiconductor heterostructures. *Phys. Rev. B*, **67**:155113, 2003.

[305] M. Kira and S. W. Koch. Quantum-optical spectroscopy of semiconductors. *Phys. Rev. A*, 73:013813, 2006.

[306] M. Kira and S. W. Koch. Cluster-expansion representation in quantum optics. 78:022102, 2008.

[307] S. Leinß , T. Kampfrath, K. v.Volkmann, M. Wolf, J. T. Steiner, M. Kira, S. W. Koch, A. Leitenstorfer, and R. Huber. Terahertz Coherent Control of Optically Dark Paraexcitons in Cu_2O. *Phys. Rev. Lett.*, 101:246401, 2008.

[308] J. Fricke. Transport Equations Including Many-Particle Correlations for an Arbitrary Quantum System. *Ann. Phys. (N.Y.)*, **252**:479–498, 1996.

[309] M. Lindberg and S.W. Koch. Effective Bloch Equations for Semiconductors. *Phys. Rev. B*, **38**:3342, 1988.

[310] T. Rappen, U.-G. Peter, M. Wegener, and W. Schäfer. Polarization dependence of dephasing processes: A probe for many-body effects. *Phys. Rev. B*, **49**:10774–10777, 1994.

[311] M. Schäfer. *Microscopic Theory of Coherent and Incoherent Optical Properties of Semiconductor Heterostructures*. PhD thesis, Philipps-Universität Marburg, 2008.

[312] W. Schäfer, R. Lövenich, N. A. Fromer, and D. S. Chemla. From Coherently Excited Highly Correlated States to Incoherent Relaxation Processes in Semiconductors . *Phys. Rev. Lett.*, **86**:344–347, 2001.

[313] J. Shah. *Ultrafast spectroscopy of semiconductors and semiconductor nanostructures*. Springer, Berlin, first edition, 1996.

[314] J.-C. Diels and W. Rudolph. *Ultrashort Laser Pulse Phenomena – Fundamentals, Techniques, and Applications on a Femtosecond Time Scale*. Academic Press, San Diego, second edition, 2006.

[315] W. Demtröder. *Laser Spectroscopy – Volume 2, Experimental Techniques*. Springer, Berlin, fourth edition, 2008.

[316] J. Eichler and H. J. Eichler. *Laser – Bauformen, Strahlführung, Anwendungen*. Springer, Berlin, sixth edition, 2006.

[317] P. Brick, C. Ell, M. Hübner J. P. Prineas, G. Khitrova, H. M. Gibbs, C. Sieh, T. Meier, F. Jahnke, A. Knorr, and S. W. Koch. Coulomb Memory Effects and Higher-Order Coulomb Correlations in the Excitonic Optical Stark Effect. *Phys. Stat. Sol. A*, **178**:459–463, 2000.

[318] A. Liu and C. Z. Ning. Near-infrared laser pumped intersubband THz laser gain in InGaAs-AlAsSb-InP quantum wells. *Appl. Phys. Lett.*, **76**:1984–1986, 2000.

[319] Y. H. Ahn, S. B. Choe, J. C. Woo, D. S. Kim, S. T. Cundiff, J. M. Shacklette, and Y. S. Lim. Quantum Interference of Virtual and Real Amplitudes in a Semiconductor Exciton System. *Phys. Rev. Lett.*, **89**:237403, 2002.

[320] m. Choi, K.-C. Je, S.-Y. Yim, and S.-H. Park. Relative strength of the screened Coulomb interaction and phase-space filling on exciton bleaching in multiple quantum well structures. *Phys. Rev. B*, **70**:085309, 2004.

[321] S. Siggelkow, W. Hoyer, M. Kira, and S. W. Koch. Exciton formation and stability in semiconductor heterostructures. *Phys. Rev. B*, **69**:073104, 2004.

[322] W. Hoyer, C. Ell, M. Kira, S. W. Koch, S. Chatterjee, S. Mosor, G. Khitrova, H. M. Gibbs, and H. Stolz. Many-body dynamics and exciton formation studied by time-resolved luminescence. *Phys. Rev. B*, **72**:075324, 2005.

[323] E. Merzbacher. *Quantum Mechanics*. Wiley, New York, first edition, 1961.

[324] M. Kira. Complementary quantum dynamics. *Report Series in Theoretical Physics, University of Helsinki*, HU-TFT-IR-95-3:1–115, 1995.

[325] E. Hecht. *Optics*. Addison Wesley, San Francisco, CA, USA, 4th edition, 2002.

[326] M. Born and E. Wolf. *Principles of Optics*. Cambridge University Press, seventh edition, 1999.

[327] S. D. Baranovskii and A. L. Efros. Band Edge Smearing in Solid Solutions. *Sov. Phys. Semicond.*, **12**:1328–1330, 1978.

[328] R. Zimmermann. Theory of Dephasing in Semiconductor Optics. *Phys. Stat. Sol. B*, **173**:129–137, 1992.

[329] R. Zimmermann and E. Runge. Exciton lineshape in semiconductor quantum structures with interface roughness. *J. Lumin.*, **60/61**:320–323, 1994.

[330] L. Schultheis, A. Honold, J. Kuhl, K. Köhler, and C. W. Tu. Optical dephasing of homogeneously broadened two-dimensional exciton transitions in GaAs quantum wells. *Phys. Rev. B*, **34**:9027–9030, 1986.

[331] B. Grote, C. Ell, S. W. Koch, H. M. Gibbs, G. Khitrova, J. P. Prineas, and J. Shah. Resonance Rayleigh scattering from semiconductor heterostructures: The role of radiative coupling. *Phys. Rev. B*, **64**:045330, 2001.

[332] S. Rudin and T. L. Reinecke. Effects of exciton-acoustic-phonon scattering on optical line shapes and exciton dephasing in semiconductors and semiconductor quantum wells. *Phys. Rev. B*, **66**:085314, 2002.

[333] A. Thränhardt, C. Ell, S. Mosor, G. Rupper, G. Khitrova, and H. M. Gibbs. Interplay of phonon and disorder scattering in semiconductor quantum wells. *Phys. Rev. B*, **68**:035316, 2003.

[334] M. Schäfer. private communication.

[335] C. Bückers. private communication.

[336] D. Hulin, A. Mysyrowicz, A. Antonetti, A. Migus, W. T. Masselink, H. Morkoc, H. M. Gibbs, and N. Peyghambarian. An ultrafast all optical gate with subpicosecond on and off response time. *Appl. Phys. Lett.*, **49**:749–751, 1986.

[337] M. Henini. NTT all-optical switch for ultra-fast processing. *III-Vs Review*, **9**:68–70, 1996.

[338] K. Tada, S. Nishimura, and T. Ishikawa. Polarization-independant optical waveguide intensity switch with parabolic quantum-well. *Appl/ Phys. Lett.*, **59**:2778–2780, 1991.

[339] J. P. Prineas, J. Y. Zhou, J. Kuhl, H. M. Gibbs, G. Khitrova, S. W. Koch, and A. Knorr. Ultrafast ac Stark effect switching of the active photonic band gap from Bragg-periodic semiconductor quantum wells. *Appl. Phys. Lett.*, **81**:4332–4334, 2002.

[340] Z. S. Yang, N. H. Kwong, R. Binder, and A. L. Smirl. Stopping, storing, and releasing light in quantum-well Bragg structures. *J. Opt. Soc. Am. B*, **22**:2144–2156, 2005.

[341] J. P. Prineas, W. J. Johnston, M. Yildirim, J. Zhao, and A. L. Smirl. Tunable slow light in Bragg-spaced quantum wells. *Appl. Phys. Lett.*, **89**:241106, 2006.

[342] X. Fu, Y. Liu, P. Zhou, and W. Sritrakool. Perfect self-similarity of energy spectra and gap-labeling properties in one-dimensional Fibonacci-class quasilattices. *Phys. Rev. B*, **55**:2882–2889, 1997.

[343] Z. Lin, M. Goda, and H. Kubo. A family of generalized Fibonacci lattices: self-similarity and scaling of the wavefunction. *J. Phys. A*, **28**:853–866, 1995.

[344] F. Schwabl. *Quantenmechanik (QM I): Eine Einführung*. Springer, Berlin, seventh edition, 2007.

[345] C. Cohen-Tannoudji, B. Dui, and F. Laloe. *Quantum Mechanics*. Wiley, New York, first edition, 1977.

[346] L. Esaki. Long journey into tunneling. *Rev. Mod. Phys.*, **46**:237–244, 1974.

[347] P. Guéret, E. Marclay, and H. Meier. Investigation of possible dynamic polarization effects on the transmission probability of n-GaAs/$Al_xGa_{1-x}As$/n-GaAs tunnel barriers. *Solid State Commun.*, **68**:977–979, 1988.

[348] P. Guéret, E. Marclay, and H. Meier. Experimental observation of the dynamical image potential in extremely low GaAs/Al_xGa_{1x}As/GaAs tunnel barriers. *Appl. Phys. Lett.*, **53**:1617–1619, 1988.

[349] L. L. Chang, L. Esaki, and R. Tsu. Resonant tunneling in semiconductor double barriers. *Appl. Phys. Lett.*, **24**:593–595, 1974.

[350] H. Mizuta and T. Tanue. *Physics and Applications of Resonant Tunnelling Diodes.* Cambridge University Press, Cambridge, first edition, 2003.

[351] K. Ebert, R. Duschl, O. G. Schmidt, U. Denker, and R. Haug. Si-based resonant inter- and intraband tunneling diodes. *J. Crystal Growth*, **227–228**:770–776, 2001.

[352] L. V. Iogansen. The possibility of Resonance Transmission of Electrons in Crystals Through a System of Barriers. *Soviet Physics: JETP*, **18**:146, 1964.

[353] R. Tsu and L. Esaki. Tunneling in a Finite Superlattice. *Appl. Phys. Lett.*, **22**:562–564, 1973.

[354] C. J. Chen. *Introduction to Scanning Tunneling Microscopy.* Oxford University Press, first edition, 1993.

[355] G. Gamow. Zur Quantentheorie des Atomkernes. *Z. Phys.*, **51**:204, 1928.

[356] R. Y. Chiao, P. G. Kwiat, and A. M. Steinberg. Analogies between electron and photon tunneling - A proposed experiment to measure photon tunneling times. *Physica B*, **175**:257–262, 1991.

[357] M. Kira, I. Tittonen, and S. Stenholm. Particle Characteristics of Conventional and Resonant Tunneling. *Physica Scripta*, 54:549–562, 1996.

[358] M. Kira, I. Tittonen, and S. Stenholm. Invariant time object in particle tunnelling. *Europhys. Lett.*, 33:689–694, 1996.

[359] E. H. Hauge and J. A. Stovneng. Tunneling times: a critical review. *Rev. Mod. Phys.*, **61**:917–936, 1989.

[360] T. E. Hartmann. Tunneling of a Wave Packet. *J. Appl. Phys.*, **33**:3427–, 1962.

[361] A. M. Steinberg, P. G. Kwiat, and R. Y. Chiao. Measurement of the single-photon tunneling time. *Phys. Rev. Lett.*, **71**:708–711, 1993.

[362] F. Capasso, K. Mohammed, and A. Y. Cho. Resonant Tunneling Through Doublke Barriers, Perpendicular Quantum Transport Phenomena in Superlattices, and Their Device Applications. *IEEE J. Quantum Electr.*, **QE-22**:1853–1869, 1986.

[363] P. Leurgans and A. F. Turner. *J. Opt. Soc. Am.*, 37:983, 1947.

[364] A. Haibel, G. Nimtz, and A. A. Stahlofen. Frustrated total reflection: The double-prism revisited. *Phys. Rev. E*, **63**:047601, 2000.

[365] R. C. Reddick, R. J. Warmack, and T. J. Ferrell. New Form of Scanning Optical Microscopy. *Phys. Rev. B*, **39**:767–770, 1989.

[366] S. Tomita, T. Yokoyama, H. Yanagi, B. Wood, J. B. Pendry, M. Fujii, and S. Hayashi. Resonant photon tunneling via surface plasmon polaritons through one-dimensional metal-dielectric metamaterials. *Opt. Express*, **16**:9942–9950, 2008.

[367] S. Hayashi, H. Kurokawa, and H. Oga. Observation of Resonant Photon Tunneling in Photonic Double Barrier Structures. *Opt. Rev.*, **6**:204–210, 1999.

[368] G. Guan, H. Jiang, Y. Zhang H. Li, H. Chen, and S. Zhu. Tunneling modes of photonic heterostructures consisting of single-negative materials. *Appl. Phys. Lett.*, **38**:114–117, 1965.

[369] C. J. Fu, Z. M. Zhang, and D. B. Tanner. Energy Transmission by Photon Tunneling in Multilayer Structures Including Negative Index Materials. *Transactions of the ASME*, 127:1046–1052, 2005.

[370] F. J. García de Abajo, G. Gómez-Santos, L. A. Blanco, A. G. Borisov, and S. V. Shabanov. Tunneling Mechanism of Light Transmission through Metallic Films. *Phys. Rev. Lett.*, **95**:067403, 2005.

[371] R. Dragila, B. Luther-Davies, and S. Vukovic. High Transparency of Classically Opaque Metallic Films. *Phys. Rev. Lett.*, **55**:1117–1120, 1985.

[372] Ch. Spielmann, R. Szip—'ocs, A. Stingl, and F. Krausz. Tunneling of Optical Pulses through Photonic Band Gaps. *Phys. Rev. Lett.*, **73**:2308–2311, 1994.

[373] Y. Jiang, C. Niu, and D. L. Lin. Resonance tunneling through photonic quantum wells. *Phys. Rev. B*, **59**:9981–9986, 1999.

[374] A. M. Steinberg and R. Y. Chiao. Subfemtosecond determination of transmission delay times for a dielectric mirror (photonic band gap) as a function of the angle of incidence. *Phys. Rev. A*, **51**:3525–3528, 1995.

[375] N. Yamamoto and N. Ohtani. All-Optical Switching and Memorizing Devices Using Resonant Photon Tunneling Effect in Multi-Layered GaAs/AlGaAs Structures. *Jap. J. Appl. Phys.*, **43**:1393–1397, 2004.

[376] N. Yamamoto, K. Akahane, S.-I. Gozu, and N. Ohtani. All-optical control of the resonant-photon tunneling effect observed in GaAs/AlGaAs multilayered structures containing quantum dots. *Appl. Phys. Lett.*, **87**:231119, 2005.

[377] T. Gruner and D.-G. Welsch. Photon tunneling through absorbing dielectric barriers. *Opt. Commun.*, **134**:447–454, 1997.

[378] I. I. Smolianinov, C. C. Davic, and A. V. Zayats. Light-controlled photon tunneling. *Appl. Phys. Lett.*, **81**:3314–3316, 2002.

[379] W. Li and S. M. Sadeghi. Asymmetric coherent photon tunneling filter in an optical waveguide structure. *Opt. Quant. Electron.*, **39**:773–780, 2007.

[380] N. Fang, H. Lee, C. Sun, and X. Zhang. Sub-diffraction-limeted optical imaging with a silver superlense. *Science*, 308:534–537, 2005.

[381] R. A. Soref. Silicon-based optoelectronics. *Proc. IEEE*, **81**:1687–1706, 1993.

[382] A. G. Rickman. Silicon Integrated Optics and Sensor Applications. *Sensor Review*, **14**:27–29, 1994.

[383] A. Loni, L. T. Canham, M. G. Berger, R. Arens-Fischer, H. Munder, H. Luth, H. F. Arrand, and T. M. Benson. Porous silicon multilayer optical waveguides. *Thin Solid Films*, **276**:143–146, 1996.

[384] V. Agarwal and J. A. del Río. Tailoring the photonic band gap of a porous silicon dielectric mirror. *Appl. Phys. Lett.*, **82**:1512–1514, 2003.

[385] M. Ghulinyan, C. J. Oton, Z. Gaburro, P. Bettotti, and L. Pavesi. Porous silicon free-standing coupled microcavities. *Appl. Phys. Lett.*, **82**:1550–1552, 2003.

[386] A. Liu, R. Jones, L. Liao, D. Samara-Rubio, D. Rubin, O. Cohen, R. Nicolaescu, and M. Paniccia. A high-speed silicon optical modulator based on a metal-oxide-semiconductor capacitor. *Nature*, **427**:615–618, 2004.

[387] A. Haché and M. Burgeois. Ultrafast all-optical switching in silicon-based photonic crystal. *Appl. Phys. Lett.*, **77**:4089–4091, 2000.

[388] F. Z. Henari, K. Morgenstern, W. J. Blau, V. A. Karavanskii, and V. S. Dneprovskii. Third-order optical nonlinearity and all-optical switching in porous silicon. *Appl. Phys. Lett.*, **67**:323–325, 1995.

[389] Q. Xu, B. Schmidt, S. Pradhan, and M. Lipson. Micrometre-scale silicon electro-optic modulator. *Nature*, **435**:325–327, 2005.

[390] Y. A. Vlasov, M. O'Boyle, H. F. Hamann, and S. J. McNab. Active control of slow light on a chip with photonic crystal waveguides. *Nature*, **438**:65–69, 2005.

[391] C. Monat, B. Corcoran, M. Ebnali-Heidari, C. Grillet, B. J. Eggleton, T. P. White, L. O'Faolain, and T. F. Krauss. Slow light enhancement of nonlinear effects in silicon engeneered photonic crystal waveguides. *Opt. Express*, **17**:2944–2953, 2009.

[392] J. F. McMillan, X. Yang, N. C. Panoiu, R. M. Osgood, and C. W. Wong. Enhanced stimulated Raman scattering in slow-light photonic crystal waveguides. *Appl. Phys. Lett.*, **77**:4089–4091, 2000.

[393] J. T. Robinson, L. Chen, and M. Lipson. Ultrafast all-optical switching in silicon-based photonic crystal. *Appl. Phys. Lett.*, **77**:4089–4091, 2000.

[394] S. Babin, A. Bugrov, S. Cabrini, S. Dhuey, A. Goltsov, I. Ivonin, E.-B. Kley, C. Peroz, H. Schmidt, and V. Yankov. Digital optical spectrometer-on-chip. *Appl. Phys. Lett.*, **95**:041105, 2009.

[395] L. Sainimei. *Cryogenic deep reactive ion etching of silicon micro and nanostructures*. PhD thesis, Helsinki University of Technology, 2009.

[396] J. M. Vigoureux and F. Baïda. Critical size of multi-resonant optical tunneling structures. Application to nonradiative effects. *Optics Commun.*, **101**:297–302, 1993.

Abbreviations

Used abbreviations in alphabetic order:

ARC	**A**nti-**R**eflection **C**oating
EID	**E**xcitation **I**nduced **D**ephasing
FIB	**F**ocused **I**on **B**eam
FWHM	**F**ull **W**idth at **H**alf **M**aximum
hh	**h**eavy **h**ole
IC	**I**ntegrated **C**ircuit
LED	**L**ight **E**mitting **D**iode
lh	**l**ight **h**ole
MBE	**M**olecular **B**eam **E**pitaxy
MOVPE	**M**etal **O**rganic **V**apor **P**hase **E**pitaxy
MQW	**M**ultiple **Q**uantum **W**ell
NMC	**N**ormal **M**ode **C**oupling
QC	**Q**uasi**C**rystal
QW	**Q**uantum **W**ell
RWA	**R**otating **W**ave **A**pproximation

Publications

Papers

- M. Werchner, M. Schafer, M. Kira, S.W. Koch, J. Sweet, J.D. Olitzky, J. Hendrickson, B.C. Richards, G. Khitrova, H.M.Gibbs, A.N. Poddubny, E.L. Ivchenko, M. Voronov, and M. Wegener, *One dimensional resonant Fibonacci quasicrystals: noncanonical linear and canonical nonlinear effects*, Opt. Express **17**, 6813 (2009)

- M. Schäfer, M. Werchner, W. Hoyer, M. Kira, and S.W. Koch, *Quantum theory of luminescenence in multiple-quantum-well Bragg structures*, Phys. Rev. B **74**, 155315 (2006)

Posters and Talks

- J. R. Hendrickson, B. C. Richards, J. Sweet, G. Khitrova, A. N. Poddubny, E. L. Ivchenko, M. Wegener, M. Werchner, M. Schäfer, M. Kira, S. W. Koch, and H. M. Gibbs, Talk: *Optical Properties of 1-D Active Fibonacci Quasicrystals*, CLEO/IQEC 2009 Baltimore, Maryland, USA (May 31-June 5, 2009)

- J. Sweet, J. R. Hendrickson, B. C. Richards, G. Khitrova, A. N. Poddubny, E. L. Ivchenko, M. Wegener, M. Werchner, M. Schäfer, M. Kira, S. W. Koch, and H. M. Gibbs, Poster: *Nonlinear Reflectivity of Fibonacci Quantum Wells*, PQE 2009 Snowbird, Utah, USA (January 4-8, 2009)

- M. Werchner, M. Schäfer, W. Hoyer, M. Kira, and S. W. Koch, Talk: *Microscopic Investigations of Luminescence from Muliple Quantum-Well Structures*, DPG spring meeting Regensburg, Germany (March 26-30, 2007)

- M. Schäfer, M. Werchner, W. Hoyer, M. Kira, and S. W. Koch, Talk: *Radiative Lifetime of Excitons in Multi Quantum-Well Systems*, DPG spring meeting Dresden, Germany (March 26-31, 2006)
- M. Werchner, M. Schäfer, W. Hoyer, M. Kira, and S. W. Koch, Talk: *Quantum-optical and classical spectroscopy with radiatively coupled quantum wells*, DPG spring meeting Frankfurt, Germany (March 13-17, 2006)
- M. Schäfer, M. Werchner, M. Kira, and S. W. Koch, Poster: *Multi Quantum-Well Luminescence*, Cliff-Hotel Sellin, Rügen, Germany (March 14-17, 2004)

Persönlicher Werdegang

Name	Marco Werchner

1987–1991	Grundschule Ernsthausen
1991–2000	Gymnasium Edertalschule in Frankenberg (Eder)
2000	Abitur am Gymnasium Edertalschule
2000	Beginn des Diplomstudiengangs Physik an der Philipps-Universität Marburg
2002	Vordiplom im Fach Physik
2005	Diplom im Fach Physik ; Thema der Diplomarbeit: "Microscopic Theory of Quantum Electrodynamical Spectroscopy in Multiple Quantum-Well Systems"
2005	Beginn der Promotion in der Arbeitsgruppe "Theoretische Halbleiterphysik"des Fachbereichs Physik der Philipps-Universität Marburg

Danksagung

Meine Danksagung möchte ich mit einem Dank an meine Eltern beginnen, die mich sowohl während meines Studiums als auch während der Doktorandenzeit stets unterstützt und mir den Rücken freigehalten haben. In diesen Dank einschließen möchte ich meine Schwestern Carolin und Nadine sowie auch meine gesamte Familie. Sie waren in allen Lebenslagen für mich da und gaben mir den Rückhalt, um die auftretenden Schwierigkeiten meistern und alle Hürden überwinden zu können. Somit haben auch sie entscheidend am Entstehen dieser Arbeit, die ich ihnen widme, mitgewirkt.

Ein besonderer Dank gilt meinem Doktorvater Professor Mackillo Kira für die Vergabe des interessanten Themas sowie für die gute Betreuung und Begleitung meiner Arbeit – nicht nur in physikalischen Belangen sondern auch darüber hinaus!
Kiitos paljon selkeistä ohjeista, asiantuntijan neuvoista ja todella motivoivasta palautteesta. Kiitos myös ymmärryksestäsi ja huolenpidostasi, kun kärsin vakavasta sairaudesta ja kun yritin saada terveyteni takaisin sairauden jälkeen.

Für die Aufnahme als Doktorand in die "Halbleitertheorie" in die MG33 und somit für die Möglichkeit, diese Arbeit in ihrer Arbeitsgruppe anfertigen zu können, danke ich Professor Stephan Koch und nochmals Mack sehr herzlich!

Bei Professor Wolfgang Stolz bedanke ich mich für die Bereitschaft, als Zweitgutachter zur Verfügung zu stehen. Ebenso gebührt mein Dank den Professoren Reinhard Noack und Bernd Harbrecht, die sich bereit erklärt haben, der Prüfungskommission anzugehören.

Nicht genug danken kann ich meinen Hausärzten Drs. Gerhard Seidel, Carsten Nordmann und Markus Schraub sowie Professor Andreas Neubauer, PD Dr. Andreas Burchert und Dr. Stephan Metzelder und dem erstklassigen Team der Station 224 "Hämatologie/ Onkologie" des Universitätsklinikums Marburg – stellvertretend seien hier Beate, Chri-

stoph und Gitta genannt – , die durch ihren Einsatz und ihre Pflege dafür gesorgt haben, dass ich im wahrsten Sinne des Wortes in letzter Sekunde noch einmal die Kurve gekriegt habe und ich heute wieder auf dem Damm bin. Ohne ihre Hilfe hätte diese Arbeit zumindest nicht mehr von mir beendet werden können. Auch für das seitdem Erlebte und das, was ich noch erleben darf, meinen herzlichsten Dank!

Allen derzeitigen und ehemaligen Mitgliedern unserer Arbeitsgruppe möchte ich für das hervorragende Arbeitsklima sowie für viele physikalische und nicht physikalische Diskussionen und Gespräche danken, wodurch sowohl das Arbeiten als auch das Miteinander sehr bereichert wurde. Meinen Zimmergenossen Johannes Blaschke, Tri Dung Doan, Daniel Golde, Eckhard Kühn, Christoph Michel und Martin Mootz danke ich für die schöne gemeinsame Zeit, die stets gute Stimmung im Büro und für so mancherlei Abwechslung von der Physik.

Insbesondere sei hier mit Martin Schäfer der andere Teil von "M&M" genannt, mit dem ich zunächst gemeinsam Seite an Seite das Studium bewältigt habe und mit dem ich später immer das Büro geteilt und eng zusammengearbeitet habe. Danke! Ebenso danke ich Walter Hoyer, der mir stets mit Rat und Tat zur Seite stand. Nicht unerwähnt bleiben darf Professor Peter Thomas, der durch seine herzliche Art und unerschöpfliche Physikbegeisterung stets und besonders auch in Durststrecken für gute Laune und neue Motivation sorgte. Danke auch für die Wanderungen im Marburger Umland, in der Pfalz oder im Elsass, die für den nötigen Ausgleich und die geselligen Momente in unserer AG sorgten.

Matthias Reichelt und Bernhard Pasenow sei Dank für ihren unermüdlichen Einsatz, die Computer am Laufen zu halten, sowie für jegliche Hilfe bei Computerproblemen!

Bei Martin, Carolin und Nadine, die die Arbeit ganz oder in Teilen gelesen haben, bedanke ich mich sehr für mancherlei Anmerkungen, die dazu beigetragen haben, die Zahl der Tippfehler zu reduzieren und die Klarheit der Aussagen und Argumentationen zu fördern.

Für die gute Zusammenarbeit bei den Fibonacci-Mehrfachquantenfilmstrukturen möchte ich mich bei Julian Sweet, Benjamin Richards, Joshua Hendrickson, JD Olitzky sowie bei Professor Galina Khitrova und Professor Hyatt Gibbs aus der Arbeitsgruppe "Quantum Nanooptics of Semiconductors" des Optical Sciences Centers der University of Arizona, Tucson USA, wie auch bei Alexander Poddubny und Professor Eugeneous Ivchenko aus der Arbeitsgruppe "Theory of Quantum Coherent Phenomena in Solids" des Ioffe Physical Technical Institutes in Sankt Petersburg, Russland, bedanken.
Thanks a lot for the good collaboration and for sharing your knowledge with me!
Большое спасибо за хорошую и приятную совместную работу и за то что я имел возможность от вас на теме "Fibonacci" мнимые кристаллы научиться!

Ebenso gilt mein Dank Nikolai Chekurov und Professor Ilkka Tittonen aus der Arbeitsgruppe "Micro and Quantum Systems" und dem Zentrum "Micronova" der technischen

Universität Helsinki, mit denen ich gemeinsam am resonanten Tunneln von Licht durch Silizium-Luft Schichtstrukturen arbeiten durfte.
Haluaisin kiittää teitä hyvästä ja innoittavasta yhteistyöstä, sekä avustanne tuoda kokeellisen fysiikan maailma minulle tutummaksi. Oli ilo työskennellä kanssanne!

Allen meinen Freunden – in der Mehrzahl aus Ernsthausen und Umgebung, natürlich auch aus Marburg, aber unter anderem auch aus Australien, Kanada, den USA und Ungarn – danke ich für die schönen Dinge abseits der Physik und das gemeinsam Erlebte. Egal ob beim Fußball, beim Musizieren, beim Platzen oder Osterfeuer, oder einfach beim gemütlichen Beisammensein, ihr habt immer für die nötige Abwechslung und Ablenkung gesorgt, sodass ich mich mit freiem Kopf wieder frisch der Physik zuwenden konnte. Danke auch für euer Verständnis, wenn ich mal wieder "keine Zeit" hatte oder "noch mal nach Marburg" musste, dafür, dass Ihr, wenn ich mich wieder rar gemacht hatte bzw. mich länger nicht gemeldet hatte, doch immer wieder den Kontakt aufrecht erhalten habt, für euren Beistand und die Hilfe während Krankheit und Rekonvalenszenz und für euer Mahnen, es nicht zu übertreiben, auf das ich aber allzu oft nicht gehört habe.

Wenn ich auch hoffe, niemanden vergessen zu haben, so möchte ich mich doch nicht davon freisprechen, dass mir genau dies doch unterlaufen sein kann. Sollte es trotz allem der Fall sein, so bitte ich, mir dies nachzusehen – es war ein Versehen. Daher möchte ich an alle gerichtet abschließend noch einmal sagen:

Danke!

Kiitos paljon! Thank you!

спасибо! Köszönöm!

Wenn man auf ein Ziel zugeht,
ist es äußerst wichtig,
auf den Weg zu achten.
Denn der Weg lehrt uns am besten,
ans Ziel zu gelangen,
und er bereichert uns,
während wir ihn zurücklegen.

Paolo Coelho